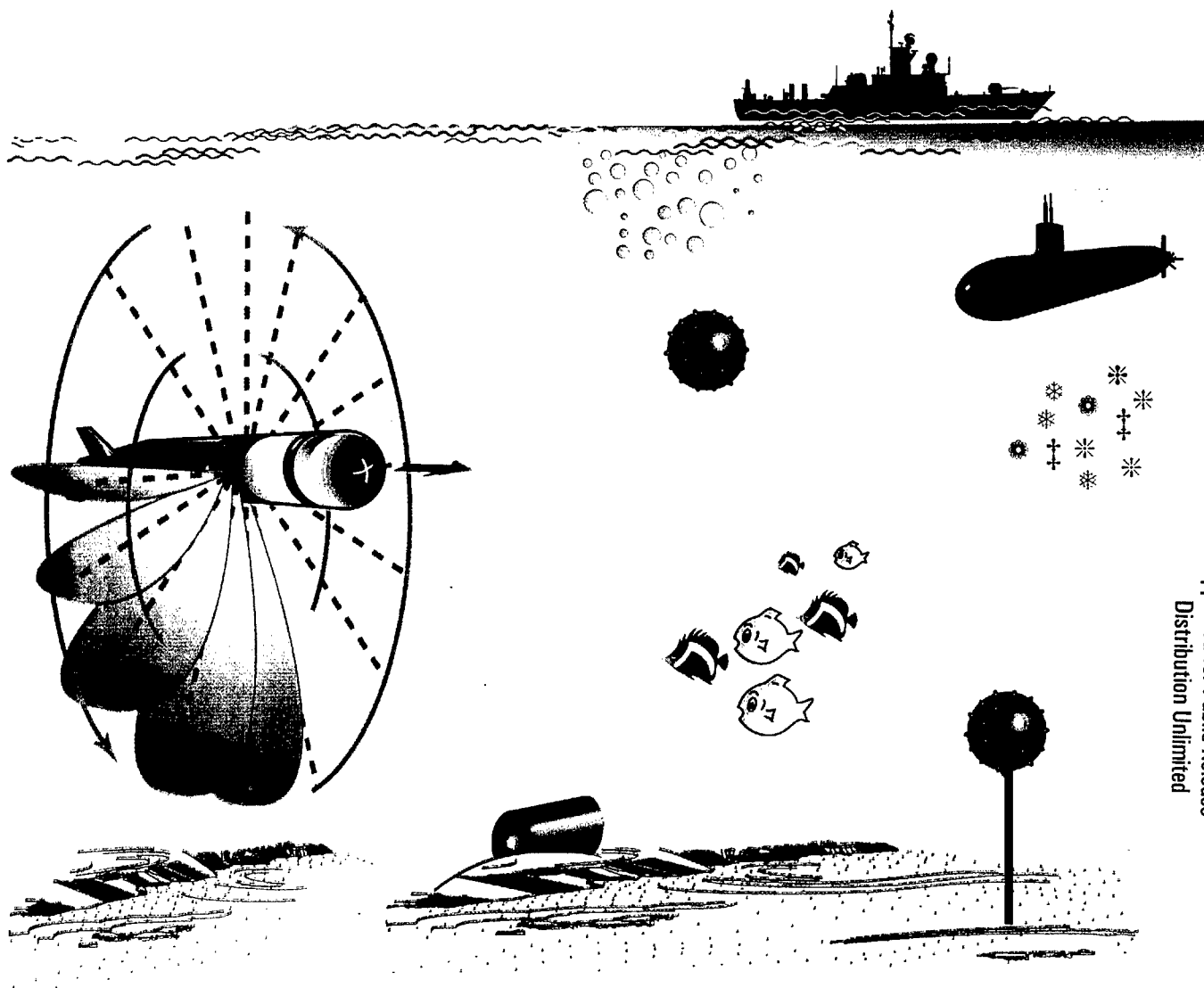


# Shallow Water Acoustic Backscatter and Reverberation Measurements Using a 68-kHz Cylindrical Array

Timothy C. Gallaudet

Marine Physical Laboratory  
*Scripps Institution of Oceanography*  
University of California, San Diego

2001



DISTRIBUTION STATEMENT A:  
Approved for Public Release -  
Distribution Unlimited

AD NUMBER	DATE 17 JUNE 02	DTIC ACCESSION NOTICE
1. REPORT IDENTIFYING INFORMATION		<b>20020710 022</b>  <b>REQUE</b> 1. Put you on reve. 2. Complet 3. Attach if mailed 4. Use unc. inform. 5. Do not c for 6 to  <b>DTIC:</b> 1. Assign. 2. Return
A. ORIGINATING AGENCY		
NAVAL POSTGRADUATE SCHOOL, MONTEREY, CA 93943		
<del>REPORT TITLE AND OR NUMBER</del> SHALLOW WATER ACOUSTIC BACKSCATTER AND REVERBERATION MEASUREMENTS USING...		
C. MONITOR REPORT NUMBER		
BY TIMOTHY C. GALLAUDET, UC SAN DIEGO		
D. PREPARED UNDER CONTRACT NUMBER		
N62271-97-G-0069		
2. DISTRIBUTION STATEMENT		
APPROVED FOR PUBLIC RELEASE; DISTRIBUTION UNLIMITED		

PREVIOUS EDITIONS ARE OBSOLETE

DTIC Form 50  
DEC 91

UNIVERSITY OF CALIFORNIA, SAN DIEGO

Shallow Water Acoustic Backscatter and Reverberation Measurements  
Using a 68-kHz Cylindrical Array

A dissertation submitted in partial satisfaction  
for the degree Doctor of Philosophy in

Oceanography

by

Timothy C. Gallaudet

Committee in charge:

Christian de Moustier, Chair  
William Hodgkiss  
William Kuperman  
Robert Lugannani  
Robert Pinkel

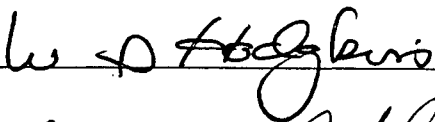
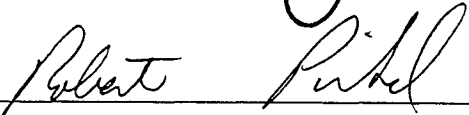
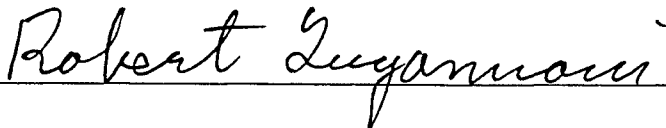

2001

20020710 022

Copyright  
Timothy C. Gallaudet, 2001  
All rights reserved



The dissertation of Timothy C. Gallaudet is approved, and it  
is acceptable in quality and form for publication on microfilm:

  
  
  
  
CHRISTIAN de MOUSTIER Chair

University of California, San Diego

2001

37 And there arose a great storm of wind, and the waves beat into the ship, so that it was now full.

38 And he was in the hinder part of the ship, asleep on a pillow; and they woke him and said unto him, Master, carest thou not that we perish?

39 And he arose, and rebuked the wind, and said unto the sea, Peace, be still. And the wind ceased, and there was a great calm.

40 And he said unto them, Why are ye so fearful? how is it that ye have no faith?

41 And they feared exceedingly, and said one to another, What manner of man is this, that even the wind and the sea obey him?

MARK 4: 37:41

## Table of Contents

<b>Signature Page .....</b>	<b>iii</b>
<b>Dedication .....</b>	<b>iv</b>
<b>Table of Contents .....</b>	<b>v</b>
<b>List of Figures .....</b>	<b>vii</b>
<b>List of Tables .....</b>	<b>ix</b>
<b>Acknowledgments .....</b>	<b>x</b>
<b>Vita, Publications, and Fields of Study .....</b>	<b>xi</b>
<b>Abstract .....</b>	<b>xiii</b>
<b>Chapter 1. Introduction .....</b>	<b>1</b>
<b>Chapter 2. On Optimal Amplitude Shading For Arrays of Irregularly-spaced or Non-coplanar Elements .....</b>	<b>3</b>
Abstract .....	3
I. Introduction .....	3
II. Optimal Array Shading .....	4
III. Resampled Amplitude Shading for Irregular-Line Arrays .....	5
IV. Resampled Amplitude Shading for Non-Coplanar Arrays .....	9
V. Application to the Toroidal Volume Search Sonar (TVSS) .....	10
VI. Summary and Conclusions .....	12
Acknowledgment .....	12
References .....	13
<b>Chapter 3. Using Environmental Information to Estimate and Correct for Errors in Bathymetry and Seafloor Acoustic Imagery .....</b>	<b>35</b>
Abstract .....	35
I. Introduction .....	35
II. TVSS Data .....	36
III. TVSS Processing .....	37
IV. Bathymetry .....	41
V. Seafloor Acoustic Backscattering Strength Imagery .....	46
VI. Conclusions .....	50
Acknowledgment .....	50
References .....	51
<b>Chapter 4. Multibeam Volume Acoustic Backscatter Imagery and Reverberation Measurements in the Northeastern Gulf of Mexico .....</b>	<b>78</b>
Abstract .....	78
I. Introduction .....	78
II. Theoretical Background .....	80
III. TVSS Data .....	83
IV. Imagery Results and Interpretation .....	88
V. Summary and Conclusions .....	97
Acknowledgments .....	98
Appendix. Two-dimensional Variance Spectrum .....	98
References .....	99

<b>Chapter 5. Sea Surface and Volume Acoustic Backscatter Imagery of the Microbubble Field of a Ship's Wake .....</b>	<b>120</b>
Abstract .....	120
I. Introduction .....	120
II. Background .....	121
III. TVSS Data .....	125
IV. TVSS Measurements of the Towship's Wake .....	131
V. Sea Surface Acoustic Backscatter and Near-surface Bubbles .....	139
VI. Summary and Conclusions .....	143
Acknowledgments .....	144
Appendix A. Factors Influencing the Kelvin Wave Pattern and Turbulent Wake of a Moving Ship .....	144
Appendix B. Sound Interaction With Bubbles .....	146
Appendix C. Geometry of the TVSS Towship's Wake .....	148
References .....	149
<b>Chapter 6. High-Frequency Volume and Boundary Acoustic Backscatter Fluctuations in Shallow Water .....</b>	<b>172</b>
Abstract .....	172
I. Introduction .....	172
II. Probability Distribution Models .....	174
III. TVSS Data .....	176
IV. Results .....	182
V. Discussion .....	186
VI. Summary and Conclusions .....	190
Acknowledgments .....	191
Appendix. Skewness and Kurtosis Descriptors .....	191
References .....	193
<b>Chapter 7. Summary and Conclusions .....</b>	<b>215</b>

## List of Figures

### Chapter 2

1. Resampled Amplitude Weights For An Irregular Line Array .....	20
2. Broadside Array Factors For a Uniform Line Array .....	21
3. Broadside Array Factors For An Irregular Line Array .....	22
4. Steered Array Factors For An Irregular Line Array .....	23
5. Broadside Array Factors For An Sparse Irregular Line Array .....	24
6. Element Patterns and Plane Wave Beamforming With a Curved Array .....	25
7. Effect of Element Pattern on the Array Pattern of a Curved Array .....	26
8. Resampled Amplitude Shading Performance .....	27
9. Array Factors For a Uniform Planar Array .....	28
10. Array Factors For a Non-Coplanar Array on a Partial Cylinder .....	29
11. Array Factors For a Non-Coplanar Array on a Partial Sphere .....	30
12. TVSS Split-Aperture Correlator .....	31
13. TVSS Bottom Echo Processing .....	32
14. Bottom Echo Backscatter Data From 1 Ping .....	33
15. Bottom Echo Backscatter Data With and Without Shading .....	34

### Chapter 3

1. TVSS AUV/UUV Deployment Scenario .....	62
2. TVSS Array and Element Patterns .....	63
3. TVSS Track Lines For Runs 1-3, 9 November 1994. ....	64
4. TVSS Split Aperture Processing and Diffraction Effects .....	65
5. A TVSS Ping Displayed in Polar Coordinates of Angle vs. Time. ....	66
6. Split-Aperture Phasor Processed For Bottom Detection .....	67
7. TVSS Acoustic Geometry .....	68
8. Depth Corrected Bathymetry Before and After Roll Error Correction .....	69
9. Roll Error Artifacts in the TVSS Bathymetry .....	70
10. Towfish Roll Errors, Roll Rate, and Corrected Roll .....	71
11. Depth and Roll-corrected Bathymetry .....	72
12. Theoretical and Experimental Bathymetric Errors .....	73
13. Theoretical Positional Errors .....	74
14. Raw and Compensated Seafloor Backscattering Strength Images .....	75
15. Compensated Seafloor Acoustic Backscattering Image .....	76
16. Standard Deviations and Standard Errors .....	77

### Chapter 4

1. TVSS AUV/UUV Deployment Scenario .....	108
2. TVSS Track Lines For Runs 1-3, 9 November 1994. ....	109
3. A TVSS Ping Displayed in Volume Backscattering Strength .....	110
4. TVSS Acoustic Geometry .....	111
5. 97-ping Mean Volume Backscattering Strength Images .....	112
6. Volume Backscattering Strength Images of Two Fish Schools .....	113
7. Three Dimensional Representation of a Fish School .....	114
8. 97-ping Mean Volume Acoustic Scattering Strength Image .....	115
9. Echo-integrated Vertical Volume Scattering Strength Images .....	116

10. Two-dimensional Variance Spectrum .....	117
11. Horizontal and Vertical Variance Spectra .....	118
12. Average Volume Reverberation Levels .....	119

## Chapter 5

1. TVSS Data Collection Deployment .....	159
2. TVSS AUV/UUV Deployment Scenario .....	160
3. Turbulent Wake and Kelvin Wave Pattern For The TVSS's Towship .....	161
4. Turbulent Wake and Kelvin Wave Pattern of the <i>USS Quapaw</i> .....	162
5. A TVSS Ping Displayed in Volume Backscattering Strength .....	163
6. TVSS Acoustic Geometry .....	164
7. Sea Surface Relief Maps .....	165
8. Sea Surface Acoustic Backscattering Strength Image and Data .....	166
9. Vertical Volume Backscattering Strength Images .....	167
10. Sea Surface Acoustic Backscattering Strength Data Comparison .....	168
11. Horizontal Volume Backscattering Strength Image At 3m Depth .....	169
12. Horizontal and Vertical Volume Backscattering Strength Images .....	170
13. Doppler Sonar Response to a Tugboat's Wake .....	171

## Chapter 6

1. TVSS Deployment of 9 November 1994 .....	204
2. TVSS AUV/UUV Deployment Scenario .....	205
3. A TVSS Ping Displayed in Volume Backscattering Strength .....	206
4. TVSS Acoustic Geometry .....	207
5. TVSS-derived Acoustic Backscatter Images .....	208
6. Center Locations of the TVSS Statistical Analysis Regions .....	209
7. $\beta_2$ vs. $\beta_1$ Plot of the TVSS Data .....	210
8. Seafloor Backscatter Amplitude Data Probability of False Alarm .....	211
9. Sea surface Backscatter Amplitude Data Probability of False Alarm .....	212
10. Near-surface Backscatter Amplitude Data Probability of False Alarm .....	213
11. Volume Backscatter Amplitude Data Probability of False Alarm .....	214

## List of Tables

### Chapter 2

1. Shading Performance For Planar and Non-Coplanar Arrays .....	17
---	----

### Chapter 3

1. TVSS Parameters and Deployment Data .....	55
2. Towfish Attitude and Motion Characteristics .....	56
3. Corrected Towfish Depth and Roll Statistics .....	57
4. Sources of Uncertainty in the TVSS Bathymetry .....	58
5. Correlation of Towfish Attitude and Motion Data .....	59
6. Composite Roughness Model Parameters .....	60
7. Sources of Uncertainty in the TVSS Seafloor Backscatter Data .....	61

### Chapter 4

1. Fish School Data .....	105
2. Scattering Layer Data .....	106
3. Average Volume Reverberation Characteristics .....	107

### Chapter 5

1. TVSS Towship Characteristics .....	156
2. Data for the Towship's Wake .....	157
3. Data for Ship-Wave Generated Bubble Clouds .....	158

### Chapter 6

1. Statistical Analysis Regions .....	196
2. Backscatter Amplitude Statistics in Each Analysis Region .....	198
3. KS-Statistics P-Values of Model CDFs Fit to the TVSS Data .....	199
4. RMS Differences Between Model CDFs and the TVSS Data .....	201
5. RMS Differences Between Model CDFs and the TVSS Data for Data With a $PFA \leq 10^{-2}$ .....	202
6. Sample Sizes of TVSS Analysis Regions .....	203

## Acknowledgments

I wish to thank my thesis advisor and committee chair, Christian de Moustier, for his expert guidance, complete loyalty, and tireless dedication. Thank you for picking me up the many times I stumbled.

I would also like to thank Christian de Moustier for his extra efforts in getting the chapters of this thesis published. The majority of chapter two appears in "On optimal amplitude shading for arrays of irregularly spaced or non-coplanar elements," T.C. Gallaudet, and C.P. de Moustier, *IEEE Journal Oceanic Engineering.*, **25**, 553-567 (2000), of which I was the primary investigator and co-author.

My dissertation committee was extremely supportive and helpful. Bill Hodgkiss' instruction in digital signal processing laid the foundation for Chapter 2. Bill Kuperman's experience in underwater acoustics and Rob Pinkel's knowledge of acoustical oceanography helped to motivate the work in chapters 3-5. Rob Lugannani's expertise in probability theory and statistics were especially important in chapter 6.

Many people at the Marine Physical Laboratory and Scripps were exceptionally helpful in my research. Jo Griffith (MPL) worked extremely hard to produce the figures in this thesis; her artistic talents were invaluable. Beve Kennedy provided the best administrative support possible. Diana Stockdale (MPL) was always responsive and helpful with computer issues. Sharon Williams (SIO) and Pat Jordan (MPL) found the means to fund my academic fees. My Master's thesis advisor, Jim Simpson (SIO), deserves special thanks for his guidance and loyalty, without which I would not have returned to Scripps. Thank you all for your help and friendship.

This work would not have been possible without the the help of many people in the Navy Oceanography community. I wish to thank RADM Paul Gaffney for giving me the opportunity to come to Scripps for the second time in 1997. My sincere thanks to LCDR John Dimento for giving me the opportunity to come to Scripps in 1989. Without his vision and hard work, I would never have been re-admitted into the PhD program. I wish to thank CAPT Tim McGee for giving me the confidence to pursue this goal.

This research also would not have been possible without the help from the Coastal Systems Station, Panama City Florida, and the Naval Research Laboratory, Stennis Space Center, MS. Maria Kalcic (NRL), Candy Robertson (CSS), and Lisa Tubridy (CSS) provided important information about the TVSS, and Sam Tooma (NRL) sponsored this research.

The Office of Naval Research funded this work under ONR-NRL Contract No. N00014-96-1-G913. I wish to thank CAPT Tim Schnoor at ONR for his support.

My family deserves all of my love and gratitude. Thank you, Mom and Dad, for believing in me. Thank you, Laurel, for reminding me what is truly important. Thank you, Caren, for showing me that with love, all things are possible.



## Vita

March 18, 1967	Born, Hollywood, California
1989	B.S. (Oceanography), United States Naval Academy, Annapolis, Maryland
1991	M.Sc (Oceanography), University of California, San Diego
1991-1993	U.S. Navy, Operations Officer Oceanographic Unit FIVE, USNS HARKNESS (TAGS-32) Arabian Gulf
1993-1995	U.S. Navy, Command Duty Officer Naval European Meteorology and Oceanography Center, Rota, Spain
1995-1997	U.S. Navy, Meteorology/Oceanography Officer USS PELELIU (LHA-5) San Diego, California
1997-2001	U.S. Navy, Research Oceanographer, Marine Physical Laboratory, Scripps Institution of Oceanography University of California, San Diego
2001	Doctor of Philosophy (Oceanography) University of California, San Diego
2001	U.S. Navy, Meteorology/Oceanography Officer USS KITTY HAWK (CV-63) Yokosuka, Japan

## Publications

T.C. Gallaudet and J. J. Simpson, "Automated cloud screening of AVHRR imagery using split-and-merge clustering," *Remote Sensing of the Environment*, **38**, 77-121 (1991).

T.C. Gallaudet and J. J. Simpson, "An empirical orthogonal function analysis of remotely sensed sea surface temperature variability and its relation to interior oceanic processes off Baja California," *Remote Sensing of the Environment*, **47**, 375-389 (1994).

T.C. Gallaudet and C. de Moustier, "FFT beamforming with cylindrical arrays: Application to the Toroidal Volume Search Sonar," *Journal of the Acoustical Society of America*, **103**(5), Pt. 2, 2898. (1998).

T.C. Gallaudet and C. de Moustier, "Optimal amplitude shading for arrays of irregularly spaced or non-coplanar elements," *Journal of the Acoustical Society of America*, **105**(2), Pt. 2, 1308. (1999).

T.C. Gallaudet and C. de Moustier, "Volume acoustic backscattering measurements with a 68-kHz cylindrical array," *Journal of the Acoustical Society of America*, **108**(5), Pt. 2, 2491 (2000).

T.C. Gallaudet, C.P. de Moustier, and M. Kalcic, "Imaging the ocean boundaries and volume with the Toroidal Volume Search Sonar (TVSS)," in: *Proceedings of the Fourth Annual Symposium on the Mine Problem*, March 13-16, 2000, Monterey, CA (2000).

T.C. Gallaudet, and C.P. de Moustier, "On optimal amplitude shading for arrays of irregularly spaced or non-coplanar elements," *IEEE Journal Oceanic Engineering.*, **25**, 553-567 (2000).

T.C. Gallaudet, and C.P. de Moustier, "Using environmental information to estimate and correct for errors in bathymetry and seafloor acoustic imagery," *IEEE Journal of Oceanic Engineering*, (submitted, 2001).

T.C. Gallaudet, and C.P. de Moustier, "Multibeam volume acoustic backscatter imagery and reverberation measurements in the northeastern Gulf of Mexico," *Journal of the Acoustical Society of America*, (submitted, 2001).

T.C. Gallaudet, and C.P. de Moustier, "Sea surface and volume backscattering strength measurements in the microbubble field of a ship's wake," *Journal of the Acoustical Society of America*, (submitted, 2001).

T.C. Gallaudet, and C.P. de Moustier, "High Frequency Volume and Boundary Acoustic Backscatter Fluctuations in Shallow Water," *Journal of the Acoustical Society of America*, (submitted, 2001).

## **Fields of Study**

### **Major Field: Oceanography**

Studies in Underwater Acoustics.  
Christian de Moustier

Studies in Digital Signal Processing.  
Professor William Hodgkiss

Studies in Digital Image Processing.  
Jim Simpson

Studies in Numerical Linear Algebra.  
Professor Philip Gill

## ABSTRACT OF THE DISSERTATION

### Shallow Water Acoustic Backscatter and Reverberation Measurements Using a 68-kHz Cylindrical Array

by

Timothy C. Gallaudet

Doctor of Philosophy in Oceanography  
University of California, San Diego, 2001  
Christian de Moustier, Chair

The characterization of high frequency, shallow water acoustic backscatter and reverberation is important because acoustic systems are used in many scientific, commercial, and military applications. The approach taken is to use data collected by the Toroidal Volume Search Sonar (TVSS), a 68 kHz multibeam sonar capable of 360° imaging in a vertical plane perpendicular to its direction of travel. With this unique capability, acoustic backscatter imagery of the seafloor, sea surface, and horizontal and vertical planes in the volume is constructed from data obtained in 200m deep waters in the Northeastern Gulf of Mexico when the TVSS was towed 78m below the surface, 735m astern of a towship. The processed imagery provides a quasi-synoptic characterization of the spatial and temporal structure of boundary and volume acoustic backscatter and reverberation.

Diffraction, element patterns, and high sidelobe levels are shown to be the most serious problems affecting cylindrical arrays such as the TVSS, and an amplitude shading method is presented for reducing the peak sidelobe levels of irregular-line and non-coplanar arrays.

Errors in the towfish's attitude and motion sensor, and irregularities in the TVSS's transmitted beampattern produce artifacts in the TVSS-derived bathymetry and seafloor acoustic backscatter imagery. Correction strategies for these problems are described, which are unique in that they use environmental information extracted from both ocean boundaries.

Sea surface and volume acoustic backscatter imagery is used to explore and characterize the structure of near-surface bubble clouds, schooling fish, and zooplankton. The simultaneous horizontal and vertical coverage provided by the TVSS is shown to be a primary advantage, motivating further use of multibeam sonars in these applications.

Whereas boundary backscatter fluctuations are well described by Weibull, K, and Rayleigh mixture probability distributions, those corresponding to volume backscatter are multi-modal, with the log-normal distribution providing the best fits to the centers of the distributions, and the Rayleigh mixture models providing the best fits to the tails of the distributions. The largest distribution tails result from resonant microbubbles and patchy aggregations of zooplankton.

The Office of Naval Research funded this work under ONR-NRL Contract No. N00014-96-1-G913.

## Chapter 1

### Introduction

The characterization of high frequency, shallow water acoustic backscatter and reverberation is important in a wide variety of scientific, commercial, and military applications. Examples include: seafloor imaging, swath bathymetry, air sea interaction and mixing studies, bioacoustic surveys, fisheries stock assessment, underwater communication, naval mine-hunting, and covert, environmental reconnaissance in support of special operations. Of primary interest in these is the statistical characterization of backscatter and reverberation, which is used to assess the performance of underwater acoustic systems, and can provide insight into the characteristics of the acoustic scatterers. Such statistics are influenced by the relationship between the sonar's acoustic geometry and the spatial distribution of scatterers. Whereas the former is usually known from calibration procedures, the latter is more difficult to assess.

This dissertation presents the results of an acoustic backscatter and reverberation study in which the data were collected by the Toroidal Volume Search Sonar (TVSS), a 68 kHz cylindrical array capable of 360° multibeam acoustic imaging in a vertical plane perpendicular to its direction of travel. The unique synoptic three-dimensional perspective afforded by this sonar system is used to relate the statistical properties of bottom, surface, and volume backscatter and reverberation to the spatial and temporal structure of acoustic scatterers. The data studied here were collected during engineering tests by the U.S. Navy's Coastal System Station (CSS), Panama City, Florida, when the TVSS was deployed on a towfish in the Northeastern Gulf of Mexico at a depth of 78m, in waters 200m deep, 735m astern of a towship.

The approach taken is to use the TVSS multibeam geometry and adapt existing oceanic imaging techniques to construct acoustic backscatter imagery of the ocean boundaries, and of horizontal and vertical planes in the ocean volume. The processing requirements of conformal arrays are considered, as well as the required accuracies of the towfish's attitude and motion data. The processed imagery is used to characterize and discriminate between scattering features such as boundary roughness, multiple boundary echoes, fish, zooplankton, and near-surface bubble clouds. These provide the means for relating different spatial distributions of scatterers to various probability distribution models.

Except for the summary and conclusions, each of the following chapters in this dissertation addresses one of the analysis procedures mentioned above, and has been published by, or submitted for publication to a refereed scientific journal. Consequently, some redundancy exists between chapters whenever the TVSS is discussed.

Chapter 2 addresses the special conformal array signal processing requirements of the TVSS. Because sidelobe interference is a significant problem for conformal arrays, the principal objective of this chapter is to examine the receive beampattern of the TVSS and determine the proper processing techniques for reducing peak sidelobe levels.

In Chapter 3, the TVSS acoustic data are used to construct bathymetry and seafloor acoustic backscatter images. Relying on comparisons with previous bathymetric and sediment surveys in the TVSS deployment region, the principal objective of this chapter is to evaluate the accuracy of the TVSS calibration data and the towfish attitude and motion sensors. A second objective is to develop corrections, as necessary, for use in the remainder of the dissertation. The paper corresponding to this chapter was submitted for publication to the *IEEE Journal Oceanic Engineering*.

Chapter 4 evaluates the contributions from biologic scatterers in the TVSS data. The principle objective is to characterize the spatial distribution of acoustic backscatter from zooplankton and fish, and boundary reverberation. As there have been relatively few bioacoustic studies which have used multibeam sonars, the TVSS data analyzed in this chapter demonstrate the advantages and limitations of these systems in such applications. The text of this chapter was submitted for publication to the *Journal of the Acoustical Society of America*.

Analogous to Chapter 4, Chapter 5 evaluates backscattering contributions from the sea surface and near-surface bubbles in the TVSS data. Because near-surface bubbles are such significant sources of acoustic scattering and reverberation, data from the microbubble field in and around the towship's wake are used to examine the physical processes controlling their spatial distributions. Additionally, this chapter intends to demonstrate the advantages and limitations of using multibeam sonars in studies of near-surface processes, which have been studied mostly with single beam systems. This chapter has been submitted for publication to the *Journal of the Acoustical Society of America*.

Using the spatial distributions of scatterers characterized in Chapters 3-5, Chapter 6 attempts to relate them to the statistics of backscatter amplitude, or envelope, fluctuations. A specific objective of this chapter is to evaluate the suitability of a number of probability distribution models for characterizing acoustic backscatter and reverberation fluctuations in shallow water environments. Although this has been done in other studies to varying degrees, none has been able to examine sea surface, seafloor, and volume reverberation simultaneously, and none has been accompanied by a spatial characterization of the scattering field as complete as that provided by the TVSS backscatter imagery.

In the summary and conclusions of Chapter 7, possible future extensions of this research are mentioned, including the use of broadband or multi-frequency toroidal sonars for bubble-size distribution studies and zooplankton biomass estimation, and the application of a system like the TVSS deployed onboard an autonomous or unmanned underwater vehicle (AUV/UUV) as an economical alternative to shipboard systems for multibeam seafloor surveys.

## Chapter 2

### On Optimal Shading For Arrays of Irregularly-Spaced Or Non-Coplanar Elements

#### ABSTRACT

The majority of optimal shading methods for arrays of irregularly spaced or non-coplanar elements rely on numerical optimizations and iterative techniques to compute the desired weighting function because analytic solutions generally do not exist. Optimality is meant here in the Dolph-Chebyshev sense to provide the narrowest mainlobe width for a given sidelobe level. We present a simple and efficient technique to compute real shading coefficients for nonuniform-line, curved-line, and non-coplanar arrays by resampling the optimal Dolph-Chebyshev window computed for a uniform line or plane array of equivalent aperture at the element position of the irregular array. Computer simulation examples of narrowband plane-wave beamforming with irregular arrays, in which phase compensation is achieved by projecting the elements on a line or plane tangent to the array, show peak sidelobe levels close to those obtainable for optimally-shaded uniform arrays of equal aperture sizes and numbers of elements, where the differences depend upon the spacing variations and numbers of elements. This resampling technique is applied to seafloor acoustic backscatter data collected at sea with the 68 kHz Toroidal Volume Search Sonar to highlight a tradeoff between peak and outer sidelobe levels and illustrate the requirement for element pattern when processing data from irregular arrays.

#### I. INTRODUCTION

Analogous to spectral windowing in time series analysis, array shading reduces sidelobes resulting from sampling a finite aperture. Optimal shading may be defined in terms of various criteria, including: directivity,<sup>1</sup> array gain,<sup>2</sup> and signal-to-interference ratio.<sup>3</sup> This paper addresses the Dolph-Chebyshev optimality of irregular arrays,<sup>4</sup> for which the narrowest mainlobe width is achieved for a specified sidelobe level.<sup>4</sup> Here, an *irregular array* is defined as any a) *nonuniform-line array* (1D), b) *curved-line array* (2D), or c) *non-coplanar array* (3D) of elements. The first two are also referred to as *irregular-line arrays*, whereas non-coplanar arrays are also known as *volumetric arrays*. Non-coplanar arrays are used in radar and sonar applications requiring economy of space and wide-angle scanning capability,<sup>sup 5</sup> and nonuniform-line arrays (NULAs) are used to achieve a required beamwidth with fewer elements than a uniform line array (ULA) of equal aperture length.<sup>6</sup> For arbitrary irregular-line arrays, optimal shading techniques for sidelobe reduction in their beampatterns are more complicated and less effective than the optimal Dolph-Chebyshev shading method for ULAs.<sup>7,8</sup> Furthermore, most optimal shading methods for irregular arrays are computationally intensive and limited to specific array geometries.<sup>9,10</sup>

These limitations are significant in bottom echo processing for high resolution multibeam bathymetry using a cylindrical array (e.g. reference [11]). The geometry of this application involves multiple, partially overlapping beams<sup>12</sup> in which the sidelobes of a given beam "look" into the mainlobes of adjacent beams,<sup>12</sup> and sidelobe control is required to unambiguously detect the time and angle of arrival of the bottom echoes. In many commercial swath bathymetry sonars, a split aperture processor is applied to the beamformed data in order to implement a bottom detection method using the

magnitude and phase of the echo, which is more accurate than methods based on magnitude data alone. For cylindrical arrays, split aperture processing often involves asymmetric subarrays whose beam patterns have higher sidelobes than symmetric arrays of equal aperture lengths.<sup>13</sup>

We address these problems by presenting a simple method of computing amplitude shading coefficients for irregular-line and non-coplanar arrays: we resample the optimal Dolph-Chebyshev window, computed for a uniform line or plane array of equivalent aperture, at the element position of the irregular array. This method is simple to formulate, successful in reducing peak sidelobe levels, and applicable to arbitrary array geometries.

After reviewing optimal shading for uniform and irregular arrays in Section II, we describe our *Resampled Amplitude Shading* method in Section III. In Sections III and IV, we use computer simulation results to evaluate the method in terms of three performance measures: (1) mainlobe width (beamwidth) at -3 dB (BW), (2) peak sidelobe level (PSLL), and (3) normalized processing gain (NPG), defined as the processing gain used by Harris<sup>14</sup> normalized by the number of elements in the array:

$$\text{NPG} = (1/N) \left[ \sum_{n=1}^N w(n) \right]^2 / \sum_{n=1}^N w(n)^2, \quad (1)$$

where  $N$  is the number of elements in the array, and  $w(n)$  is the amplitude shading weight for the  $n$ -th element in the array. These measures demonstrate the method's sidelobe reduction capability and the effects of array geometry and individual element pattern. Finally in Section V, we show results of our resampled amplitude shading method applied to seafloor acoustic backscatter data collected by a 68 kHz cylindrical array operating in a shallow water environment.

## II. OPTIMAL ARRAY SHADING

### A. Uniform Line Arrays

The *array pattern* for an arbitrary  $N$ -element shaded line array is

$$f(\theta) = \sum_{n=1}^N g_n(\theta) w(n) \exp \left[ -i \frac{2\pi}{\lambda} x_n \sin \theta \right] \quad (2)$$

where index  $n$  refers to the array's  $n$ -th element with complex pattern  $g_n(\theta)$ , shading coefficient or weight  $w(n)$ , and position  $x_n$ .  $\theta$  is the angle with respect to broadside ( $\theta=0^\circ$ ), and  $\lambda$  is the acoustic wavelength. The corresponding *array factor* is computed with isotropic element patterns, i.e.  $g_n(\theta) = 1$  for all  $n$ . For ULAs with isotropic elements and element spacings greater than or equal to one-half a wavelength, the optimal weights are real-valued (amplitudes) and have an analytical solution derived by Dolph.<sup>4</sup> The solution is found by representing the array factor as a function of Chebyshev polynomials and a parameter specifying the ratio of beamwidth to sidelobe level. The resulting pattern, known as the Dolph-Chebyshev pattern, is characterized by uniform sidelobe levels. Dolph's method has been extended to several classes of uniform line arrays, including ULAs with spacings less than or equal to one-half a wavelength,<sup>15</sup> endfire arrays,<sup>16</sup> and steered arrays.<sup>17</sup> Other extensions include the optimal distribution for a continuous line source,<sup>18</sup> the two-dimensional case for rectangular arrays,<sup>19,20</sup> and approximate methods for circular planar arrays.<sup>21</sup>

### B. Irregular Arrays

For non-coplanar and irregular-line arrays, analytical solutions for the optimal shading weights  $w(n)$  generally do not exist.<sup>6,22</sup> Due to nonuniform and non-coplanar element spacings, the array factors for these arrays cannot be expressed in terms of simple polynomials.<sup>2,23,13</sup> The limited number of irregular arrays which have analytically optimal solutions for their shading weights have highly specific geometries in which the element spacings form a Chebyshev basis.<sup>9,24</sup> Thus, in most cases, optimal shading for irregular arrays is less effective than for ULAs of equal aperture lengths and numbers of elements.

Lewis and Streit<sup>25</sup> have shown that optimal shading solutions for nonuniform-line arrays are real-valued. However, complex weights are used in a large number of optimal shading methods for non-coplanar arrays (e.g. references [1,22,26-31]). The difficulty in determining optimal shading weights for irregular arrays has led many to apply suboptimal shading weights derived from deterministic,<sup>32</sup> empirical,<sup>33</sup> or ad-hoc<sup>34</sup> criteria. It is also common to simply apply the optimal shading weights for a ULA of the same number of elements.<sup>35</sup> Nevertheless, a large number of optimal shading methods exists which involve deterministic or numerical approximation methods. These methods can be categorized as *pattern* and *excitation approximation* techniques.

Pattern approximation methods determine complex or real shading weights, which approximate an ideal pattern as closely as possible. The closed form expression for the Dolph-Chebyshev pattern<sup>36</sup> normally is used. Although deterministic formulations have been used,<sup>37</sup> the majority of these methods involve the minimization of a cost function which expresses the difference between the ideal pattern and the pattern resulting from a set of computed amplitudes. A wide variety of algorithms has been used to this end, including: (a) linear programming<sup>1,5,10,38</sup>; (b) dynamic programming<sup>39</sup>; (c) nonlinear programming<sup>6</sup>; (d) Remez exchange<sup>24</sup>; (e) modified Remez exchange<sup>40</sup>; (f) iterative least squares<sup>29,41</sup>; and (g) Lagrange multipliers.<sup>42-44</sup> These and other methods also have been applied to optimization of both element spacing and amplitude weights,<sup>6,39,44-49</sup> but their main disadvantage is complexity. Cost functions for these techniques are difficult to formulate, and algorithms for their solution are computationally intensive. Other difficulties include local optima<sup>6,22</sup> and restrictions to symmetric array geometries.<sup>6,10,24,28,47,50,51</sup>

Excitation approximation methods determine real-valued shading weights which approximate the ideal excitation for a continuous aperture. It is common to sample the ideal excitation for a continuous line source<sup>18</sup> when amplitude shading irregular arrays.<sup>29,52,53</sup> This excitation has singularities at the end points, so a modified version known as the Taylor distribution is sampled in practical applications. The discrete Taylor weights for a ULA have been derived by Villeneuve.<sup>54</sup> For non-coplanar arrays, the continuous distributions of Harris and Shanks<sup>55</sup> or the generalized functions of Nuttall<sup>37</sup> would be sampled. Like the majority of shading methods for irregular arrays, these techniques have the disadvantage that they are based upon approximations, and therefore are suboptimal by definition.

In the following, we present an excitation approximation method of amplitude shading for irregular arrays including NULAs (e.g. reference [56]), curved-line arrays projected to a cophasal line (e.g. references [5,57]), or non-coplanar arrays projected to a cophasal plane. Applications such as interference rejection<sup>3</sup> and failed element compensation<sup>58</sup> are not considered.

### III. RESAMPLED AMPLITUDE SHADING FOR IRREGULAR-LINE ARRAYS

#### A. Array Factor



The array factor is a sampled approximation to the response of a continuous aperture.<sup>56</sup> Sampling the Taylor distribution to construct the shading weights ( $w(n)$ ) approximates the optimal excitation for a continuous line source, such that the number of elements  $N$  is assumed to be infinite and the element spacing  $d_n$  is assumed to be zero. As the array geometry departs from the line source, i.e. as  $N$  decreases and  $d_n$  increases, performance degrades. The largest  $N$  is limited for reasons of economy, and the smallest  $d_n$  is limited by mutual coupling between elements and by the physical constraints of element size.

We propose an alternative way of computing the shading weights by *resampling* the optimal Dolph-Chebyshev excitations for an *equivalent-ULA* at the element positions along the array aperture. By equivalent-ULA, we mean an array of equal aperture length  $L$  and number of elements  $N$ . This construct is an accepted basis for comparing uniform and irregular arrays.<sup>57</sup> Consider the broadside array factor for a  $N$ -element optimally-shaded uniform line array of length  $L = Nd$ :

$$f_o(\theta)_{ula} = \sum_{n=0}^{N-1} w_o(n)_{ula} \exp \left[ -i \frac{2\pi}{\lambda} n d \sin \theta \right] \quad , \quad (3)$$

where  $w_o(n)_{ula}$  is the Dolph-Chebyshev weight of the  $n$ -th element for some specified sidelobe level,  $d$  is the element spacing, and all other terms are identical to those in (2) with  $g_n(\theta) = 1$ . If we express (3) in terms of the direction sine  $u = \sin \theta$ , and express the element spacing in wavelengths of the radiation, yielding the dimensionless quantity  $D = d/\lambda$ , (3) becomes

$$f_o(u)_{ula} = \sum_{n=0}^{N-1} w_o(n)_{ula} \exp \left[ -i 2\pi n D u \right] \quad (4)$$

which has the form of an Fourier Transform. If we define  $w_o(x)_{ula}$  as the continuous form of the optimal ULA weights  $w_o(n)_{ula}$ , i.e. the optimal current density for a ULA (Fig. 1d), and apply the time-shift and linearity properties of Fourier Transforms, the array factor can be written

$$\begin{aligned} f_o(u)_{ula} &= FT \left\{ \sum_{n=0}^{N-1} w_o(n)_{ula} \delta(x-nD) \right\} \\ &= FT \left\{ w_o(x)_{ula} \sum_{n=0}^{N-1} \delta(x-nD) \right\} \quad , \end{aligned} \quad (5)$$

where  $FT$  denotes the Fourier Transform, and the summation term in the brackets is the uniform sampling function. Defining  $X_n = (n-1)D$  such that  $X_1 = 0$  and applying the convolution property of Fourier Transforms, we have

$$f_o(u)_{ula} = FT \left\{ w_o(x)_{ula} \right\} * FT \left\{ \sum_{n=1}^N \delta(x-X_n) \right\} \quad , \quad (6)$$

where  $*$  denotes convolution. Thus, the optimal array factor for a ULA is the Fourier Transform of the optimal current density  $w_o(x)_{ula}$  times that of the uniform sampling function.

Now the broadside array factor for a shaded  $N$ -element irregular-line array (ILA) of length  $L$  is:

$$f(\theta)_{ila} = \sum_{n=1}^N w(n)_{ila} \exp \left[ -i \frac{2\pi}{\lambda} x_n \sin \theta \right] , \quad (7)$$

where  $w(n)_{ila}$  is the amplitude shading weight of the  $n$ -th element and  $x_n$  is the element position on the line. Expressing  $x_n$  in wavelengths of the radiation  $x'_n = x_n/\lambda$  and following (3)-(6), we can write the array factor as:

$$\begin{aligned} f(u)_{ila} &= FT \left\{ w(x)_{ila} \sum_{n=1}^N \delta(x-x'_n) \right\} \\ &= FT \left\{ w(x)_{ila} \right\} * FT \left\{ \sum_{n=1}^N \delta(x-x'_n) \right\} . \end{aligned} \quad (8)$$

Here, the term within the brackets on the right side of (8) is the nonuniform sampling function defined by the element spacing of the ILA. For Dolph-Chebyshev optimality, an analytic solution for the optimal weights  $w_o(n)_{ila}$  may not exist and must be approximated. An intuitive choice would be a set of weights for which (3) is closely approximated by (7). This implies that (6) would be approximated by (8). By comparing these two equations, it is apparent that such a set of weights would be:

$$w_o(x)_{ila} = w_o(x)_{ula} , \quad (9)$$

so that

$$\begin{aligned} f_o(u)_{ila} &= FT \left\{ w_o(x)_{ula} \right\} * FT \left\{ \sum_{n=1}^N \delta(x-x'_n) \right\} \\ &= FT \left\{ w_o(x)_{ula} \sum_{n=1}^N \delta(x-x'_n) \right\} . \end{aligned} \quad (10)$$

Therefore, the weights for which the array factor of the ILA approximates that of the optimal ULA are found by resampling the continuous Dolph-Chebyshev current density  $w_o(x)_{ula}$  at the element locations of the ILA.

Fig. 1 illustrates the method for a -30dB Dolph-Chebyshev window applied to an irregular-line array of 31 elements with asymmetric spacings. This geometry is representative of that used for split-aperture processing with a phase-compensated cylindrical array that will be discussed in Section V. Resampling the Dolph-Chebyshev weights for an equivalent-ULA approximates the corresponding continuous excitation (Figs. 1c,d). The technique is analogous to spatial tapering in which nonuniform element positions are derived to approximate an optimal current density or amplitude shading weight taper,<sup>34</sup> but in resampling, the optimal equivalent-ULA weights are adjusted for each element number to compensate for the irregular spacing (Fig. 1e).

The effect of resampled shading can be assessed by comparing the patterns of an irregular-line array shaded with (1) resampled weights and (2) the optimal weights for an equivalent ULA, hereafter referred to as *uniform Dolph-Chebyshev* shading (Fig. 2). We make this comparison because, as mentioned in the Introduction, it is common to shade irregular-line arrays with the optimal weights derived for equivalent-ULAs, e.g. reference [35], rather than with weights derived using the techniques described in Section II.B. -30 dB uniform Dolph-Chebyshev shading applied to the irregular-line array of Fig. 1a yields a PSLL of -16.4 dB (Fig. 3, dashed line), whereas shading with resampled amplitudes improves the pattern (Fig. 3, solid line) by lowering the PSLL to -23.5dB with only a 1 percent loss in NPG and no change in -3 dB BW. The

improvement is the same for steered arrays (Fig. 4).

The relative improvement of the resampling method compared to uniform Dolph-Chebyshev shading is the same for a sparse irregular-line array (Fig. 5), in which the average element spacing is greater than half a wavelength. However, the performance of the irregular-line array with resampled shading weights cannot equal that of the optimally-shaded equivalent ULA (Fig. 2), because the element spacings of an asymmetric irregular-line array do not form a Chebyshev basis; hence, higher sidelobes will appear in the array factor of such an array compared to that of an optimized equivalent ULA.

## B. Array Pattern

Practical applications with irregular-line arrays require consideration of both geometry and the complex response pattern of each individual element  $g_n(\theta)$ .<sup>5,6,13,31,53,62</sup> Element patterns vary between individual elements and must be measured in the array's environment because they may be affected by mutual coupling<sup>5,53,62</sup>, shadowing, diffraction, and/or creeping/circumferential waves.<sup>5,27,53,62</sup> Most of these observations have been made for radar arrays, but an extension to conformal sonar arrays should be made in view of the literature.<sup>11,63</sup> If element patterns are not taken into account, gain and phase offsets are introduced into (3) which may produce higher sidelobes.<sup>64</sup> Differences between the element patterns also can raise the peak sidelobe levels,<sup>61</sup> but their effect can be reduced by shading.<sup>65</sup>

Figs. 6-7 illustrate these points for the irregular-line array of Fig. 1a. When the actual element gain patterns of the array are displayed over each other (Fig. 6a, reference [66]), the variation between the element response functions is obvious. Another important point is that the element gain patterns are usually non-isotropic yielding a beam pointing offset when isotropic elements are assumed (e.g. reference [67]). For example, consider the curved array in Fig. 6b in which the element gain pattern is:

$$|g_n(\theta)| = \cos^{1/2}(\text{MRA}_n - \theta) \quad (11)$$

and the element phase pattern is:

$$\arg[g_n(\theta)] = \sin^2(\text{MRA}_n - \theta) \quad (12)$$

where  $\text{MRA}_n$  is the maximum response axis of the  $n$ -th element. For plane wave beamforming, the combined effects of non-isotropic element patterns and element orientation on the array surface produce gain and phase offsets between the elements. If these offsets are not corrected during beamforming, a beam pointing error results (Fig. 7). When we apply gain and phase corrections for these effects, as well as resampled amplitude shading, the pointing error is removed and the peak sidelobe level is reduced, as in Fig. 3. Although the element pattern in this example is approximated with a function, exact knowledge of the individual element response functions is necessary to reduce sidelobes and eliminate pointing offsets. Precise knowledge of element phase center location also is needed to prevent these errors.<sup>14,68</sup>

In addition to the beam pointing error, an interesting feature in Fig. 7 is the reduction in outer sidelobe level which results from the combined effect of non-isotropic element response patterns and array curvature. This has been observed by other investigators<sup>34,61,69</sup> and is caused by the amplitude taper produced by the shift in element MRA from broadside (Fig. 6b). Outer<sup>59</sup> or average sidelobe level may be more important than PSLL in certain applications.

## C. Performance Evaluation

Comparison of the resampling method to the large number of amplitude shading techniques reviewed in Section II is beyond the scope of this paper. However, we evaluate the performance of the resampled window by comparing its effects on the beam pattern of an irregular-line array to those obtained with uniform Dolph-Chbyshev shading. Two example array patterns are presented in Fig. 8, in which gain and phase corrections for element pattern have been applied. For each example, the two methods are compared by computing the ratio of the resampled over uniform performance measure for the three measures described in Section I (BW, PSL, NPG). The patterns in Fig. 8a, computed for an irregular-line array with symmetric element spacings and  $N = 21$  elements, show nearly identical performance for the two methods. The peak sidelobe is merged with the mainlobe in both patterns, and the PSL of the pattern with resampled shading is only 0.5 dB lower than that with uniform shading. By contrast, the array patterns in Fig. 8b, computed for an array with much larger variation in element spacing and 10 more elements than the array in Fig. 8a, show that the resampling method outperforms the uniform method with a PSL reduction of 7.1 dB, a modest 1% loss in NPG, and no change in BW.

Qualitative criteria relating to complexity and applicability also are useful in evaluating the resampled shading method. The method has the advantage of simplicity because the computation of the uniform and resampled weights requires few operations and is simple to formulate using knowledge of the element positions. Another advantage is applicability to arbitrary irregular-line array geometries, particularly asymmetric arrays that are used in several applications (Section IV), but a given asymmetric array will have higher sidelobes than a symmetric array of equal aperture length and number of elements.<sup>13,24</sup>

The resampling method is limited by the assumption that gain and phase offsets are applied to each element to account for individual element pattern. Other methods have been developed which specifically optimize the array pattern using information about the array geometry and element pattern.<sup>6,13,31,70</sup> These methods are complex, and information about individual element pattern may not be available in practical applications. Our technique also offers limited design control. More complicated techniques allow specification of the design sidelobe level, beamwidth, and/or null locations (e.g. references [28,31,32,39,51,71]).

Lastly, the resampling method is not designed to shade arbitrarily sparse arrays or those with failed elements, which may produce array patterns with high sidelobes.<sup>38,40,48,72</sup> We have not fully characterized the performance of the resampling method for very sparse arrays (geometries sparser than that used in Fig. 5). This applies also to arrays with failed elements. Although results below indicate that the method performs well for a cylindrical array with one failed element, it cannot be guaranteed to perform equally well for arrays with arbitrary numbers of failed elements in arbitrary locations. Techniques exist which optimize the shading weights for arrays with element failures,<sup>58</sup> but again they are more complex and computationally intensive than the resampling method.

## IV. RESAMPLED AMPLITUDE SHADING FOR NON-COPLANAR ARRAYS

### A. Arrays Projected Onto a Rectangular Planar Aperture

Two-dimensional resampling for non-coplanar arrays is developed as in (2)-(10) if we replace the elevation angle  $\theta$  in (2) with the vector  $[\theta, \phi]$ , where  $\phi$  is the azimuthal angle, the projected element position  $x_n \sin\theta$  with the term  $(x_n \sin\theta \cos\phi + y_n \sin\theta \sin\phi)$ , and the number of elements  $N$  with  $P = M \times N$  which corresponds to the total number of elements in the array with  $N$  rows in the  $x$  direction

and  $M$  columns in the  $y$  direction. For non-coplanar arrays, which are phase compensated to a plane tangent to the array, resampling is performed on either the optimum two-dimensional Dolph-Chebyshev weights<sup>19,20</sup> or those obtained by pattern-multiplication of the optimum weights for a ULA.<sup>21</sup> The former is optimum in all directions, whereas the latter is optimum only across the principle cross sections<sup>20</sup> (Fig. 9).

Fig. 10 illustrates the method for an  $(N=21) \times (M=21)$  array of elements distributed on a partial-cylinder, phase projected to a plane. Compared to shading the array with the optimum Dolph-Chebyshev weights for an equivalent planar array,<sup>19,20</sup> resampling maintains the -3dB BW and PSLL, decreases the outer sidelobes, and exhibits a small decrease in NPG (Table 1, Fig. 10b). The results are most apparent in directions off the principle axes ( $\theta = 0$  and  $\phi = 0$ ), such as  $\phi = 45^\circ$ . Resampling the pattern-multiplied Dolph-Chebyshev weights for a  $M \times N$  array (Fig. 10c) significantly improves the results in directions off the principle axes. Peak and average sidelobe levels fall nearly 30dB, with no change to the -3dB beamwidth and a large increase in NPG. The only drawback is the very slight increase in main beam width at the PSLL and first nulls, but these effects are acceptable for most applications in which sidelobe level reduction is important. Table 1 presents similar results for an array distributed on a half-cylinder. These suggest that the resampling method performs well for larger arrays with greater spacing variation.

## B. Arrays Projected Onto a Non-Rectangular Planar Aperture

To the best of our knowledge, no optimum shading function exists for planar arrays of arbitrary geometries whose aperture projected on a plane is not rectangular. Therefore, we modify our resampling method for non-coplanar arrays which are phase compensated to non-rectangular planar apertures by resampling the optimum two-dimensional weights (Fig. 9b) or pattern multiplied Dolph-Chebyshev weights (Fig. 9c) for a uniform plane array (Section IV.B.) with length and width corresponding to the principle-axes of the non-coplanar array projected to a plane, and truncate these weights at the edge element positions (e.g. reference [21]).

Results for non-coplanar arrays distributed on a partially-spherical surface (Fig. 11) show these methods actually degrade the array pattern compared to non-shaded patterns. This is understood by the fact that the weighting functions are not matched to the entire aperture. We found similar results for computer simulations of arrays distributed on hemispherical surfaces (Table 1). For irregular-line and non-coplanar arrays projected to rectangular planar apertures, resampling is performed on optimum weights for those projected apertures. When the array cannot be projected to a rectangular aperture, resampling should be performed on the optimum weighting function for its projected aperture. For planar-circular, hemispherical, and spherical arrays, we should resample the functions which produce the optimum (or "ideal") patterns<sup>37</sup> for their specific projected apertures, but singularities in these functions preclude this.

## V. APPLICATION TO THE TOROIDAL VOLUME SEARCH SONAR (TVSS)

### A. TVSS

Resampled amplitude shading was applied to data collected by the TVSS, a cylindrical acoustic array built by Raytheon for the U.S. Navy's Coastal System Station (CSS). The TVSS includes separate projector and hydrophone arrays,<sup>66</sup> both of which are 0.53m in diameter and are deployed on a cylindrical towed vehicle for prototype testing. The projector array has 32 elements equally spaced  $11.25^\circ$  apart. Its beam pattern is meant to be omni-directional in the across-track direction and has a -3

dB beamwidth of  $3.7^\circ$  in the along-track direction. The hydrophone array has 120 elements equally spaced every  $3^\circ$ . Individual element pattern magnitude data were provided by the manufacturer (Fig. 6a), but element pattern phase data were unavailable.<sup>66</sup> The receive beam pattern is variable, depending upon the size of the subarray of elements used in beamforming and whether broadside or steered beams are formed. Data displayed here are from one ping collected by the TVSS southeast of Panama City, Florida. The tow vehicle was deployed approximately 748m behind a vessel traveling 8 knots (4.12 m/s), and the tow vehicle depth was 78m in 200m of water depth.<sup>73</sup>

## B. TVSS Processing

For each ping, the acoustic signals from the 120 individual receive array elements are heterodyned from 68 kHz to 6.25 kHz, low-pass filtered, and digitally recorded at a sampling frequency of 25 kHz. In the processing scheme that we have developed for these data, quadrature sampling, resampled amplitude shading, and broadside beamforming are performed on phase-compensated, overlapping subarrays with asymmetric projected element spacings. This procedure permits split aperture processing<sup>12</sup> of the beamformed output (Fig. 12). We form beams in the directions perpendicular to the lines tangent to 59 of the 120 TVSS elements (Fig. 12). Hence, to form a beam in the elevation direction  $\theta$  at each time sample, acoustic signals from 29 elements are phase delayed to form the total aperture tangent to the direction  $\theta$ . This total aperture is subdivided into two overlapping 21-element apertures spaced 8 elements apart. For each time sample  $t$ , the signals from these two subapertures are beamformed separately to produce beams  $A(\theta, t)$  and  $B(\theta, t)$ , and a phasor  $P(\theta, t)$  is formed from the product

$$A(\theta, t) \times B^*(\theta, t) \quad , \quad (13)$$

where  $*$  denotes complex conjugation. The split aperture method is used here because the zero-crossing of the phasor phase is the most accurate means to detect the time of arrival of boundary reflections on the maximum response axis of the beam. After performing this operation at every time sample for each ping, in  $3^\circ$  steps spanning  $\pm 87^\circ$  about nadir, the result is 59 phasor time-series.

Sidelobe interference in the multiple beams (Fig. 13a) is a significant problem for swath bathymetry applications<sup>12</sup> and provides the motivation for effective amplitude shading. This is illustrated in a cartoon of the acoustic geometry for the bottom echoes in polar (Fig. 13b) and Cartesian coordinates (Fig. 13c). Bottom echo data consist of a complex matrix whose rows are the time samples and whose columns are the angles of arrival. In a polar plot of the corresponding echo envelopes (Figs. 13b, 14a), the bottom returns lie on a nearly horizontal line (this geometry will vary depending upon bottom slope and roughness). In a Cartesian plot, the bottom returns outline a parabola (Figs. 13c, 14b). The log magnitudes of TVSS bottom echo data processed without shading and displayed in Fig. 14, show high magnitude levels (68-78 dB) at all angles at the time of arrival of the bottom echo at nadir (75.1 ms) due to sidelobe interference.

## C. Results

Fig. 15a presents bottom echo data processed as in Figs. 12 and 13 with uniform -30 dB Dolph-Chebyshev shading, and Fig. 15b presents the same with resampled shading. The two methods are compared by evaluating the difference between images 15a and 15b displayed in Fig. 15c. The higher peak sidelobes of the uniform shading are evident by the +5 dB (red) values in the beams from  $\theta = 10^\circ$  to  $40^\circ$ . Sidelobes

were higher for these beams because they were processed using subarrays containing a failed element. Thus, the resampling method appears to perform well for this situation. The higher gain of the uniform shading is evident by the +2 dB (yellow) values within the bottom echo (parabolic feature), also confirming the simulation results. The negative (blue) values surrounding the bottom echo correspond to higher values for the data with resampled shading. This may be explained by the higher outer sidelobes in the resampled array pattern (Section III.B.). For example, beams formed on one side of nadir have sidelobes pointed at bottom echoes arriving from the opposite side (Fig. 13a). These outer sidelobes are +3 dB higher for the pattern with resampled shading than those for the pattern with uniform shading, and therefore produce negative difference values in Fig. 15c.

A source of error in these results, common to the two shading methods, stems from approximating the element gain and phase patterns. The element gain pattern information in Fig. 6a were approximated with (11) to make processing more efficient. The element phase pattern information were approximated with (12) for three reasons: (a) these data were not provided by the manufacturer; (b) the function approximates a nearly uniform phase response with fall off at high angles of arrival as expected for real element phase patterns; and (c) when corrections for this pattern were applied in the beamforming (e.g. Figs. 6-7), an observed beam pointing error was removed. However, these approximations introduced errors in the beamforming which combined to produce higher sidelobe levels than those predicted in the simulations.

## VI. SUMMARY AND CONCLUSIONS

Optimal shading for irregular arrays is more difficult than for uniform linear arrays. The majority of methods used to compute optimal shading weights are limited by complexity, computation time, and restrictions of array geometry. We have presented two simple, efficient, and effective methods for shading irregular arrays that involve resampling the optimal Dolph-Chebyshev amplitude weights at the appropriate element positions of the array projected upon a line or plane tangent to the array. For irregular-line arrays, resampled shading (1) reduces the peak sidelobe significantly, (2) maintains the main beam width, and (3) produces a negligible loss in normalized processing gain compared to shading with the Dolph-Chebyshev weights for an equivalent uniform array. For non-coplanar arrays which may be projected to rectangular planar apertures, resampled shading with the weights obtained by pattern-multiplication of the Dolph-Chebyshev weights for a uniform line array (1) reduces the peak and average sidelobe level significantly, (2) only slightly increases the main beam width, and (3) improves the normalized processing gain significantly compared to shading with the optimum Dolph-Chebyshev weights for a uniform planar array of equal aperture. The resampling method does not perform well for non-coplanar arrays which may be projected to non-rectangular planar apertures (e.g. arrays distributed on spherical surfaces), and the method requires further evaluation for various sparse array geometries. Nevertheless, resampled amplitude shading is applicable to a large class of irregular-line and non-coplanar arrays, assuming the effects of individual element patterns are considered. Results for data collected by a 68 kHz cylindrical acoustic array in a shallow water environment confirm these conclusions.

## ACKNOWLEDGMENT

This work was funded by the Office of Naval Research under ONR-NRL Contract No. N00014-96-1-G913. The authors would like to thank Sam Tooma and Maria

Kalcic (Naval Research Laboratory) for their support, and Candy Robertson and Lisa Tubridy (Coastal Systems Station) for information on the TVSS. Thanks are also due to Jo Griffith for help with the figures.

## REFERENCES

1. McMahon, G.W., Hubley, B., and Mohammed, A. (1972). "Design of optimum directional arrays using linear programming techniques," *J. Acoust. Soc. Am.*, **51**(1), Pt. 2, pp. 304-309.
2. Ziehm, G. (1964). "Optimum directional pattern synthesis of circular arrays." *Radio Electron. Eng.*, **28**, pp. 341-355.
3. Wang, H.S.C. (1977). "Interference rejection by amplitude shading of sonar transducer arrays." *J. Acoust. Soc. Am.*, **61**(5), p. 1251-1259.
4. Dolph, C.L. (1946). "A current distribution for broadside arrays which optimizes the relationship between beamwidth and side-lobe level." *Proc. IRE*, **34**, June, pp. 335-348.
5. Borgiotti, G. (1983). "Conformal arrays". in *The Handbook of Antenna Design*, Rudge, A.W., Milne, K., Olver, A.D., Knight, P. (eds.). London: P. Peregrinus. pp. 227-297.
6. Jarske, P., Saramaki, T., Mitra, S., and Neuvo, Y. (1988) "On the properties and design of nonuniformly spaced linear arrays," *IEEE Trans. Acoust., Speech, Signal Processing*, **ASSP-36**, pp. 372-380.
7. Streit, R.L., and Nuttall, A.H. (1982). "A general Chebyshev complex function approximation procedure and an application to beamforming," *J. Acoust. Soc. Am.*, **72**(1), pp. 181-189.
8. Jiao, Y., Wei, W., Huang, L., and Wu, H. (1993). "A new low sidelobe pattern synthesis technique for conformal arrays." *IEEE Trans. Antennas Propagat.*, **41**(6), pp. 824-831.
9. Streit, R.L. (1975a). "Sufficient conditions for the existence of optimum beam patterns for unequally spaced linear arrays with an example," *IEEE Trans. Antennas Propagat.*, **AP-23**, pp. 112-115.
10. Wilson, G.L. (1976). "Computer optimization of transducer array patterns." *J. Acoust. Soc. Am.*, **59**(1), pp. 195-203.
11. Chakraborty, B. (1995). "Studies on a 120 deg segmented circular array for multi-beam multi-frequency bathymetric applications," *J. Sound and Vibration*, **179**(1), pp. 1-12.
12. de Moustier, C.P. (1993). "Signal processing for swath bathymetry and concurrent seafloor acoustic imaging," in *Acoustic Signal Processing For Ocean Exploration*. J.M.F. Moura and I.M.G. Lourie, eds., NATO ASI Series, Kluwer, pp. 329-354.
13. Sureau, J., and Keeping, K. (1982). "Sidelobe control in cylindrical arrays." *IEEE Trans. Antennas Propagat.* **AP-30**(5), pp. 1027-1031.
14. Harris, F.J. (1978). "On the use of windows for harmonic analysis with the Discrete Fourier Transform," *Proc. IEEE*, **66**(1), pp. 51-83.
15. Riblet, H.J. (1947). "A discussion of Dolph's paper." *Proc. IRE*, **35**, p. 489-492.
16. Duhamel, R.H. (1953). "Optimum pattern for endfire arrays." *Proc. IRE*, **40**, p. 652-659.
17. Pritchard, R.L. (1953) "Optimum directivity patterns for linear point arrays." *J. Acoust. Soc. Amer.*, **25**(5), p. 879-891.
18. Taylor, T.T. (1955). "Design of line-source antennas for narrow beamwidth and



- low side lobes." *IRE Trans. Antennas Propagat.*, **AP-3**, pp. 16-28.
19. Baklanov, Y.V. (1966). "Chebyshev distribution of currents for a plane array of radiators." *Radio Eng. and Electronic Phys.*, **11**, pp. 640-642.
  20. Tseng, F., and Cheng, D. (1968). "Optimum scannable planar arrays with an invariant sidelobe level." *Proc. IEEE*, **56**(11), pp. 1771-1778.
  21. Davids, N., Thurston, E. G., and Mueser, R.E. (1952). "The design of optimum directional acoustic arrays." *J. Acoust. Soc. Amer.*, **24**, p. 50-56.
  22. Bucci, O.M., D'Elia, G., and Romito, G. (1995). "Power synthesis of conformal arrays by a generalized projection method." *IEE Proc.-Microw. Antennas Propag.*, **142**(6), pp. 467-471.
  23. Lee, S.W., and Lo, Y.T. (1965). "On the pattern function of circular arc arrays." *IEEE Trans. Antennas Propagat.*, **AP-13**, pp. 649-650.
  24. Streit, R.L. (1975b). "Optimized symmetric discrete line arrays," *IEEE Trans. Antennas Propagat.*, **AP-23**, pp. 860-862.
  25. Lewis, J.T. and Streit, R.L. (1982). "Real excitation coefficients suffice for sidelobe control in a linear array," *IEEE Trans. Antennas and Propagat.*, **AP-30**(6), pp. 1262-1263.
  26. Goto, N., and Tsunodo, Y. (1977). "Sidelobe reduction of circular arrays with a constant excitation amplitude." *IEEE Trans. Antennas Propagat.*, **AP-25**(6), pp. 896-897.
  27. Watanabe, F., Goto, N., Nagayama, A., and Yoshida, G. (1980). "A pattern synthesis of circular arrays by phase adjustment." *IEEE Trans. Antennas Propagat.*, **AP-28**(6), pp. 857-863.
  28. Prasad, S., and Charan, R. (1984). "On the constrained synthesis of array patterns with applications to circular and arc arrays." *IEEE Trans. Antennas Propagat.*, **32**(7), pp. 725-730.
  29. Schuman, H.K. (1994). "Conformal array synthesis." *Proc. IEEE Antennas and Propagation Society Int. Symp. 1994*. Seattle, WA. 20-24 June 1994. pp. 526-529.
  30. Gabriel'yan, D.D., and Mishchenko, S.E. (1995). "Amplitude-phase synthesis of an acoustic antenna array on a circular cylinder." *Acoustical Physics*, **41**(1), pp. 137-139.
  31. Vaskelainen, L.I. (1997). "Iterative least squares synthesis methods for conformal array antennas with optimized polarization and frequency properties." *IEEE Trans. Antennas. Propagat.*, **45**(7), pp. 1179-1185.
  32. Welkowitz, W. (1955). "Directional circular arrays of point sources." *J. Acoust. Soc. Am.*, **28**(3), pp. 362-366.
  33. Lepage, W.R., Roys, C.S., and Seely, S. (1950). "Radiation from circular current sheets." *Proc. IRE*, **38**, p. 1069-1072.
  34. James, C.M. (1965). "Polar patterns of phase-corrected circular arrays." *Proc. IEE*, **112**(10), pp. 1839-1848.
  35. McDonald, R.J., Wilbur, J., and Manning, R. (1997). "Motion-compensated beamforming algorithm for a circular transducer array." *U.S. Navy J. Underwater Acoust.*, **47**(2), pp. 905-920.
  36. van der Maas, G.L. (1954). "A simplified calculation for Dolph-Tchebysheff Arrays" *Jour. Appl. Phys.*, **25**, pp. 121-124.
  37. Nuttall, A.H. (1982). "A two-parameter class of Bessel weightings with controllable sidelobe behavior for linear, planar-circular, and volumetric-spherical arrays; the ideal weighting-patterns pairs." NUSC Technical Report 6761, Newport, RI/New London, CN: Naval Underwater Systems Center, 1 July 1982.
  38. Holm, S., Elgetun, B., and Dahl, G. (1997). "Properties of the beampattern of weight- and layout-optimized sparse arrays," *IEEE Trans. U.F.F.C.*, **44**, pp. 983-991.

39. Lan, J., Jeffers, R.K., and Boucher, S.G. (1995). "Optimum unequally-spaced arrays and their amplitude shading," *Proc. IEEE Ultras. Symp.*, Seattle, Wa., vol. 2, pp. 965-969.
40. Erstad, J.O., and Holm, S. (1994). "An approach to the design of sparse array systems," *Proc. IEEE Ultras. Symp.*, Cannes, France, vol. 3, pp. 1507-1510.
41. Tseng, C., and Griffiths, L.J. (1992). "A simple algorithm to achieve desired patterns for arbitrary arrays," *IEEE Trans. Sig. Proc.*, **40**(11), pp. 2737-2746.
42. Wang, H.S.C. (1975). "Amplitude shading of sonar transducer arrays," *J. Acoust. Soc. Am.*, **57**(5), pp. 1076-1084.
43. Sullivan, E.J. (1978). "Amplitude shading of irregular acoustic arrays," *J. Acoust. Soc. Am.*, **63**(6), pp. 1873-1877.
44. Ng, Boon Poh. (1992) "Designing array patterns with optimum inter-element spacing and optimum weights using a computer aided approach," *Int. J. Electronics*, **73**(3), p. 653-664.
45. Ma, M.T. (1965). "Another method of synthesizing nonuniformly spaced arrays," *IEEE Trans. Antennas Propagat.*, **AP-13**, pp. 833-834.
46. Stutzman, W.L. (1970). "Synthesis of shaped-radiation patterns using the iterative sampling method," *IEEE Trans. Antennas Propagat.*, **AP-19**, pp. 36-41.
47. Redlich, R. (1972) "Iterative least-squares synthesis of nonuniformly spaced linear arrays," *IEEE Trans. Antennas Propagat.*, **AP-20**, pp. 106-108.
48. Lockwood, G.R., Li, P.C., O'Donnell, M., and Foster, F.S. (1996). "Optimizing the radiation pattern of sparse periodic linear arrays," *IEEE U.F.F.C.*, **43**, pp. 7-14.
49. Murino, V., Trucco, A., Regazzoni, C.S. (1996). "Synthesis of unequally spaced arrays by simulated annealing," *IEEE Trans. Sig. Proc.*, **44**, pp.119-123.
50. Vu, T.B. (1993). "Sidelobe control in circular ring array," *IEEE Trans. Antennas Propagat.*, **41**(8), pp. 1143-1145.
51. Vescovo, R. (1995). "Constrained and unconstrained synthesis of array factor for circular arrays," *IEEE Trans. Antennas Propagat.*, **43**(12), pp. 1405-1410.
52. Davies, D.E.N. (1983). "Circular arrays," in: *The Handbook of Antenna Design*, Rudge, A.W., Milne, K., Olver, A.D., Knight, P. (eds.), London: P. Peregrinus, pp. 298-329.
53. Mailloux, R. J. (1994), *Phased array antenna handbook*, Boston: Artech House, 527 pp.
54. Villeneuve, A. T. (1984). "Taylor pattern for discrete arrays," *IEEE Trans. Antennas Propagat.* **AP-32**(10), pp. 1089-1093.
55. Harris, J. H., and Shanks, H.E. (1961). "A method for synthesis of optimum directional patterns from nonplanar apertures," *IRE Trans. Antennas Propagat.*, p. 228-236.
56. Wiley, R.E. (1962). "Space tapering of linear and planar arrays," *IRE Trans. Antennas Propagat.*, **AP-10**, pp.369-277.
57. Fenby, R.G. (1965). "Limitations on directional patterns if of phase-compensated circular arrays," *Radio Electron. Eng.*, **30**, pp. 206-222.
58. Sherrill, M.S., and Streit, R.L. (1987). "In-situ optimal reshaping of arrays with failed elements," *IEEE J. Ocean. Eng.*, **OE-12**(1), pp. 155-162.
59. Steinberg, B.D. (1976). *Principles of Aperture and Array System Design: Including Random and Adaptive Arrays*. New York: John Wiley & Sons, 356 pp.
60. Kelly, J.G., Sullivan, E.J., and Salisbury, J.I. (1979). "Comments on "Conformal array beam patterns and directivity indices" [J.Acoust. Soc. Am. 63, 841-847]." *J.Acoust. Soc. Am.*, **65**(2), pp. 531-534.
61. Fletcher, P.N., and Darwood, P. (1998). "Beamforming for circular and semicircular array antennas for low-cost wireless LAN data communications systems." *IEE Proc.-Microw. Antennas Propag.*, **145**(2), pp. 153-157.

62. Shapira, J. Felsen, B., and Hessel, A. (1974). "Ray analysis of conformal antenna arrays." *IEEE Trans. Antennas Propagat.*, **AP-22**(1), pp. 49-63.
63. Neubauer, W.G. (1969) "Pulsed circumferential waves on an aluminum cylinder in water." *J. Acoust. Soc. Am.*, **45**(5), pp. 1134-1144.
64. Kanno, M., Hashimura, T., Katada, T., Watanabe, T., Iio, S., Soga, H., Nakada, T., and Miyano, N. (1996). "An active conformal array antenna with very small thickness." in: *Proc. 1996 IEEE Int. Symp. on Phased Array Systems and Technology*, Boston, Mass., 15-18 Oct. 1996. pp. 155-158.
65. Aumann, H.M., (1994). "Eigenvalue analysis of phased array element patterns." *Proc. IEEE Antennas and Propagation Society Int. Symp. 1994*. Seattle, WA. 20-24 June 1994. pp. 510-513.
66. Raytheon Company, Submarine Signal Division (1993). "Volume Search Sonar Array Program: Preliminary Hydrophone Test Data."
67. Mano, S., Ono, M., and Takeichi, Y. (1974). "Effects of element pattern on the directive properties of a scanning planar array." *IEEE Trans. Antennas Propagat.*, **AP-22**(2), pp. 169-172.
68. Worms, J. G. (1996). "Effects of element errors to the radiation pattern and the angular resolution of an phased array antenna." *Proc. IEEE International Symposium on Phased Array Systems and Technology*.o Boston, MA, 15-18 October, 1996, pp. 297-300.
69. Longstaff, I.D., Chow, P.E.K., and Davies, D.E.N. (1967). "Directional properties of circular arrays." *Proc. IEE*, **114**(6), pp. 713-718.
70. Tseng, F.I., and Cheng, D.K. (1968). "Pattern synthesis of circular arrays with many directive elements." *IEEE Trans. Antennas Propagat.*, **AP-16**, pp. 758-759.
71. Ishimaru, A. (1962). "Theory of unequally spaced arrays," *IRE Trans. Antennas Propagat.*, **AP-10**, pp. 131-136.
72. Ramsdale, D.J., and Howerton, R.A. (1980). "Effect of element failure and random errors in amplitude and phase on the sidelobe level attainable with a linear array." *J. Acoust. Soc. Am.*, **68**(3), pp. 901-906.
73. Tubridy, Lisa. (1995). "Users Manual For The Toroidal Volume Search Sonar." Coastal Systems Station, Panama City, Florida.

The majority of this chapter appears in "On optimal amplitude shading for arrays of irregularly spaced or non-coplanar elements," T.C. Gallaudet, and C.P. de Moustier, *IEEE Journal Oceanic Engineering.*, **25**, 553-567 (2000). The dissertation author was the primary investigator and and co-author of this paper.

TABLE 1. Performance of shading techniques for computer simulations of uniform planar and non-coplanar arrays. The uniform arrays are square with  $N \times N$  elements and lengths  $L = N \lambda/2$ . When projected to planes tangent to their surfaces, the partial- and half-cylinder arrays are square with lengths  $L = N \lambda/2$ . The projections of the partial- and hemi-sphere arrays have diameters  $D = N \lambda/2$ .  $\theta$  and  $\phi$  are the azimuth and elevation angles, respectively.

		21×21-element uniform planar square array (Figure 9)		21×21-element non-coplanar array on a partial cylinder (Figure 10)	
		$\phi=0^\circ$	$\phi=45^\circ$	$\phi=0^\circ$	$\phi=45^\circ$
-3dB BW (deg)	no shading	4.84	4.84	4.85	4.90
	-30dB uniform DC	6.00	6.00	5.95	6.00
	resampled -30dB uniform DC	NA	NA	5.95	6.00
	pattern multiplied -30dB uniform DC	6.00	6.05	5.95	6.05
	resampled pattern multiplied -30dB uniform DC	NA	NA	5.95	6.05
PSLL (dB)	no shading	-13.3	-26.0	-12.5	-25.2
	-30dB uniform DC	-30.0	-30.0	-23.6	-29.1
	resampled -30dB uniform DC	NA	NA	-26.3	-28.2
	pattern multiplied -30dB uniform DC	-30.0	-60.0	-23.6	-53.8
	resampled pattern multiplied -30dB uniform DC	NA	NA	-26.3	-56.5
NPG	no shading	1.00		1.00	
	-30dB uniform DC	0.67		0.67	
	resampled -30dB uniform DC	NA		0.69	
	pattern multiplied -30dB uniform DC	0.75		0.75	
	resampled pattern multiplied -30dB uniform DC	NA		0.75	

TABLE I. (Continued).

		31×31-element uniform planar square array (not shown)		31×31-element non-coplanar array on a half cylinder (not shown)	
		$\phi=0^\circ$	$\phi=45^\circ$	$\phi=0^\circ$	$\phi=45^\circ$
-3dB BW (deg)	no shading	3.25	3.25	3.25	3.30
	-30dB uniform DC	5.95	6.00	4.02	4.02
	resampled -30dB uniform DC	NA	NA	3.90	3.97
	pattern multiplied -30dB uniform DC	4.02	4.05	3.90	4.00
	resampled pattern multiplied -30dB uniform DC	NA	NA	3.90	4.00
PSLL (dB)	no shading	-13.3	-26.0	-15.6	-24.6
	-30dB uniform DC	-30.0	-30.0	-21.8	-29.4
	resampled -30dB uniform DC	NA	NA	-24.8	-27.5
	pattern multiplied -30dB uniform DC	-30.0	-60.0	-21.8	-52.1
	resampled pattern multiplied -30dB uniform DC	NA	NA	-24.8	-55.2
NPG	no shading	1.00		1.00	
	-30dB uniform DC	0.58		0.58	
	resampled -30dB uniform DC	NA		0.53	
	pattern multiplied -30dB uniform DC	0.77		0.77	
	resampled pattern multiplied -30dB uniform DC	NA		0.75	

TABLE I. (Continued).

		31-element diameter non-coplanar array on a partial sphere (Figure 11)		61-element diameter non-coplanar array on a hemisphere (not shown)	
		$\phi=0^\circ$	$\phi=45^\circ$	$\phi=0^\circ$	$\phi=45^\circ$
-3dB BW (deg)	no shading	4.80	4.80	1.84	1.84
	-30dB uniform DC	5.20	5.20	2.10	2.00
	resampled -30dB uniform DC	5.20	5.20	2.15	2.15
	pattern multiplied -30dB uniform DC	5.70	5.70	2.50	2.48
	resampled pattern multiplied -30dB uniform DC	5.70	5.70	2.50	2.50
PSLL (dB)	no shading	-15.1	-15.1	-14.7	-14.7
	-30dB uniform DC	-11.5	-12.9	-10.7	-11.7
	resampled -30dB uniform DC	-12.9	-12.9	-11.4	-12.2
	pattern multiplied -30dB uniform DC	-11.5	-12.9	-12.2	-12.8
	resampled pattern multiplied -30dB uniform DC	-12.4	-12.4	-12.6	-13.1
NPG	no shading	1.00		1.00	
	-30dB uniform DC	0.76		0.47	
	resampled -30dB uniform DC	0.85		0.61	
	pattern multiplied -30dB uniform DC	0.85		0.80	
	resampled pattern multiplied -30dB uniform DC	0.85		0.81	

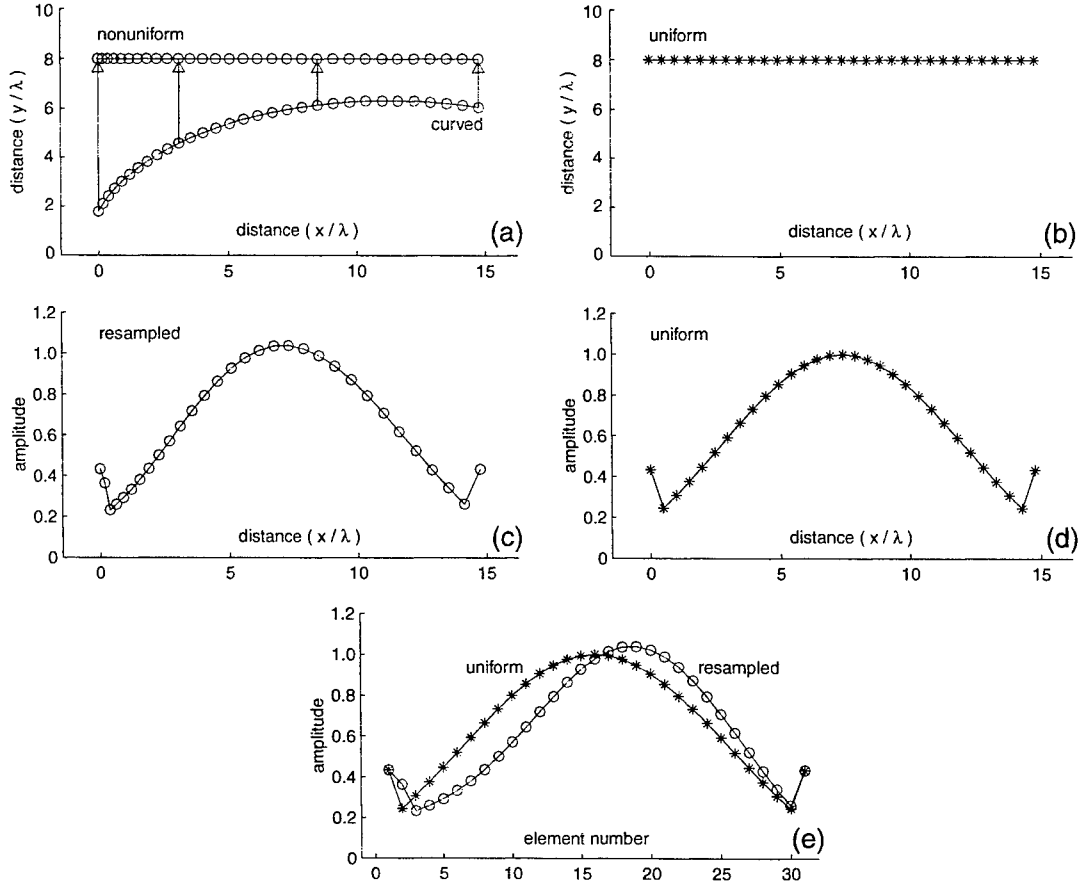


Fig. 1. (a) Irregular-line array with  $N = 31$  elements and aperture length  $L = N\lambda/2$ , which may be either a phase-compensated curved-line array or a nonuniform-line array (NULA). (b) Equivalent-ULA with  $N = 31$  elements and  $d = \lambda/2$ . (c) Resampled -30 dB Dolph-Chebyshev amplitude weights vs. aperture distance. (d) Uniform line array -30 dB Dolph-Chebyshev amplitude weights vs. aperture distance. (e) Resampled and ULA weights vs. element number.

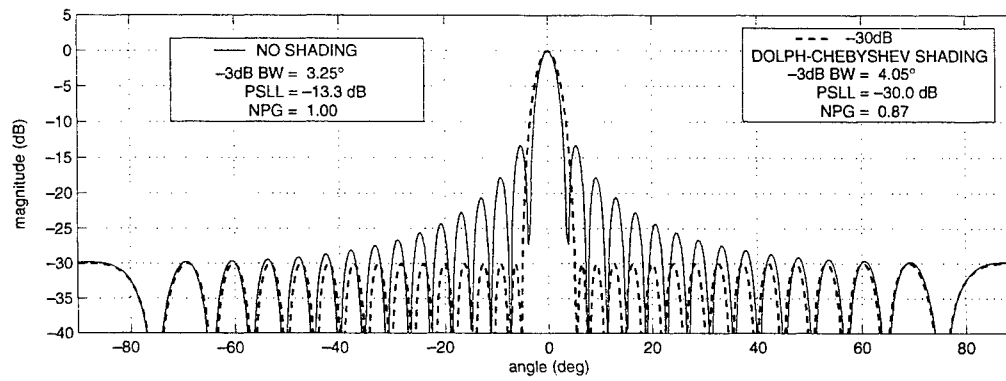


Fig. 2. Optimal amplitude shading for a uniform linear array (ULA): broadside array factors for the  $N = 31$  element ULA depicted in Fig. 1b.



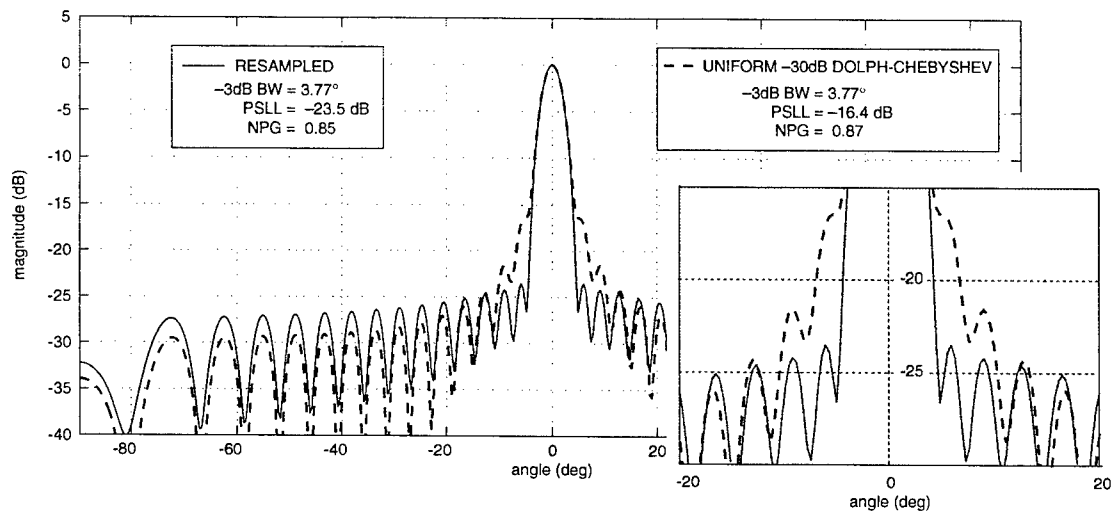


Fig. 3. Resampled amplitude shading for an irregular-line array: broadside array factors for the  $N = 31$  element array depicted in Fig. 1a.

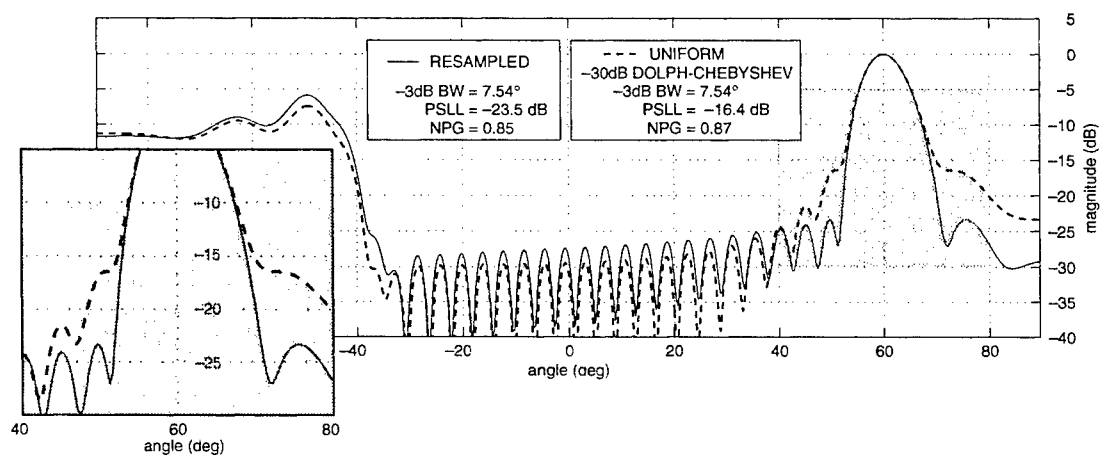


Fig. 4. Resampled amplitude shading for an irregular-line array: same as Fig. 3 with beam steered to  $\theta = 60$ .

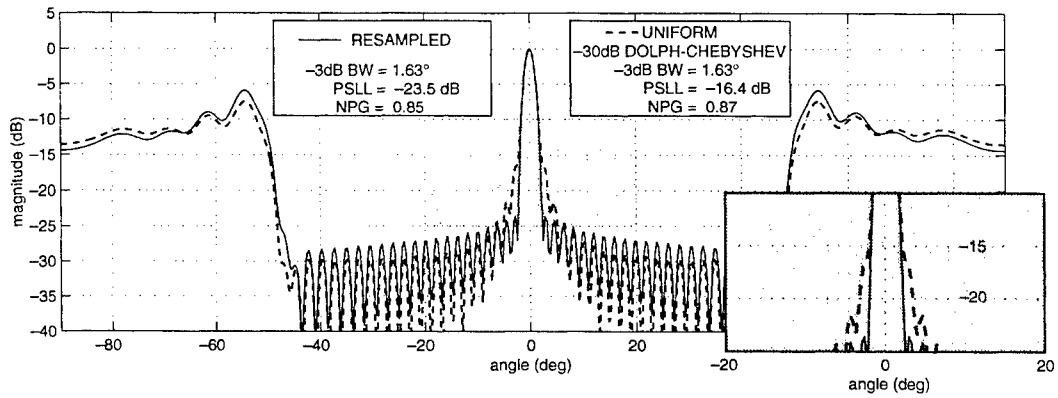


Fig. 5. Resampled amplitude shading for a sparse irregular-line array: broadside array factors for a  $N = 31$  element array with relative spacings between elements similar to those of the array depicted in Fig. 1a, but with an average element spacing of  $\lambda$  rather than  $\lambda / 2$  such that  $L = N \lambda$ .

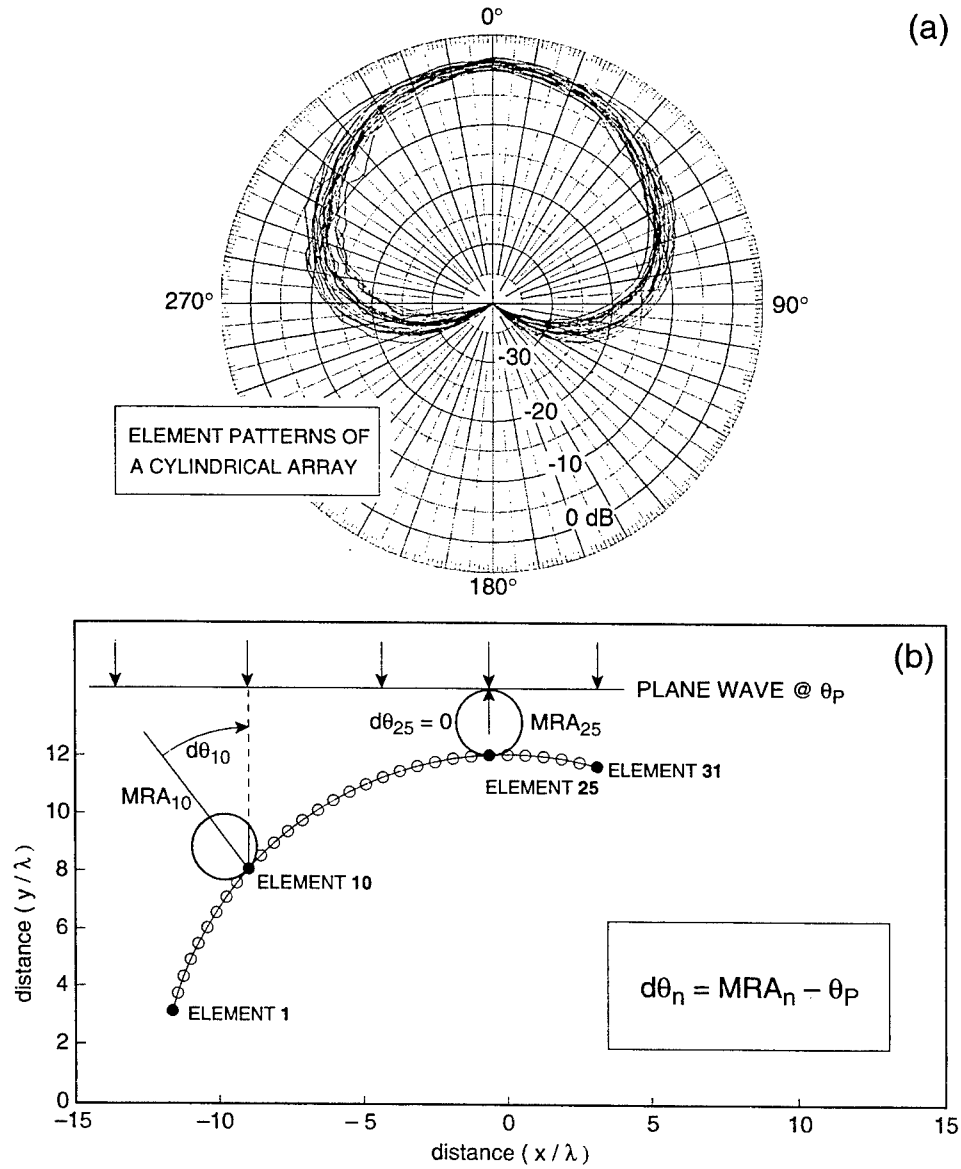


Fig. 6. (a) Magnitude response patterns of 120 individual elements of the cylindrical array described in Section V [66]. (b) Depiction of a plane wave arriving from direction  $\theta_p$  incident on a 31 element subarray of a 120-element cylindrical array.  $d\theta_n$  is the difference between the maximum response axis of the  $n$ th element ( $MRA_n$ ) and the plane wave direction  $\theta_p$ .

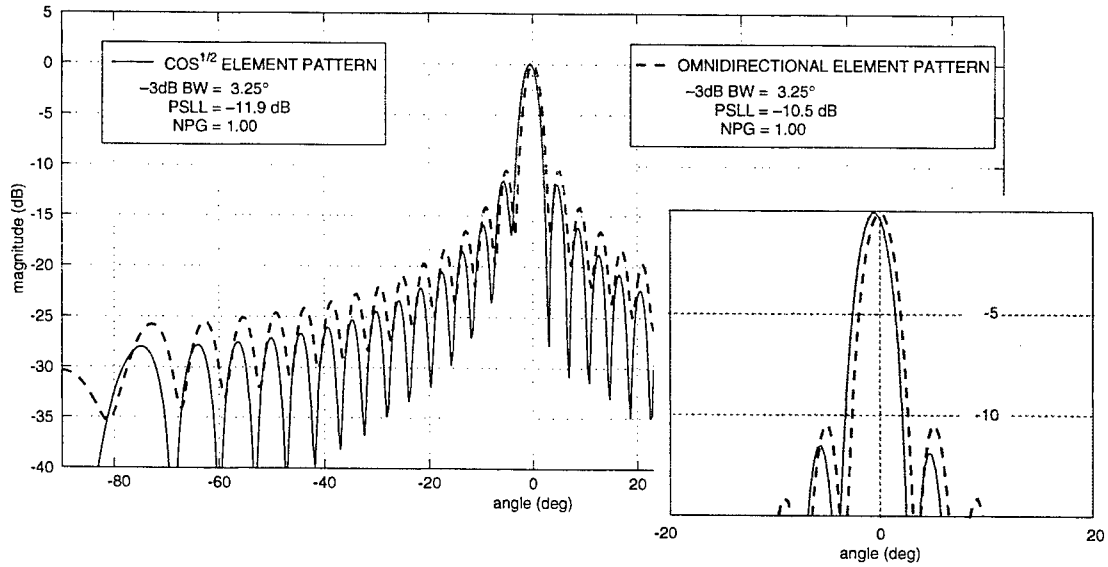


Fig. 7. Non-shaded array patterns for the curved subarray in Fig. 6b with element gain and phase patterns given by equations (11) and (12) in the text. The pattern obtained when incorrectly assuming omnidirectional element patterns (dashed line) exhibits a main beam pointing error, unlike the pattern obtained when compensating for actual element gain and phase patterns (solid line).

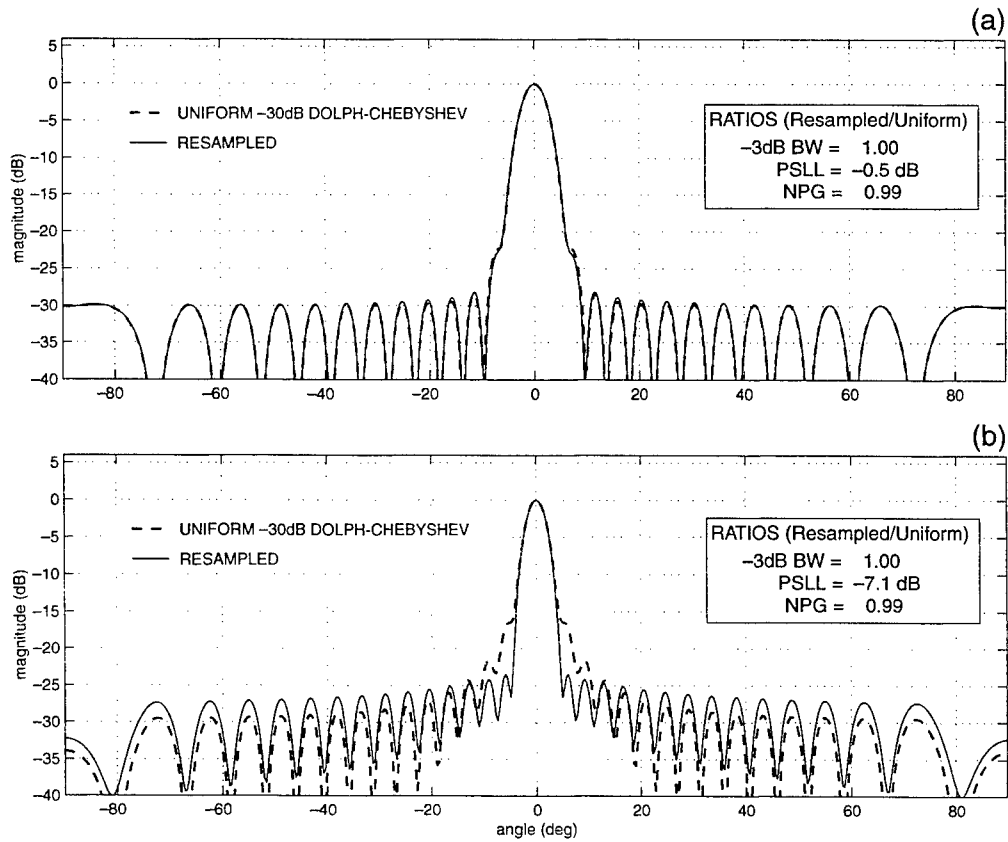


Fig. 8. Performance comparison of resampled amplitude shading for two irregular-line arrays: (a) array patterns with resampled and uniform -30 dB Dolph-Chebyshev shading for a 21 element NULA array with symmetric element spacings; (b) array patterns with resampled and uniform -30 dB Dolph-Chebyshev shading for a 31 element NULA array with asymmetric element spacings.

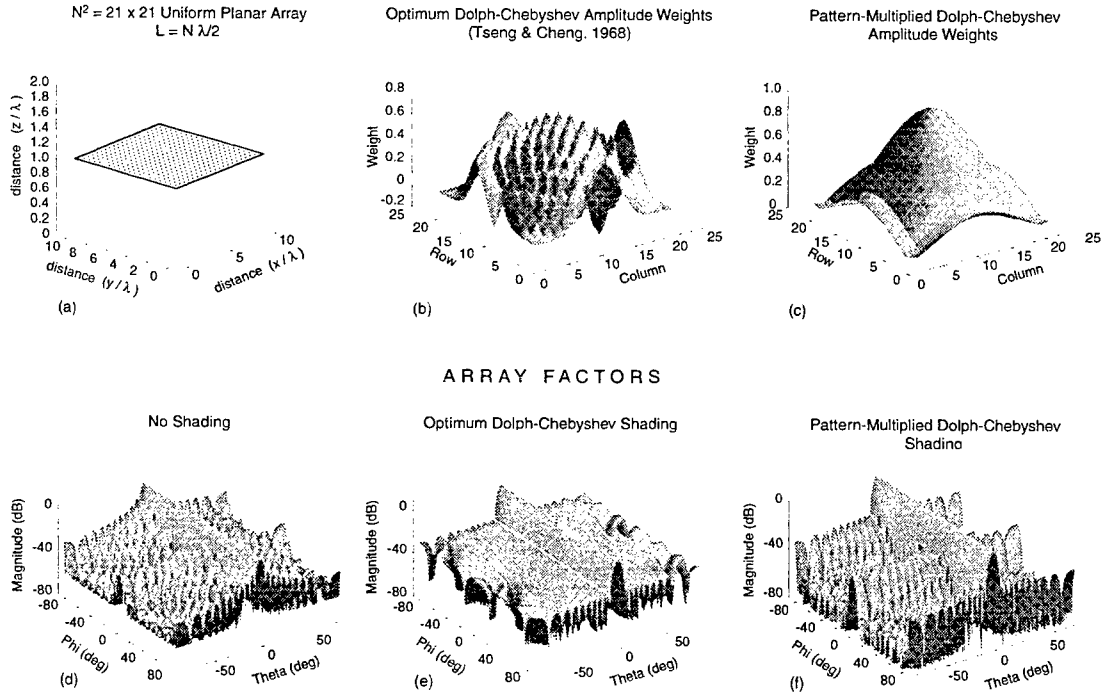


Fig. 9. (a) Uniform square planar array with  $21 \times 21$  elements spaced  $\lambda/2$  apart.  $L = N \lambda/2$ . (b) Optimum Dolph-Chebyshev amplitude weights [19,20] for the uniform planar array in (a). (c) Amplitude weights obtained by pattern-multiplication of the Dolph-Chebyshev amplitude weights for a 21-element ULA with  $\lambda/2$  element spacing. Array factors for the array in (a): (d) without shading; (e) with the optimum Dolph-Chebyshev amplitudes of (b); (f) with the pattern-multiplied Dolph-Chebyshev amplitudes of (c).

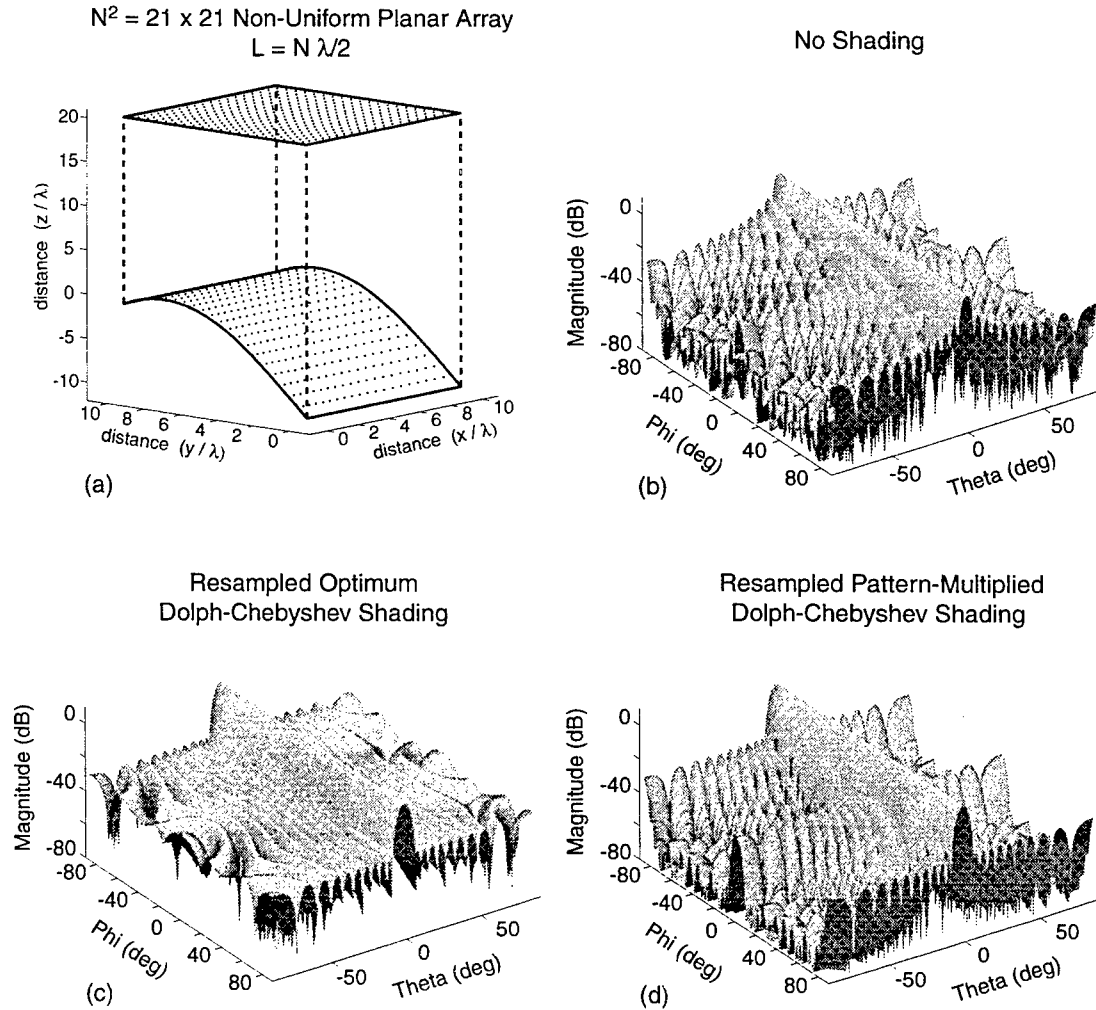


Fig. 10. (a) Non-coplanar array on a partial-cylinder, projected to a square planar array with  $N \times M = 21 \times 21$  nonuniformly-spaced elements and length and width  $L = N \lambda/2$ . Array factors: (b) without shading; (c) with resampling of the optimum Dolph-Chebyshev amplitudes for the equivalent uniform square planar array (e.g. Fig. 9a, b); (d) with resampling the pattern-multiplied Dolph-Chebyshev amplitudes for the equivalent uniform square planar array (e.g. Fig. 9a, c).



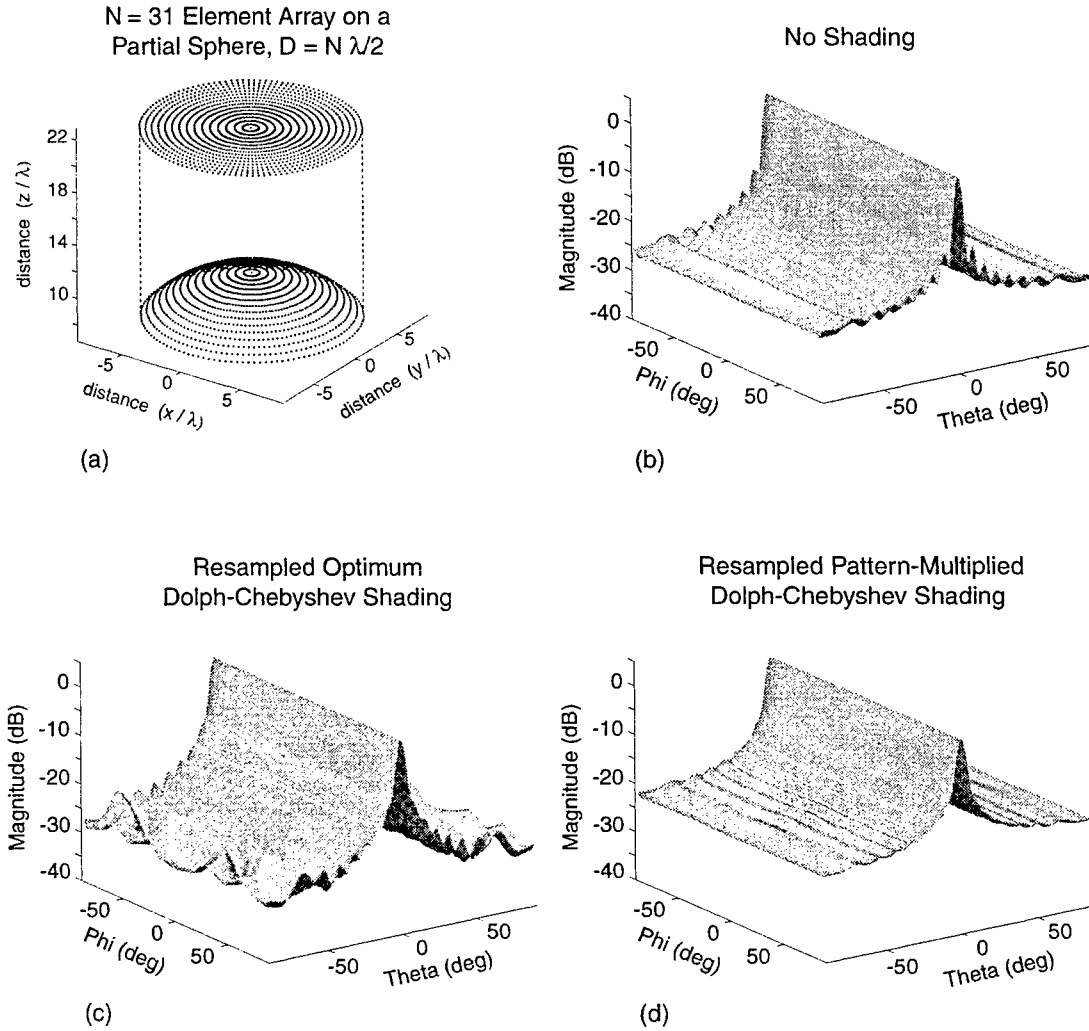


Fig. 11. (a) Non-coplanar array on a partial-sphere, projected to a circular-planar array with  $N = 31$  nonuniformly-spaced elements across the diameter with length  $L = N \lambda/2$ . Array factors: (b) without shading; (c) with resampling and truncating the optimum Dolph-Chebyshev amplitudes for the equivalent uniform square planar array (e.g. Fig. 9a, b); (d) with resampling and truncating the pattern-multiplied Dolph-Chebyshev amplitudes for the equivalent uniform square planar array (e.g. Fig. 9a, c).

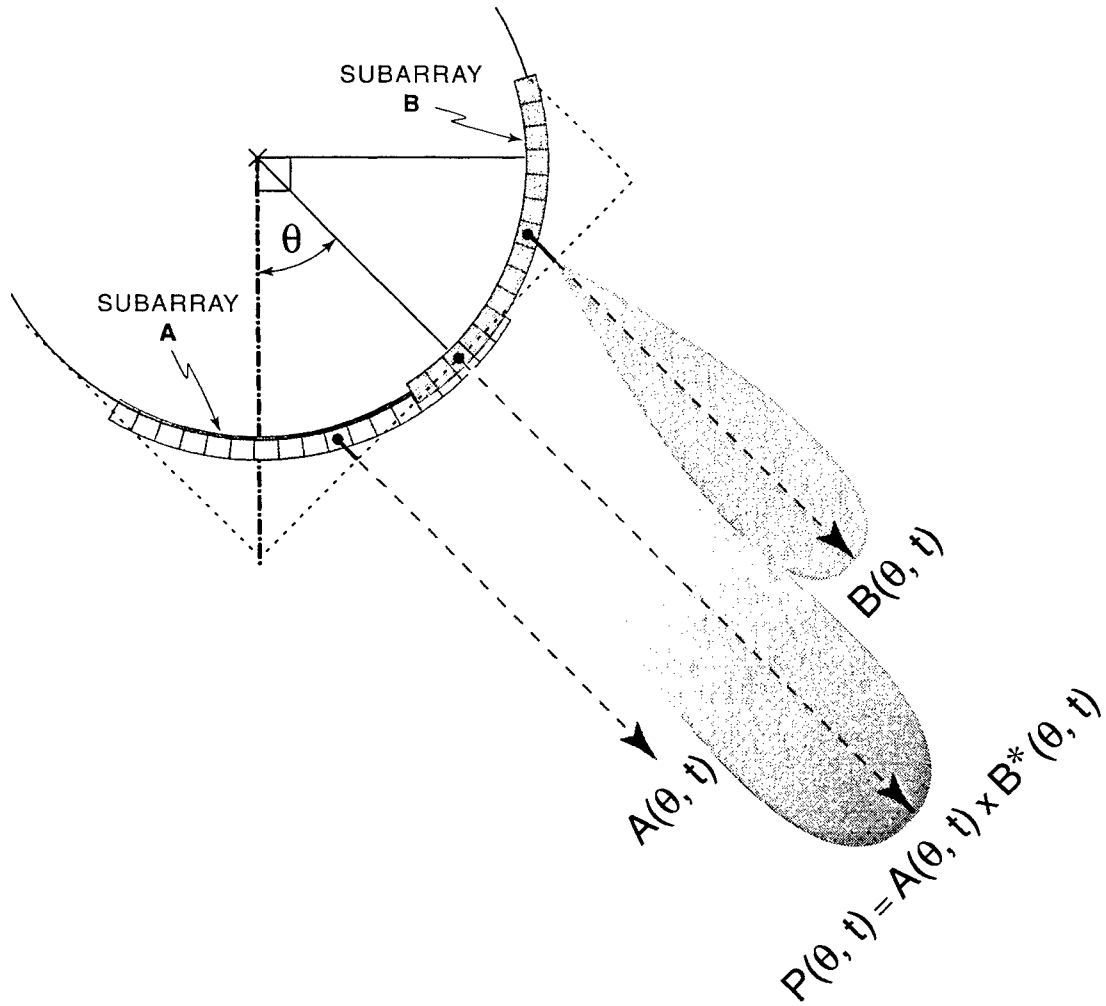


Fig. 12. TVSS split aperture correlator: at each time  $t$  and for each beam direction  $\theta$ , a symmetric arc array is subdivided into two asymmetric subarrays. Two parallel beams  $A(\theta, t)$  and  $B(\theta, t)$  are formed from each subarray using resampled -30 dB Dolph-Chebyshev amplitude shading, and the phasor  $P(\theta, t) = A(\theta, t) \times B^*(\theta, t)$  is formed.

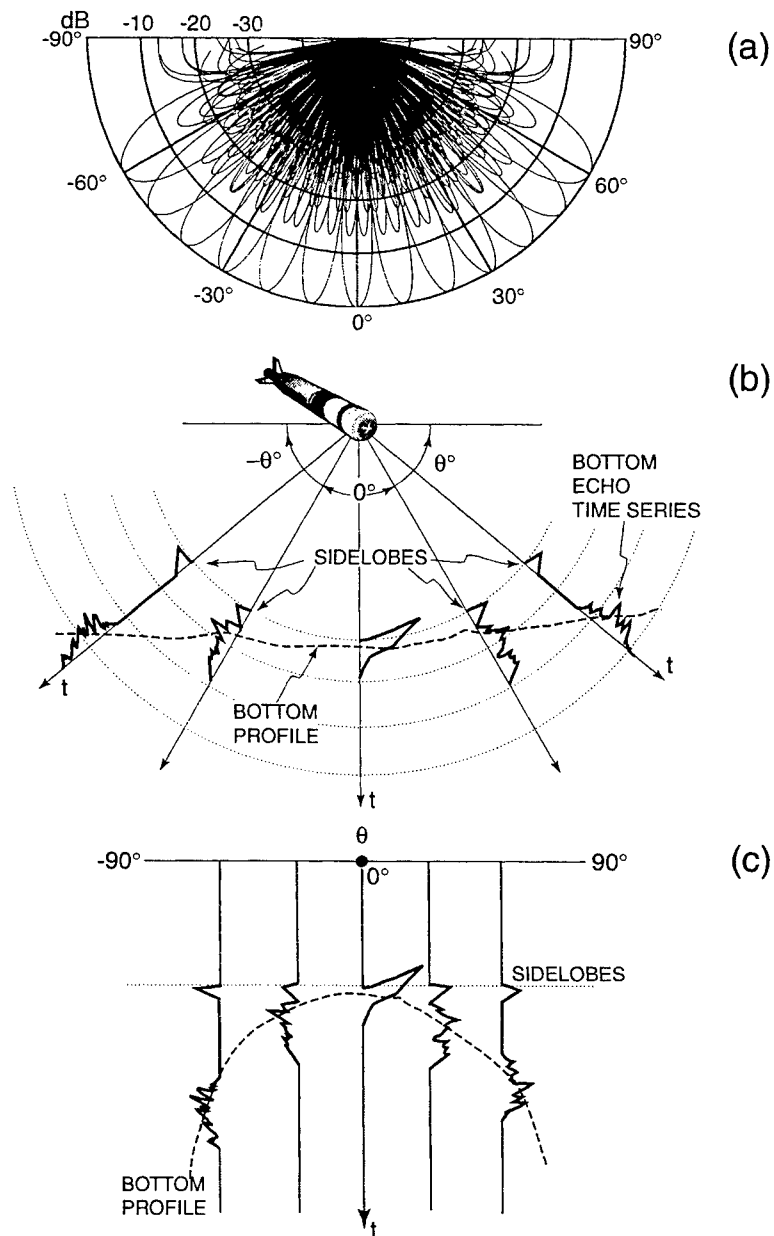


Fig. 13. TVSS bottom echo processing: (a) geometry for multibeam bathymetric processing using the TVSS; the sidelobes of each beam look into the mainlobe of other beams; (b) polar plot of the bottom echoes, with time increasing along radial lines which correspond to beam pointing directions  $\theta$ ; (c) Cartesian plot of the bottom echoes with lines of equal time parallel to the x-axis, and lines of equal beam direction  $\theta$  parallel to the y-axis.

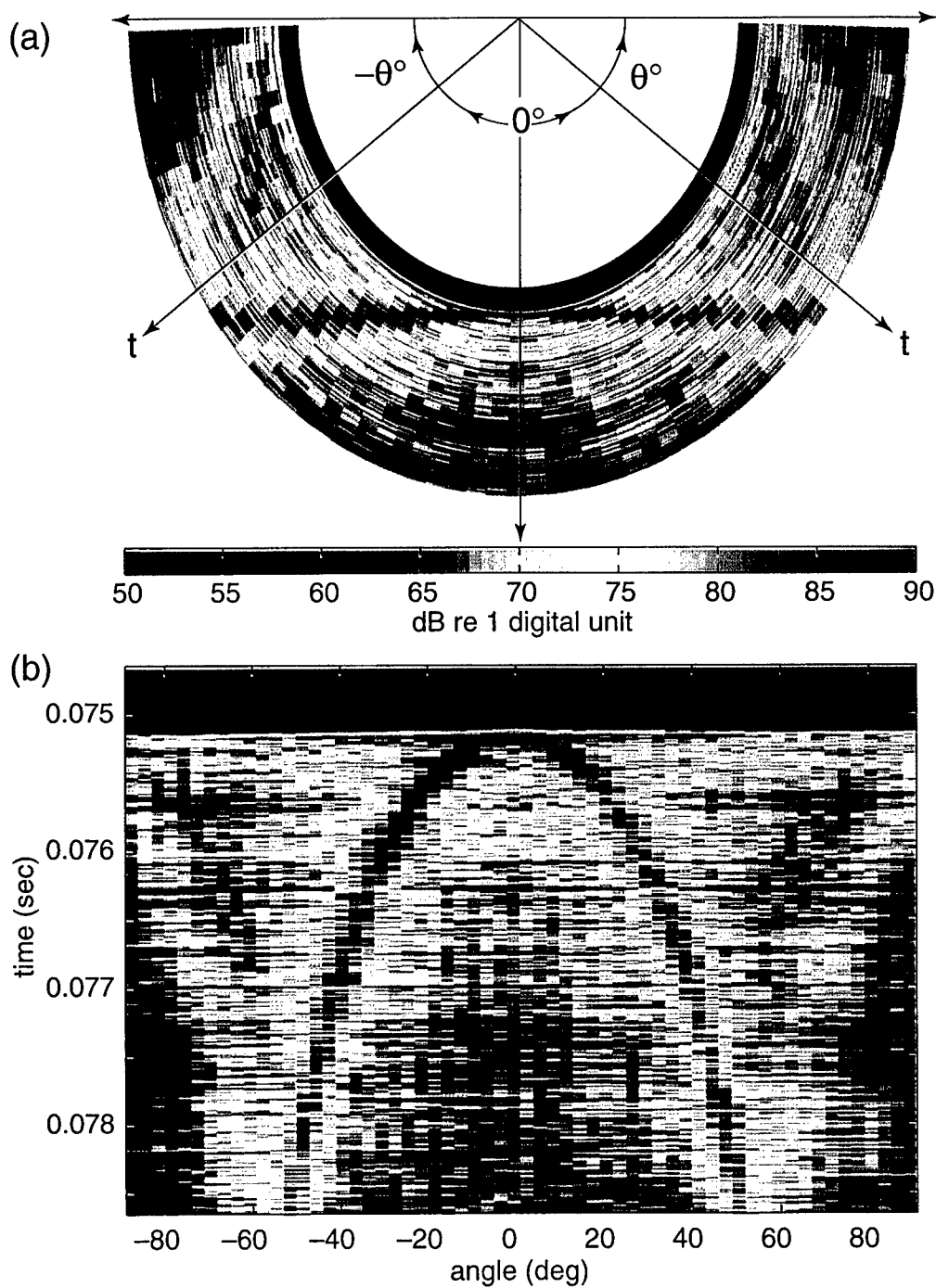


Fig. 14. Bottom echo: TVSS split aperture phasor magnitude (dB) without shading, in which each beam is formed as in Fig. 13: (a) polar plot as in Fig. 13b; (b) Cartesian plot as in Fig. 13c. Sidelobe interference from the nadir ( $\theta = 0$ ) bottom echo is evident in all beams at the same time slice ( $t = 0.0752$  sec).

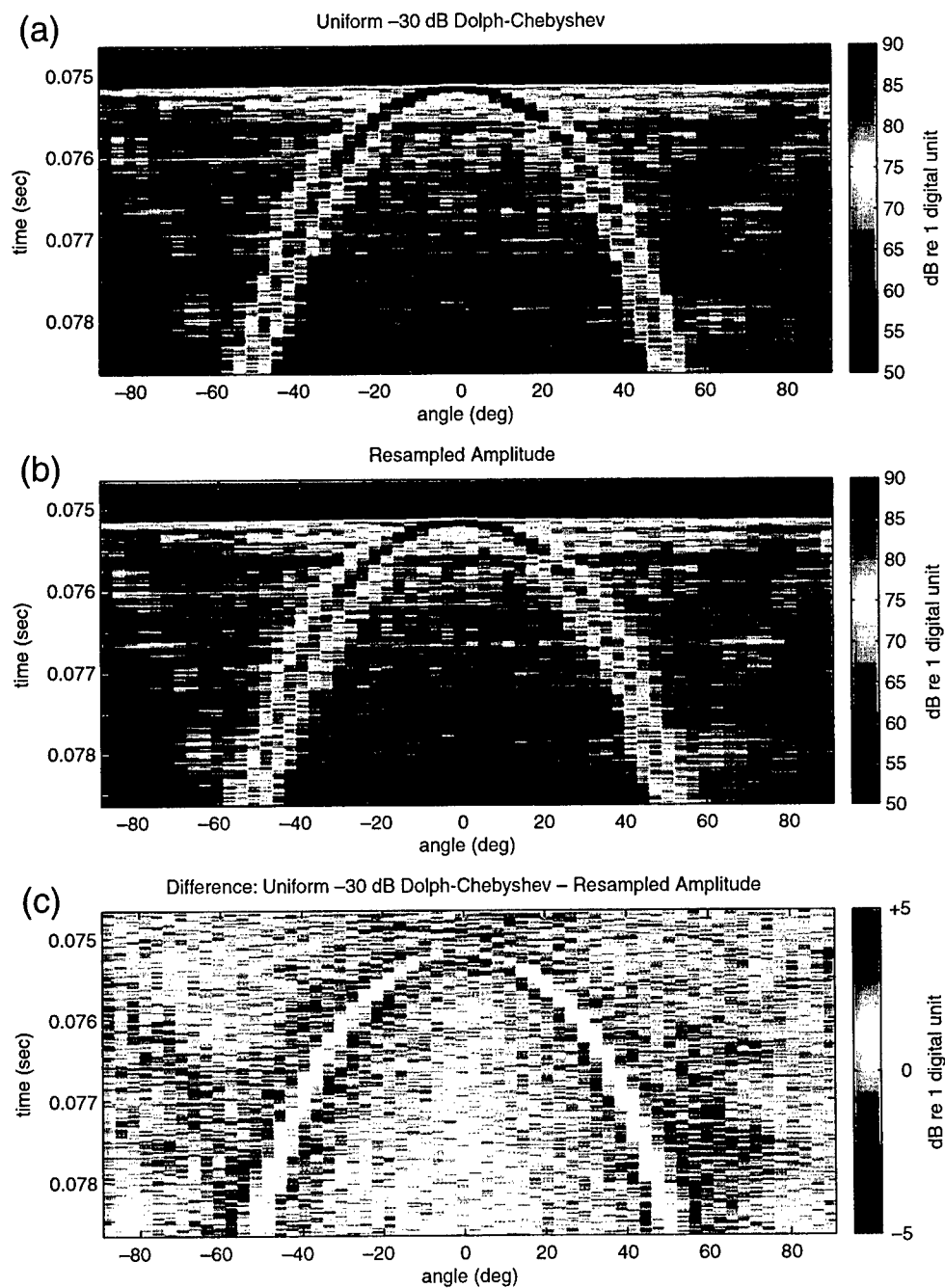


Fig. 15. Bottom echo: TVSS split aperture phasor magnitude (dB) with -30 dB Dolph-Chebyshev shading: (a) using uniform line array amplitudes; (b) using resampled amplitudes; (c) difference (a) - (b).

## Chapter 3

### Using Environmental Information to Correct For Errors in Bathymetry and Seafloor Acoustic Backscattering Strength Imagery

#### ABSTRACT

Bathymetry and seafloor acoustic backscatter imagery are derived from data collected in waters 200m deep in the northeastern Gulf of Mexico by the Toroidal Volume Search Sonar (TVSS), a 68 kHz cylindrical acoustic array deployed on a towfish and operated by the U.S. Navy's Coastal System Station, Panama City, Florida. The acoustic data received by the TVSS were beamformed to construct 120 narrow beams spaced every 3° around the circumference of the array. Swath bathymetry and seafloor acoustic backscattering strength imagery constructed with the down-looking beams reveal a 14m negative bias in the towfish depth sensor, which is estimated using the acoustic backscatter from upward-looking beams. The depth-corrected bathymetry suffers from along-track errors that are negatively correlated on opposite sides of the track and result from undersampling in the towfish roll data. Roll errors are estimated from the across-track slope angles of detrended, depth corrected bathymetry and added to the initial roll data. The depth- and roll- corrected bathymetry show a relatively flat and featureless seafloor, consistent with the large scale bathymetry derived from surveys conducted by the U.S. Naval Oceanographic Office. Acoustic backscattering strength images corresponding to the bathymetry exhibit systematic across-track biases resulting from the combined transmit and receive beam pattern. To compensate for these biases, two procedures are described, one which is for use with non-calibrated sonars, and another which is for use with calibrated systems and is based upon the composite roughness model of Jackson, Winebrenner, and Ishimaru [J. Acoust. Soc. Am., 102, pp. 1410-1422, 1986]. Both methods are effective in improving the quality of the imagery.

#### I. INTRODUCTION

In 1993, the Naval Research Laboratory (NRL) Stennis Space Center developed a program for environmental sensing with tactical mine-countermeasures (MCM) systems. Several MCM reconnaissance sensors, designed for deployment aboard autonomous and unmanned or untethered underwater vehicles (AUV/UUVs), were evaluated for their potential application to environmental monitoring.<sup>1,2</sup> One of these sensors is the Toroidal Volume Search Sonar (TVSS), a 68kHz cylindrical acoustical array designed to detect mines at the ocean's boundaries and in its volume up to ranges of 750m (Fig 1).<sup>3</sup> Acoustic data collected by the TVSS in 1994 was supplied to researchers at several institutions (WHOI, ARL-UT, APL-UW, MPL/SIO) for the purpose of assessing the sonar's potential for scientific studies. Whereas most of these focused on the seafloor, our approach was to adapt existing multibeam imaging techniques to the TVSS data in order to simultaneously study the seafloor, sea surface<sup>4</sup> and volume.<sup>5</sup>

As with almost all data collection efforts, the TVSS data presented a number of signal processing and data reconciliation challenges. The first of these was addressed in,<sup>6</sup> where we developed the signal processing methods most appropriate for the conformal array geometry. In this paper, our intent is to show how we used environmental information to correct for errors associated with the towfish attitude and depth sensors, and to eliminate bias errors resulting from angular variations in the

transmitted beam pattern. Although our methods are specifically adapted to the cylindrical geometry of the TVSS, they can be generalized to other sonars with different acoustic geometries. The methods are limited, however, to regions where the seafloor is relatively flat, and during calm or moderately calm sea states.

This paper makes several contributions to the field of seafloor remote sensing. For signal processing, we present a new, efficient method for bottom detection which uses a simple 2D image representation of the seafloor bottom echoes in each ping in time and angle of arrival. In addition, we demonstrate that most bathymetric and/or seafloor imaging applications with towed or autonomous vehicles probably require attitude sampling rates greater than 1Hz. Lastly, our correction methods are intended to be adaptable in future AUV/UUV applications, which are increasing dramatically for reasons of economy, mobility, and utility.<sup>7-9</sup>

For example, several AUV/UUVs, each equipped with a multibeam sonar, could perform the survey work of a fleet of ships at a fraction of the cost. Two of the greatest difficulties with such an application relate to sensor design and navigation. For acoustic sensors onboard AUV/UUVs, economic reasons necessitate compact or conformal array designs, but these require more complex signal processing than linear or planar arrays. AUV/UUV navigation techniques usually combine dead-reckoning or inertial navigation with acoustic transponders or resets with Global Positioning System (GPS) fixes,<sup>10</sup> but these are not economically or tactically feasible in many operational scenarios. The processing methods that we have developed for the TVSS address both of these issues because cylindrical geometries are perfectly suited for future AUV/UUVs,<sup>11</sup> and because environmental data may be used to bound the navigation error in dead-reckoning and inertial navigation systems.<sup>10</sup> Moreover, unlike others which use only seafloor data,<sup>8,12,13</sup> our methods benefit from quasi-synoptic 3D acoustic backscatter measurements.

We begin in section II with a description of the TVSS and the data collection, emphasizing the sources of error. Section III outlines the signal processing steps used to construct bathymetric maps and seafloor acoustic backscattering strength imagery from the TVSS data. We also describe the acoustic geometry to support our subsequent interpretation and analysis of the processed data. In section IV, we describe our methods for correcting the errors and bias in the bathymetry and backscatter imagery, and we evaluate the results before concluding in section V.

## II. TVSS DATA

### A. The Toroidal Volume Search Sonar

The TVSS includes separate cylindrical projector and hydrophone arrays (Table Ia,b), both 0.53m in diameter and deployed on a cylindrical towed vehicle for prototype testing. The projector array has 32 elements equally-spaced 11.25° apart. Although its beampattern was meant to be omni-directional in the across-track direction, the actual pattern exhibited angular variations of  $\pm 4.5$ dB (Fig 2a). Its -3dB beamwidth is 3.7° in the along-track direction (Fig 2b). The hydrophone array consists of 120 elements equally-spaced every 3°. Individual element pattern magnitude data were provided by the manufacturer (Fig 2c,d), but element pattern phase data were unavailable.<sup>14</sup> Prior to beamforming, the acoustic signals from the 120 hydrophones are heterodyned in the data acquisition system (DAS) from 68 kHz to 6.25 kHz, low-pass filtered, and digitally recorded using 16 bit signed integer 2's complement coding at a sampling frequency of 25 kHz. The full scale of the recorded data is  $\pm 5$ V, so we converted the digital data to volts by:

$$d_v = 10 \left[ \frac{d_l + 2^{n-1}}{2^n - 1} \right] - 5 \quad , \quad (\text{volts}) \quad (1)$$

where  $n=16$  bits,  $d_l$  is the recorded digital value, and  $d_v$  is the output voltage. The beamforming used in this study resulted in receive beams with -3dB beamwidths of  $4.95^\circ$  and is described in section III.

## B. Data Collection

The acoustic data were collected by the TVSS in a  $2 \text{ nm}^2$  area 65nm southeast of Panama City, Florida, in the northeastern Gulf of Mexico (Table Ic). The TVSS was towed at a nearly-constant depth of 78m (Fig 3). Three runs of 100 consecutive pings of acoustic backscatter data from a  $200\mu\text{s}$  CW pulse of 68 kHz were obtained while the towship speed was nearly constant at 4.1m/s (Fig 3b). Towfish attitude and motion data were sampled at 1Hz (once per ping) and included roll, roll rate, pitch, heading, speed, and depth. Statistics for the roll, pitch, yaw, speed, and depth values in each TVSS run are listed in Table II. The yaw values were estimated by subtracting the towfish's heading for each ping from the ship's average course during the run. Of these parameters, the towfish roll varied the most, with the largest standard deviations and ranges. The yaw and pitch varied less, and the speed and depth values were nearly constant.

## C. Environmental Conditions

A single CTD cast was taken at 0658AM, which revealed the presence of an isothermal mixed layer with a temperature of  $24.8^\circ\text{C}$  extending to a depth of 49m, a thermocline between 49m-150m depth, and a nearly-isothermal layer above the bottom with a temperature of  $15.6^\circ\text{C}$ . The surface salinity was 35.1 ppt, and the surface sound speed was 1534m/s. The wind speed recorded at 0658AM onboard *Mr. Offshore* was 6 knots (3m/s). The sea state was 1.5, which corresponds to significant wave heights of 0.25m, and rms wave heights of 0.06m according to World Meteorological Organization (WMO) codes.<sup>15</sup> Coarse resolution ( $O(1\text{km}^2)$ ) bathymetry for the region was obtained during surveys conducted by the U.S. Naval Oceanographic Office (NAVO) indicated that the TVSS deployment site was directly over the 100 fathom line, where the seafloor was relatively flat with a 3m/km south-westward slope. Sediment samples collected by the Naval Coastal Systems Laboratory (NCSL) in 1972 within 1km of the TVSS deployment site consisted of 78% fine sediments (grain diameter  $d_g \leq 0.062\text{mm}$ ), 21% sand ( $0.062 < d_g \leq 1.0\text{mm}$ ), and 1% gravel ( $d_g > 1.0\text{mm}$ ).<sup>16</sup> These sediments fall within the western Florida lime-mud facies, consisting of calcium carbonate, quartz, and clay minerals.<sup>17</sup> Although bulk grain size ( $M_z$ ) measurements were not made, we used Hamilton and Bachman's (1982)<sup>18</sup> regression equations to estimate  $M_z$  from the measured porosity, and grain diameter from the equation:

$$M_z = -\log_2 d_g \quad , \quad (2)$$

where  $d_g$  is in mm (Table Ic).

## III. TVSS PROCESSING

### A. Split Aperture Processing

The processing scheme that we have developed for these data is designed for conformal arrays and includes: quadrature sampling, resampled amplitude shading, element-pattern compensation, and broadside beamforming on phase-compensated,



overlapping subarrays with asymmetric projected element spacings.<sup>6</sup> This procedure permits split aperture processing<sup>19</sup> of the beamformed output (Fig 4a). We use this method because the zero-crossing of the output phase is the most accurate means to detect the arrival time of boundary reflections on the maximum response axis of the beam.<sup>19</sup> Split-aperture processing is often referred to as "interferometric" processing, and is becoming standard in commercial multibeam bathymetric sonars.<sup>20,21</sup> The advantages of applying this technique to a circular array is that all the beams are equally spaced with the same -3dB beamwidths, and that greater than 180° of coverage is possible. These characteristics are not possible with conventional linear arrays, and make circular arrays desirable for target detection,<sup>11</sup> bathymetric mapping,<sup>22</sup> and seafloor imaging. The difficulty with using circular arrays is that the maximum aperture achievable is limited to a 90° sector between the array endpoints because of diffraction effects from creeping waves<sup>23,24</sup> (Fig 4b). Therefore, we use at most 29 elements to form each beam (Fig 4a), so that the total TVSS output each ping consists of 120 4.9°-wide beams equally-spaced 3° apart in the directions perpendicular to the tangent lines to the 120 TVSS elements (e.g. Fig 1b). Tests using 180° apertures to form 2°-wide beams were performed as in,<sup>5</sup> but the large grating lobes make bottom detection difficult.

For each ping, beams are formed in each angle  $\theta$  relative to the TVSS at each time sample  $t$  by adjusting the phases of the acoustic signals from 29 elements to project the aperture on the tangent to the direction  $\theta$  (Fig 4a). The split aperture process is achieved by dividing this aperture into two overlapping 21-element apertures whose phase centers are spaced 8 elements apart. For each time sample  $t$ , the signals from these two subapertures are phased and summed separately to produce beams  $B_1(\theta, t)$  and  $B_2(\theta, t)$ , and a phasor  $P(\theta, t)$  is formed from the product

$$P(\theta, t) = B_1(\theta, t) \times B_1^*(\theta, t) \quad , \quad (3)$$

where  $*$  denotes complex conjugation. The magnitude of  $P(\theta, t)$  is the product of the magnitudes of  $B_1(\theta, t)$  and  $B_2(\theta, t)$ , hence it has units of volts squared, and its phase is the phase difference between  $B_1(\theta, t)$  and  $B_2(\theta, t)$ .  $B_1(\theta, t)$ ,  $B_2(\theta, t)$ , and  $P(\theta, t)$  are all broadside with respect to the total aperture. Each of the angles  $\theta$  are corrected for the towfish's roll and for the difference between the sound speed used in the beamforming and that of seawater at the face of the array.<sup>19</sup> At every time sample, the elements used to form the total aperture are "slipped" around the array in order to beamform every 3° for directions spanning 360° around the TVSS axis. For each ping, the result is 120 phasor time-series which may be displayed as a vertically oriented image in polar coordinates of  $\theta$  versus  $t$  (Fig 5). In this representation,  $\theta$  increases clockwise from the towfish zenith at  $\theta = 0^\circ$  through the towfish nadir at  $\theta = 180^\circ$  in the vertical plane perpendicular to the towfish's fore-aft axis. The sampling and resolution characteristics of this image are discussed in reference [5].

## B. Bottom Echo Processing

The first step in constructing a bathymetric map from the TVSS data is to detect the bottom echoes in each ping. To describe this procedure, let us define the angle of arrival  $\theta_a \equiv \theta - 180^\circ$ , where  $\theta$  is the angle relative to the TVSS in eqn (3) and Fig 5, so that  $\theta_a$  is positive on the right side of the towfish and negative on the left side when facing the direction of travel. For each ping (Fig 5), we select the phasors  $P(\theta_a, t)$  corresponding to  $\theta_a = +60^\circ$  to  $-60^\circ$ . Because the seafloor examined here is nearly flat, when these 43 phasors are displayed in Cartesian coordinates ( $x = t$ ,  $y = \theta_a$ ), boundary reflections appear as parabolas with high magnitude (Fig 6a) and quasi-linear phase (Fig 6b). The quasi-linear portion of the phase in each phasor corresponds to a plane wave echo within the beam, and the phase zero-crossing corresponds to a plane wave

echo arriving on the axis of the beam.<sup>19</sup> We use a combination of magnitude- and phase-based processing because such an approach is known to be the most effective in unambiguously determining the bottom echo time of arrival in each beam.<sup>25</sup>

We have developed a two-dimensional image processing procedure for bottom detection. Although it is similar to Yang *et al.*'s (1997)<sup>21</sup> active contour method in that it uses both the magnitude and phase components of the phasor, it is more direct because theirs uses an iterative algorithm. For each  $\theta_a$ , we first apply a maximum-likelihood filter<sup>26</sup> to the noisy quadrature components of the phasor for each time sample using a window function,  $W(n)$ , whose length ( $wl$ ) has been set to the number of samples in 5 pulse lengths (1ms). The resulting phasor estimate is:

$$\hat{P}(\theta_a, t) = \left[ \sum_{n=1}^{wl} W^2(n) P(\theta_a, i - wl/2 + n) \right] / \left[ \sum_{n=1}^{wl} W^2(n) \right] \quad (4)$$

where  $i$  is the sample number corresponding to time  $t$ .

Next, we detect the samples in each beam whose magnitude  $|\hat{P}(\theta_a, t)|$  exceeds the standard deviation of all samples in that beam. A second magnitude threshold is performed for each time sample where the threshold is the standard deviation of the samples across the 43 beams from  $\theta_a = +60^\circ$  to  $-60^\circ$ . The common output from the two thresholding steps isolates the high backscatter boundary echoes which are then searched for samples with a phase value ( $\arg(\hat{P}(\theta_a, t))$ ) between  $+\pi/12$  and  $-\pi/12$ . From these samples (Fig 6c, black), the bottom echo time of arrival in each beam is determined as the sample for which  $\arg(\hat{P}(\theta_a, t)) = 0$  (Fig 6c, red). Within  $\pm 15^\circ$  of nadir, the phase values are noisy and zero crossings are not reliable, so a weighted mean time procedure<sup>19</sup> is performed on the samples output from the two magnitude threshold procedures.

The resulting angle-time pairs are used to compute corresponding depths ( $z$ ) and horizontal distances ( $x$ ) relative to the towfish using standard constant-gradient ray-tracing techniques<sup>27</sup> and values for the towfish pitch and yaw. Because accurate towfish navigation data was unavailable, towfish speed and heading were used to estimate the horizontal spacing between pings and the along-track location ( $y$ ) for each bathymetric sample relative to the mean towfish track. We provide expressions for these calculations in the error analysis in section IV.

### C. Acoustic Backscatter Processing

Acoustic backscattering strength imagery is created by first selecting the magnitude of the phasor ( $P(\theta_a, t)$ ) at each bathymetric sample. Multibeam sidescanning<sup>28</sup> is then performed, in which the acoustic backscatter data is averaged for each quadrature sample between the bottom echo arrivals of two adjacent beams. The across-track locations corresponding to each of these samples are computed by interpolating between the locations of the bottom echo arrivals in the two adjacent beams. This results in a finer across-track sampling interval than the beam spacing (see below). As with the bathymetry, along-track coordinates relative to the track center of the first ping are estimated using towfish speed and yaw. The sidescanned backscatter is then converted to bottom acoustic *backscattering strength* using the active sonar equation:<sup>27</sup>

$$S_B = RL - SL + 2TL - 10 \log_{10} A, \quad (5)$$

$$\text{with } RL = EL - (RVR + FG + DI + TVG),$$

in which the echo level  $EL = 10 \log_{10} \left( \frac{1}{2} |P(\theta_a, t)|^2 \right)$ ,  $RVR = -168 \text{ dB re: } 1 \text{ V}_{rms}/\mu\text{Pa}$  is the average receive voltage response of each hydrophone,<sup>14</sup>  $FG = 29 \text{ dB}$  is the preamplifier

fixed gain,  $DI = 13$  dB is the array gain associated with the beamforming and split aperture processing, TVG is the system time-varying gain,<sup>29</sup> SL is the calibrated transmit source level of 216.8dB *re* 1 $\mu$ Pa @ 1 m,<sup>30</sup>  $TL = 20 \log_{10} R + \alpha R$  is the one-way transmission loss due to spherical spreading and absorption with the logarithmic absorption coefficient  $\alpha = 0.024$  dB/m,<sup>31</sup> range  $R$  is determined from  $t$  and  $\theta$  using constant-gradient raytracing techniques,<sup>27</sup> and  $A$  is the area on the seafloor within the receive beam that is ensonified by the transmitted pulse.

#### D. TVSS Acoustic Geometry

The sampling and resolution characteristics of the TVSS data are defined by the acoustic geometry (Fig 7). In a single ping (Fig 5), the angular sample spacing between the maximum response axes of adjacent beams is  $\theta_s = 3^\circ$  and the quadrature sampled time increment within each beam is  $\tau_s = 160$   $\mu$ s, which corresponds to a 12cm slant range sampling interval assuming a sound speed of  $c = 1500$  m/s. The range resolution for each sample is a function of the bandwidth  $W$ :

$$\Delta r = c / 2W \quad (\text{m}). \quad (6)$$

With the TVSS pulse length  $\tau_p = 200$   $\mu$ sec, the bandwidth  $W = 0.88/\tau_p = 4.4$  kHz, which yields a range resolution  $\Delta r = 17$  cm with  $c = 1500$  m/s. Between multiple pings, the along-track separation is given by:

$$\Delta y_{ping} = V_{TVSS} / \text{prf} \quad (\text{m}), \quad (7)$$

where  $V_{TVSS}$  is the towship's speed, and prf is the pulse repetition rate of 1 Hz. In this experiment, the average  $V_{TVSS} = 4.1$  m/s and prf = 1 Hz, hence  $\Delta y_{ping} = 4.1$  m.

Data points in the processed bathymetry and seafloor acoustic backscattering strength images are separated by an along-track sample spacing  $\delta y_B = \Delta y_{ping}$ . Because the seafloor at the experiment site was mostly flat, the across-track sample spacing in the processed bathymetry is approximately:

$$\delta x_B = H_{TVSS} [ \tan |\theta_a| - \tan(|\theta_a| - \theta_s) ] \quad (\text{m}) \quad (\text{relief maps}), \quad (8)$$

where  $H_{TVSS}$  is the towfish's altitude above the seafloor, and  $\theta_a$  is  $0^\circ$  at nadir and increases towards the right of nadir when facing the direction of travel. Thus, sample spacing in the bathymetry increases across-track. On the other hand, the across-track sample spacing in the seafloor acoustic backscattering strength imagery decreases across-track, and is given by:

$$\delta x_B = c \tau_s / 2 \sin |\theta_a| \quad (\text{m}) \quad (\text{images}), \quad (9)$$

where, again, we have assumed a flat seafloor. This is a consequence of the sidescanning procedure, which records samples in each receive beam at the quadrature sampling rate  $1/\tau_s$  as the transmitted pulse travels across the beam footprint (Fig 7).

The resolution of samples in the bathymetry and backscattering strength images depends upon the area of the transmitted pulse that ensonifies the seafloor within each receive beam. For  $\theta_a$  near normal incidence, the area is defined approximately by an ellipse (Fig. 7):

$$A = \pi \Delta R (1 + 2H_{TVSS}/\Delta R)^{1/2} H_{TVSS} \theta_T / 2 \quad (\text{m}^2) \quad (10)$$

When the trailing edge of the pulse touches the seafloor, its along-track, across-track, and vertical extent at nadir are given by:

$$\begin{aligned}
\Delta x_B &= 2 \Delta R (1 + 2H_{TVSS} / \Delta R)^{1/2} \\
\Delta y_B &= H_{TVSS} \theta_T \quad (m) \\
\Delta z_B &= \Delta R \cos(\theta_R / 2) \quad ,
\end{aligned} \tag{11}$$

where  $\Delta z_B$  is less than the range resolution because of the curvature of the pulse.

Beyond a delimiting angle of  $\cos^{-1}(H_{TVSS} / (H_{TVSS} + \Delta R))$ , the ensonified area is defined by an annulus sector (Fig. 7). An approximate expression for this area on a flat seafloor is:

$$A \approx (R \Delta R \theta_T) / \sin(|\theta_a|) + (\Delta R^2 \theta_T) / (2 \sin(|\theta_a|)) \quad , \quad (m^2) \tag{12}$$

with spatial dimensions given by:

$$\begin{aligned}
\Delta x_B &= R (\theta_R / 2) \cos(|\theta_a|) + \Delta R \sin(|\theta_a| + \theta_R / 2) \\
\Delta y_B &= R' \theta_T \quad (m) \\
\Delta z_B &= R (\theta_R / 2) \sin(|\theta_a|) \quad .
\end{aligned} \tag{13}$$

Thus, as  $x$  increases, the across-track width ( $\Delta x_B$ ) of the ensonified area decreases while the along-track width ( $\Delta y_B$ ) increases. The across-track increase in the vertical extent of the pulse ( $\Delta z_B$ ) implies that vertical resolution degrades across-track.

## IV. BATHYMETRY

### A. Depth Bias Estimation and Correction

Comparison of the TVSS bathymetry initially processed for each run with the NAVO bathymetry for the region uncovered two types of errors: the mean depths in each run were 14-15m too shallow, and the profiles sloped downward symmetrically on either side of the track centerline. Because sound speed uncertainty is one of the largest sources of error in multibeam bathymetry,<sup>28,32-35</sup> the symmetric downward sloping errors were found to result from a 6m/s positive sound speed error. The systematic depth errors, however, could not be explained by any realistic deviation in the sound speed profile, and inspection of the upward-looking beams in individual pings (e.g. Fig 5) indicated that the towfish was actually 14-15m deeper than the depths recorded by the towfish depth sensor (Table IIe). This bias most likely resulted from referencing the depth sensor in the laboratory rather than at sea level. A towfish depth bias also would explain the symmetric bending of each profile because an increase in depth from 64m to 78m corresponded to a 6m/s decrease in sound speed according to the CTD profile collected during the experiment.

To re-process the bathymetry in each run, we incorporated a procedure which used the upward-looking TVSS beams to determine the towfish depth in each ping. Sea surface boundary detection was performed using the bottom echo processing methods described above, with an additional step designed to prevent false boundary detection from the dense clouds of resonant microbubbles in the towship's wake, which extended 6-7m below the sea surface above the towfish.<sup>4</sup> First, an estimate of the sea surface altitude relative to the TVSS was computed for each ping by fitting a horizontal plane to sea surface detections in beams outside the wake ( $> 30^\circ$  and  $< -30^\circ$  from the towfish's zenith). Then, surface detection was performed on samples in the upward-looking beams within  $\pm 5^\circ$  from the towfish's zenith, and within a range gate of  $\pm 1.5m$  of the first sea surface boundary estimate. As with the initial depth values (Table IIe), the new towfish depth estimates (Table IIIa) changed little over each run, supporting our conclusion that the depth bias was a sensor-related artifact. The depth corrected bathymetry did not exhibit the symmetric downward bending which

appeared when the bathymetry was initially processed.

## B. Roll Error Estimation and Correction

The depth corrected bathymetry suffered from two other types of artifacts. The first type appeared as random spikes with heights on the order of the TVSS vertical resolution. These resulted from false bottom detections produced by noise spikes associated with saturation in the DAS electronics. We identified these by inspecting the backscatter in individual pings (e.g. Fig 5), where saturated samples appeared as arc-like features which extended only 1-2 samples in time and  $6-24^\circ$  in angle (see Figs in reference [5]). To reduce the effects of these false bottom detections on our subsequent analyses, we used a two-dimensional median filter with a window  $3 \times 3$  beamwidths in size. The result for the depth corrected bathymetry is displayed in Fig 8a.

The other artifact appeared as along-track corrugations that increased in height with distance from the track centerline (Fig 8a). Even though fine-resolution bathymetry for the region was not available for comparison, it was apparent that these features were not due to actual seafloor morphology because they were identical in each of the three TVSS runs and because they were similar to the bathymetric artifacts produced by roll errors in other multibeam systems (e.g. reference [36]). We verified that these artifacts were due to roll errors by plotting the along-track bathymetric profiles in the outermost beams to the left and right of the track centerline (Fig 9a), which showed that the variations in the positive beams were of the opposite sign as those in the negative beams. Sample correlation coefficients between the unfiltered bathymetric data in positive and negative beam angles were highly negative in the outermost beams for all three runs (e.g. Fig 9b), indicating that the artifacts were related to an error in the towfish roll data.

Because the NAVO bathymetry for the region is nearly flat, we estimated the roll error for each ping by detrending the depth corrected bathymetry along- and across-track, and computing the residual across-track slope for each ping. Detrending removed the influence of the large scale slope, and the residual along-track slopes were computed for each ping by fitting a line to the across-track bathymetric profile. These slopes were then used as corrections to the initial towfish roll data (Fig 10a). We did not estimate roll errors from sea surface relief maps because they suffered also from artifacts resulting from bottom echo sidelobe interference and scattering from resonant microbubbles in the towship's wake.<sup>4</sup> Thus, consistent and reliable line fitting was more difficult than that applied to bathymetry. The depth corrected bathymetry for run 3 (Fig 8a) after roll correction (Fig 8b) has most of the negative correlation between positive and negative beams removed (Fig 9b).

The roll errors are most likely the result of undersampling of the towfish's roll signal. Because the roll data are sampled once per ping at the pulse transmission time ( $t=0$ ), the roll errors (Fig 10a) are the result of the towfish's motion from the time the pulse is transmitted to the time the bottom echo is received by the sonar. Power spectra of the towfish's roll (not shown) revealed several low and high frequency components. The periods corresponding to the peaks in the spectrum included a  $\sim 50$ s component associated with the motion after the ship turns (e.g. Fig. 10c) and several components between 3-6s just above the 2s Nyquist interval. In the absence of any roll components with frequencies higher than the Nyquist limit of 0.5Hz, one should be able to integrate the roll rate (Fig 10b) or interpolate between roll samples for each ping to determine the correct roll for each time sample within a ping (e.g. reference [3]). We found that none of these methods succeeded in removing the roll-related artifacts. Fig 10c compares the roll samples estimated from the bathymetry, and those estimated from using the roll rate, and linear or quadratic interpolation between roll

samples in each ping. Differences between the roll estimated from the bathymetry and that estimated using the other methods are up to  $0.8^\circ$ , and generally occur when the roll rate is changing sign. These results suggest that there are components in the towfish roll which are higher than the 0.5Hz maximum frequency detectable at the 1Hz sampling rate. The cause for this is probably related to the fact that the TVSS towfish was negatively buoyant (weighted by the tow cable) and that the cable was attached to the towfish nose, both of which are characteristics associated with poor attitude stability in towed platforms.<sup>37,38</sup>

For this, and other applications in which bathymetric data are collected by sonars on towed and autonomous vehicles, it is desirable to know the sampling rate required for the bathymetry to meet the International Hydrography Organization (IHO) error standard of 1% of the sonar's altitude. The minimum sampling rate should be at least two times the highest frequency component of the platform roll. Because we could not detect such components with the TVSS towfish's 1Hz sampling rate, we estimate a useful sampling rate as twice the maximum ping-to-ping roll difference divided by the minimum roll error tolerance required to meet the IHO bathymetry standard,  $\Delta\theta_r = 0.01/\tan(|\theta_a|)$ . The maximum ping-to-ping roll difference was  $1.21^\circ$  (Table IIa), and the minimum  $\Delta\theta_r = 0.33^\circ$  for  $\theta_a = 60^\circ$ , yielding a sampling rate of  $\sim 7.3$  Hz. This is a reasonable lower bound on the attitude sampling rate required for bathymetric and acoustic imaging applications involving both towed and autonomous platforms because the sea state during the TVSS experiment was relatively calm, and because roll variations greater than 1Hz also can affect submerged AUVs.<sup>39</sup>

### C. Evaluation of the Corrected Bathymetry

The depth and roll corrected bathymetry (Fig 11) are generally consistent with the large scale NAVO bathymetry for the region, but proper evaluation requires precise, high resolution sounding data as well as cross-check tracks. Because the resolution of the NAVO bathymetry was too coarse for this, and the cross-check data collected during the TVSS deployment were classified, we evaluated our results by calculating the average standard deviation of the bathymetry in each angle of arrival, after along- and across-track detrending, and displaying the result in percent of towfish altitude. ( $\sigma_z/H_{TVSS} \times 100\%$ , Fig 12). This approach is routinely used for assessing the bathymetric error when the seafloor is relatively smooth.<sup>40-42</sup> The results for all three runs were similar, and showed that the roll error corrections improved the results dramatically. Although the estimated roll errors (Fig 10a) were not excessively large, they produced significant bathymetric errors. For example, the maximum roll error in run 3 was  $0.93^\circ$  and produced a depth error in Fig 8a of 3.2m at  $x = -200$  ( $\theta_a \approx 60^\circ$ ), which is over twice the IHO error standard. These results are consistent with numerous studies which have demonstrated the effect of roll error on multibeam bathymetry.<sup>33,34,36</sup>

Several other system related sources of error are revealed by Fig 12. Errors associated with the bottom detection scheme produce the relative peaks near  $\theta_a = +15^\circ$  and  $-15^\circ$ , which correspond to the transition region where amplitude-based detection near nadir changes to phase-based detection. This type of error is known to produce bathymetric artifacts in other interferometric multibeam systems.<sup>43</sup> The relative peaks are higher for positive angles of arrival because one hydrophone on the lower right side of the array was inoperable, which resulted in higher sidelobe levels and a slight decrease in DI for these beams. Errors associated with system noise and resolution are represented by the difference between the unfiltered and median filtered bathymetry.

### D. Error Budget for the Corrected Bathymetry

To derive an error budget for the depth- and roll-corrected TVSS bathymetry (Fig. 11), we begin with our calculations for  $x$ ,  $y$ , and  $z$ :

$$\begin{aligned} x &= x_{ray} \cos(\omega + \phi) \\ y &= x_{ray} \sin(\omega + \phi) + V_{TVSS} \text{ prr} , \\ z &= z_{ray} \cos(\phi) + Z_{TVSS} \end{aligned} \quad (14a)$$

where  $Z_{TVSS}$  and  $V_{TVSS}$  are the towfish's depth and speed, prr is the pulse repetition rate of 1Hz, and  $x_{ray}$  and  $z_{ray}$  are the  $x$  and  $z$  locations obtained from raytracing, before correcting for towfish pitch ( $\phi$ ) and yaw ( $\omega$ ). We estimated the  $y$  coordinates by dead reckoning from the nadir sample of the first ping ( $(x,y) = (0,0)$ ) with the towfish heading and speed data because accurate towfish navigation data were not available.

The locations derived from raytracing are related to the slant range ( $R$ ) and angle of arrival ( $\theta_a$ ) by:

$$\begin{aligned} x_{ray} &= R \sin(|\theta_a|) \\ z_{ray} &= R \cos(|\theta_a|) , \end{aligned} \quad (14b)$$

so that

$$\begin{aligned} x &= R \sin(|\theta_a|) \cos(\omega + \phi) \\ y &= R \sin(|\theta_a|) \sin(\omega + \phi) + V_{TVSS} \text{ prr} . \\ z &= R \cos(|\theta_a|) \cos(\phi) + Z_{TVSS} \end{aligned} \quad (14c)$$

Note that  $\theta_a$  is the angle of arrival for a non-refracting ray following a raypath along  $R$  (Fig 7), which was smaller than the actual angle of arrival at the face of the array ( $\theta_A$ ) due to the downward refracting sound speed profile at the TVSS deployment site. Although we used the measured time of arrival ( $t_a$ ) and  $\theta_A$  in the raytracing procedure, we choose to derive an error budget from (14c) rather than (14a) because the CTD specifications were unavailable, hence, raytracing errors due to sound speed uncertainty were difficult to estimate. Thus, we assume that bathymetric errors due to uncertainties in  $\theta_a$  and  $t_a$  are approximately equal to those for  $\theta_A$  and  $R$ .

Bathymetric errors arise from the propagation of uncertainties in each of the terms in these expressions (Table IV). The angle of arrival uncertainty ( $\delta\theta_a$ ) is the sum of the roll uncertainty ( $\delta\theta_r$ ), and the beam pointing angle uncertainty associated with the beamforming, split aperture processing, and uncertainties concerning the sound speed profile. Beam pointing angle errors of up to  $1.0^\circ$  resulted from irregularities in the TVSS element patterns (Fig 2c,d) but were corrected using the gain and phase compensation methods described in reference [6]. Sound speed uncertainties could not be obtained, as discussed previously. The uncertainty in the corrected towfish roll is estimated from the experimental TVSS data in Fig 12 and the beam geometry (Fig 7) as the roll required to produce the 1% of altitude increase in  $\sigma_z$  from  $\theta_a = 0^\circ$  to  $60^\circ$ :

$$\delta\theta_r \approx \delta z_r / (H_{TVSS} \tan(|\theta_a|)) , \quad (\text{radians}) \quad (15)$$

where  $\delta z_r = \sigma_z$  is the depth error associated with a roll error of  $\delta\theta_r$ . Thus,  $\delta\theta_r \approx 0.3^\circ$  for an average TVSS altitude  $H_{TVSS} = 115\text{m}$ ,  $\theta_a = 60^\circ$ , and  $\delta z_r / H_{TVSS} = 0.01$ .

The uncertainties in pitch ( $\delta\phi$ ) and yaw ( $\delta\omega$ ) are defined by the accuracy and repeatability of the towfish's inertial measurement sensor. Because manufacturer specifications for the Doppler sonar used to measure the TVSS speed were not available,  $\delta V_{TVSS}$  is estimated from the maximum standard deviation of speed in Table II, rounded to the nearest 0.1m/s. The uncertainty in depth associated with the depth correction procedure depends upon the bandwidth-defined range resolution and sea state. With the 0.17m TVSS range resolution and the 0.25m significant wave heights during the experiment, the maximum  $\delta Z_{TVSS}$  is estimated to be  $\pm 0.2\text{m}$ .

The range uncertainty ( $\delta R$ ) is associated with the bottom detection procedure, which depends upon the range resolution, sampling rate, and system noise. As with  $\delta\theta_a$ , the maximum range uncertainty may be estimated from the experimental data in Fig 12. The largest artifact associated with the bottom detection procedure is the peak near  $\theta_a = +15^\circ$ , where the procedure transitions from phase based detection to magnitude-based detection near nadir. Therefore, we estimate the maximum  $\delta R$  associated with the bottom detection procedure to be that which produces the 0.5% of altitude increase in  $\sigma_z$  from  $\theta_a = 10^\circ$  to  $15^\circ$ . If  $\delta z_{bd}$  is the depth uncertainty associated with the bottom detection procedure, then

$$\delta R \approx \delta z_{bd} / \cos(|\theta_a|) \quad (m) \quad (16)$$

Thus,  $\delta R \approx 0.6m$  with  $\theta_a = 15^\circ$ ,  $H_{TVSS} = 115m$ , and  $\delta z_{bd} = 0.005(H_{TVSS})$ ,

To estimate the total error in eqn (14c) using these uncertainties (Table IV), we consider two cases. The first is the upper bound on the uncertainty calculated from the following formula:<sup>44</sup>

$$\delta q_{upper\ bound} \leq \left| \frac{\partial q}{\partial a} \right| \delta a + \dots + \left| \frac{\partial q}{\partial h} \right| \delta h \quad , \quad (17)$$

where  $q(a, \dots, h)$  is a function computed from the measured quantities  $a, \dots, h$ , which have associated uncertainties  $\delta a, \dots, \delta h$ . The second case applies when the uncertainties  $\delta a, \dots, \delta h$  are independent and random:<sup>44</sup>

$$\delta q_{random} = \sqrt{\left( \frac{\partial q}{\partial a} \delta a \right)^2 + \dots + \left( \frac{\partial q}{\partial h} \delta h \right)^2} \quad . \quad (18)$$

Applying (17) to (14c), upper bounds on the positional errors in the TVSS bathymetry may be expressed as:

$$\begin{aligned} \delta e_x &\leq |\cos(\phi+\omega)| (|\sin\theta_a| \delta R + R |\cos\theta_a| \delta\theta_a) + R |\sin\theta_a \sin(\phi+\omega)| (|\delta\phi| + |\delta\omega|) \\ \delta e_y &\leq |\sin(\phi+\omega)| (|\sin\theta_a| \delta R + R |\cos\theta_a| \delta\theta_a) + R |\sin\theta_a \cos(\phi+\omega)| (|\delta\phi| + |\delta\omega|) + \delta V_{TVSS} \quad . \quad (19) \\ \delta e_z &\leq |\cos\theta_a| (|\cos\phi| \delta R + R |\sin\phi| \delta R) + R |\sin\theta_a \cos\phi| \delta\theta_a + \delta Z_{TVSS} \end{aligned}$$

If the parameters in Table IV are independent and random, then (19) may be used to express the positional uncertainties as:

$$\begin{aligned} \delta e_x &= \sqrt{\cos^2(\phi+\omega) [(\sin\theta_a \delta R)^2 + (R \cos\theta_a \delta\theta_a)^2] + [R \sin\theta_a \sin(\phi+\omega)]^2 [(\delta\phi)^2 + (\delta\omega)^2]} \\ \delta e_y &= \sqrt{\sin^2(\phi+\omega) [(\sin\theta_a \delta R)^2 + (R \cos\theta_a \delta\theta_a)^2] + [R \sin\theta_a \cos(\phi+\omega)]^2 [(\delta\phi)^2 + (\delta\omega)^2] + (\delta V_{TVSS})^2} \quad . \quad (20) \\ \delta e_z &= \sqrt{\cos^2\theta_a [(\cos\phi \delta R)^2 + (R \sin\phi \delta R)^2] + [R \sin\theta_a \cos\phi \delta\theta_a]^2 + (\delta Z_{TVSS})^2} \end{aligned}$$

Error estimates from (19) and (20) in percent of the towfish altitude versus angle of arrival are displayed in Fig 12 (with the experimental estimate) and Fig 13. Whereas the upper bound model (19) probably overestimates the actual errors for most angles of arrival, the random error model (20) probably underestimates them for all but small angles of arrival because it assumes that the towfish attitude and depth parameters are independent and random. Independent and random variables are uncorrelated,<sup>45</sup> but moderate correlations were observed between several of the towfish attitude and motion parameters (Table V). Furthermore, the lack of correlation between many of the parameters in Table V does not necessarily imply that they were independent or random. A comparison between Fig 12 and Fig 13c shows that the actual  $\delta e_z$  in the TVSS bathymetry is probably less than that predicted by (19), but greater than that predicted by (20). Therefore, we conclude that the actual bathymetric errors in  $x$ ,  $y$ , and  $z$  probably lie somewhere in between the upper bound and random error estimates in Fig. 7.

Despite the good correspondence between Fig 12 and 13c, seafloor roughness probably contributed to the standard deviations of the TVSS bathymetry, in addition



to attitude and motion uncertainties. Because acoustic backscatter is strongly influenced by seafloor roughness and sediment type, we will analyze the angular dependence of seafloor acoustic backscattering strength in order to further evaluate the TVSS data.

## V. SEAFLOOR ACOUSTIC BACKSCATTERING STRENGTH IMAGERY

### A. Transmit and Receive Directivity Compensation

The acoustic backscattering strength images were contaminated by several types of artifacts. The first consisted of random hydrophone dropouts and noise spikes resulting from saturation in DAS electronics, which we discussed previously for the bathymetry. Pings suffering from hydrophone dropouts appeared as individual scan lines containing anomalously low  $S_B$  data. This occurred in only 1-3 pings for each run, and they were replaced with data interpolated between samples in adjacent pings. Data points affected by noise spikes were replaced with data interpolated between adjacent samples in time.

The most significant artifact can be seen in Fig 14a as the pattern of high- and low-backscatter bands which extend along the entire length of the track and "bend" with the roll of the towfish (Fig 10c). The across-track variations associated with these artifacts are about  $\pm 3$ dB (Fig 14b), significantly different from the smooth type of angular dependence function expected from the silt and sand sediment mixture in the region.<sup>46-49</sup> This artifact is explained by the combined transmit and receive beam-patterns (Fig. 2). Because eqn (5) assumes that the source level (SL) is a constant function of  $\theta_a$ , across-track biases in the acoustic backscatter data result from not accounting for the nonuniform transmit beampattern in Fig 2a. Differences between individual hydrophone element patterns also contribute to the artifact by making the effective receive directivity in eqn (5) (RVR+FG+DI+TVG) vary with  $\theta_a$  as well.

The calculation of ensonified area is affected because eqns (10) and (12) assume that both the transmit and receive array beampatterns are uniform for all  $\theta_a$ . Therefore, the area term in eqn (5) should be replaced with:

$$A(R, \theta_a) = \frac{c}{2W \sin \theta_a} R \int_{-\theta_r/2}^{+\theta_r/2} b(\theta_a, \phi_a) b'(\theta_a, \phi_a) d\phi_a, \quad (21)$$

in which  $\phi_a$  is the azimuthal angle,  $b(\theta_a, \phi_a)$  is the transmit pattern, and  $b'(\theta_a, \phi_a)$  is the receive pattern. Although the transmit pattern was designed to be omni-directional in the roll plane (e.g. Fig 1a), such uniform array patterns are difficult to achieve, and many seafloor acoustic backscattering studies have been affected by non-uniformity in sonar transmit beam patterns.<sup>50-52</sup>

The correspondence between the TVSS directivity and the biases in the backscattering strength image is clearly seen by comparing the mean backscattering strength ( $S_B$ , Fig 14b) computed from 27 pings in Fig 14a with the TVSS transmit pattern in Fig 2a. The portion of the transmit pattern responsible for the biases in the backscatter image is the  $121^\circ$  wide sector centered at  $191^\circ$ . It is shifted from nadir due to the  $11^\circ$  mean towfish roll for the 27 pings used to form the average. Because the representation in Fig 2a is that facing the towfish, the sector between  $130^\circ$  and  $190^\circ$  contributed to the biases on the left side of the image ( $\theta_{inc} < 0^\circ$  in Fig 14b), and the sector between  $191^\circ$  and  $250^\circ$  contributed to the biases on the right side ( $\theta_{inc} > 0^\circ$ ). Thus, the nulls and peaks in  $S_B$  plotted in Fig. 14b are closely associated with those in the transmit pattern. The  $S_B$  values for  $\theta_{inc} = 3^\circ$  to  $45^\circ$  exceed those of the corresponding negative angles because the overall levels in the transmit pattern were 2-3dB higher on the left side of the array and the receive beams in this sector suffered a

slight drop in gain due to the previously mentioned failed hydrophone on this part of the array. The inoperable hydrophone also caused the sidelobes of these beams to be 7-10dB higher than the design level of -30dB. This led to the systematic early bias in bottom detections near  $\theta_a = 15^\circ$ , and hence, a slight negative bias in backscattering strength.

We initially attempted to correct these artifacts by recalculating  $S_B$  using the angular dependent transmit SL and ensonified area in eqn (5), but this approach was unsuccessful. This was most likely due to uncertainties in the corrected towfish roll (Table IV) and the receive pattern terms of eqn (5). The receive patterns for the various beams were assumed to be identical because the manufacturer provided element pattern data for only a subset of the 120 TVSS hydrophones. Another possibility is that the hydrophone and projector beampatterns may have changed during the year between the time the TVSS was received by CSS and the time it was deployed for the experiment.<sup>30</sup>

Consequently, we tested two alternative methods for removing the biases in the backscatter imagery, both of which incorporated environmental and system-related information. The first method is adapted from Hellequin *et al.* (1997),<sup>50</sup> and is applicable to calibrated and non-calibrated sonars. For data collected over a flat bottom, which we know is the case for the TVSS data (Fig 12), the artifacts are assumed to result mostly from the sonar's directivity. A function is fit to the mean backscattering strength data ( $S_B(\theta_{inc})$ ) computed over a number ( $N_p$ ) of pings (e.g. Fig 14b) which is Gaussian near normal incidence, and Lambertian away from normal:

$$S_{B_f}(\theta_{inc}) = 10\log_{10}(A_f \exp(-a_f \theta_{inc}^2) B_f \cos^{b_f} \theta_{inc}) , \quad (22)$$

where  $\theta_{inc}$  is the angle of incidence, equal to  $\theta_a$  minus the bottom slope, and the constants  $A_f$ ,  $B_f$ ,  $a_f$ , and  $b_f$  are adjusted to fit the data.  $N_p$  is selected for along-track increments during which the roll changes less than  $1^\circ$ . Thus, when the roll is rapidly changing, as in Fig. 10c, the mean and model function are computed over smaller intervals than of those for when the roll changes little.

The fit is adjusted so that the normal incidence value of  $S_{B_f}(\theta_{inc})$  is equal to that of  $S_B(\theta_{inc})$  at normal incidence ( $\theta_{inc} = 0^\circ$ ), minus the relative value of the mean roll-adjusted transmit pattern. For example,  $S_{B_f}(\theta_{inc})$  is fit 6dB above the mean  $S_B(\theta_{inc})$  at normal incidence because the transmit pattern value from Fig 2a at  $191^\circ$  is about -6dB. The combined transmit and receive directivity is estimated as

$$[\Delta SL(\theta_{inc}) + DI(\theta_{inc})] = S_B(\theta_{inc}) - S_{B_f}(\theta_{inc}) \quad (23)$$

and is used to compensate each ping in the backscattering strength image by

$$S_{B_c}(\theta_{inc}, j) = S_B(\theta_{inc}, j) - [\Delta SL(\theta_{inc}) + DI(\theta_{inc})] , \quad (24)$$

where  $j$  denotes the ping number. A new estimate for  $[\Delta SL(\theta_{inc}) + DI(\theta_{inc})]$  is computed from eqn (23) when the roll changes by  $1^\circ$  from the roll value corresponding to the first ping used to compute the previous estimate. Thus, the procedure removes the curved banding in Fig. 14a that results from the transmit pattern as it translates with the towfish roll (Fig. 10c) across-track (Fig 14c).

The second method is applicable to calibrated sonars and uses the same approach as the first method, but with APL-UW's (1994)<sup>53</sup> seafloor backscattering strength model in place of eqn (22). The earliest version of the model was presented by Jackson (1986),<sup>54</sup> and further developed by Mourad and Jackson (1989).<sup>55</sup> Because it has been described extensively in the literature,<sup>46,48,49,56</sup> we provide only a brief description as it relates to the TVSS data. The model is valid for frequencies between 10-100kHz and breaks bottom backscattered energy into one component due to interface roughness and another due to sediment volume inhomogeneities. Scattering from surface

roughness is modeled using the Kirchhoff approximation near normal incidence and the composite roughness approximation for  $\theta_{inc} \approx 10^\circ$  to  $90^\circ$ .

Ideally, all input parameters (Table VI) are measured with the exception of the sediment volume parameter ( $\sigma_2$ ), which is fit to the data (e.g. references [49][54][55][57]). Because *in-situ* sediment data were unavailable for our experiment, we used the regression equations in Hamilton and Bachman (1982)<sup>18</sup> to estimate bulk grain size ( $M_z$ ) from the porosity measurements of McLeroy (1972)<sup>16</sup> (Table Ie).  $M_z$  was then used to compute the sound speed ratio ( $v$ ), the density ratio ( $\rho$ ), and the loss parameter ( $\delta$ ) using the regression equations in reference [53] and Hamilton (1972)<sup>58</sup>. The model assumes that the bottom relief is governed by Gaussian statistics with an isotropic two dimensional spectrum obeying a simple power law with a slope  $-\gamma$  and strength  $w_2$ . We were unable to verify this because the spatial resolution of the TVSS was insufficient for determining the  $\text{cm}^{-1}$ -scale roughness spectrum required by the model. Therefore, we used the APL-UW model<sup>53</sup> default of  $w_2 = 0.000518$  and obtained the best fit to the data with  $\gamma = 3.00$  and  $\sigma_2 = 0.003$  (Table IV, Fig 15a). As with the model in eqn (22), this model is fairly effective in compensating the acoustic backscattering strength image in Fig 14a for the combined transmit and receive directivity (Fig 15b).

## B. Evaluation of the Compensated Imagery

The two ways we choose to evaluate the compensated backscattering strength imagery are with respect to target detection, and seafloor classification. From the target detection perspective, both methods appear to perform equally well. Most of the across track bias associated with the TVSS directivity pattern is removed. The compensated images are relatively homogeneous away from nadir, consistent with the featureless bathymetry (Fig 12). Compared to the theoretical model, the advantages of eqn (22) are that it is simple, that it does not require the sonar to be calibrated, and that it does not require *in situ* data regarding the geoacoustic properties of the bottom. Thus, it is the preferred method when *a priori* information regarding the seafloor is unavailable. Unfortunately, a more thorough analysis from this perspective is not possible because no targets were present in the three TVSS runs studied here.

From the seafloor classification perspective, eqn (22) has limited potential. It may be used for first order discrimination of sediment type owing to the differing shapes of the angular dependence functions corresponding to bedrock, sand, and mud.<sup>28,46,59,60</sup> For quantitative seafloor classification, the theoretical model is preferred, particularly in view of its success in characterizing the acoustic backscattering strength from a wide range of sediment types.<sup>41,48,49,57</sup> For the TVSS experiment, the major limitation of using the theoretical model to compensate for the array directivity is that it performs best when the input parameters are measured. Our data set was limited to the general composition and porosity in Table Ie. Furthermore, it was not stated whether the porosity measurement was the surficial value or bulk estimate.<sup>16</sup> Vertical and horizontal inhomogeneities in sediment sound speed, density, attenuation, and porosity affect acoustic backscattering strength significantly<sup>49,61</sup> and are likely to have influenced our results because the sediment distribution at the TVSS experiment site was bimodal.<sup>16</sup> This may explain some of the difference between the data and the model in addition to beam pattern effects (Fig 15a). Our estimated roughness parameters are another source of uncertainty. The spectral exponent ( $\gamma$ ) and spectral strength ( $w_2$ ) are best measured optically to sub cm resolution,<sup>48</sup> but system noise and the TVSS resolution limited our ability to adequately estimate these parameters.

## C. Error Budget for the Backscattering Strength Imagery

To construct an error budget for the seafloor acoustic backscattering strength ( $S_B$ ) image data (Figs 14a,c, 15b), we assess the contributions from each term in eqn (5) (Table VII), and separate the total error into systematic (bias) and random components:

$$\delta S_{B,tot} = \delta S_{B,sys} + \delta S_{B,ran} \quad (25)$$

There are no standard error analysis methods for data contaminated by both types of error,<sup>44</sup> so we will form separate error budgets for each. Such an approach is useful when the source and characteristics of the systematic errors are known, which is the case for the TVSS data.

Echo level uncertainties ( $\delta EL$ ) had systematic components near  $\theta_a = -15^\circ$  and  $+15^\circ$  due to the bottom detection scheme, and random components for all  $\theta_a$  due to random bathymetric errors. We estimated the maximum systematic component to be  $-0.5\text{dB}$  by analyzing the backscatter time series and bathymetry detected in the beams near  $\theta_a = +15^\circ$ . The bathymetry in these beams exhibited a  $-0.2\text{m}$  bias, indicating that the detected echo was early, which caused the average  $S_B$  to be biased low. Using the same approach, we estimated the random component of  $\delta EL$  from the random bathymetric errors (Figs 12, 13) to be  $\pm 0.5\text{dB}$ . The errors were largest for the positive beam angles because the inoperable hydrophone on the lower right side of the array caused the sidelobes for these beams to be  $7\text{--}9\text{dB}$  higher than for beams in the negative angles.

Uncertainties associated with the TVSS transmit and receive arrays included  $\pm 2.0\text{dB}$  random variations between the receiver voltage responses ( $\delta RVR$ ) of the 120 hydrophones.<sup>14</sup> Random uncertainties in the fixed gain ( $\delta FG$ ) and time varying gain ( $\delta TVG$ ) were estimated to be  $\pm 1.0\text{dB}$  and  $\pm 2.0\text{dB}$ , respectively, according to the manufacturer's specifications. The only uncertainty in the directivity index ( $\delta DI$ ) was a systematic  $0.2\text{dB}$  negative bias error for the beams directed towards negative angles because these beams were formed from subarrays which contained the inoperable hydrophone. Much larger systematic uncertainties in the TVSS source level resulted from the angular variations in the TVSS transmit pattern (Fig 2a). We estimated the maximum error to be  $-9\text{dB}$  from the difference between the maximum and minimum values in the pattern of Fig 2a. The error is negative because we used the peak measured value for source level.<sup>30</sup>

The calculation of ensonified area ( $A$ ) was affected by beam pattern variation and bathymetric uncertainties. We performed computer simulations to calculate the effect of both the bathymetric errors and potential variations in the transmit and receive beamwidths on the random error in  $10\log_{10}A$ . Conservative estimates using variations of  $\pm 0.5^\circ$  in beamwidth and  $\pm 2\text{m}$  in bathymetry were no greater than  $\pm 1.0\text{dB}$ . Similarly, we calculated the effect of the bathymetric errors on two-way transmission loss ( $\delta 2TL$ ) to be no more than  $\pm 0.1\text{dB}$ . The effects of the systematic early bottom echo detections near  $\theta_a = -15^\circ$  and  $+15^\circ$  were less than  $0.1\text{dB}$ .

To estimate  $\delta S_{B,tot}$ , we use the rule for the sums and differences in uncertainties, which states that if measured quantities  $a, \dots, h$  with uncertainties  $\delta a, \dots, \delta h$ , are used to compute  $q = a + \dots + f - (g + \dots + h)$ , the upper bound on the uncertainty in  $q$  is:

$$\delta q_{upper\ bound} \leq \delta a + \dots + \delta f + \delta g + \dots + \delta h \quad (26)$$

Thus, from Table VII,  $\delta S_{B,sys}$  is estimated to be  $9.7\text{dB}$ , which represents the maximum value of the negative bias in the  $S_B$  image samples. Our analysis of across-track scan lines in the uncompensated  $S_B$  images (e.g. Fig 14a) indicated that this was a fairly accurate estimate.  $\delta S_{B,ran}$  is estimated from eqn (26) to be  $\pm 6.6\text{dB}$ , which is slightly greater than the along-track standard deviations of the seafloor backscattering strength ( $\sigma_{S_B}$ ) (e.g. Fig 16). Because surface roughness should increase  $\sigma_{S_B}$  over the theoretical estimate of  $S_{B,ran}$ , eqn (26) probably overestimates the random uncertainty. When the

quantities  $a, \dots, g$  in eqn (26) are independent and random, the total uncertainty in a sum or difference may be expressed as:

$$\delta q_{\text{random}} = \sqrt{(\delta a)^2 + \dots + (\delta f)^2 + (\delta g)^2 + \dots + (\delta h)^2} . \quad (27)$$

This yields  $\delta S_{B,\text{ran}} = 3.2\text{dB}$ , which is 2dB less than the average  $\sigma_{S_g}$ . Thus, we conclude that  $\delta S_{B,\text{ran}}$  is probably between the random and upper bound predictions, which is consistent with our conclusions regarding the bathymetric errors.

The effectiveness of our backscattering strength correction techniques can be partially evaluated in terms of these error estimates. Both of the methods described in the text fit a function to the mean backscattering strength ( $S_B(\theta_{\text{inc}})$ ) computed over  $N_p$  pings. The fit depends in part on the random uncertainty in the mean backscattering strength, which can be represented by the standard error ( $\sigma_{S_g(\theta_{\text{inc}})}$ ).<sup>44</sup> For the three TVSS runs,  $\sigma_{S_g(\theta_{\text{inc}})}$  was typically about 0.6dB (Fig 16). The maximum systematic component of backscattering strength error ( $\delta S_{B,\text{sys}}$ ) removed by our correction methods is equivalent to the maximum systematic variation in the mean backscattering strength ( $S_B(\theta_{\text{inc}})$ ) computed over  $N_p$  pings. For the data in Fig 14b, this was about 6-8dB. Because, the maximum observed values for  $\delta S_{B,\text{sys}}$  in the images (Fig 14a) were close to our upper bound estimate of 9.7dB, the corrected images (e.g. Figs 14c, 15b) retain a maximum residual systematic error of 1.7-3.7dB. The random errors ( $\delta S_{B,\text{ran}}$ ) in the the corrected images were the same as those for the raw images, because the compensation methods are not designed to handle these.

## VI. CONCLUSIONS

Bathymetric mapping and seafloor acoustic backscatter imaging using AUV/UUVs or towed vehicles are ultimately limited by environmental variability and sensor characteristics. The desired scenario is for the sensor beampatterns to be precisely calibrated and uniform, the platform attitude and navigation data to be accurate and highly sampled, and the *in-situ* data collected with the acoustic data to explain and correct for sound speed fluctuations and reverberation from the boundaries and volume. In real world applications, such a scenario rarely exists, but many limitations can be removed by using the environmental data collected by the sensor. During low sea states, the sea surface boundary may be used to correct errors in platform attitude which may result from undersampling or inaccuracy in the attitude measurement unit. Acoustic backscatter data collected over a flat seafloor can be used to derive correction factors which may be used to compensate for artifacts associated with nonuniform or irregular beampatterns. Even though we have demonstrated these methods by using data collected by a cylindrical array, they are not restricted to sensors with full sea surface, volume, and seafloor coverage. For example, a multibeam sonar designed for conventional bathymetry and seafloor imaging might be used with an inexpensive, upward-looking two or three-beam sonar to obtain results similar to those for the TVSS, but with less reverberation and at reduced operating cost. Regardless of the system, the techniques described here are valuable for AUV/UUV applications which are unable to use transponder navigation, such as covert reconnaissance, mine-hunting, and rapid environmental assessment of denied, littoral regions.

## ACKNOWLEDGMENT

This work was funded by the Office of Naval Research under ONR-NRL Contract No. N00014-96-1-G913. The authors would like to thank CAPT Tim Schnoor, USN

(ret) (ONR), Sam Tooma, and Maria Kalcic (NRL) for their support. Candy Robertson, Lisa Tubridy, and Jim Bryan (CSS) provided much needed information about the TVSS. Thanks are also due to Pat Jordan (MPL) for administrative support and jo Griffith (MPL) for help with the figures.

## REFERENCES

1. Gallaudet, T.C., de Moustier, C.P., and Kalcic, M. (2000). "Imaging the ocean boundaries and volume with the Toroidal Volume Search Sonar (TVSS)." in: *Proceedings of the Fourth Annual Symposium on the Mine Problem*, March 13-16, 2000, Monterey, CA.
2. Tooma, S.G., Walter, D. J., and Chotiros, N. (1997). "Environmental Estimation Using Navy Sensors," NRL Report NRL/MR/7430--97-0839, Stennis Space Center, MS: Naval Research Laboratory.
3. McDonald, R.J., Wilbur, J., and Manning, R. (1997). "Motion-compensated beamforming algorithm for a circular transducer array." *U.S. Navy J. Underwater Acoust.*, **47**(2), pp. 905-920.
4. Gallaudet, T.C., and de Moustier, C.P. (2001). "Sea surface and volume acoustic backscatter imagery of the microbubble field of a ship's wake." *J. Acoust. Soc. Am.*, (submitted).
5. Gallaudet, T.C., and de Moustier, C.P. (2001). "Multibeam volume acoustic backscatter imagery and reverberation measurements in the Northeastern Gulf of Mexico." *J. Acoust. Soc. Am.*, (submitted).
6. Gallaudet, T.C., and de Moustier, C.P. (2000). "On optimal amplitude shading for arrays of irregularly spaced or non-coplanar elements." *IEEE J. Ocean. Eng.*, **25**, pp. 553-567.
7. Woodward, B. and Cannelly, P.R. (1998). "An autonomous underwater vehicle as an imaging platform." *Proc. IEE Colloquium on Underwater Applications of Image Processing*. London, UK, 25 March 1998, IEE, p. 6/1-6.
8. Feder, H.J.S., Leonard, J., and Smith, C. (1998). "Incorporating environmental measurements in navigation." in: *Proc. 9th International Symposium on Unmanned Untethered Submersible Technology*, 25-27 September, 1995, pp. 115-122.
9. Committee on Undersea Vehicles and National Needs, National Research Council (1996). "Undersea vehicles and national Needs." Washington, DC: National Academy Press, 99 pp.
10. Carpenter, R.N. (1998). "Concurrent mapping and localization with FLS." in: *IEEE Workshop on Autonomous Underwater Vehicles*, 20-21 August, 1998, Cambridge, MA., pp. 133-148.
11. Stergiopoulos, S., Dhanantwari, A.C., and Grodski, J.J. (1998). "Implementation of adaptive processing in integrated active-passive sonars deploying cylindrical arrays." *Proc. 1998 Int. Symposium on Underwater Technology*, Tokyo, Japan. 15-17 April 1998, pp. 289-294.
12. Negahdaripour, S., Xu, X., Jin, J. (1999). "Direct estimation of motion from sea floor images for automatic station keeping of submersible platforms." *IEEE J. Oceanic Eng.*, **24**(3), pp. 370-382.
13. Cobra, D.T., Oppenheim, A.V., and Jaffe, J.S. (1992). "Geometric distortions in side-scan sonar images: a procedure for their estimation and correction." *IEEE J. Oceanic Eng.*, **24**(3), pp. 370-382.
14. Raytheon Company, Submarine Signal Division (1993). "Volume Search Sonar Array Program: Preliminary Hydrophone Test Data." Raytheon Company, Portsmouth, RI (unpublished).
15. Groves, D.G., and Hurt, L.M. (1980). *Ocean World Encyclopedia*. New York:

McGraw-Hill.

16. McLeroy, E.G. (1972). "Measurement and correlation of acoustic reflection and sediment properties off Panama City, Florida." Informal Report NCSL 112-72, Naval Coastal Systems Laboratory, Panama City, FL.
17. Ludwick, J.C. (1964). "Sediments in northeastern Gulf of Mexico." in: *Papers in Marine Geology*, R.L. Miller (ed.), New York: MacMillan, pp. 204-238.
18. Hamilton, E.L., and Bachman, R.T. (1982). "Sound velocity and related properties of marine sediments." *J. Acoust. Soc. Am.*, **72**(6), pp. 1891-1904.
19. de Moustier, C.P. (1993). "Signal processing for swath bathymetry and concurrent seafloor acoustic imaging." in: *Acoustic Signal Processing For Ocean Exploration*. J.M.F. Moura and I.M.G. Lourie, eds., NATO ASI Series, Kluwer, 1993, pp. 329-354.
20. Hammerstad, E., Asheim, S., Nilsen, K., Bodholt, H. (1993). "Advances in multibeam echo sounder technology." *Proc. IEEE Oceans '93*, **vol. 1**, pp. 482-487.
21. Yang, L., and Tøxt, T. (1997). "Multibeam sonar bottom detection using multiple subarrays." *Proc. IEEE Oceans '97*, **vol. 2**, pp. 932-938.
22. Chakraborty, B. (1995). "Studies on a 120 deg segmented circular array for multi-beam multi-frequency bathymetric applications," *J. Sound and Vibration*, **179**(1), pp. 1-12.
23. Neubauer, W.G. (1969) "Pulsed circumferential waves on an aluminum cylinder in water." *J. Acoust. Soc. Am.*, **45**(5), pp. 1134-1144.
24. Mailloux, R. J. (1994), *Phased Array Antenna Handbook*. Boston: Artech House, 527 pp.
25. Yang, L., Tøxt, T., and Albrechtsen, F. (1997). "Bottom detection for multibeam sonars with active contours." *Proc. IEEE Oceans '97*, **vol. 2**, pp. 943-950.
26. Masnadi-Shirazi, M.A., de Moustier, C.P., and Cervenka, P. (1992). "Differential phase estimation with the SeaMARC II bathymetric sidescan sonar system," *IEEE J. Oceanic Eng.*, **17**(3), pp. 239-251.
27. Urlick, R.J. (1983). *Principles of Underwater Sound*. 3rd edition. Los Altos, CA: Peninsula, 423 pp.
28. Hughes Clarke, J.E., Mayer, L.A., and Wells, D.E. (1996). "Shallow-water imaging multibeam sonars: a new tool for investigating seafloor processes in the coastal zone and on the continental shelf." *Mar. Geophys. Res.*, **18**, pp. 607-629.
29. Robertson, C.J., and Tubridy, L.H. (1995). "User's Manual for the Toroidal Volume Search Sonar (TVSS) Sea Test Data". Coastal Systems Station, Panama City, FL.
30. Bryan, J.F. (2001). Personal communication, 7 March 2001. The transmit source level was measured by Raytheon in their laboratories in November 1993 to be 220dB *re*: 1μPa. Signal measurements made by CSS immediately after showed the transmit source level to be approximately 216.8dB *re*: 1μPa. Further measurements were not made prior to the TVSS deployment in November 1994, so any degradation in source level, as well as hydrophone sensitivities, are unknown.
31. Francois, R.E., and Garrison, G.R. (1982). "Sound absorption based on ocean measurements: Part II: Boric acid contribution and equation for total absorption." *J. Acoust. Soc. Am.*, **72**, pp. 1879-1890.
32. Angelari, R. (1978). "A deterministic and random error model for a multibeam hydrographic ship sonar system." in: *Proc. IEEE Oceans '78*, pp. 48-53.
33. Blackinton, J.G. (1991). "Bathymetric resolution, precision, and accuracy considerations for swath bathymetry mapping sonar systems." *Proc. IEEE Oceans '91*, pp. 550-557.
34. Ambrose, J.T., and Geneva, A. (1995). "Wide swath bathymetric sonar error

- modeling for a hydrographic survey ship." *Proc. MTS/IEEE OCEANS '95* MTS/IEEE, vol. I, pp.339-346.
35. Caress, D.W., and Chayes, D.N. (1996). "Improved processing of Hydrosweep DS multibeam data on the R/V *Maurice Ewing*." *Mar. Geophys. Res.*, **18**, pp. 631-650.
  36. Bourillet, J.F., Edy, C., Rambert, F., and Loubrieu, B. (1996). "Swath mapping system processing: bathymetry and cartography." *Mar. Geophys. Res.*, **18**, pp. 487-506.
  37. Chapman, D.A. (1984). "A study of the ship induced roll-yaw motion of a heavy towed fish," *Ocean Engng.*, **11**(6), pp. 627-649.
  38. Hubbard, R.M. (1993). "On the towfish motion characteristics of single-body 6s. two-body sidescan systems." *Proc. IEEE Oceans '93*, vol. 1, pp. 365-370.
  39. An, P.E., and Smith, M. (1998). "An experimental self-motion study of the Ocean Explorer AUV in controlled sea states," *IEEE J. Ocean. Eng.*, **23**(3), pp. 274-284.
  40. Jantti, T. (1989). "Trials and experimental results of the ECHOS XD multibeam echo sounder." *IEEE J. Ocean. Eng.*, **14**(4), pp. 306-313.
  41. Miller, J., Ferguson, J.S., and Byrne, J.S. (1995). "Shallow water multibeam sonar performance, results from a modern hydrographic survey system." *Proc. IEEE Oceans '93*, vol. 2., pp. 985-990.
  42. Hammerstad, E., Pohner, F., Parthiot, F., and Bennett, J. (1991). "Field testing of a new deep water multibeam echo sounder." *Proc. IEEE Oceans '91*, vol. 1., pp. 743-748.
  43. Mitchell, N.C. (1996). "Processing and analysis of Simrad multibeam sonar data." *Mar. Geophys. Res.*, **18**, pp. 729-739.
  44. Taylor, J.R. (1997). *An Introduction to Error Analysis: the Study of Uncertainties in Physical Measurements*. Sausalito: University Science Books. 327pp.
  45. Bendat, J.S., Piersol, A.G. (1986). *Random Data: Analysis and Measurement Procedures*. New York: John Wiley & Sons, p. 100.
  46. Stewart, W.K., Chu, D., Malik, S., Lerner, S., and Singh, H. (1994). "Quantitative seafloor characterization using bathymetric sidescan sonar." *IEEE J. Oceanic Eng.*, **19**(4), pp. 599-610.
  47. Jackson, D.R., Baird, A.M., Crisp, J.J., and Thomson, P.A.G. (1986). "High frequency bottom backscatter measurements in shallow water." *J. Acoust. Soc. Am.*, **80**(4), pp. 1188-1199.
  48. Jackson, D.R., Briggs, K.B., Williams, K.L., and Richardson, M.D. (1996). "Tests of models for high-frequency seafloor backscatter." *IEEE J. Oceanic Eng.*, **21**(4), pp. 458-470.
  49. Jackson, D.R., and Biggs, K.B. (1992). "High frequency bottom backscatter: Roughness versus sediment volume scattering." *J. Acoust. Soc. Am.*, **92**(2), Pt. 1, pp. 962-977.
  50. Hellequin, L., Lurton, X., and Augustin, J.M. (1997). "Postprocessing and signal corrections for multibeam echosounder images." *Proc. IEEE Oceans '97*, vol. 1, pp. 1-4.
  51. Hughes-Clark, J.E., Danforth, B.W., and Valentine, P. (1997). "Areal seabed classification using backscatter angular response at 95kHz." in: *High Frequency Acoustics in Shallow Water*, editors: N.G. Pace, E. Pouliquen, O. Bergem, and A.P. Lyons, La Spezia: NATO SACLANT Undersea Research Center, pp. 243-250.
  52. Cervenka, P., and de Moustier, C. (1993). "Sidescan sonar image processing techniques." *IEEE J. Ocean. Eng.*, **18**(2), pp. 108-122.
  53. Applied Physics Laboratory, University of Washington (1994). *APL-UW High Frequency Ocean Environmental Acoustic Models Handbook*. Technical



Report, APL-UW TR 9407.

54. Jackson, D.R., Winebrenner, D.P., and Ishimaru, A. (1986). "Application of the composite roughness model to high frequency bottom backscattering." *J. Acoust. Soc. Am.*, **79**(5), pp. 1410-1422.
55. Mourad, P.D., and Jackson, D.R. (1989). "High frequency sonar equation models for bottom backscatter and forward loss." *Proc. IEEE Oceans '89*, vol. 4, pp. 1168-1175.
56. Michalopoulou, Z., Alexandrou, D., and de Moustier, C. (1994). "Application of a maximum likelihood processor to acoustic backscatter for the estimation of seafloor roughness parameters." *J. Acoust. Soc. Am.*, **95**(5), pp. 2467-2477.
57. Stanic, S., Briggs, K.B., Fleischer, P., Ray, R.I., and Sawyer, W.B. (1988). "Shallow-water high-frequency bottom scattering off Panama City, Florida." *J. Acoust. Soc. Am.*, **83**(6), pp. 2134-2144.
58. Hamilton, E.L. (1972). "Compressional wave attenuation in marine sediments." *Geophysics*, **37**, pp. 620-646..
59. de Moustier, C. (1986). "Beyond bathymetry: mapping acoustic backscattering from the deep seafloor with Sea Beam." *J. Acoust. Soc. Am.*, **79**(2), pp. 316-331.
60. Augustin, J.M., Le Suave, R., Lurton, X., Voisset, M., Dugelay, S., and Satra, C. (1996). "Contribution of the multibeam acoustic imagery to the exploration of the sea bottom." *Mar. Geophys. Res.*, **18**, pp. 459-486.
61. Yamamoto, T. (1996). "Acoustic scattering in the ocean from velocity and density fluctuations in the sediments." *J. Acoust. Soc. Am.*, **99**(2), pp. 866-879.

TABLE I.  
TVSS PARAMETERS AND DEPLOYMENT DATA

(a) TRANSMIT ARRAY	
radius	26.5cm
acoustic frequency	68 kHz
pulse type	CW
pulse length	200 $\mu$ s
source level	216.8 dB <i>re:</i> 1 $\mu$ Pa @ 1m
transmit beamwidth	3.7° (along-track)
(b) RECEIVE ARRAY	
radius	26.5cm
number of elements	120
element spacing	3°
receive beamwidth	4.9° (across-track)
average hydrophone	-168 dB <i>re:</i> 1 V <sub>rms</sub> / $\mu$ Pa
receive voltage response (RVR)	
(c) DEPLOYMENT INFORMATION	
towcable payed out	760 m
estimated towfish layback	735 m
mean towfish depth ( $Z_{TVSS}$ )	77-78m
mean towfish speed ( $V_{TVSS}$ )	8kts (4.1m/s)
(d) ENVIRONMENTAL DATA	
location	29°30'N , 86°30'W
water depth	190-205 m
wind speed	6 kts (3m/s)
sea state	1.5
(e) GEOACOUSTIC DATA	
porosity (%)	66
fine fraction (%)	78
sand fraction (%)	21
gravel fraction (%)	1
bulk grain size# ( $M_z$ )	6.36
bulk grain diameter# (mm)	0.012
# estimated from porosity data in [16] using regression relations in [18]	

TABLE II.  
TVSS TOWFISH ATTITUDE AND MOTION STATISTICS

For each parameter,  $\mu$  is the mean over the run,  $\sigma$  is the standard deviation,  $R$  is the range,  $\delta_{\max}$  is the maximum ping-to-ping difference, and  $\delta_{\text{mean}}$  is the mean ping-to-ping difference.

	Run 1	Run 2	Run 3
(a) ROLL (°)			
$\mu$	15.8	18.1	12.1
$\sigma$	1.04	0.67	1.88
$R$	3.88	2.60	6.76
$\delta_{\max}$	1.21	0.77	0.79
$\delta_{\text{mean}}$	0.20	0.19	0.26
(b) PITCH (°)			
$\mu$	-1.73	-1.82	-1.74
$\sigma$	0.20	0.16	0.23
$R$	0.88	0.71	1.14
$\delta_{\max}$	0.46	0.39	0.49
$\delta_{\text{mean}}$	0.10	0.11	0.11
(c) YAW (°)			
$\mu$	6.7	5.3	7.8
$\sigma$	0.39	0.37	0.79
$R$	1.59	1.76	3.29
$\delta_{\max}$	0.70	0.43	0.53
$\delta_{\text{mean}}$	0.16	0.15	0.19
(d) SPEED (m/s)			
$\mu$	4.33	3.92	4.06#
$\sigma$	0.25	0.01	0.03#
$R$	0.67	0.04	0.15#
$\delta_{\max}$	0.67	0.04	0.12#
$\delta_{\text{mean}}$	0.07	0.00	0.03#
(e) DEPTH (m)			
$\mu$	63.0	64.9	65.4
$\sigma$	0.07	0.11	0.11
$R$	0.20	0.40	0.40
$\delta_{\max}$	0.10	0.10	0.10
$\delta_{\text{mean}}$	0.01	0.01	0.04
# estimated from ship speed due to gross errors in the towfish speed recorded for this run			

TABLE III.  
CORRECTED TOWFISH  
DEPTH AND ROLL STATISTICS

	Run 1	Run 2	Run 3
(a) DEPTH (m)			
$\mu$	77.3	78.3	78.4
$\sigma$	0.11	0.18	0.14
$R$	0.58	0.84	0.70
$\delta_{\max}$	0.40	0.58	0.26
$\delta_{\text{mean}}$	0.09	0.11	0.07
(b) ROLL ( $^{\circ}$ )			
$\mu$	15.7	18.0	12.1
$\sigma$	1.01	0.62	1.83
$R$	3.61	2.46	6.61
$\delta_{\max}$	1.16	0.61	0.71
$\delta_{\text{mean}}$	0.19	0.14	0.22

TABLE IV.  
SOURCES OF UNCERTAINTY IN TVSS BATHYMETRY

Error Component		Error Source	Estimated Uncertainty
angle	$\delta\theta_a$	-element patterns -beamforming procedure -sound speed profile -motion sensor -roll sampling rate -roll correction procedure	$\pm 0.3^\circ$
pitch	$\delta\phi$	-motion sensor -sampling rate	$\pm 0.2^\circ$
yaw	$\delta\omega$	-motion sensor -sampling rate	$\pm 0.5^\circ$
speed	$\delta V_{tvss}$	-motion sensor -sampling rate	$\pm 0.3\text{m/s}$
depth	$\delta Z_{tvss}$	-depth sensor -sampling rate -bandwidth -depth correction procedure	$\pm 0.2\text{m}$
range	$\delta R$	-bottom detection procedure -sampling rate -bandwidth -system noise	$\pm 0.6\text{m}$

TABLE V.  
CORRELATION COEFFICIENTS FOR TOWFISH ATTITUDE  
AND MOTION DATA AVERAGED OVER RUNS 1-3

	Roll#	Pitch	Yaw	Speed	Depth#
Roll#	1.0	-0.15	0.32	0.02	-0.40
Pitch	-0.15	1.0	-0.32	-0.12	0.00
Yaw	0.32	-0.32	1.0	-0.03	-0.31
Speed	0.02	-0.12	-0.03	1.0	0.11
Depth#	-0.40	0.00	-0.31	0.11	1.0
# corrected values					

TABLE VI.  
SEAFLOOR ACOUSTIC BACKSCATTERING STRENGTH  
COMPOSITE ROUGHNESS MODEL INPUT PARAMETERS

parameter	definition	symbol	value(s)
density ratio	ratio of sediment mass density to water mass density	$\rho$	1.1483
sound speed ratio	ratio of sediment sound speed to water sound speed	$v$	0.9864
loss parameter	ratio of imaginary wavenumber to real wavenumber for the sediment	$\delta$	0.0033
volume parameter	ratio of sediment volume scattering cross section to sediment attenuation coefficient	$\sigma_2$	0.003
spectra exponent	exponent of two-dimensional bottom relief spectrum	$\gamma$	3.00
spectral strength	strength of bottom relief spectrum ( $\text{cm}^4$ ) at wavenumber $2\pi/\lambda_a = 1\text{cm}^{-1}$	$w_2$	0.000518

TABLE VII.  
SOURCES OF UNCERTAINTY IN THE TVSS  
SEAFLOOR ACOUSTIC BACKSCATTERING STRENGTH DATA

Error Component		Error Source	Systematic Uncertainty	Random Uncertainty
echo level	$\delta EL$	-bathymetric uncertainty	-0.5dB	$\pm 0.5$ dB
receive array	$\delta RVR$	-variations between hydrophone receive voltage responses	-	$\pm 2.0$ dB
		-element pattern variations		
	$\delta FG$	-gain uncertainty in the data acquisition system	-	$\pm 1.0$ dB
	$\delta DI$	-inoperable hydrophone on lower left of the TVSS	-0.2dB	-
	$\delta TVG$	-gain uncertainty in the data acquisition system	-	$\pm 2.0$ dB
transmit array	$\delta SL$	-angular variation of transmit beam pattern	-9.0dB	-
transmission loss	$\delta 2TL$	-bathymetric uncertainty	-	$\pm 0.1$ dB
		-spatial variability in absorption coefficient		
sonified area	$\delta (10 \log_{10} A)$	-bathymetric uncertainty	-	$\pm 1.0$ dB
		-angular variation of transmit beam pattern		
		-variations between hydrophone receive voltage responses		
		-element pattern variations		



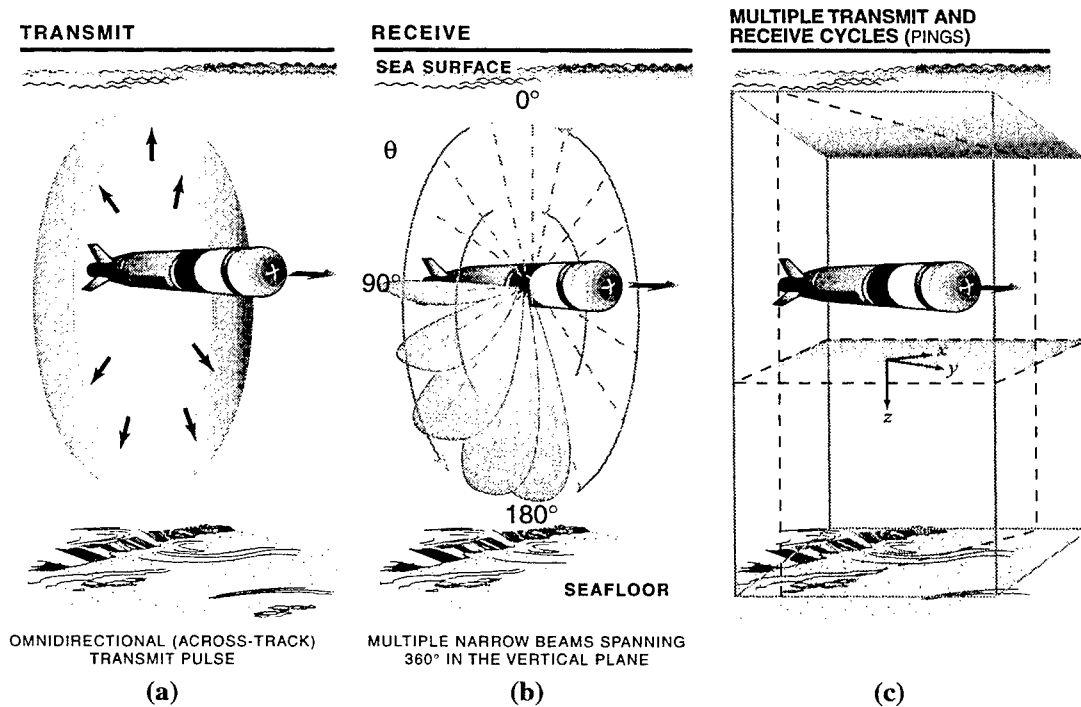


Fig. 1. The TVSS is designed for deployment onboard an AUV/UUV. After transmission of a "toroidal" pulse (a), the sonar records the returned signal in directions ( $\theta$ ) spanning  $360^\circ$  equally-spaced every  $3^\circ$  about the TVSS axis (b). (c) Data collected over successive transmit-receive cycles may be used to construct boundary relief maps, boundary backscatter imagery, and volume backscattering imagery in multiple horizontal and vertical planes in the water column (e.g. references [4][5]).  $x$ ,  $y$ , and  $z$  correspond to across- and along-track directions relative to the towfish and depth relative to the sea surface, respectively.

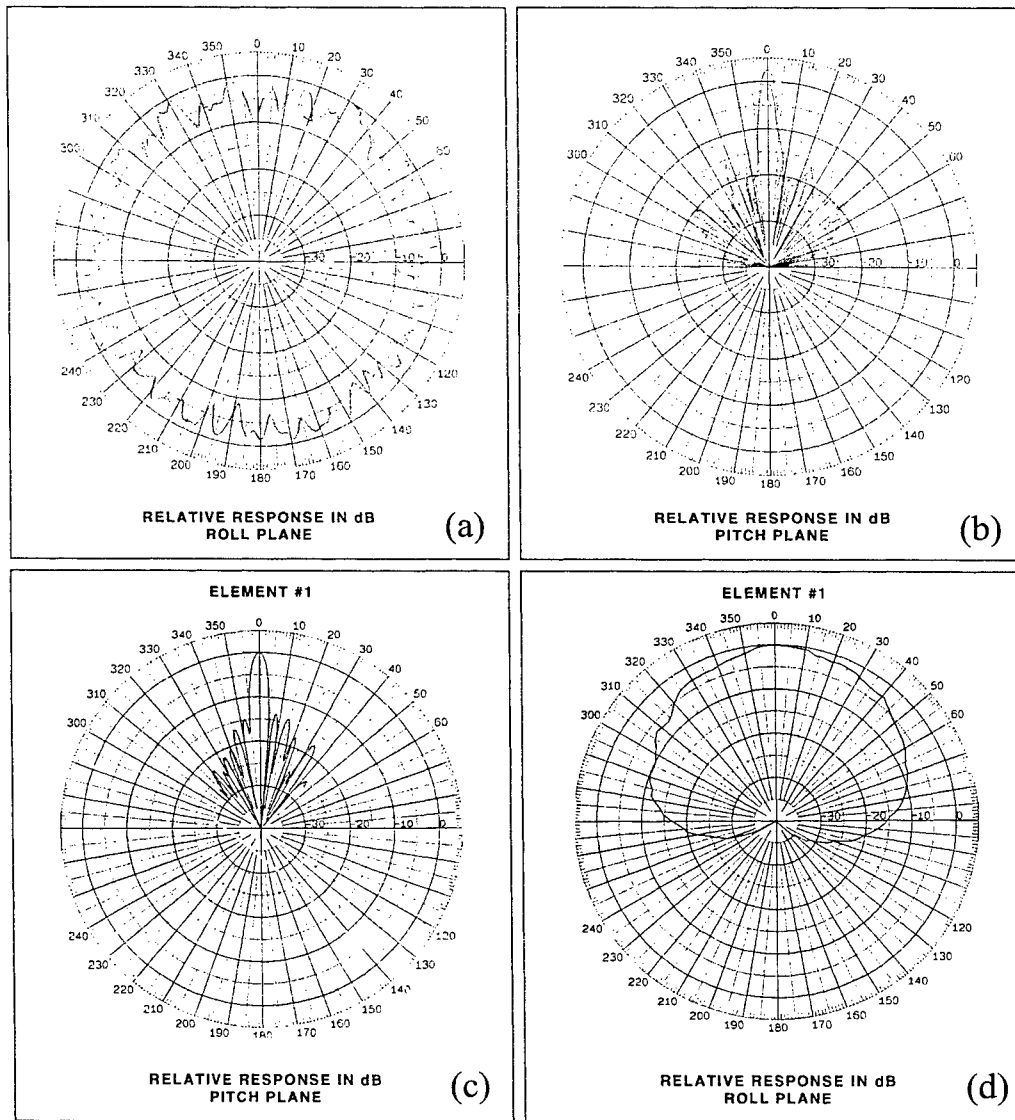


Fig. 2. (a) TVSS projector-array pattern in the roll plane facing the TVSS, and (b) pitch plane before (dotted) and after (solid) hydrostatic testing. (c) Example TVSS hydrophone-array element receive pattern in the roll plane, and (d) pitch plane [14]. Angular variations in the roll plane of the projector-array pattern (a) produce artifacts in the imagery which require removal. The non-omni-directional characteristics and between-element variation of the individual hydrophone gain and phase patterns produce beam pointing errors for plane wave beamforming on the TVSS and therefore require correction as described in reference [6].

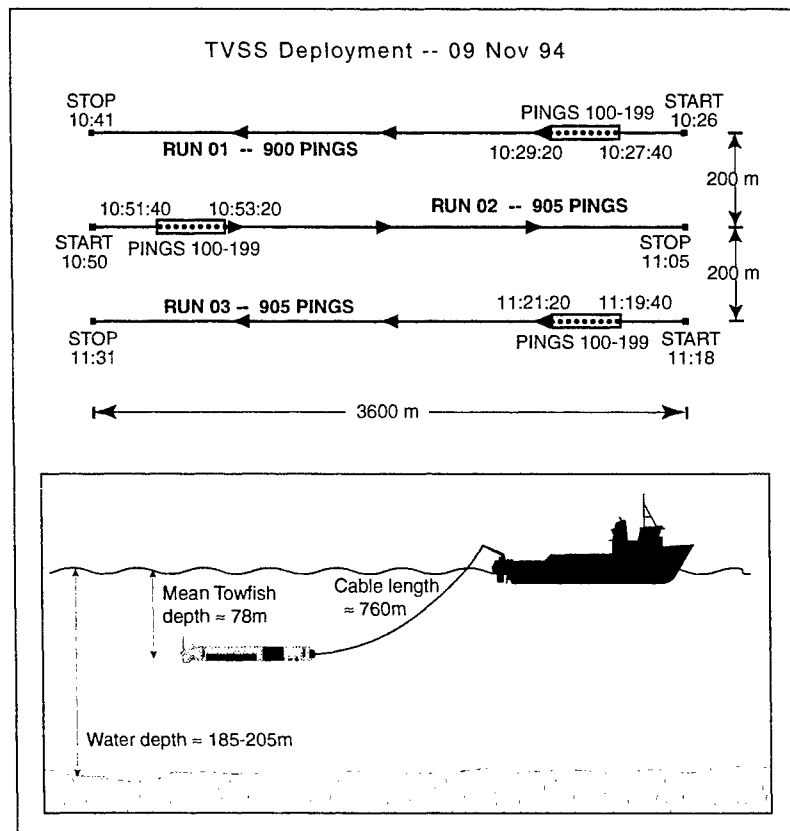


Fig 3. TVSS track lines for runs 1-3, 9 November 1994. The data presented in this paper are processed from pings #100-199 in each of the three east-west runs. The bathymetric slope was oriented west-southwest. With a layback of approximately 735m, the towfish maintained nearly constant depths between 77-78m during each run..

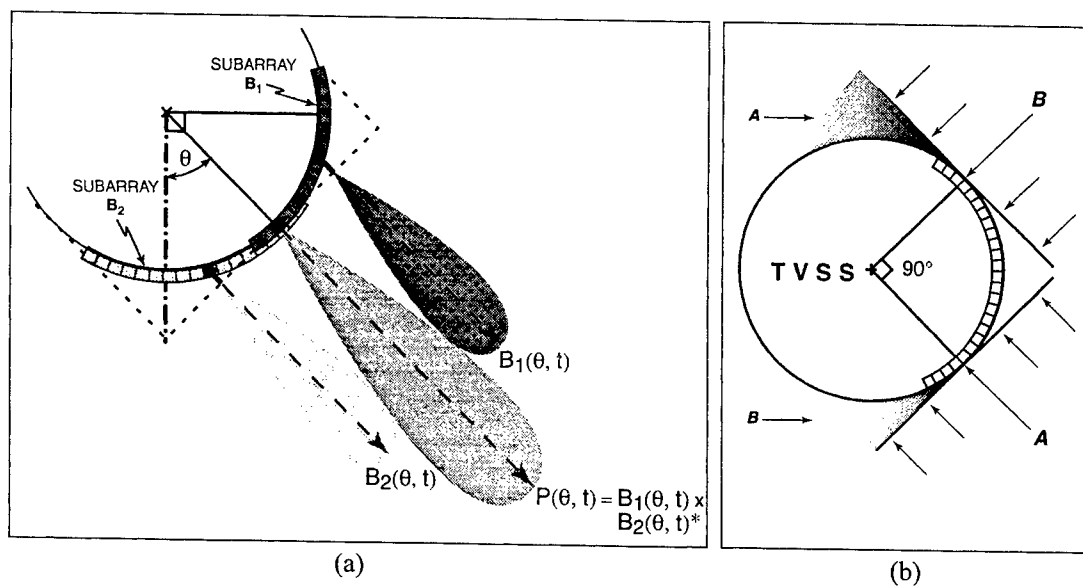


Fig. 4. (a) TVSS split aperture processing. (b) Diffraction and creeping wave effects occur in the shaded regions for plane waves A and B incident upon the TVSS and illustrate the 90° limit to the total usable TVSS aperture for narrowband plane-wave beamforming.

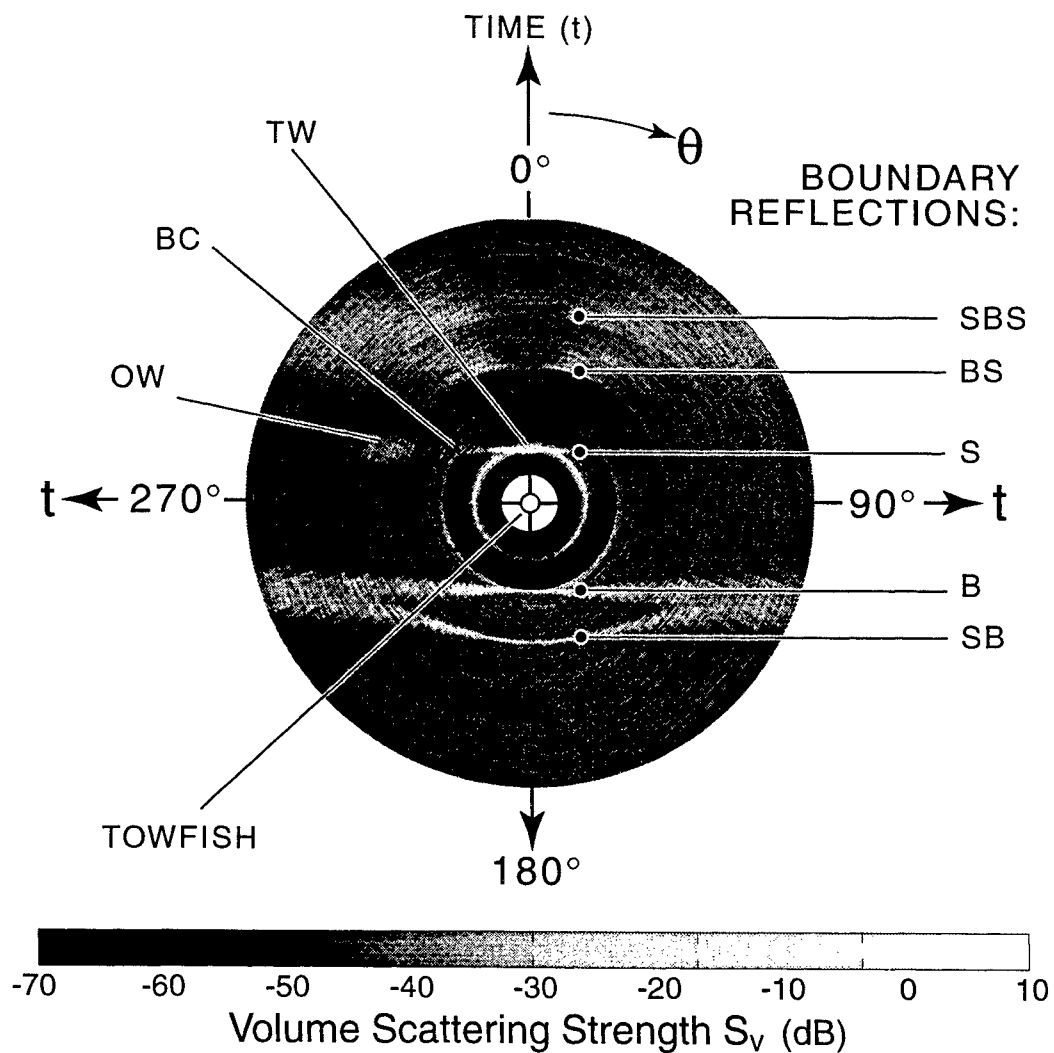


Fig. 5. One TVSS ping displayed in polar coordinates of angle vs. time. The acoustic backscatter data are converted to acoustic volume scattering strength ( $S_v$ ) using eqn (5) in the text with the ensonified volume ( $V$ ) in place of the ensonified area ( $A$ ). The towfish direction of travel was into the page. Labels refer to the following features: W - towship wake; OW - towship wake generated during previous run; BC - bubble cloud generated by a breaking bow wave from the towship; B - seafloor echo; S - sea surface echo; SB - surface-bottom (multiple) echo; BS - bottom-surface (multiple) echo; SBS - surface-bottom-surface (multiple) echo.

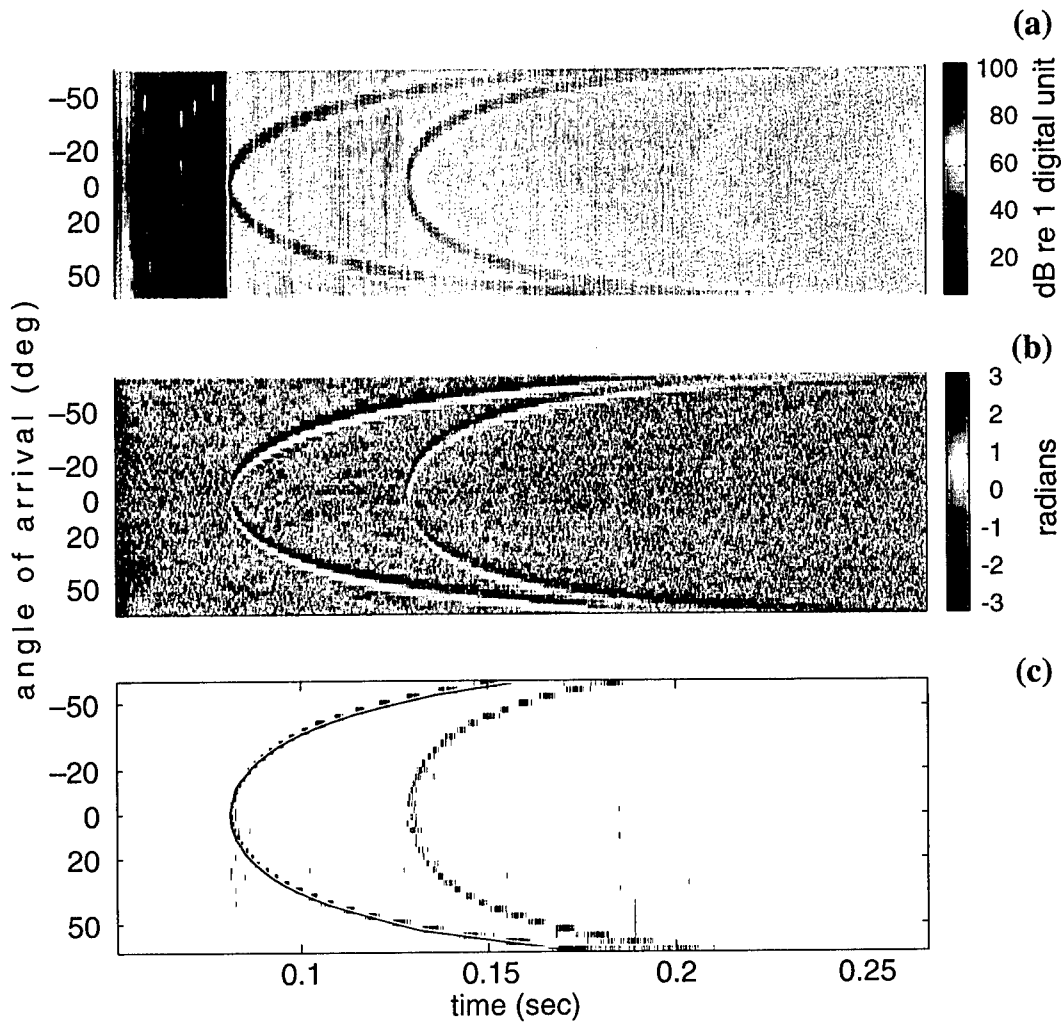


Fig. 6. (a) Raw backscatter magnitude (dB) and (b) phase (radians) of the TVSS split aperture processed phasor  $P(\theta, t)$  for the bottom and surface-bottom echoes. In this Cartesian representation of the beams in Fig. 5, from  $\theta_a = +60^\circ$  to  $-60^\circ$ , the boundary reflections appear as high-magnitude quasi-linear phase features. (c) The output of the magnitude thresholding and phase zero-crossing procedure described in the text (black) is used to search for the unique bottom echo times of arrival across all beams (red).

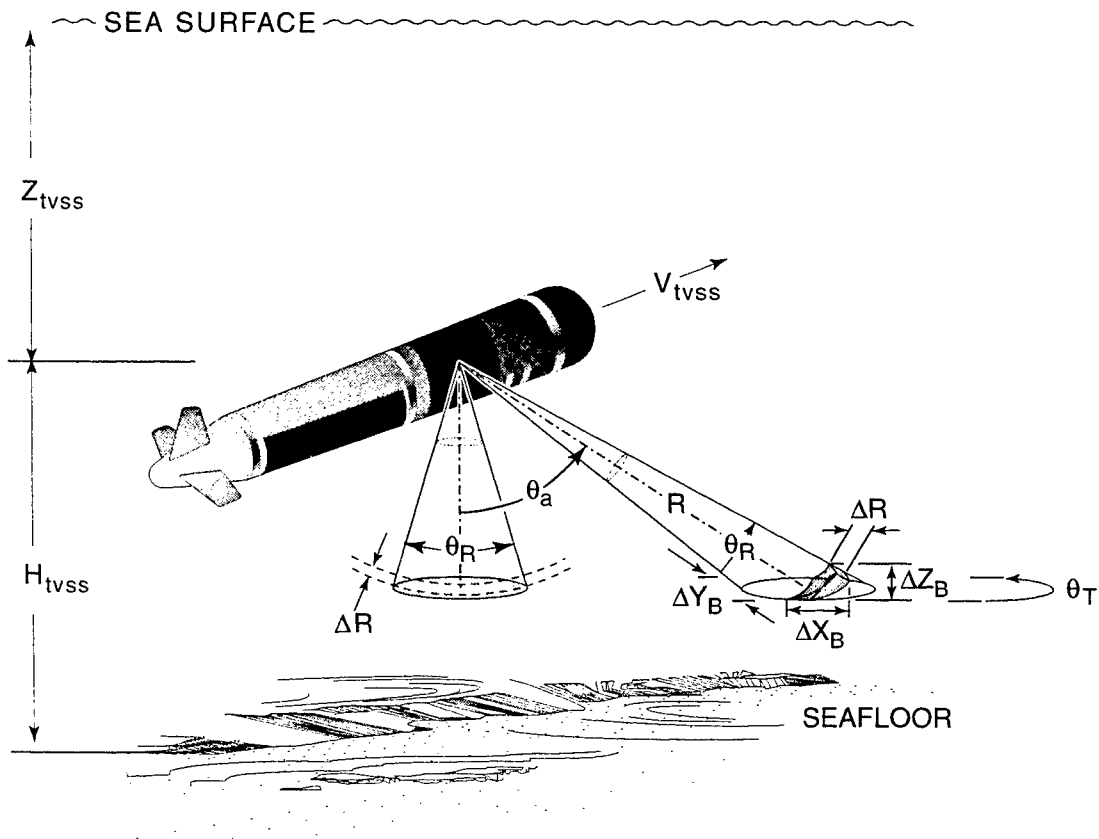


Fig 7. TVSS acoustic geometry for processing bathymetry and seafloor backscatter imagery. The area (A) ensonified by the transmitted pulse within the receive beam is approximately an ellipse at nadir, and an annulus sector at larger angles of arrival ( $\theta_a$ ). The area A increases with the TVSS altitude ( $H_{tvss}$ ), the receive beamwidth ( $\theta_R$ ), the transmit beamwidth ( $\theta_T$ ), and the range resolution ( $\Delta R$ ). The x, y, and z resolution of the TVSS bathymetry and seafloor backscattering strength image data is defined by the across-track, along-track, and vertical dimensions of the transmitted pulse on the seafloor ( $\Delta x_B$ ,  $\Delta y_B$ , and  $\Delta z_B$ ).

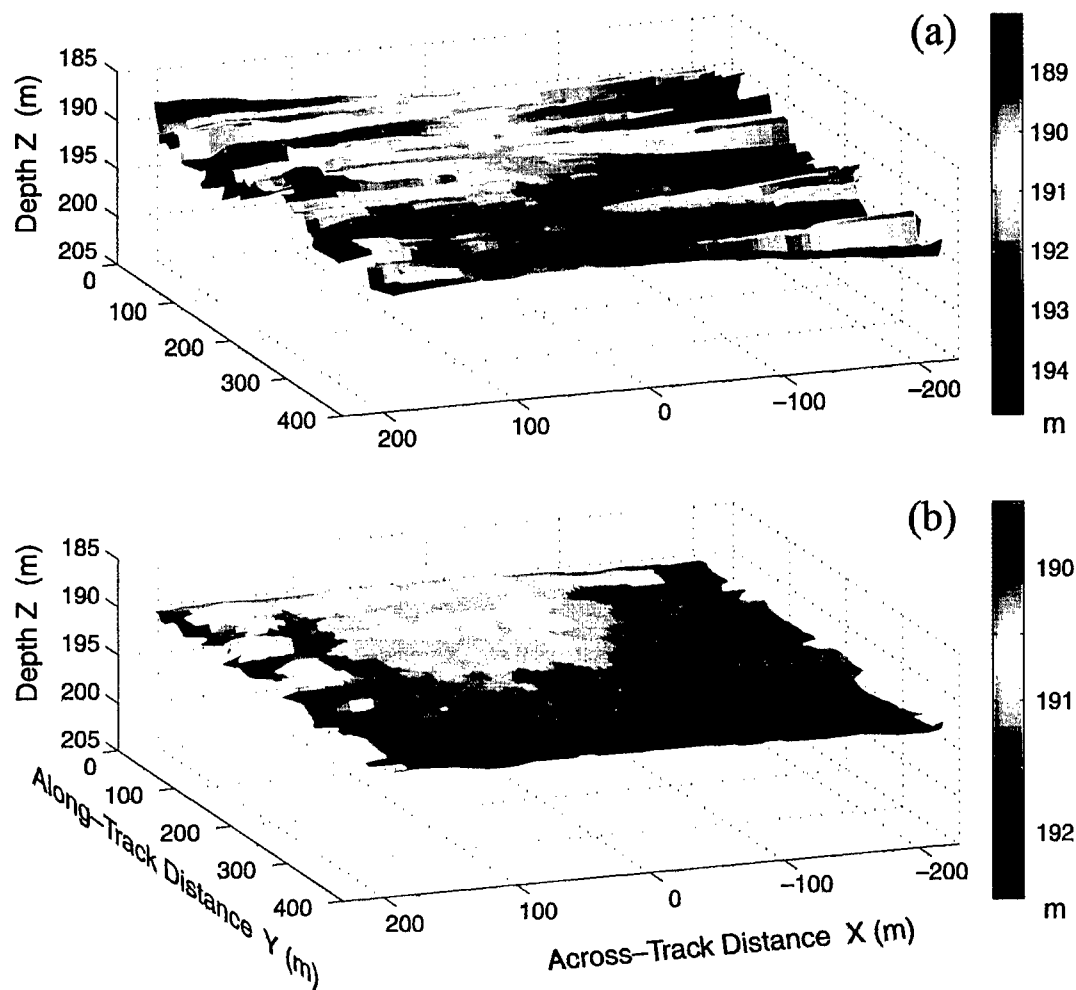


Fig. 8. Depth corrected bathymetry for run 3 (a) before and (b) after roll error estimation and correction. Because the raw bathymetric data were noisy, both (a) and (b) were processed with a two-dimensional median filter with a window size of 3x3 beamwidths.



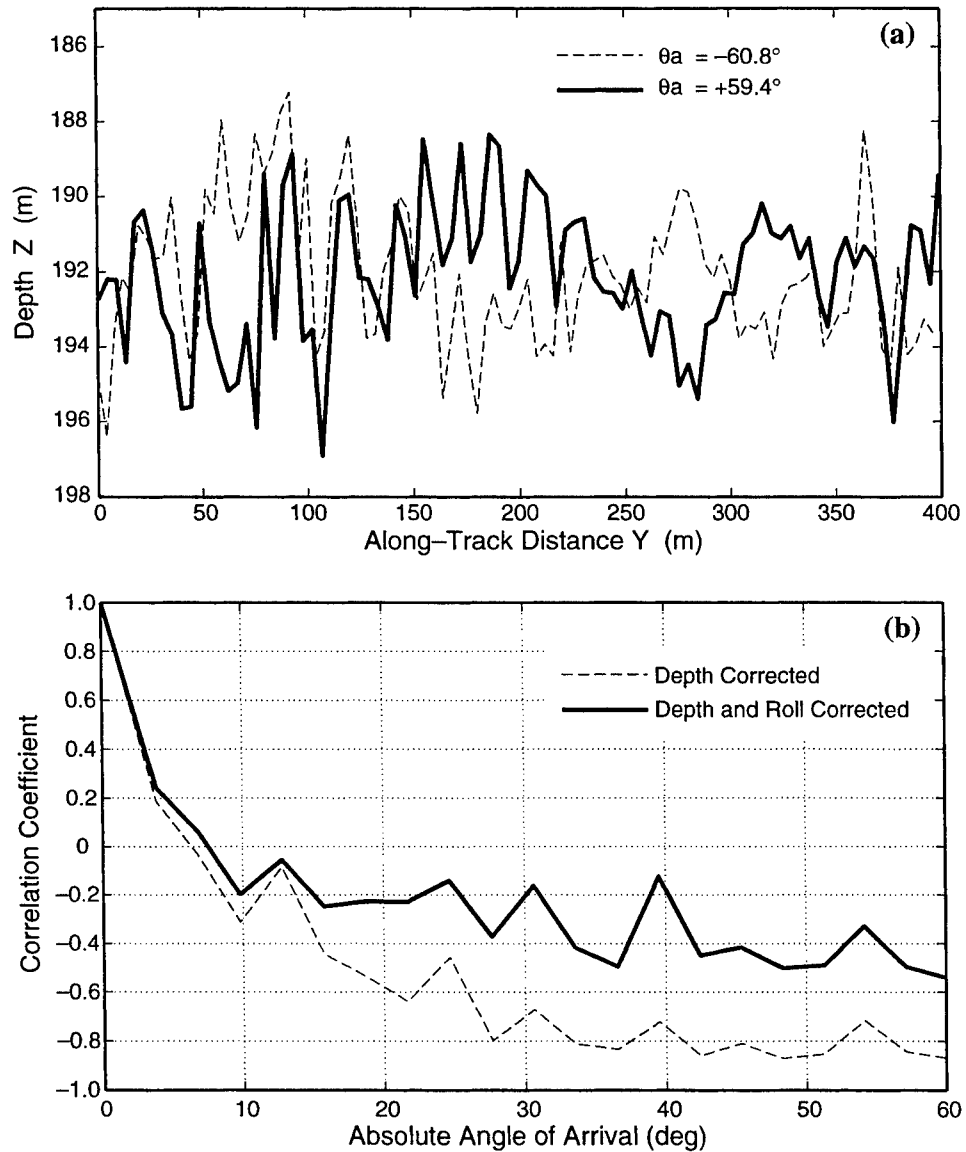


Fig. 9. (a) Along-track bathymetric profiles from run 3 for  $\theta_a = -60.8^\circ$  and  $+59.4^\circ$  appear negatively correlated, as shown by the sample correlation coefficients (b), which show that high negative correlations are evident between positive and negative beams of the bathymetry before roll correction.

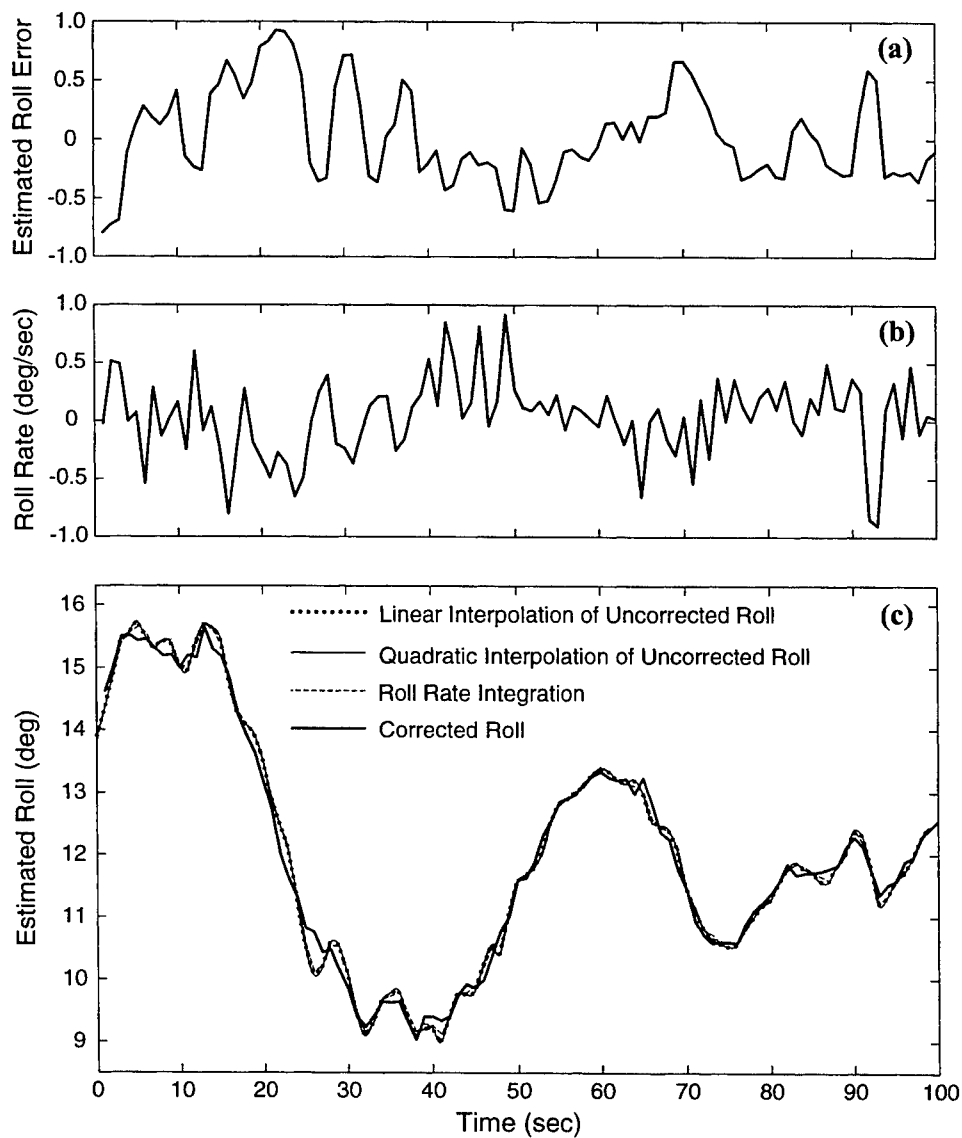


Fig. 10. Towfish roll data for run 3: (a) Roll error estimated as the across-track slopes computed from the detrended, depth corrected bathymetry; (b) Towfish roll rate, sampled at 1Hz (once per ping); and (c) Towfish roll corrected for the error estimated in (a) (thick solid line), and towfish roll estimated from linear (...) and quadratic (thin solid line) interpolation of the initial (uncorrected) roll sampled at 1Hz, and from integrating the roll rate samples in (b) (--).

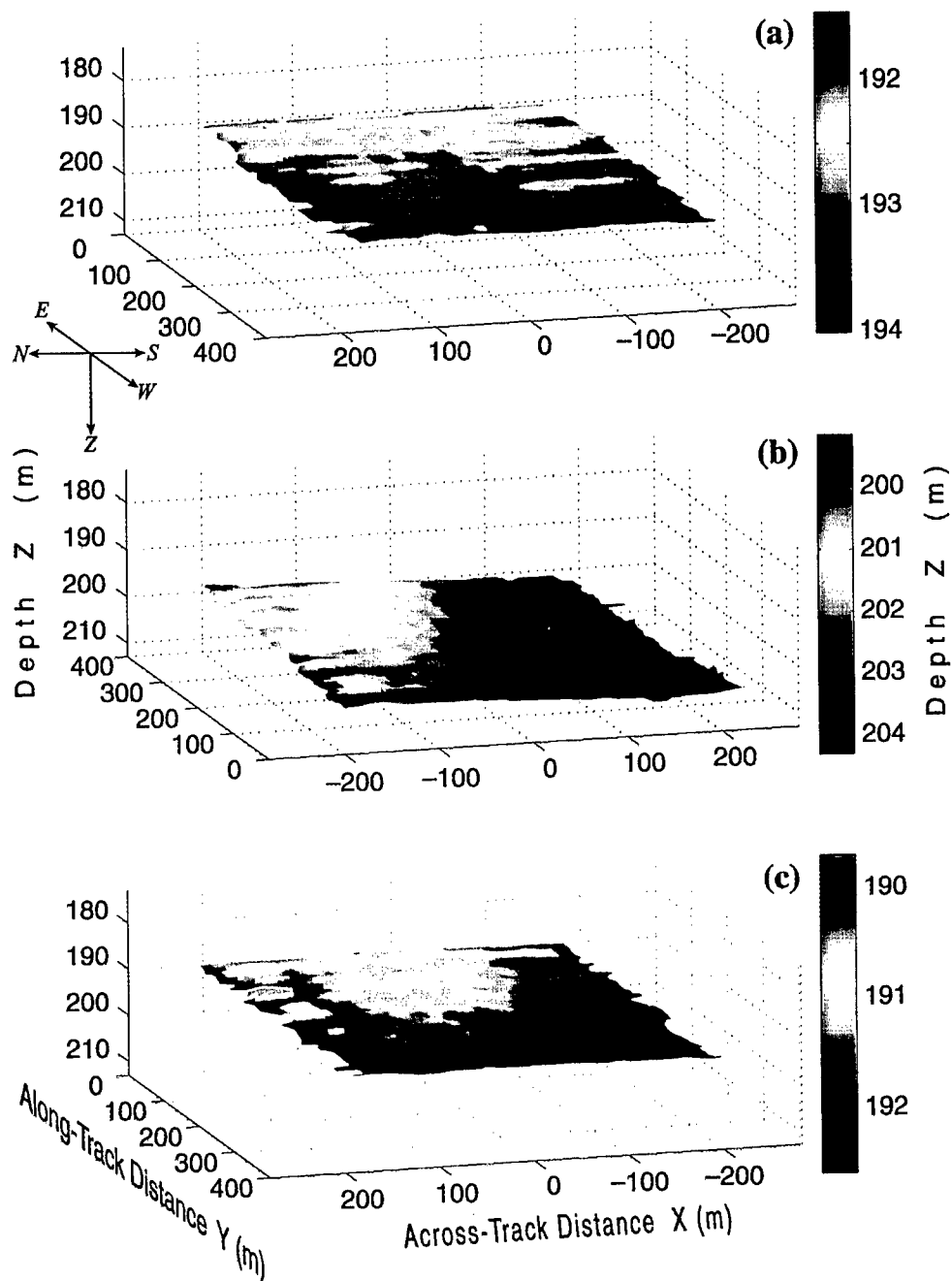


Fig. 11. Depth and roll-corrected bathymetry for runs 1-3 (a)-(c) after median filtering, as in Fig 8. The bathymetric surfaces are depicted with greater depths in blue and shallower depths in red and correspond to three separate areas in the data collection region. North, South, East, and West are to the left, right, rear, and forward of each panel, respectively, such that the towfish direction of travel (with increasing along-track distance  $y$ ) was from East to West in (a) and (c), and from West to East in (b).

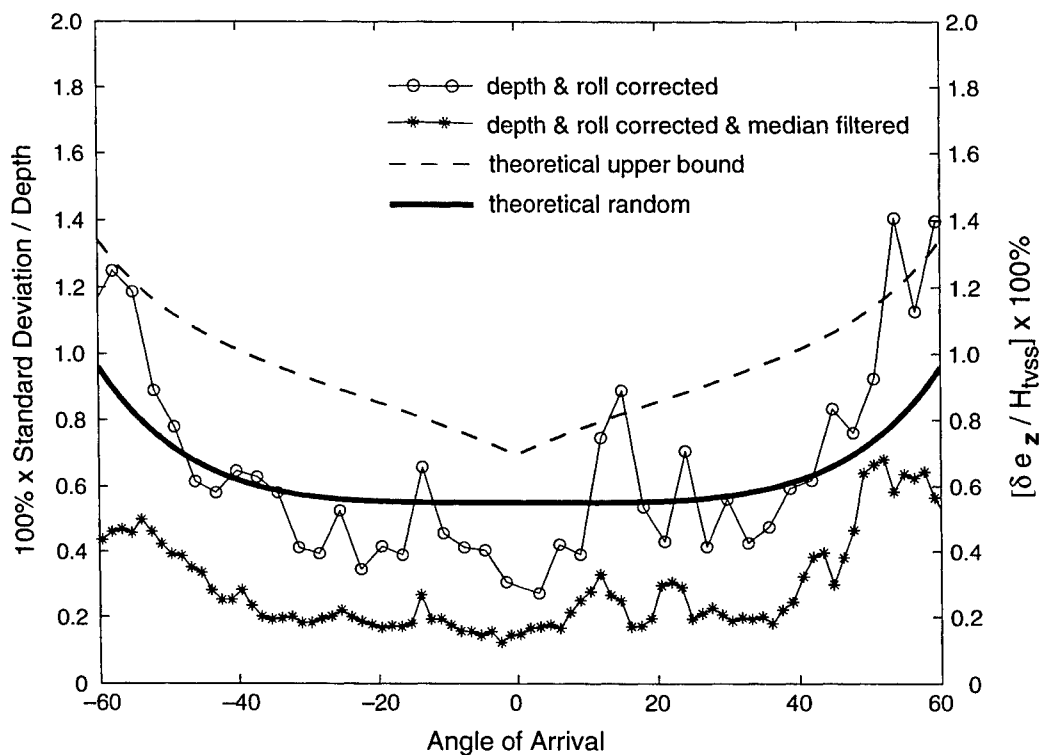


Fig. 12. Theoretical and experimental bathymetric error estimates. The experimental data are the standard deviations in percent of towfish altitude for the detrended bathymetry in run 3. Eqns (19) and (20) were used to compute the theoretical errors with the uncertainties in Table IV and the median value of  $H_{TVSS} = 115\text{m}$  for the three TVSS runs. The depth and roll corrected bathymetry (solid) meet the IHO standard (1% of sonar altitude) for all beams within  $50^\circ$  of nadir. After median filtering, the depth and roll corrected bathymetry meet the IHO standard for all beams up to  $\pm 60^\circ$ .

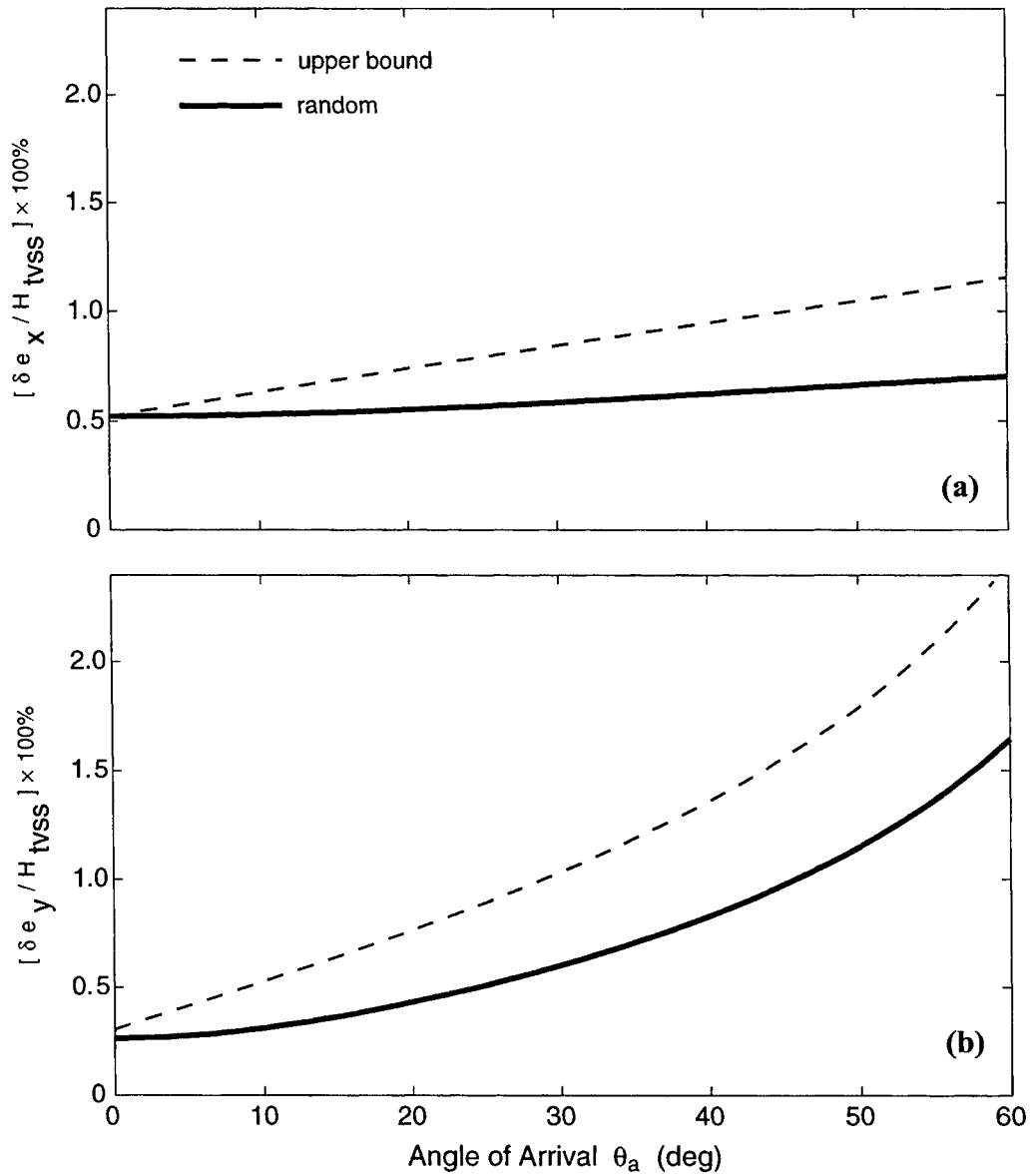


Fig 13. (a)  $x$  and (b)  $y$  error estimates ( $\delta e_x$ ,  $\delta e_y$ ) for the TVSS bathymetry in percent of the towfish altitude ( $H_{tvss}$ ) versus angle of arrival ( $\theta_a$ ). Eqns (19) and (20) were used to compute the theoretical errors with the uncertainties in Table IV and the following median values for three TVSS runs:  $H_{tvss} = 115\text{m}$ , pitch  $\phi = -1.76^\circ$ , and yaw  $\omega = 6.6^\circ$ .

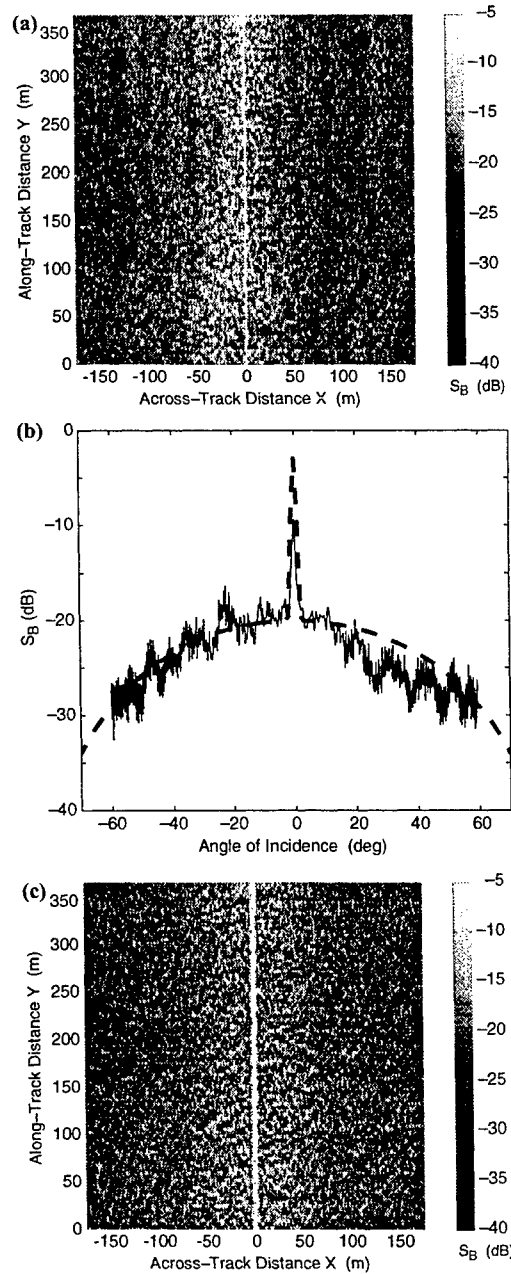


Fig. 14. (a) Seafloor backscattering strength  $S_B$  image for run 3 before compensating for array directivity. The towfish direction of travel is from bottom to top. (b) 27-ping mean backscattering strength ( $\bar{S}_B$ ) vs. angle of incidence ( $\theta_{inc}$ ) for the data in Fig. 14a (thin line) computed for pings #170-197 ( $y = 288$ -393m). The angle of incidence is defined as the angle of arrival ( $\theta_a$ ) minus the bottom slope. The dashed line is the best fit of the function  $S_{B_f}$  described in the text with  $A_f = 2 \times 10^3$ ,  $B_f = 3.0$ ,  $a_f = 0.10$ , and  $b_f = 0.012$ . (c)  $S_B$  image after compensating for transmit and receive array directivity using  $S_{B_f}$ .

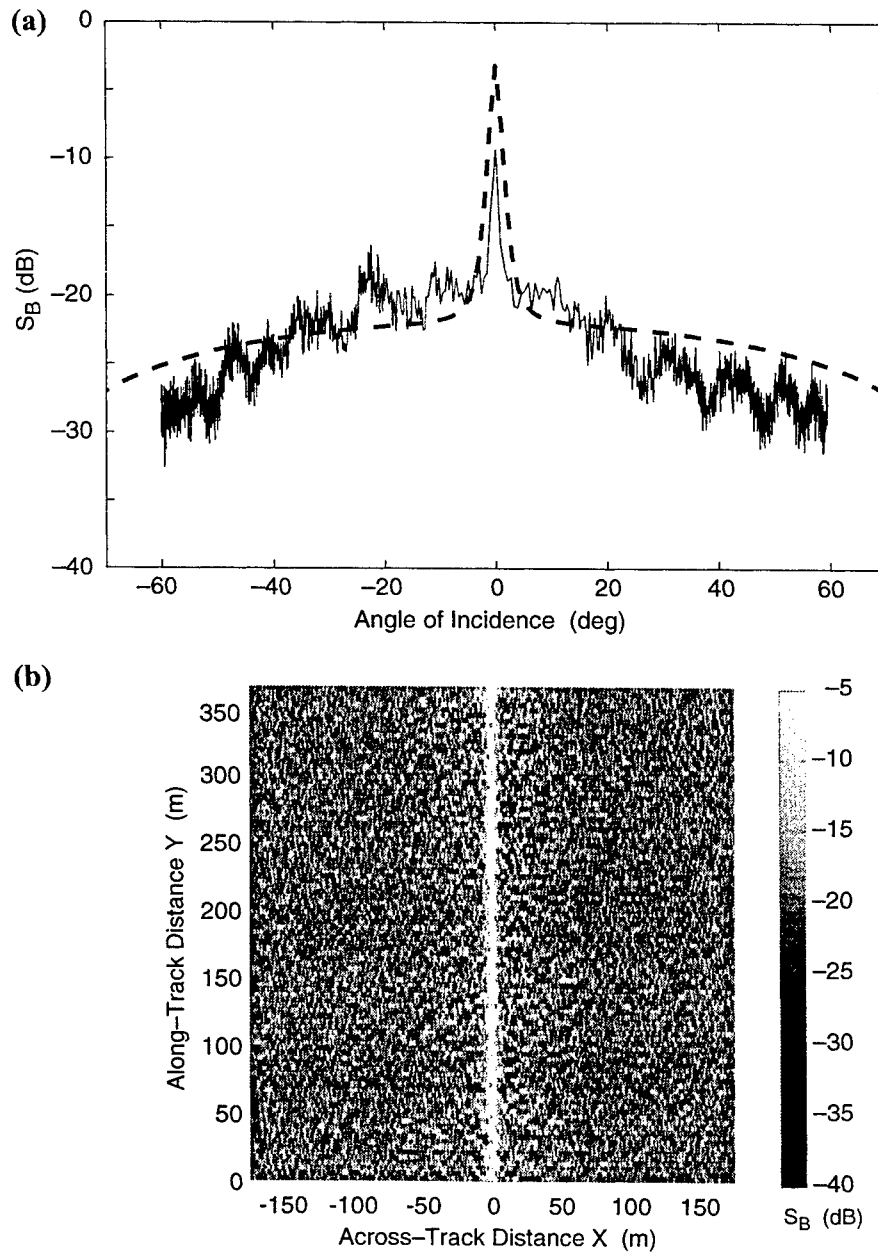


Fig 15. (a)  $\bar{S}_B$  vs.  $\theta_{inc}$  for the data in Fig 14a (thin line), as in Fig. 14b. The dashed line is the best fit of the composite roughness model described in the text using the parameters in Table VI. (b)  $S_B$  image after compensating for transmit and receive array directivity using the composite roughness model fit.

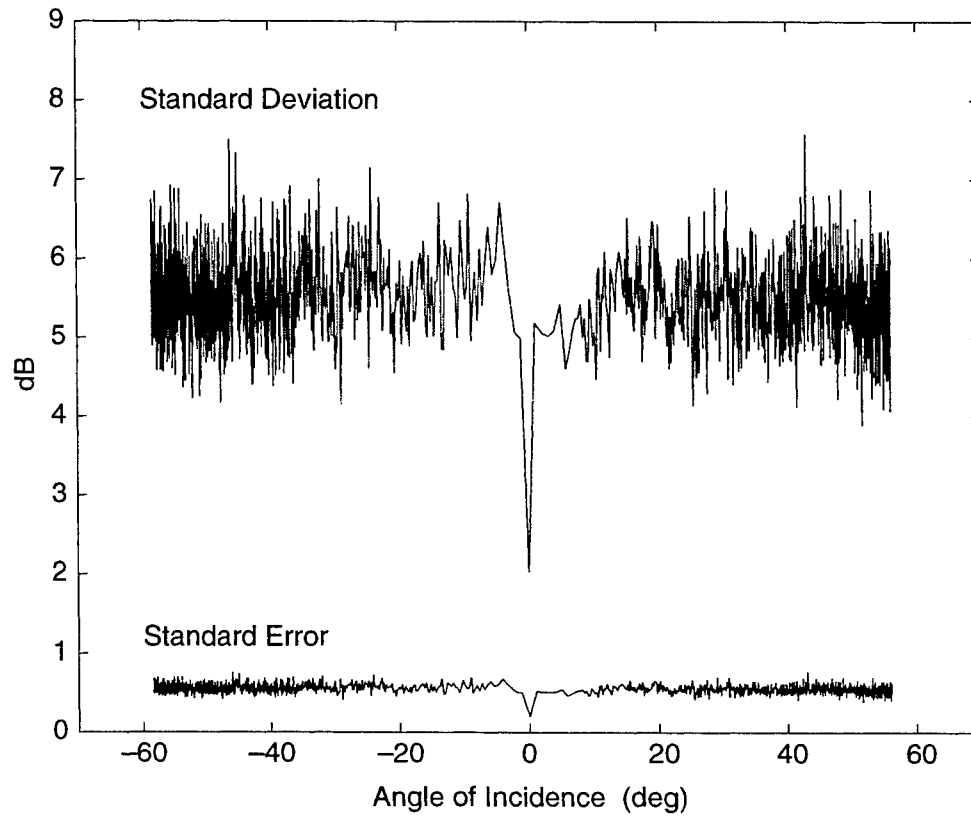


Fig 16. Standard deviation of seafloor backscattering strength ( $\sigma_{S_B}$ ) vs  $\theta_{inc}$  for run 3, and standard error of seafloor backscattering strength ( $\sigma_{\bar{S}_B}$ ) vs.  $\theta_{inc}$ . Both are computed over  $N_p = 97$  pings.



## Chapter 4

### Multibeam Volume Acoustic Backscatter Imagery and Reverberation Measurements in the Northeastern Gulf of Mexico

#### ABSTRACT

Volume acoustic backscatter imagery and reverberation measurements are derived from data collected in 200 m deep waters in the northeastern Gulf of Mexico, with the Toroidal Volume Search Sonar (TVSS), a 68 kHz cylindrical sonar operated by the U.S. Navy's Coastal System Station. The TVSS's 360° vertical imaging plane allows simultaneous identification of multiple volume scattering sources and their discrimination from backscatter at the sea surface or the seafloor. This imaging capability is used to construct a three-dimensional representation of a pelagic fish school near the bottom. Scattering layers imaged in the mixed layer and upper thermocline are attributed to assemblages of epipelagic zooplankton. The fine scale patchiness of these scatterers is assessed with the two-dimensional variance spectra of vertical volume scattering strength in the upper and middle water column. Plots of the vertical directionality of mean volume reverberation levels show a strong influence of the zooplankton layers whereas contributions from turbulent microstructure, bubbles, and the ambient noise from breaking waves are deemed unlikely. Boundary echo sidelobe interference and reverberation, as well as scattering from resonant microbubbles below the sea surface, are shown to be the major limitations in bioacoustic data obtained with the TVSS. Ensonification in discrete angular sectors is recommended for future multibeam sonar applications of the kind presented here. Because net tow and trawl samples were not collected, the analysis presented is based upon comparison to previous biologic surveys in the northeastern Gulf of Mexico and an extensive reference list from the bioacoustic literature.

#### I. INTRODUCTION

Demographic pressures, overharvesting of marine fish stocks, and pollution are threatening marine ecosystems world wide and provide incentives to focus fisheries management and plankton research efforts on conservation measures, thus requiring comprehensive knowledge of population dynamics and habitat variability.<sup>2</sup> Such knowledge may be gained through ocean volume acoustic backscatter measurements that have been used to study populations of fish and plankton since the deep scattering layer was identified by Eyring, Christensen, and Raitt (1948).<sup>3</sup> Upward looking echo-sounders have been used to estimate fish densities<sup>4</sup>, and horizontally directed sonars have been used to characterize fish school structure, shape, and movement<sup>5-8</sup>, as well as zooplankton distributions.<sup>9,10</sup> Multi-frequency sonar methods have been used to distinguish species/size classes in mixed species/size assemblages of zooplankton<sup>4,10-12</sup>, and to characterize components of their habitats such as near-surface bubble distributions<sup>13,14</sup>, estimates of air-sea gas transfer and mixing processes, or bathymetry and seafloor morphology.<sup>15</sup> Most of these measurements are made against a background of acoustic reverberation in the ocean volume that sets the noise floor for target detection<sup>1</sup> and for acoustic studies of the ocean boundaries.<sup>13,15</sup>

Recent advances in sonar systems, signal processing, and data storage have extended the geographic coverage and analysis capabilities in bioacoustic surveys.<sup>6,7,16-18</sup> This is particularly true for multibeam echo-sounders that have been used in a few bioacoustic studies to observe the swimming behavior of individual

zooplankters<sup>19</sup>, to demonstrate that vertical and lateral vessel avoidance by fish negatively bias abundance estimates derived from vertical echo-sounding sonars<sup>20</sup>, and to provide more precise mapping and abundance of pelagic fish stocks in near-surface schools than can be obtained by vertical echo-sounding.<sup>21</sup> In addition, over two decades of modeling efforts, coupled with laboratory and field measurements, have increased our understanding of scattering from marine organisms and improved the accuracy of acoustic estimates of size distributions, biomass, abundance, and behavior.<sup>22-27</sup>

In this context, we present volume acoustic backscatter and reverberation measurements derived from data collected by the US Navy's Toroidal Volume Search Sonar (TVSS), a 68 kHz multibeam sonar capable of 360° imaging in a vertical plane perpendicular to its direction of travel. We take advantage of the unique synoptic three-dimensional perspective afforded by this sonar system to explore and characterize the spatial and temporal structure of pelagic fish schools and the patchiness of epipelagic zooplankton found in the northeastern Gulf of Mexico. The data were collected during engineering tests of the TVSS conducted by the US Navy's Coastal System Station, Panama City, Florida, in a 2 nm<sup>2</sup> area centered at 29°30'N, 86°30'W. This is a relatively flat area on the continental shelf, with water depths ranging from 190 m to 200 m, situated roughly 65 nm southwest of Panama City, and 20 nm southeast of De Soto Canyon.

The TVSS includes separate cylindrical projector and hydrophone arrays, with the same 0.53 m diameter, mounted coaxially on a cylindrical tow body.<sup>15</sup> The projector array has 32 elements equally spaced 11.25° apart around the cylinder and designed to produce a "toroidal" beam pattern that is meant to be omni-directional in the plane perpendicular to the cylinder's axis (usually across-track) and 3.7° wide at -3 dB in any plane containing the cylinder's axis (usually along-track). The hydrophone array consists of 120 elements equally spaced every 3° around the cylinder. In the work presented here, beamforming of the hydrophone array yielded 120 receive beams, each 4.95° wide at -3 dB and spaced 3° apart to cover the full 360° around the array in the plane perpendicular to the array's axis.

Using this multibeam geometry, we have adapted existing oceanic imaging techniques to construct acoustic backscatter imagery of horizontal and vertical planes in the ocean volume (Fig. 1). Only vertical imagery are presented in this study to characterize the spatial distributions of bioacoustic scatterers and to partially discriminate between desired bioacoustic signals and volume or boundary reverberation. This is not possible with conventional single or dual-beam echo-sounders because of the temporal lags introduced by the successive transects required to cover a volume of ocean comparable to that sampled by the multibeam sonar on one track.<sup>17</sup> However, multibeam echo-sounders have important limitations due to the beamforming process and our intent is to demonstrate some of the capabilities and limitations of multibeam sonars in bioacoustic applications.

After a brief review of the relevant high frequency volume acoustic backscatter and reverberation concepts and theory used in this work, we describe our signal processing methods and the TVSS acoustic geometry necessary for interpreting the acoustic backscatter images. Because net tow or trawl samples were not collected in parallel with the acoustic data, our interpretations of these images rely on comparison and reference to previous biologic surveys in the northeastern Gulf of Mexico, and on the general bioacoustic literature. An extensive reference list is provided for this purpose.

## II. THEORETICAL BACKGROUND

### A. Quantitative Acoustic Measures

Sonar echoes from volume scatterers are usually quantified by measuring their amplitude, computing their energy, or through statistical measures of their amplitude time series. The latter can be used to classify scatterers<sup>18</sup> or estimate their density.<sup>4,24,28,29</sup> Here, we shall restrict our discussion to quantities based on either the amplitude ( $EL(t)$ ) of the echo at time  $t$  or its energy,  $EI$ , computed over a time interval  $\delta t$  according to the general *echo-integration* formula<sup>30</sup>:

$$EI = \int_t^{t+\delta t} EL^2(t) dt \quad . \quad (1)$$

For studies of biological scatterers, the energy is usually averaged over several pings because the random positions of the scatterers in the sonar beam and the random phases of the echo from each of these scatterers cause random energy fluctuations from ping to ping. The echo energy averaged over  $n_p$  pings at a given range ( $R$ ) (or time of arrival  $t$ ) is then:

$$\langle EI(R) \rangle = (1 / n_p) \sum_1^{n_p} EI(R) \quad . \quad (2)$$

The quantities most often computed from eqns (1) and (2) are the target strength (TS) and volume backscattering strength ( $S_V$ ). The latter is defined by Urick<sup>31</sup> as:

$$S_V = 10 \log_{10} (I_{\text{scat}} / I_{\text{inc}}) \quad , \quad (\text{dB}) \quad (3)$$

where  $I_{\text{scat}}$  is the acoustic intensity scattered from a unit volume ( $1 \text{ m}^3$ ), measured 1 m away from the volume, and  $I_{\text{inc}}$  is the acoustic intensity of a plane wave incident on the volume. For volume scattering from  $n_V$  organisms per unit volume each with a mean differential scattering cross section  $\langle \sigma_{\text{bs}} \rangle$ ,<sup>32</sup>  $S_V$  may be written as<sup>30</sup>

$$S_V = 10 \log_{10} (n_V \langle \sigma_{\text{bs}} \rangle) \quad . \quad (\text{dB}) \quad (4)$$

The corresponding target strength is defined as:

$$TS = 10 \log_{10} (\sigma_{\text{bs}}) = S_V - 10 \log_{10} (n_V) \quad . \quad (\text{dB}) \quad (5)$$

Some volume scattering applications such as target detection and bubble acoustic backscattering measurements use the target strength of ensonified volumes ( $V$ ), which is related to scattering strength by:

$$TS = S_V + 10 \log_{10} (V) \quad , \quad (\text{dB}) \quad (6)$$

showing that  $S_V$  is the target strength of a unit volume.<sup>31</sup> For comparison with results found in the literature in terms of the total scattering cross section ( $\sigma$ ), which when integrated over a unit volume is referred to as the backscattering cross section per unit volume ( $M_V$  in the radar and bubble acoustic backscatter literature<sup>13</sup>) we use the following formula:<sup>30-32</sup>

$$\sigma = 4\pi \sigma_{\text{bs}} \quad , \quad (\text{m}^{-1}) \quad (7)$$

which assumes that scattering is omnidirectional.<sup>32</sup> Likewise for the backscattering coefficient  $s_V$ <sup>32</sup>

$$S_V = 10 \log_{10}(s_V) \quad . \quad (8)$$

Either  $\langle EI(t) \rangle$  or  $EL(t)$  may be used to compute the volume backscattering strength from the sonar equation.<sup>31</sup> Given a source level  $SL$ , a one-way transmission loss  $TL$  at range  $R$  from the sonar due to spherical spreading and absorption, with absorption coefficient  $\alpha$  in dB/m, and a volume  $V$  in  $m^3$  ensonified by the transmitted pulse within the receive beam we have:

$$S_V = 10 \log_{10} (\langle EI \rangle, EL^2) - SL + 2TL - 10 \log_{10} V \quad (\text{dB}), \quad (9)$$

with  $TL = 20 \log_{10} R + \alpha R$ .

$S_V$  is related to the equivalent plane wave reverberation level (RL) by:<sup>31</sup>

$$RL = SL - 2TL + S_V + 10 \log_{10} V. \quad (10)$$

Of interest in target detection applications, RL is the level of the axial plane wave producing the same mean-squared hydrophone voltage as the reverberation<sup>31</sup>, which, from eqn (9), is identical to  $10 \log_{10} (EL^2)$ .

## B. Bioacoustic Scattering Models

The majority of bioacoustic studies have been performed with ship mounted or towed down-looking echo-sounders.<sup>32</sup> These acoustic studies are often supplemented with towed nets or video systems to provide a measure of the relationship between fish or zooplankton concentrations, size distribution, taxonomic composition, and volume acoustic backscattering.<sup>33</sup> In all cases, the objectives include estimating abundance, biomass, and/or density of organisms within a survey area, as well as obtaining some knowledge of the species composition and/or spatial distribution of organisms in specified regions. This is usually performed by measuring  $S_V$  with a high frequency sonar and estimating  $\langle \sigma_{bs} \rangle$  from trawl or net tow samples using an appropriate scattering model, then computing  $n_V$  from (4) and (5). To do this with a single frequency sonar system, one must make a number of unrealistic assumptions, including: (a) scattering is dominated by a single type of organism; (b) the size of the organism is known; and (c) there exists a validated model which relates the acoustic frequency and organism size to the organism's target strength.<sup>11</sup>

The dominant source of scattering from fish is their swimbladders, and much of the variability in fish target strength measurements comes from variations in this gas-filled organ.<sup>25</sup> At high frequencies, swimbladder scattering is non-resonant and omni-directional<sup>34</sup>, and has been shown to contribute 90-95% of the total backscattered sound for ratios of fish length  $L$  to acoustic wavelength  $\lambda$  satisfying  $8 \leq L/\lambda \leq 36$ .<sup>25</sup> Other parts of the body contribute to the total acoustic scattering and are directional in nature.<sup>34</sup> Consequently, most scattering models for fish are based on simple regression equations in which  $\sigma$  or  $TS$  is a function of the fish's length  $L$ . For a fish at dorsal aspect Love's regression yields two parameters  $a_r$  and  $b_r$ :

$$\sigma / \lambda^2 = a_r (L / \lambda)^{b_r}. \quad (11)$$

Love (1978)<sup>23</sup> provides a simpler empirical formulation valid for a single fish at any aspect with  $1 \leq L/\lambda \leq 100$ :

$$\sigma = m L^2, \quad (12)$$

where  $m$  is a constant averaged from data at various target aspect angles for 14 fish families. Others<sup>36,37</sup> have presented single species target strength relationships of the form:

$$TS = 20 \log_{10} L + w, \quad (\text{dB}) \quad (13)$$

in which  $L$  is in cm and  $w$  is determined by fitting the acoustic data to *in-situ* length

data. Most values for  $w$  are between -85 dB and -65 dB. Theoretical scattering models which include the physiological characteristics of the fish have been developed as well and are described in Medwin and Clay (1998).<sup>32</sup>

For zooplankton, the most widely referenced scattering model is Johnson's (1977)<sup>22</sup> simplified version of Anderson's (1950)<sup>38</sup> fluid sphere model:

$$\sigma_{bs} = a_{esr}^2 \alpha_r (ka_{esr})^4 [2(2 + 3(ka_{esr})^4)]^{-1} \quad (14)$$

where  $a_{esr}$  is the equivalent spherical radius of the animal,  $k = 2\pi/\lambda$ , and  $\alpha_r$  given by:

$$\alpha_r = (4/9) [(1 - gh^2)/(3gh^2) + (1 - g)/(1 + 2g)]^2, \quad (15)$$

in which  $h$  and  $g$  are the sound speed and density ratios of the animal to seawater. The equivalent spherical radius of a biological scatterer may be computed from its displacement volume or by approximating the scatterer as a sum of simple geometrical volumes.<sup>22</sup> This model resembles a high-pass two-pole filter, in that eqn (14) agrees with Anderson's model for  $ka_{esr} \ll 1$  (Rayleigh scattering) and for  $ka_{esr} \gg 1$  (geometric scattering), but it smoothes the scattering near  $a_{esr} = 1$  by letting  $\sigma_{bs}$  increase monotonically with  $ka_{esr}$  (see Fig. 1 in reference (22)). At the TVSS's acoustic wavelength,  $\lambda = 2.2$  cm,  $ka_{esr} = 1$  corresponds to  $a_{esr} = 0.35$  cm. However, in studies using single-frequencies near 68 kHz, backscattering can occur from animals with a broad range of sizes, so the oscillations near  $ka_{esr} = 1$  are expected to average to an intermediate value.<sup>30</sup>

Although Johnson's model has been shown to perform reasonably well for species that do not contain gas bubbles, and are partially or totally enclosed in exoskeletons, such as euphausiids, copepods, and decapod shrimp<sup>10,39</sup>, it may fall short in many situations because it fails to completely describe the physics of the problem. Using eqn (14) in eqn (4) to estimate abundance from measured scattering strength assumes that the total acoustic backscatter from aggregations of scatterers is the sum of contributions from individuals. Although Foote (1983)<sup>40</sup> demonstrated this for fisheries acoustics, it is not likely to be the case for zooplankton. Populations of zooplankton typically contain a wide variety of animal types, and the anatomical features across and within species result in a large variation in scattering properties. Because these properties vary spatially and temporally, it has been notoriously difficult to link echo energy directly to the biomass of the animals.

In the last decade, experimental evidence and continued modeling efforts have produced more complete theories for acoustical backscattering from zooplankton and have shown that such scattering depends on the material properties, orientation, shape, and size.<sup>32</sup> For example, Stanton *et al.* (1994)<sup>41</sup> showed that the relative average echo energy per unit biomass can vary by up to 43 dB between fluid-like (e.g. krill, salp), gas-bearing (e.g. siphonophore), and elastic-shelled (e.g. gastropod) zooplankton. Strong dependencies on  $g$  and  $h$  have been observed by numerous investigators (e.g. Fig. 13 in reference (16)), whereas orientation alone has been shown to produce variations of  $\sim 100/m^3$  in zooplankton density estimates<sup>12</sup> and 18 dB in target strength measurements.<sup>42</sup> In addition, the bent or deformed cylinder model<sup>27</sup> has proven to be more appropriate than the spherical model of eqn (14) for euphausiids.<sup>42</sup>

### C. Environmental Context

The preceding discussion presumes that biologic scattering sources are responsible for scattering features in our data. Even though we lacked the net tow and trawl data required to verify such a presumption, historical and concurrent data provide sufficient evidence. The abundance and distribution of pelagic fish in the Gulf of Mexico (GOM) were investigated by the US National Marine Fisheries Service (NMFS) during 15 cruises in the spring and fall seasons between 1988 and 1996.<sup>43</sup> Trawling was

performed only during daylight hours near the bottom, with the highest concentration of sampling stations centered approximately 10 nm northwest of the TVSS experiment site. For several species, the highest abundances were sampled at four sites within 1 nm of the TVSS experiment site. Thus, the NMFS survey encompassed the year, season, time of day, geographic location, and depth corresponding to the collection of the TVSS data.

Zooplankton species known to scatter sound near 68kHz, such as euphysiids, have been observed in the Northeastern and central GOM as well. Hopkins' (1982)<sup>44</sup> observations in a region about 120 nm south of the TVSS experiment showed that zooplankton biomass was concentrated in the upper 50m of the water column. Zimmerman and Biggs (1999)<sup>45</sup> observed acoustic scattering due to zooplankton in warm- and cold-core eddies in the eastern central GOM during June 1995 using a 153kHz acoustic Doppler current profiler. Also in the eastern central GOM, Hopkins *et al.* (1981)<sup>46</sup> examined the landward distributions of zooplankton between May and June, 1977, and found many oceanic species distributed across the Florida shelf. Ortner *et al.* (1984)<sup>47</sup> investigated the vertical distributions of zooplankton during January and February, 1981, and found zooplankton distributions to be closely tied to mixed layer depth. Ortner *et al.* (1989)<sup>48</sup> reported observations of euphysiids and decapod shrimp in a region about 50 nm southeast of the TVSS experiment site.

### III. TVSS DATA

#### A Environmental Conditions

The acoustic data presented here were collected on 9 November, 1994 between 1026AM and 1131AM local time. The wind speed and sea state recorded at 0658AM were 6 knots (3m/s) and 1.5, respectively. A CTD cast, taken at 0658AM approximately 100m north of the location for run 1 (Fig. 2), revealed the presence of a 24.8°C isothermal mixed layer extending to a depth of 49m, a thermocline between 49 m and 150 m depth, and a nearly-isothermal layer above the bottom with a temperature of 15.6°C. The surface salinity was 35.1 PSU, and the surface sound speed was 1534 m/s. Historical data<sup>49</sup> indicate a relatively weak circulation in the region during fall months, which, with the light winds suggests that the surface currents were either weak or absent.

The TVSS was towed at a depth of 78 m, approximately 735 m astern a ship moving at a nearly-constant speed of 4.1 m/s. Three runs of 100 consecutive pings of acoustic backscatter data from a 200  $\mu$ s CW pulse of 68 kHz transmitted at 1 Hz were obtained. Towfish roll, pitch, heading, speed, and depth were sampled at 1 Hz (once per ping). Further information regarding the TVSS, the data collection, and the signal processing is described in references (52),(15), and (13).

#### B. Processing Methods

The processing scheme that we have developed for these data is designed for conformal arrays and includes: quadrature sampling, resampled amplitude shading, element-pattern compensation, and broadside beamforming on phase-compensated, overlapping subarrays with asymmetric projected element spacings.<sup>52</sup> This procedure permits split aperture processing of the beamformed output, which is performed because the processed data also were used to study acoustic backscatter from the ocean boundaries<sup>13,15</sup>, and the phase zero-crossing of the output phasor is the most accurate means to detect the arrival time of boundary reflections on the maximum response axis of the beam.<sup>15</sup>

For each ping, the acoustic signals from the 120 hydrophones are heterodyned in the data acquisition system (DAS) from 68 kHz to 6.25 kHz, low-pass filtered, and digitally recorded using 16 bit signed integer 2's complement coding at a sampling frequency of 25 kHz. The full scale of the recorded data is  $\pm 5V$ , so we converted the digital data to volts by:

$$d_v = 10[ (d_l + 2^{n-1}) / (2^n - 1) ] - 5, \quad (\text{volts}) \quad (16)$$

where  $n=16$  bits,  $d_l$  is the recorded digital value, and  $d_v$  is the output voltage value.

To form a beam in the direction  $\theta$ , at each time sample  $t$ , the phases of the quadrature sampled acoustic signals from 29 contiguous elements are adjusted to project the curved aperture on the tangent perpendicular to the direction  $\theta$ . We define  $\theta$  as the roll-corrected angle in the  $x$ - $z$  plane perpendicular to the axis of the towfish, such that the towfish's zenith is at  $\theta = 0^\circ$ , with  $\theta$  increasing clockwise around the towfish when facing the direction of travel (Fig. 1). The split aperture process is achieved by dividing this aperture into two overlapping 21-element subapertures whose phase centers are spaced 8 elements apart. For each time sample  $t$ , the signals from these two subapertures are phase shifted and summed separately to produce beams  $B_1(\theta, t)$  and  $B_2(\theta, t)$ , and a phasor  $P(\theta, t)$  is formed as:

$$P(\theta, t) = B_1(\theta, t) \times B_2^*(\theta, t), \quad (17)$$

where  $*$  denotes complex conjugation. The magnitude of  $P(\theta, t)$  is the product of the magnitudes of  $B_1(\theta, t)$  and  $B_2(\theta, t)$ , hence it has units of volts<sup>2</sup>, and its phase is the phase difference between  $B_1(\theta, t)$  and  $B_2(\theta, t)$ .  $B_1(\theta, t)$ ,  $B_2(\theta, t)$ , and  $P(\theta, t)$  are all broadside with respect to the 29-element aperture. This operation is performed at every time sample  $t$  for each ping, every  $3^\circ$  for directions spanning  $360^\circ$  around the TVSS axis. The beam directions are corrected for the difference between the sound speed used in the beamforming and that of seawater at the face of the array because  $B_1(\theta, t)$  and  $B_2(\theta, t)$  are not broadside to their respective subapertures. The -3dB beamwidth of each output beam product is  $4.95^\circ$  in the across-track direction.

Before an acoustic backscattering strength image is formed, backscatter data from eqn (17) are converted to the squared echo amplitude according to:

$$10\log_{10}(EL^2(\theta, t)) = 10\log_{10}(\frac{1}{2} |P(\theta, t)|) - RVR - FG - DI - TVG, \quad (18)$$

where  $RVR = -168$  dB *re*:  $1V_{rms}/\mu Pa$  is the receive voltage response of each hydrophone,  $FG = 29$ dB is the preamplifier fixed gain,  $DI = 13$ dB is the array gain associated with the beamforming and split aperture processing, and  $TVG$  is the system time-varying gain. The result, which is equivalent to  $RL$  in eqn (10), is used to compute  $S_v$  from eqn (9) with the calibrated TVSS source level  $SL = 216.8$ dB *re*:  $1\mu Pa$  @ 1m,  $\alpha = 0.024$  dB/m<sup>31</sup>, and  $R$  determined from  $t$  and  $\theta$  using constant-gradient ray-tracing techniques.<sup>31</sup>

Echo-integrated vertical volume backscattering strength images on either side of the towfish were constructed using eqns (1),(2),(9), and (18) with a time gate  $\delta t$  corresponding to a 1.4 m depth interval, and a ping averaging interval  $n_p = 3$  before computing  $S_v$  with eqn (9). All other images were constructed by first computing  $S_v$  directly from  $EL^2$  for each beamformed sample in each ping, yielding 120 backscattering strength times series. These may be displayed together as a vertical slice of volume acoustic scattering strength in polar coordinates of angle vs. time (Fig. 3). In this representation, echoes from the sea surface and seafloor appear as the high backscatter, horizontal features. Scattering from resonant microbubbles in the towship's wake and from bubble clouds formed by breaking ship waves are responsible for the high backscattering strength features near the sea surface. Other scattering structures are apparent upon adjusting the dynamic range of the display, and these will be

discussed in the results section.

#### D. TVSS Beam Geometry

The sampling and resolution characteristics of the backscattering strength images are determined by the acoustic geometry of each TVSS ping. The angular sample spacing between the maximum response axes of adjacent beams in Fig. 3 is  $\theta_s = 3^\circ$ , whereas the quadrature sampled time increment within each beam is  $\tau_s = 160 \mu s$ , which corresponds to a 12cm sampling interval assuming a sound speed in seawater  $c=1500m/s$ . The range resolution for each sample is defined in terms of the bandwidth  $W$ :

$$\Delta R = c / 2W \quad . \quad (m) \quad (19)$$

With the TVSS pulse length  $\tau_p = 200 \mu s$ , the bandwidth  $W = 0.88/\tau_p = 4.4kHz$ , which yields a range resolution of 17cm with  $c=1500m/s$ .

The volumetric resolution in each ping is determined by the spatial dimensions of the volume ( $V$ ) ensounded by the TVSS transmit pulse within each receive beam (Fig. 4). We compute  $V$  as the ellipsoidal shell section formed from the intersection of the pulse, the transmit beam pattern, and the receive beam pattern at each sampling point:

$$V = \frac{2}{3} \theta_T \sin(\theta_R / 2) [R'^3 - R^3] \quad , \quad (m^3) \quad (20)$$

where  $R$  is the range from the center of the TVSS in meters,  $R' = R + \Delta R$ , the -3dB receive beamwidth ( $\theta_R$ ) is  $4.95^\circ$ , and the -3dB transmit beamwidth ( $\theta_T$ ) is  $3.7^\circ$ . The spatial dimensions of  $V$  in the across-track, along-track, and vertical dimensions ( $\Delta x_V$ ,  $\Delta y_V$ ,  $\Delta z_V$ , Fig. 4) vary with range. The along-track dimension is the same for all beam angles  $\theta$ :

$$\Delta y_V = 2R' \sin(\theta_T / 2) \quad . \quad (21)$$

However, the across-track and vertical dimensions of  $V$  vary with range and  $\theta_a$ , which is defined in relation to  $\theta$  in Fig. 3 as:  $\theta_a = \theta$  for  $\theta = 0^\circ$  to  $90^\circ$ ;  $\theta_a = |180^\circ - \theta|$  for  $\theta = 91^\circ$  to  $270^\circ$ ; and  $\theta_a = (360^\circ - \theta)$  for  $\theta = 271^\circ$  to  $359^\circ$ . Thus, for volume cells in beams directed towards zenith and nadir,

$$\begin{aligned} \Delta x_V &= 2R' \sin(\theta_R / 2) \\ \Delta z_V &= \Delta R + R(1 - \cos(\theta_R / 2)) \end{aligned} \quad \text{for } \theta_a = 0^\circ \quad , \quad (m) \quad (22a)$$

and for volume cells in horizontal beams,

$$\begin{aligned} \Delta x_V &= \Delta R + R(1 - \cos(\theta_R / 2)) \\ \Delta z_V &= 2R' \sin(\theta_R / 2) \end{aligned} \quad \text{for } \theta_a = 90^\circ \quad , \quad (m) \quad (22b)$$

where  $\Delta x_V$  exceeds the range resolution at  $\theta_a = 90^\circ$ , and  $\Delta z_V$  exceeds  $\Delta R$  at  $\theta_a = 0^\circ$  because of the curvature of the wavefront. For angles between the horizontal and vertical, the  $x$  and  $z$  dimensions of  $V$  can be expressed as:

$$\begin{aligned} \Delta x_V &= 2R \sin(\theta_R / 2) \cos \theta_a + \Delta R \sin(\theta_a + \theta_R / 2) \\ \Delta z_V &= 2R \sin(\theta_R / 2) \sin \theta_a + \Delta R \cos(\theta_a - \theta_R / 2) \end{aligned} \quad \text{for } 0^\circ < \theta_a < 90^\circ - \theta_R / 2 \quad . \quad (22c)$$

Samples in adjacent beams overlap because  $\theta_s < \theta_R / 2$ . The overlapping volume increases with range:

$$V_{ol} = \frac{2}{3} \theta_T \sin((\theta_R - \theta_s) / 2) [R'^3 - R^3] \quad . \quad (m^3) \quad (\text{adjacent beams}) \quad (23)$$



The percent of overlapping volume between adjacent beams is:

$$VP_{ol} = [ V/V_{ol} ] \times 100\% , \quad (24)$$

which can be written from eqns (20) and (23) as:

$$VP_{ol} = [ (\sin((\theta_R - \theta_s) / 2) / \sin(\theta_R / 2) ] \times 100\% , \quad (\text{adjacent beams}) \quad (25)$$

yielding a range independent volume overlapping percentage of 39.4% between TVSS beams.

Along-track, ensonified volume cells in the same angle of arrival and range cell overlap over successive pings. An approximate upper bound on this overlapping volume is:

$$V_{ol} \leq \frac{2}{3} \theta_T \sin(\theta_R / 2) [ (R' - R_{ol})^3 - (R - R_{ol})^3 ] , \quad (m^3) \quad (26)$$

where the vertical range from the TVSS at which the beams first overlap along-track is:

$$R_{ol} = \Delta y_{ping} / 2 \tan(\theta_T / 2) , \quad (m) \quad (27)$$

and the along-track separation between pings is defined as:

$$\Delta y_{ping} = (V_{tvss} / prr) , \quad (m) \quad (28)$$

where  $V_{tvss}$  is the speed of the towfish, and prr is the pulse repetition rate. Because the average  $V_{tvss}$  was 4.1m/s, and the prr of the TVSS was 1Hz, the average  $\Delta y_{ping}$  and  $R_{ol}$  for consecutive pings were 4.1m and 62m, respectively.  $V_{ol}$  decreases with ping separation and the towfish's speed. Using (20), (24), and (26), an upper bound on the percent overlap is approximately:

$$VP_{ol} \leq [ \frac{ [ (R' - R_{ol})^3 - (R - R_{ol})^3 ] }{ [ R'^3 - R^3 ] } ] \times 100\% \quad (29)$$

Thus, the percent overlap of volume cells between pings increases with range, but decreases with ping separation and towfish speed. This geometry also indicates that the ping-to-ping correlation of samples close to the TVSS will be less than for samples at greater ranges.

The backscatter images in this study were constructed using the sidescanning techniques described in reference (15), where samples of acoustic backscatter are extracted for the time and angle pairs that correspond to the desired horizontal or vertical plane (Fig. 1). Between discrete beam angles, samples are interpolated in time increments corresponding to the quadrature sampling interval  $\tau_s$ . Thus, the sample spacings in the images depend upon  $\tau_s$ , as well as  $R$ ,  $V_{tvss}$ , and  $\theta_a$ . The along-track sample spacing is the ping separation distance i.e.,  $\delta y_v = \Delta y_{ping}$ , whereas across-track and vertical sample spacings are:

$$\begin{aligned} \delta x_v &= c\tau_s / 2\sin\theta_a , & \text{for } \theta_a > \theta_R \\ \delta z_v &= c\tau_s / 2\cos\theta_a , & \text{for } \theta_a < 90^\circ - \theta_R \end{aligned} \quad (m) \quad (30)$$

A consequence of the sidescanning procedure is that the number of samples per beam angle increase as  $\theta_a$  decreases.

## E. System-related Sources of Error

Using eqn (20) to compute  $V$  in  $S_v$  calculations assumes that scattering comes from a uniformly ensonified volume, and that TVSS receive beam patterns are identical for each subarray of elements. Ensonification from the TVSS transmit beam pattern was in fact not uniform but contained many irregularities about the array axis

with maximum variations of -9dB from the calibrated source level (see Figs in reference (15)). Moreover, the beam patterns of the 120 individual hydrophones were slightly different, and their RVR's, FG's, and TVG's varied as much as  $\pm 2$ dB from average values. Ideally, one should use Foote's (1983) sampling volume theory which incorporates the transmit and receive beam patterns, and the influence of scatterer concentration, cross section, and orientation.<sup>33</sup> When such observations are unavailable, as is the case here, the following may be used:

$$V(R, \theta_a) = \frac{c}{2W} R^2 \int_{-\theta_r/2}^{+\theta_r/2} \int_{\theta_a - \theta_r/2}^{\theta_a + \theta_r/2} b(\theta_a, \phi) b'(\theta_a, \phi) d\theta_a d\phi, \quad (31)$$

where  $W$  is the bandwidth,  $c$  is the speed of sound,  $\phi$  is the azimuthal angle,  $b(\theta_a, \phi)$  is the transmit beam pattern, and  $b'(\theta_a, \phi)$  is the receive beam pattern.

We were unable to use the actual transmit beam pattern, hence eqn (31), because the towfish's attitude variations were undersampled at 1 Hz, and therefore aliased. Corrections to the platform's roll and depth data were estimated from seafloor and sea surface backscatter data using the techniques described in reference (15). In beam-forming the hydrophone array, we used an average of the calibrated hydrophone sensitivity values of -168 dB *re*:  $1V_{\text{rms}}/\mu\text{Pa}$ , and we approximated the beam patterns of individual hydrophones with a cardioid-shaped magnitude response that closely matched that provided by the manufacturer.<sup>32</sup> In the absence of a measured phase response, we used a  $\sin^2$  function. From the error analysis in reference (15) and computer simulations that used the TVSS transmit pattern and roll data for each run, we estimated a maximum of 7dB for the negative bias error and  $\pm 3$ dB for the random errors due to the TVSS array patterns. These error estimates were reduced to 5dB and  $\pm 1$ dB when the data were echo-integrated and averaged along-track.

Because eqn (20) assumes a monostatic scenario, the forward and angular motion of the TVSS reduced the effective sampling volume, and therefore produced errors in our  $S_V$  calculations. For the data in this study, the maximum slant range from the TVSS was 120m. With the 4.1m/s speed of the towfish, this corresponds to a maximum horizontal displacement of 0.6m between transmit and receive cycles, whereas the maximum angular displacement due to the towfish's roll was approximately  $0.2^\circ$ . The reduction in sampling volume associated with these displacements is approximately 17%. However, this results in about -0.9dB of error in our  $S_V$  calculation because the sampling volumes at this range are  $\sim 13\text{m}^3$ . Moreover, this is the maximum error, and for most of the data in this study, errors due to horizontal motion are less than 0.5dB.

An important limitation of the data presented here is that boundary echoes at normal incidence ( $\theta = 0^\circ$  or  $180^\circ$ , Fig. 3) received through the sidelobes of beams directed towards the volume, contaminate the acoustic reverberation or volume back-scattering signals received in their mainlobes. This problem is illustrated in the returns for a single ping (Fig. 3) and for a 97-ping average (Fig. 4a), where boundary echoes appear as high backscatter circular features tangent to the sea surface and seafloor.

The linear bands extending diagonally from the bottom into the volume in Figure 4a also result from bottom sidelobe returns. We verified through computer simulations that their unique structure is a consequence of the uniform  $3^\circ$  spacing between the receive beams, and of the nonuniform sidelobe spacing within each receive beam pattern. The simulation results appear in Fig. 4b as dashed lines that match closely the underlying linear bands and represent the times and angles of each volume beam with a sidelobe directed at the bottom during the time of the bottom echo arrival. Minor differences probably result from uncertainties in the towfish's attitude estimates.

This sidelobe interference is somewhat enhanced by our choice of a resampled Dolph-Chebyshev amplitude shading window<sup>32</sup> designed to produce a nearly uniform sidelobe level between -28 dB and -30 dB for all the receive beam patterns. Lower sidelobe levels are achievable, but the corresponding increase in mainlobe beam width would overly degrade the spatial resolution in the images. Our conclusion from this analysis is that we could not process volume imagery at slant ranges beyond the average towfish altitude of 115m because boundary echo sidelobe interference dominated the volume acoustic backscatter beyond this range.

## IV. IMAGERY RESULTS AND INTERPRETATION

### A. Fish Schools

In this section, we use two- and three-dimensional (2D/3D) characterizations of near bottom fish schools derived from the TVSS data to demonstrate the potential advantages and limitations of multibeam sonars in fisheries acoustics. 2D characterizations of schooling<sup>6</sup>, diel migration<sup>54</sup>, seasonal migration<sup>5</sup>, and feeding<sup>55</sup> have been useful in understanding fish behavior, but as far as we know, the economic and scientific advantages of multibeam sonars for 3D characterization of fish schools have only been suggested<sup>56</sup> and not documented. Because fish distributions are heterogeneous, 3D analyses may provide important information about the structure and composition of aggregations not available in 2D studies.

We begin with volume acoustic backscattering strength images processed from the TVSS data and presented as vertical sections parallel and perpendicular to the towfish's track. Along-track sections (Fig. 6a,c) were formed by using a vertical echo-sounding procedure to extract backscatter data in the down-looking beams at each along-track sampling point. Across-track sections (Fig. 6b,d) were formed by using the same procedure as that used to create Fig. 3. The prominent backscatter features centered at ( $y=285\text{m}$ ,  $z=190\text{m}$ ) in Fig. 6a and ( $y=340\text{m}$ ,  $z=200\text{m}$ ) in Fig. 6b are attributed to schools of small pelagic fish, based on the nearly concurrent NMFS trawl data. Together, the orthogonal image pairs in Figs 6a,b and 6c,d characterize the size and scattering characteristics of the two fish schools (Table I). Although the images are limited by surface echo sidelobe interference and saturated samples, these artifacts were distinguished from biologic scatters by their arc-like across-track structure. Had we only constructed the along-track sections (Figs 6a,c), these samples might have been incorrectly attributed to the acoustic backscattered from individual fish.

We constructed a 3D shape representation of the school in Fig. 6a,c by processing multiple along-track sections ( $x,z$ ) over successive pings. Bottom detection processing<sup>15</sup> was used first to discriminate between acoustic backscatter from the seafloor and from the school. A threshold of 5dB over the ambient scattering strength level was applied to detect samples in the school, and their corresponding ( $x,y,z$ ) positions were determined using constant gradient ray tracing. The result (Fig. 7a) resembles a "stack" of elongated "tubes" extending across-track, with a few apparently suspended above the "stack". These features are a consequence of the TVSS sampling and resolution characteristics that are fundamental limitations for any sonar (cf. Misund *et al.* (1995)<sup>6</sup>). The resolution of each sample is defined by the spatial dimensions of the ensonified volume (eqns (21) and (22)), which are  $\Delta x = 9.9\text{m}$ ,  $\Delta y = 7.4\text{m}$ , and  $\Delta z = 0.28\text{m}$  at the school's center. Therefore, the elongated features in Fig. 6a are most likely returns from individual fish above the center of the school because ensonified volumes in adjacent beams overlap by 39.4%, and beams adjacent to those directed towards large scatterers or boundaries exhibit a significant sidelobe response.

Sidelobe response from the fish school appears in Fig. 6b as light blue samples at depths of 180-185 m, 40 m across-track on either side of center. These samples are about 5 dB greater than the ambient level and immediately precede the arc corresponding to the bottom echo sidelobe response.

To compensate for these artifacts and produce a shape characterization potentially more representative of the actual fish school, a  $3 \times 3 \times 3$ -sample moving average filter was applied to the scattering strength samples in and around the school. Filtered samples with scattering strengths greater than 5dB above the ambient scattering strength were retained, yielding an oblong volumetric shape that extends slightly diagonally to the across-track direction (Fig. 7b). The shape's maximum length is three times its maximum width and over seven times its maximum height (Table I). In this representation, the school appears to be concentrated near the bottom, which was generally flat with a mean depth of 193 m in this run. Although the thresholds and filter dimensions were subjectively chosen to produce a 3D map which best represented the acoustic data, the school shape is generally what is expected for small pelagic fish near the bottom during daytime.<sup>56</sup> However, this 3D representation has not been corrected for the relative motion between the school and the TVSS. If the school were moving, the actual shape of the school would be different from the apparent shape in Fig. 6b because different fish velocities could produce a variety of shapes.

With our limited data, we have no way of verifying the species of fish responsible for the enhanced volume acoustic backscatter seen in Fig. 6. However, three species representing 73% of the total catch between 150-200m in the NMFS trawls<sup>82</sup> could be considered candidates: the round herring (*Etrumeus teres*), the rough scad (*Trachurus lathami*), and the Gulf butterfish (*Peprilus burti*). The latter is the least likely candidate because it does not have a swimbladder for sizes greater than 75mm.<sup>51</sup> The rough scad is a good candidate because its maximum observed length was 75.8cm, and there was a tendency for the largest fish of most species to be found deeper than 150 m depth. Nonetheless, we favor the round herring (*E. teres*) as the most likely candidate because it was the most abundant species caught in the NMFS trawls near the TVSS experiment site and over all stations between 150-200m depths, with an average catch rate of 2341/hr for the entire GOM. Similar inferences were made by Nero *et al.* (2000)<sup>55</sup> in their detailed acoustic study of schooling fish about 3 nm southwest of the TVSS experiment site with a 38kHz echo-sounder in July 2000. They concluded that *E. teres* was responsible for the features in their acoustic backscatter data because of the tendency of this species to form compact schools near the bottom during the day, and ascend to the middle of the water column and disperse at night.

The school shapes in Fig. 6-7 are generally similar to those observed for Atlantic herring (*Clupea harengus*), which is in the same *Clupeidae* family as *E. teres*. Partridge *et al.* (1980)<sup>58</sup> observed herring schools in a laboratory tank to have roughly circular shapes, with horizontal dimensions 3-4 times greater than their vertical dimensions. Although the horizontal dimensions of the schools in Fig. 6 are roughly 3-9 times greater than the vertical dimensions, some exaggeration of the horizontal dimension is expected because the horizontal dimensions of the ensonified volumes ( $\Delta x, \Delta y$ ) in the school were about 30 times smaller than the vertical dimensions ( $\Delta z$ ). Misund *et al.* (1995)<sup>6</sup> observed that Atlantic herring in the North Sea most frequently form oval and square shapes, somewhat similar to Fig. 7b. Because herring school structure is relatively constant<sup>59</sup>, these observations lend support to our *E. teres* hypothesis. Unfortunately, a more substantial comparison is not possible because the environmental conditions in these two studies were very different from those at the TVSS experiment site, and because species-specific behavioral and physiological differences may have existed. Moreover, these studies had sample sizes much larger than the two schools in the TVSS data.

The acoustic characteristics of the schools in the TVSS data are also consistent

with our *E. teres* hypothesis. *E. teres* lengths recorded during the NMFS survey averaged 13.2 cm ( $L/\lambda=6$  at 68 kHz) and had a maximum of 51.2cm, corresponding respectively to mean and maximum target strengths of -42 dB and -31 dB according to Love's model (eqn (12)), or -49.5 dB and -37.5 dB using Foote's<sup>36</sup> empirical relation for clupeoids (herring and sprat) ( $TS = 20 \log_{10} L - 71.9$  dB). The mean and maximum target strengths of ensonified volumes within the two schools (Table I) span these model predictions, suggesting that they could be explained by approximately 1-10 fish in each volume cell. Hence, fish densities in both schools were approximately between 0.1 to 1/m<sup>3</sup>. This is a reasonable estimate, as average fish densities of  $O(0.1)$ - $O(10)/m^3$  have been observed in schools of a wide variety of species.<sup>6,29</sup> However, considerable uncertainty exists in such a density estimate because the maximum scattering and target strengths in the two schools (Table I) could be due to single, large fish, or relatively high fish densities. The single fish hypothesis is unlikely by itself because the maximum values in Table I exceed what could be predicted for the largest *E. teres* caught. This implies that high fish densities or several large fish are responsible for the maximum scattering levels reported in Table I.

As with all target strength measurements, the TVSS data are most likely affected by physiological and behavioral factors that limit comparisons with other data. Large variations in fish target strength arise from changes in the swimbladder's size that results from vertical migration. Clupeoids like *E. teres* are unable to regulate their swimbladder volume in a controlled manner under depth excursions<sup>36,24</sup>, so differences are expected when comparing measurements of fish from different depths. Similar variations in target strength occur when the swimbladder orientation changes. Of relevance to this study are Foote's (1985)<sup>25</sup> measurements for pollack (*Pollachius pollachius*), in which a 45° tilt from dorsal aspect caused 68.4kHz target strengths to drop by over 30dB. Individual tilt variations such as these could explain the differences between maximum and mean scattering strengths of the schools in Fig. 6 (Table I).

Two other behavioral aspects which affect both fish stock assessment and scientific studies are vessel and trawl avoidance. Trawl avoidance can lead to large errors during model verification. Stanton (1989)<sup>30</sup> estimated errors of 30dB due to trawl avoidance by fish. Vessel avoidance<sup>20</sup> can occur at ranges as far as 300m-500m<sup>6</sup> but is more apparent at close ranges and can lead to systematic downward biases in biomass estimates from ship mounted sonars. Even though these factors were not relevant to this experiment, the TVSS geometry is well-suited for assessing both vessel and towfish avoidance by fish. Consider the single ping from run 2 (Fig. 3). Even though the maximum volume backscattering strength of the wake from run 1 (labeled "OW") is only -55dB, it is easily distinguished from boundary and volume reverberation. Because the scattering strength from a fish shoal near the surface or school near the bottom would most likely exceed -55dB<sup>21</sup>, it would not be difficult to detect these features up to 500m from the TVSS if they were present.

## B. Volume Scattering Layers

We constructed two types of volume backscattering strength images from the TVSS data collected in the middle and upper water column, and both revealed distinct scattering layers most likely due to assemblages of epipelagic zooplankton in the upper thermocline and at the base of the mixed layer. The first type of these images (Fig. 8a) was formed by averaging 97 pings along the length of run 2 (Fig. 2). The figure also shows the sidelobe response of the surface echo for beams directed away from zenith, as well as the high backscattering near zenith due to resonant microbubbles in the towship's wake.<sup>13</sup> The second type of image consisted of vertical slices of volume acoustic backscattering strength formed along-track on each side of the TVSS by echo-integrating between 30 m and 130 m depth, and then averaging in 3-ping

intervals along-track (Fig. 9). As with the fish schools, historical data provide evidence that zooplankton is the primary cause for the scattering layers, particularly the previously cited studies which showed that zooplankton distributions in the GOM are centered near the mixed layer depth<sup>47</sup> and upper 50m of the water column.<sup>44</sup>

The results of other studies using single-frequency sonars near 68kHz provide more clues to the types of scatterers in the layers. Pluddemann and Pinkel (1989)<sup>34</sup> observed the diel migration of scattering layers in the eastern North Pacific using a 67kHz Doppler sonar, and used Johnson's fluid sphere model to reason that the majority of scattering in their data was due to organisms with equivalent spherical radii  $0.1\text{cm} \leq a_{\text{esr}} \leq 0.4\text{cm}$ , and lengths  $0.5\text{cm} \leq L \leq 2.0\text{cm}$ , which includes micronekton and large zooplankton such as decapod shrimp and euphasiids. However, their reasoning assumed that the animals were well described by the fluid sphere model because they also lacked coincident *in situ* data. The 70kHz results of Stanton *et al.* (1989)<sup>30</sup> are more insightful because they collected mid water trawl samples and compared them to their acoustic data. The peak scattering strengths in their data were 1-5 dB lower than those observed during the TVSS experiment (Table II) and were associated with fish or a large number of arthropods, which include euphasiids and shrimp. Their scattering strength predictions based on Love's (1971)<sup>35</sup> model for fish and Johnson's (1977)<sup>22</sup> model for arthropods and were within 5 dB of those measured acoustically, indicating that the Pluddemann and Pinkel's length estimates were probably valid for their experiment, hence for the TVSS data.

Two scenarios are equally likely for the TVSS data in Figs 8-9. In any case, we assume, as in Stanton *et al.* (1987)<sup>30</sup>, that scattering from animals less than 1cm in length is negligible, even though copepod densities greater than 500/m<sup>3</sup> have been observed near the TVSS experiment site<sup>48,62</sup>. Such an assumption is most likely valid because, for example, the target strength of a 4 mm *Calanus* copepod at 68 kHz is -110 dB.<sup>22</sup> The first is that the scattering layers are composed of mixed assemblages of zooplankton and small fish, similar to those observed by Stanton *et al.* (1989).<sup>30</sup> This might explain why the maximum observed scattering strengths in our study are close to theirs. Likewise, Zimmerman and Biggs (1999)<sup>45</sup> attributed anomalously high backscatter measurements to variable numbers of micronekton in the central Gulf of Mexico. According to eqns (5) and (14), the target strength of a preserved 2 cm euphasiid is -86 dB (using  $g=1.016$  and  $h=1.033$  from Greenlaw (1977)<sup>39</sup>), whereas the target strength of a non-swimbladder fish of the same size is -57 dB according to eqn (12) with Love's (1977)<sup>26</sup> regression coefficients for side aspect. Even though preservation tends to decrease the target strength of euphasiids by about 8 dB<sup>30</sup>, it is apparent that a small number of small fish can still produce the backscattering strength of a large number of zooplankton, which means that a mixed assemblage of zooplankton and small fish could explain the average scattering layer scattering strengths in Fig. 8-9 and Table II.

The other possibility is that the scatterers consist exclusively of large zooplankton, mostly euphasiids. This also could explain their vertical distribution and scattering levels. Most euphasiids undergo a diel migration to the surface at night, then back to an intermediate depth at dawn, and their daytime distribution has been related to specific light levels.<sup>60</sup> The average depth of the euphotic zone in the GOM is 75m<sup>61</sup>, which is approximately the lower bound of scattering layer depths in Figs 8-9. The density of euphasiids required to produce the scattering strengths in the layers (Table II) can be estimated from eqns (14) and (4) with the values for  $g$ ,  $h$ , and  $a_{\text{esr}}$  corresponding to the species present. Euphasiid species found by Hopkins *et al.* (1981)<sup>46</sup> in the upper 100m of the water column in the shallow (<200m depth) eastern Gulf of Mexico included *Euphasia tenera*, *Nematoscelis microps/atlantica*, and *Stychocheiron carinatum*. To the best of our knowledge, fluid sphere model parameters have not been measured for these species, so we assume for simplicity that the  $g$

and  $h$  values for the species present are similar to those of the well documented euphasiid *Euphasia Pacifica*.<sup>39,22,60</sup> In this case, the target strength of 2 cm euphasiid would be about -78 dB, and if the scattering layers were composed entirely of these types of organisms, their densities would be 12-80/m<sup>3</sup>. These are realistic values in view of previous observations of euphasiids in sound scattering layers (cf. references (63),(64), and (12)).

The foregoing discussion is meant to show that, in the absence of net and trawl data, the scattering layers in the TVSS imagery are due to some assemblage of zooplankton and possibly micronekton. Even when net tow and trawl samples are available, estimation of zooplankton size distribution, species composition, overall abundance, and density is extremely difficult because scattering models cannot account for every species present, and therefore must approximate the total acoustic backscatter from an assemblage of organisms by grouping them into similar classes.<sup>41</sup> Errors arise because many permutations of taxonomic group densities can create a given level of backscatter<sup>30</sup>. Moreover, relating observed acoustic backscatter to *in-situ* data depends on the sampling efficiency of the net or trawl, which may be strongly variable between different types of equipment.<sup>42</sup> For example, euphasiids have been observed to swim at speeds of 2-41cm/s<sup>19</sup>, and net avoidance is commonly found to produce downward biases in sampled zooplankton densities.<sup>9,12</sup>

One of the largest sources of error in biomass estimates of oceanic zooplankton is their fine-scale patchiness (i.e. spatial variability on scale of 1m-1km)<sup>65</sup>, so we examined this aspect of the scattering layers in the TVSS data. Most studies of zooplankton patchiness have relied on one-dimensional variance spectra<sup>66</sup> or patch-finding methods, where "patch" is defined by some arbitrary criteria.<sup>67</sup> Wiebe's definition of a patch<sup>68</sup> as "a concentration of individuals exceeding the central value in the data set" implies that patch sizes vary with the length scales covered by the data set, the "window" of samples over which the patch is determined, and the threshold concentration beyond which a patch is defined. Nero and Magnuson (1989)<sup>67</sup> used two-dimensional acoustic transect data of the Gulf Stream to illustrate the dependencies of patch size and internal patch characteristics on threshold values and window size. With knowledge of the water mass boundaries and characteristics in their data set, they were able to determine the thresholds and window sizes which produced patches that best represented the finescale features of interest. The limited coverage and *in-situ* data in our experiment prevented us from using their approach without a large degree of subjectivity, so we characterized the patchiness of the scattering layer data by estimating the 2D variance spectra from the volume scattering coefficients corresponding to the six  $S_V$  images in Fig. 9 (see Appendix). The average of the six spectra is displayed in Fig. 10. In addition, horizontal variance spectra were averaged over all vertical spatial frequencies separately for each run to produce Fig. 11a. Likewise, vertical variance spectra averaged over horizontal spatial frequencies are represented in Fig. 11b. Their respective averages are displayed in Figs 11c-d.

The average 2D variance spectrum (Fig. 10) reveals the dominant scales of variability in the TVSS scattering layer data. Vertical variability is distributed over a relatively wide portion of the available range of spatial frequencies, with corresponding length scales of 8-33 m. These values are close to the scattering layer thicknesses in Figs 8-9. Horizontal variability is confined to a relatively narrow portion of the range of available spatial frequencies, with corresponding length scales of 30-100 m. These values are consistent with other upper water column observations of zooplankton patch lengths (cf. references (68)-(70)). The two dominant peaks in the region near the horizontal spatial frequency ( $\mu$ ) of 0.02 m<sup>-1</sup> and between the vertical spatial frequencies ( $\nu$ ) of 0.03 and 0.09 m<sup>-1</sup> may indicate a coupling between the vertical and horizontal variability at the dominant horizontal scale of 50m. Greenlaw and Pearcy (1985)<sup>71</sup> suggested that such a phenomenon affected the distributions of 20kHz

biologic scatterers off Oregon, but they based their hypothesis on separate one-dimensional vertical and horizontal variance spectra. The two-dimensional spectra in Fig. 10 provides strong evidence for this type of coupling in the TVSS scattering layer data.

The average spectra for each run (Fig. 11) show that the patterns in the individual images are similar, but the magnitudes vary with mean scattering strengths. The spectral levels from imagery on the left side of the TVSS always exceeds their counterparts on the right side because a hydrophone on the right side of the TVSS failed during the experiment, yielding a decreased gain on the right side of the array. The spectral levels for run 2 were half an order of magnitude lower than those for runs 1 and 3, suggesting that a larger scale of variability might exist which could not be resolved by the spectra in each run. These differences are most likely due to patches longer than 1 km because the 3 parallel runs were roughly 3.6 km long and spaced 200 m apart (Fig. 2), and coarse scale ( $O(1-100\text{km})$ ) horizontal patchiness of zooplankton is common.<sup>16,65,67,69</sup>

The slopes of the average spectra (Fig. 11) provide clues to the physical processes affecting the scattering layers. Both the vertical and horizontal spectra are "red", with one order of magnitude separating the spectral levels for the lowest and highest spatial frequencies. The negative slopes of all spectra are consistent with the general expectation that the largest changes in volume backscatter (or biomass) tend to occur on the largest spatial scales.<sup>9,71</sup> A convenient reference is the  $-5/3$  slope of the log-log plot of the power spectrum of velocity fluctuations in a turbulent flow field, over a range of length scales between turbulent generation and dissipation (the inertial subrange). Quantities following a  $-5/3$  spectral slope are likely to be controlled by turbulent mixing processes, and even though this assumes homogeneity and spatial isotropy, it has been demonstrated for temperature and chlorophyll.<sup>33</sup> All spectral slopes in Fig. 11 are much larger than  $-5/3$ . The average horizontal variance spectrum across all vertical spatial frequencies (Fig. 11a) exhibits a slope of  $-1$  on a log-log scale, whereas the slope of the average vertical variance spectrum is approximately  $-2/3$ . These observations may indicate that factors other than or in addition to turbulent mixing are controlling the spatial variability of the scattering layers. This is not unlikely because the surface currents and winds during the TVSS experiment were relatively weak, and turbulent mixing was most likely limited to the upper 10m of the water column in the region near the towship's wake<sup>13</sup> (Fig. 8a).

We hypothesize that vertical stability was the strongest physical factor affecting the spatial variability in the scattering layers. The density profile during the TVSS experiment indicated that the upper water column was vertically stable. Potential vertical stability can be represented by the Richardson number  $Ri$  (ratio of buoyancy to vertical shearing force). Legendre and Demers (1984)<sup>65</sup> present data from the St. Lawrence Estuary for which the horizontal variance spectral slope of  $Ri$  is greater than the  $-5/3$  slope for temperature. Their conclusion that an active hydrodynamic property like  $Ri$  may be more appropriate for assessing the hydrodynamic control of phytoplankton, may also apply to the TVSS scattering layer data. Stable conditions would result in a relatively strong thermocline, which then would act as a barrier to downward and upward vertical migrations, thereby concentrating aggregations of similar species. Observations of this phenomenon may be found in Nash *et al.* (1989) for the Gulf Stream, and may be inferred from the close association between thermal microstructure and scattering layer structure in the results described by Holliday and Pieper (1980).<sup>10</sup> Ortner *et al.*'s (1984)<sup>47</sup> observations in the eastern central GOM support these ideas as well. They found the centroid of zooplankton biomass to descend with the mixed layer depth from 10m depth to 85m depth after the passage of an atmospheric front.

Another observation in Ortner *et al.* (1984)<sup>47</sup> was that the vertical distribution of



zooplankton became decoupled from the phytoplankton distributions, suggesting that physical, rather than biological factors controlled their spatial variability during frontal passage. We avoid such a statement regarding the TVSS data because fine-scale zooplankton patches are typically multi-species aggregations, hence they also are influenced by biological factors such as grazing, predation, social interaction, and reproductive behaviors. These species-level interactions may partially explain why the average spectral slopes (Fig. 11) are larger than  $-5/3$ . In the eastern central GOM, Hopkins (1982)<sup>44</sup> reported that the vertical distribution of zooplankton coincided directly with the depth of maximum primary production near 50 m, which is roughly in the range of depths of maximum  $S_V$  in the TVSS data (Table II). A common conclusion in most studies of zooplankton distribution is that they are controlled by some combination of physical and biological factors, and it is usually not possible to unambiguously identify the relative roles of each.<sup>65</sup> Therefore, it is most likely that the horizontal and vertical patchiness of zooplankton at the TVSS experiment site were influenced by both the spatial distribution of phytoplankton and the mixed layer depth.

Despite the limitations of boundary sidelobe interference, we contend that the multibeam geometry of the TVSS provides a bioacoustic remote sensing capability superior to that of the conventional single beam echo-sounder. Because distributions of marine organisms vary in four dimensions ( $x, y, z, t$ ), they can be sampled more completely by a multibeam sonar system that provides quasi-synoptic coverage through simultaneous horizontal and vertical soundings. Multibeam systems such as the TVSS also are perfectly suited for three-dimensional visualizations of biological scattering fields, such as those presented in Green *et al.* (1998).<sup>17</sup> These possess enormous qualitative and quantitative value, and could easily be processed from images like those in Fig. 8 with their 2D-point-kriging/3D-gridding techniques to produce 3D scattering strength visualizations. With this type of process, the TVSS could be used for a variety of bioacoustic applications which have been mostly studied with single beam systems. TVSS data collected over the same track at various intervals (hours, days, weeks) could be used to characterize the 4D spatio-temporal dynamics of diel migration, interaction with dynamic features, and seasonal migration. In the future, we envision merging the multibeam geometry with a multi-frequency or broadband capability to provide information regarding the 4D dynamics of species interactions and community structure that is presently unobtainable.

### C. Mean Volume Reverberation

High frequency acoustical scattering from zooplankton is important in non-bioacoustic applications because it can be a significant component of the total volume reverberation level. To quantify this for the TVSS experiment site, we used eqn (10) to compute reverberation levels in each beam angle ( $RL(\theta)$ ) and averaged them over all pings and samples prior to the first echo from the towship's wake. Pings which suffered from saturation in the DAS electronics were not used in computing the averages, so the number of pings used to average  $RL(\theta)$  was less than 100 in each run. The average reverberation levels ( $\overline{RL}(\theta)$ ) for the three TVSS runs (Fig. 12) exhibit a similar angular dependence where reverberation levels in the beams directed towards the surface exceed those in beams directed towards the bottom by over 10dB (Table III). Comparison between the image in Fig. 8 and the plots in Fig. 12 indicates that the scattering layers between 40-80 m depth, directly above the TVSS, are the primary cause for the vertical directionality of the mean volume reverberation levels, as well as the relative peaks near  $\theta = \pm 70^\circ$  in each run. The smaller peaks and nulls in  $\overline{RL}(\theta)$  correspond to peaks and nulls in the transmit pattern.

Fig. 12 directly quantifies the angular dependent noise floor for non-bioacoustic applications with the TVSS data set. It also emphasizes that detection near the surface

will be more difficult than near the bottom. Although we can expect similar results in many shallow water environments, the shape of  $RL(\theta)$  will vary with changes in scattering layer depths and thicknesses, as well as the sonar's depth, beam pattern, source level, and receiver characteristics. This information is important in Naval applications (target detection) as well as acoustic studies of the sea surface, seafloor, air-sea interaction, and mixing processes. A potential application of the TVSS in a passive mode would be to image the ambient noise field of the sea surface to determine the spatial characteristics of breaking waves and the time variability of the sea surface wave spectrum.<sup>72</sup>

#### D. Environmental Sources of Uncertainty

All bioacoustic studies are limited to some degree by biological, system-related, and/or environmental uncertainties. We have previously discussed some of the biological and system related sources of uncertainty, so here we assess those relating to the physical environment. By discussing how the ambiguities resulting from these factors were identified and partially resolved, we intend to illustrate the strengths and weaknesses of multibeam systems in bioacoustic applications.

The most significant environmental source of uncertainty was the boundary echo sidelobe interference illustrated in Figs 3 and 5. The scattering layer data (Table II) were not affected because we limited the slant range coverage of Fig. 9 to distances shorter than the first echo from the towship's wake. Although the fish school  $S_V$  and TS data (Table I) were obtained after the wake and surface echo, analysis of the scattering strength time series in beams directed towards the fish schools showed that the upward bias in the fish school TS and  $S_V$  due to surface reverberation was no greater than 0.5dB. This was fortunate, because the fish school echoes would have been significantly biased if they were closer to the TVSS or if the TVSS were towed at a greater depth, particularly if they were received at the same time as the surface echo. This illustrates that, in any shallow water multibeam application, the extent to which the data are limited by boundary echo sidelobe interference depends on the experimental geometry.

There was some uncertainty regarding the sound speed used in this study because only one CTD cast was obtained about 100m north of the location for run 1 (Fig. 1b), approximately 4.5 hours prior to the acoustic data collection. Any spatial variability in the local sound speed environment would have produced distortions in the processed imagery, hence errors in the scattering layer depth and thickness estimates (Table II), and fish school shape representation (Fig. 7). To evaluate the presence and effects of variability in the local sound speed environment, we processed seafloor bathymetry<sup>15</sup> and sea surface relief maps<sup>13</sup> and compared them to known environmental data. If the sound speed profile were not representative of the local sound speed environment, ray-bending would produce errors in the echo arrival angles, causing the sea surface relief maps and bathymetry to "curl" upward or downward in a symmetric manner about the track's centerline. Because the processed bathymetry were consistent with that previously obtained during bathymetric surveys performed by the Naval Oceanographic Office, and the relatively flat sea surface relief maps were consistent with the calm conditions observed during the experiment, we deemed sound speed errors negligible. The TVSS' capability of assessing the local sound speed variability with only a single sound speed profile is a distinct advantage in bioacoustic remote sensing applications, because such variability can distort target range, location, and shape, especially for lower frequencies.

Conditions near the seafloor that may adversely affect the the acoustic backscatter from near-bottom fish include seafloor relief, vegetation, and suspended sediment, but none was seen to influence our results. Drastic seafloor relief can act to shadow the

pulse from ship-mounted echo-sounder<sup>73</sup>, especially in deeper waters. As shown in Fig. 6, this factor was irrelevant because the seafloor in the region was relatively flat. In shallow waters, aquatic vegetation can strongly scatter high frequency sound and potentially be mistaken for schooling fish.<sup>74</sup> Such scattering was not possible in our data because the seagrasses capable of strongly scattering sound in the Northeastern GOM are limited to depths shallower than 30m.<sup>61</sup> Acoustic backscatter from suspended sediment may sometimes be mistaken for biologic scatterers, but was extremely unlikely in the TVSS data for several reasons. First, the bottom currents expected over the Florida shelf in the winter<sup>50</sup> were most likely less than the 20-50cm/s erosional velocity<sup>75</sup> required to lift the fine grained sediments sampled in the region.<sup>15</sup> In addition, suspended sediment clouds over a flat bottom would not have a compact structure, as that of the fish schools in Fig. 6, rather a more layered or diffuse structure. Lastly, the scattering strengths expected from sediments at the site would have been much less than those in Table I. This can be illustrated by a comparison with results in Wiebe *et al.* (1997)<sup>16</sup>, who observed scattering strengths near -53dB due to suspended sediment concentrations estimated to be in the low millions per cubic meter. The grain diameter estimated in their paper (0.20mm) were much larger than the bulk grain diameters at the TVSS experiment site (0.012mm). The numerical density of sediment grains of this size required to produce the scattering strengths in Table would be unrealistic.

In the both the fish and zooplankton  $S_V$  and TS estimates, errors due to multiple scattering and extinction also were deemed negligible. Multiple scattering occurs when acoustic energy from the incident wave is retained for a time within the group of scatterers by repeated scattering between them. Extinction is the excess attenuation of sound through the group of scatterers. These effects can occur in fish schools at densities of 50/m<sup>3</sup> and greater.<sup>30</sup> It is not known if these effects have been observed in zooplankton aggregations, but Foote (1990)<sup>76</sup> has suggested the possibility for dense swarms of macrozooplankton. The estimated zooplankton densities in the TVSS data (Figs 6,7; Table II) were not large enough to produce multiple scattering or extinction effects. To evaluate the effects of extinction through the fish schools, we compared the mean normal incidence bottom backscattering strength over runs 1 and 2 to the instantaneous bottom backscattering strength values below the fish schools. Values below the school were less than a standard deviation from the mean values, demonstrating that extinction was insignificant (Table I). In a similar manner, multiple scattering was ruled out by analyzing the backscatter imagery under the schools. Multiple scattering returns would be evident as a "tail" below each school and "under" the bottom (cf. Fig. 4 in Stanton (1984)<sup>77</sup> and Fig. 7 in MacLennan (1990)<sup>24</sup>). Even though the bottom echo saturated the return below the schools, adjusting the dynamic range (not shown) showed that multiple scattering returns were not present. This is consistent with Stanton's (1983,1984)<sup>34,77</sup> calculations, which showed that multiple scattering is significant only when excess attenuation is significant.

For the TVSS scattering layer data, a potential source of error is acoustic scattering from turbulent microstructure. At high frequencies, such scattering may exceed that due to zooplankton, and arises from turbulence-induced gradients in the acoustic index of refraction, which are mostly due to temperature.<sup>78</sup> We considered two potential sources for this type of error and rejected both. The first was turbulent scattering in the towship's wake,<sup>13</sup> which was found to be negligible compared to that from resonant microbubbles<sup>13</sup>, and irrelevant in any case because we excluded samples near the wake from our scattering layer imagery. The second potential source of turbulent scattering is internal wave breaking at the boundary between the mixed layer and upper thermocline (Fig. 8b). The TVSS was towed 33m below this boundary, and if internal wave breaking occurred, the turbulence-induced scattering could be comparable to those in Figs 8 and 9. An excellent example of this is found in Wiebe *et al.*

(1997).<sup>16</sup> We ruled out this mechanism because the TVSS maintained a near-constant depth below the sea surface, which was verified by vertical volume imagery of the sea surface.<sup>13</sup> If internal waves were present, they would have produced depth fluctuation in the towfish, which was negatively buoyant and weighted by the tow cable to maintain a constant depth.

Scattering and attenuation from resonant microbubbles are more common sources of uncertainty near the sea surface. They can be formed by breaking waves, propeller cavitation, and even zooplankton and fish.<sup>32,13</sup> As with boundary reverberation, they can produce upward biases in TS and  $S_v$  estimates when they are undetected. At the TVSS's acoustic frequency of 68kHz, resonant scattering comes from bubbles with radii equal to 48 $\mu$ m, and the target strength of just one of these bubbles will be -66dB. For down-looking sonars near the surface, attenuation through the bubble layer will decrease the backscattered energy.<sup>79</sup> We assessed these effects to be negligible in this study because we used the acoustic backscatter imagery to delineate regions where acceptable data could be taken. The vertical volume images in Fig. 8 and reference (13) were used to define maximum bubble depth of the wake, which then established the maximum usable slant range for both the scattering layer imagery and mean volume reverberation calculations. We also used horizontal volume imagery to distinguish near-surface bubble clouds from schooling fish.<sup>13</sup> Large scale bubble clouds were observed at 3m depth 50-100m to either side of the ship track, with mean volume scattering strengths of -35dB, suggesting that they might be due to dense schools of large fish. Comparison between the near-surface horizontal imagery and other acoustic observations of ship wakes showed them to be bubble clouds generated by the towship's breaking bow waves, so they were not investigated with the other fish school data.

Ambient noise was a final source of uncertainty suggested by the similarity between the vertical directionality in mean volume reverberation levels (Fig. 12) and that observed for high frequency ambient noise.<sup>80</sup> However, for biologic, surface, and ship generated ambient noise sources, the contributions were evaluated as insignificant. Biologic sources known to generate sound around 68 kHz include several species of dolphin and porpoise, and snapping shrimp.<sup>81</sup> Although both are found in the Gulf of Mexico, acoustic backscatter from large scatterers like dolphin and porpoise were not observed in any of the volume and near-surface imagery, and snapping shrimp are not likely in water depths deeper than 60m.<sup>81</sup> Because the sea state was only 1.5, surface generated noise contributions were probably less than 30 dB *re* 1 $\mu$  Pa. Even in the towship's wake, where bubble oscillations could generate ambient noise at 68kHz<sup>14</sup>, the contribution would have been small relative to the mean volume reverberation levels (Fig. 12). Propeller cavitation, as evidenced by the dense bubble clouds in the towship's wake (Fig. 8a) would have dominated the towship-generated noise sources, but the contribution would also have been insignificant. After a careful review of cavitation noise data at frequencies near 68 kHz for ships with characteristics similar to the TVSS towship's<sup>82</sup> (e.g. Fig. 10.15 in Urick (1983)<sup>31</sup>) we estimate the cavitation noise level during the TVSS experiment to have been 90-100 dB *re* 1  $\mu$ Pa @1m, and even less at the TVSS due to spherical spreading and absorption losses. Had the TVSS operated at a lower frequency, and closer to the towship, the cavitation noise levels may have been significant.

## V. SUMMARY AND CONCLUSIONS

In this study, we have used the data collected by the TVSS to demonstrate the advantages and limitations of multibeam sonars in bioacoustic applications. TVSS imagery showed that the most significant limitation was boundary echo sidelobe

interference, which prevented zooplankton remote sensing in the volume beyond the range of the first boundary echo, and near-bottom fish detection beyond the range of the first bottom echo. The 3D representation of a near bottom fish school demonstrated the fundamental limitation of sonar resolution inherent in both multibeam and single beam characterizations of scattering fields. Angular variation in the transmit array beam pattern also contributed to uncertainties in the TVSS data.

Despite these limitations, the TVSS still provided more coverage than that possible with a single beam sonar, and we used this advantage to characterize the 3D acoustic structure of near-bottom schooling fish and zooplankton scattering layers in a shallow water region of the Northeastern Gulf of Mexico. Supporting previous studies in the region, the TVSS scattering layer imagery indicated that the vertical distribution of zooplankton is closely associated with the mixed layer depth. The TVSS geometry also provided the unique capability to characterize the angular dependence of volume reverberation in multiple narrow beams, which was then shown to result from bioacoustic scattering layers when compared to concurrent volume scattering strength imagery. In the future, modifications of the transmit array beam pattern or ping repetition cycle could reduce the effects of boundary reverberation and increase the potential for toroidal sonars in bioacoustic remote sensing applications.

## ACKNOWLEDGMENTS

This work was funded by the Office of Naval Research under ONR-NRL Contract No. N00014-96-1-G913. The authors would like to thank CAPT Tim Schnoor, USN (ONR), Sam Tooma, and Maria Kalcic (NRL) for their support; Candy Robertson and Lisa Tubridy (CSS) for information on the TVSS; and Pat Jordan (MPL) for administrative support. Chris Gledhill (NMFS) and Jason Link (NMFS) are thanked for providing the NMFS Small Pelagics Report.<sup>43</sup> Thanks are due to Jo Griffith (MPL) for help with the figures.

## APPENDIX. TWO-DIMENSIONAL VARIANCE SPECTRUM

The two-dimensional variance spectrum in Fig. 10 is calculated from the back-scattering coefficients ( $s_v$ ) corresponding to each image in Fig. 9 by first resampling vertically to 1.4m depth intervals. Because the sidescanning procedure resulted in nonuniform sample spacing which decreases away from normal incidence, the majority of the samples have spacing smaller than 1.4m, so they were subsampled. A few samples near normal incidence ( $z=78m$ ) are spaced 2.5m apart, so these were interpolated to 1.4m spacing. The average horizontal sample spacing in each image is 4.1m. The resulting  $M \times N$  image, denoted  $s_v(m,n)$ , is demeaned according to:

$$s'_v(m,n) = s_v(m,n) - (1/MN) \sum_{m=1}^M \sum_{n=1}^N s_v(m,n) \quad (m^{-1}) \quad (A1)$$

The two-dimensional discrete Fourier transform of  $s'_v(m,n)$  is computed as<sup>83</sup>

$$F_v(p,q) = (1/MN) \sum_{m=1}^M \sum_{n=1}^N s'_v(m,n) e^{-i2\pi(p(m-1)/M + q(n-1)/N)} \quad (A2)$$

where  $p$  and  $q$  are vertical and horizontal spatial frequency indices, respectively. The variance spectrum is then:

$$V_V(p,q) = (1/MN) |F_V(p,q)|^2 \quad (m^{-2}) \quad (A3)$$

Thus, the variance spectrum is simply the two-dimensional power spectrum of the demeaned image. Fig. 10 is the result of averaging the six spectra corresponding to Fig. 9.

The relationship between the indices  $p$  and  $q$  and their corresponding spatial frequencies  $\mu$  and  $\nu$  is:

$$\begin{aligned} \nu &= (1/dz) (p - M/2)/M \\ \mu &= (1/dy) (q - N/2)/N \end{aligned} \quad (A4)$$

where  $dz$  and  $dy$  are the vertical and horizontal sampling intervals, respectively. The maximum and minimum positive resolvable spatial frequencies are given by:

$$\begin{aligned} \nu_{\max} &= 1/(2dz) & \mu_{\max} &= 1/(2dy) \\ \nu_{\min} &= 2/(Mdz) & \mu_{\min} &= 2/(Ndy) \end{aligned} \quad (A5)$$

If the total depth and along-track distance spanned by each image in Fig. 9 are denoted  $Z$  and  $Y$ , then the minimum resolvable spatial frequencies are also given by:

$$\nu_{\min} = 2/Z, \quad \mu_{\min} = 2/Y \quad (A6)$$

Thus, for Figs 9 and 10,  $dz=1.4m$ ,  $dy=4.1m$ ,  $Z=100m$ , and  $Y=410m$ , so that:

$$\begin{aligned} \nu_{\max} &= 0.35m^{-1} & \mu_{\max} &= 0.12m^{-1} \\ \nu_{\min} &= 0.02m^{-1} & \mu_{\min} &= 0.005m^{-1} \end{aligned} \quad (A7)$$

The total sample variance in the backscattering coefficients  $s_V(m,n)$  corresponding to each image in Fig. 9 is given by<sup>84</sup>

$$(1/MN) \sum_{m=1}^M \sum_{n=1}^N |s'_V(m,n)|^2, \quad (A8)$$

which can be related to the variance spectrum by applying Parseval's theorem generalized for the two-dimensional Fourier Transform to eqn (A2):

$$(1/MN)^2 \sum_{p=1}^M \sum_{q=1}^N |F_V(p,q)|^2 = (1/MN) \sum_{m=1}^M \sum_{n=1}^N |s'_V(m,n)|^2 \quad (A9)$$

Substituting (A3) into (A9) yields:

$$(1/MN) \sum_{p=1}^M \sum_{q=1}^N V_V(p,q) = (1/MN) \sum_{m=1}^M \sum_{n=1}^N |s'_V(m,n)|^2, \quad (A10)$$

which shows that the average value of the variance spectrum is equal to the total sample variance in the original data.

## REFERENCES

1. T.C. Gallaudet, C.P. de Moustier, and M. Kalcic, "Imaging the ocean boundaries and volume with the Toroidal Volume Search Sonar (TVSS)," in *Proceedings of the Fourth Annual Symposium on the Mine Problem*, March 13-16, 2000, Monterey, CA (2000).
2. G. Rose., "Acoustics in fisheries in the 21st century," *J. Acoust. Soc. Am.*, **108**, 2457 (2000).
3. C.F. Eyring, R.J. Christensen, and R.W. Raitt, "Reverberation in the sea," *J. Acoust. Soc. Am.*, **20**, 462-475 (1948).

4. M.V. Trevorrow, "Multifrequency acoustic investigations of juvenile and adult fish in Lake Biwa, Japan," *J. Acoust. Soc. Am.*, **100**, 3042-3052 (1996).
5. B. Pedersen, and M. Trevorrow, "Continuous monitoring of fish in a shallow channel with a fixed horizontal sonar," *J. Acoust. Soc. Am.*, **105**, 3126-3135 (1999).
6. O.A. Misund, A. Aglen, and E. Fronaes, "Mapping the shape, size, and density of fish-schools by echo-integration and a high resolution sonar," *ICES J. Mar. Sci.*, **52**, 11-20 (1995).
7. T.W. Steig, and S.V. Johnston, "Monitoring fish movement patterns in a reservoir using horizontally scanning split-beam techniques," *ICES J. Mar. Sci.*, **53**, 435-441 (1996).
8. D.M. Farmer, M. V. Trevorrow, and B. Pedersen, "Intermediate range fish detection with a 12kHz sidescan sonar," *J. Acoust. Soc. Am.*, **105**, 2481-2490 (1999).
9. P. Greenblatt, "Distributions of volume scattering observed with an 87.5kHz sonar," *J. Acoust. Soc. Am.*, **71**, 879-885 (1982).
10. D.V. Holliday, and R.E. Pieper, "Volume scattering strengths and zooplankton distributions at acoustic frequencies between 0.5 and 3 MHz," *J. Acoust. Soc. Am.*, **67**, 135-146 (1980).
11. D.V. Holliday, and R.E. Pieper, "Bioacoustical oceanography at high frequencies," *ICES J. Mar. Sci.*, **52**, 279-296 (1995).
12. N.A. Cochrane, D. Sameoto, A.W. Herman, and J. Neilson, "Multiple-frequency acoustic backscattering and zooplankton aggregations in the inner scotian shelf basins," *Can. J. Fish. Aquat. Sci.*, **48**, 340-355 (1991).
13. T.C. Gallaudet, and C.P. de Moustier, C.P., "Sea surface and volume back-scattering strength measurements in the microbubble field of a ship's wake," *J. Acoust. Soc. Am.*, submitted (2001).
14. P.A. Crowther, "Bubble noise creation mechanisms," in *Sea Surface Sound*, edited by B.R. Kerman (Boston: Kluwer), 131-150 (1988).
15. T.C. Gallaudet, and C.P. de Moustier, "Using environmental information to estimate and correct for errors in bathymetry and seafloor acoustic imagery," *IEEE J. Ocean. Eng.*, submitted (2001).
16. P.H. Wiebe, T.K. Stanton, M.C. Benfield, D.G. Mountain, and C. H. Greene, "High-frequency acoustic volume backscattering in the Georges Bank coastal region and its interpretation using scattering models," *IEEE J. Oceanic Eng.*, **22**, 445-464 (1997).
17. C.H. Greene, P.H. Wiebe, C. Pelkie, M. C. Benfield, and J.M. Popp, "Three-dimensional acoustic visualization of zooplankton patchiness," *Deep-Sea Res. Part II*, **45**, 1201-1217 (1998).
18. L.V.M. Traykovski, T.K. Stanton, P.H. Wiebe, and J.F. Lynch, "Model-based covariance mean variance classification techniques: Algorithm development and application to the acoustic classification of zooplankton," *IEEE J. Ocean. Eng.*, **23**, 344-364 (1998).
19. D. McGehee, and J.S. Jaffe, "Three-dimensional swimming behaviour of individual zooplankters: observations using the acoustical imaging system FishTV," *ICES J. Mar. Sci.*, **53**, 363-369 (1996).
20. M. Soria, P. Freon, and F. Gerlotto, "Analysis of vessel influence on spatial behaviour of fish schools using multi-beam sonar and consequences for biomass estimates by echo-sounder," *ICES J. Mar. Sci.*, **53**, 453-458 (1996).
21. O. Misund, A. Aglen, J. Hamre, E. Ona, I. Rottingen, D. Skagen, and J. Valdemarsen, "Improved mapping of schooling fish near the surface: comparison of abundance estimates obtained by sonar and echo integration," *ICES J. Mar. Sci.*, **53**, 383-388 (1996).

22. R.K. Johnson, "Sound scattering from a fluid sphere revisited," *J. Acoust. Soc. Am.*, **61**, 375-377 (1977).
23. R. Love, "Resonant acoustic scattering by swimbladder-bearing fish," *J. Acoust. Soc. Am.*, **64**, 571-580 (1978).
24. D.N. MacLennan, "Acoustical measurement of fish abundance," *J. Acoust. Soc. Am.*, **87**, 1-16 (1990).
25. K.G. Foote, "Rather-high-frequency sound scattering by swimbladdered fish," *J. Acoust. Soc. Am.*, **78**, 688-700 (1985).
26. R. Love, "Target strength of an individual fish at any aspect," *J. Acoust. Soc. Am.*, **62**, 1397-1403 (1977).
27. T.K. Stanton, D.Z. Chu, and P.H. Wiebe, "Sound scattering by several zooplankton groups. II. Scattering models," *J. Acoust. Soc. Am.*, **103**, 236-253 (1998).
28. T.K. Stanton, "Volume scattering: Echo peak PDF," *J. Acoust. Soc. Am.*, **77**, 1358-1366 (1985).
29. M.L. Peterson, C.S. Clay, and S.B. Brandt, "Acoustic estimates of fish density and scattering function," *J. Acoust. Soc. Am.*, **60**, 618-622 (1976).
30. T.K. Stanton, R.D. Nash, R.L. Eastwood, and R.W. Nero, "A field examination of acoustical scattering from marine organisms at 70kHz," *IEEE J. Oceanic Eng.*, **12**, 339-348 (1987).
31. Urlick, R.J. (1983). *Principles of Underwater Sound*, 3rd edition (Los Altos, CA: Peninsula, 1983), 423 pp.
32. Medwin, H., and Clay, C.S., *Fundamentals of Acoustical Oceanography*. (San Diego: Academic Press, 1998), 712 pp.
33. P.H. Wiebe, D.G. Mountain, T.K. Stanton, C.H. Greene, G. Lough, S. Kaartvedt, J. Dawson, and N. Copley, "Acoustical study of the spatial distribution of plankton on Georges Bank and the relationship between volume backscattering strength and the taxonomic composition of the plankton," *Deep-Sea Res. Part II*, **43**, 1971-2001 (1996).
34. T.K. Stanton, "Multiple scattering with applications to fish-echo processing," *J. Acoust. Soc. Am.*, **73**, 1164-1169 (1983).
35. R.H. Love, "Dorsal-aspect target strength of an individual fish," *J. Acoust. Soc. Am.*, **49**, 816-823 (1971).
36. K.G. Foote, "Fish target strengths for use in echo integrator surveys," *J. Acoust. Soc. Am.*, **82**, 981-987 (1987).
37. O.A. Misund, and A.K. Beltestad, "Target-strength estimates of schooling herring and mackerel using the comparison method," *ICES J. Mar. Sci.*, **53**, 281-284 (1996).
38. V.C. Anderson, "Sound scattering from a fluid sphere," *J. Acoust. Soc. Am.*, **22**, 426-431 (1950).
39. C.F. Greenlaw, "Backscattering spectra of preserved zooplankton," *J. Acoust. Soc. Am.*, **62**, 44-52 (1977).
40. K.G. Foote, "Linearity of fisheries acoustics, with addition theorems," *J. Acoust. Soc. Am.*, **73**, 1932-1940 (1983).
41. T.K. Stanton, P.H. Wiebe, D.Z. Chu, M.C. Benfield., L. Scanlon, L. Martin, and R. Eastwood, "On acoustic estimates of zooplankton biomass," *ICES J. Mar. Sci.*, **51**, 505-512 (1994).
42. A. Kristensen, and J. Dalen, "Acoustic estimation of size distribution and abundance of zooplankton," *J. Acoust. Soc. Amer.*, **80**, 601-611 (1986).
43. J.S. Link, T.A. Henwood, and C.T. Gledhill, "Small Pelagics in the Gulf of Mexico: A Description of the Abundance Geographic Distribution, Size, and Depth Distribution of Major Pelagic Species," (Pascagoula, MS: National Marine Fisheries Service, Southeast Fisheries Science Center, 1997).
44. T.L. Hopkins, "The vertical distribution of zooplankton in the eastern Gulf of



- Mexico," *Deep-Sea Res.*, **29**, 1069-1083 (1982).
45. R.A. Zimmerman, and D.C. Biggs, "Patterns of distribution of sound scattering zooplankton in warm- and cold-core eddies in the Gulf of Mexico, from a narrowband acoustic Doppler current profiler survey," *J. Geophys. Res.*, **104**, 5251-5262 (1999).
  46. T.L. Hopkins, D.M., Milliken, L.M., Bell, E.J., McMichael, J.J. Heffernan, and R.V.Cano, "The landward distribution of oceanic plankton and micronekton, over the west Florida continental shelf as related to their vertical distribution," *J. Plankton Res.*, **3**, 645-658 (1981).
  47. P.B. Ortner, R.L. Ferguson, S.R. Piotrowicz, L. Chesal, G. Berberian, and A.V. Palumbo, "Biological consequences of hydrographic and atmospheric advection within the Gulf Loop Intrusion," *Deep-Sea Res.*, **31**, 1101-1120 (1984).
  48. P.B. Ortner, L.C. Hill, and S.R. Cummings, "Zooplankton community structure and copepod species composition in the Northern Gulf of Mexico," *Continental Shelf Res.*, **9**, 387-402 (1989).
  49. The overall circulation in the region is strongly influenced by the bathymetry and extensions of the Gulf Loop Current, which is the portion of the Gulf Stream flowing westward through the Yucatan Channel, then northward into the central Gulf of Mexico before turning anti-cyclonically in the eastern central region of the Gulf and exiting through the Florida Straits. This pattern has been observed to follow an annual cycle in phase with the historical annual cycle of current speeds and transports of the Gulf Stream, reaching a maximum in the spring and summer, and a minimum in the fall and winter months.<sup>50</sup> Although oceanic fronts and eddies can introduce significant horizontal variability in water properties in the northern Gulf of Mexico, these typically occur in the spring and summer during Gulf Loop Current extensions<sup>51</sup>, and are not likely to have affected the TVSS experiment.
  50. G.A. Maul, "The annual cycle of the Gulf Loop Current Part I: Observations during a one-year time series," *J. Mar. Res.*, **35**, 29-47 (1977).
  51. R.C. Herron, T.D. Leming, and J. Li, "Satellite-detected fronts and butterfly aggregations in the northeastern Gulf of Mexico," *Cont. Shelf Res.*, **9**, 569-588 (1989).
  52. T.C. Gallaudet, and C.P. de Moustier, "On optimal amplitude shading for arrays of irregularly spaced or non-coplanar elements," *IEEE J. Ocean. Eng.*, **25**, 553-567 (2000).
  53. K.G. Foote, "Acoustic sampling volume," *J. Acoust. Soc. Am.*, **90**, 959-964 (1991).
  54. A.J. Plueddemann, and R. Pinkel, "Characterization of the patterns of diel migration using a Doppler sonar," *Deep-Sea Res.*, **36**, 509-530 (1989).
  55. R.W. Nero, C.H. Thompson, J.R. Dubberley, and R.H. Love, "Herring hydroglyphics in littoral waters of the northern Gulf of Mexico," *J. Acoust. Soc. Am.*, **108**, 2489 (2000).
  56. L. Lecornu, V. Burdin, C. Scalabrin, and C. Hamitouche, "Fish school analysis from multibeam sonar image processing," *Proc. IEEE Oceans '98*, vol. **1**, 587-591 (1989).
  57. Schooling usually has an antipredator function, and different shapes may be associated with different behaviors and different species. Parabolic-shaped schools may indicate a combined feeding/migration behavior<sup>58</sup>, whereas circular- or disc-shaped schools might be formed to reduce the chance of being detected by predators.<sup>6</sup> Echograms obtained by the NMFS have shown that the small pelagics in the Northeastern Gulf of Mexico frequently form small, compact schools near the bottom during the daytime.<sup>43</sup>
  58. B.L. Partridge, T. Pitcher, J.M. Cullen, and J. Wilson, "The three-dimensional

- structure of fish schools," *Behav. Ecol. Sociobiol.*, **6**, 277-288 (1980).
59. Herring are obligative schoolers, which means they are always found in polarized schools and become agitated if isolated. Therefore, they school often, and as a consequence, their schools are fairly constant in structure.
  60. R.E. Pieper, "Euphasiid distribution and biomass determined acoustically at 102kHz," *Deep-Sea Res.*, **26**, 687-702 (1979).
  61. S.Z., El-Sayed, W.M. Sackett, L.M. Jeffrey, A.D. Fredricks, R.P. Saunders, P.S. Conger, G.A. Fryxell, K.A. Steidinger, and S.A. Earle, "Chemistry, primary productivity, and benthic algae of the Gulf of Mexico," in *Serial atlas of the marine environment folio 22* (New York : American Geographical Society, 1972).
  62. M.J. Dagg, P.B. Ortner, and F. Al-Yamani, "Winter-time distribution and abundance of copepod nauplii in the northern Gulf of Mexico," *Fish. Bull.*, **86**, 319-330 (1987).
  63. D.D. Sameoto, "Quantitative measurements of euphasiids using a 120-kHz sounder and their in situ orientation," *Can. J. Fish. Aquat. Sci.*, **37**, 693-702 (1980).
  64. C.F. Greenlaw, "Acoustical estimation of zooplankton populations," *Limnol. Oceanogr.*, **24**, 226-242 (1979).
  65. L. Legendre, and S. Demers, "Towards dynamic biological oceanography and limnology," *Can. J. Fish. Aquat. Sci.*, **41**, 2-19 (1984).
  66. D.L. Mackas, and C.M. Boyd, "Spectral analysis of zooplankton spatial heterogeneity," *Science*, **204**, 62-64 (1979).
  67. R.W. Nero, and J.J. Magnuson, "Characterization of patches along transects using high resolution 70kHz integrated acoustic data," *Can. J. Fish. Aquat. Sci.*, **46**, 2056-2064 (1989).
  68. P.H. Wiebe, "Small scale distribution in oceanic zooplankton," *Limnol. Oceanogr.*, **15**, 205-217 (1970).
  69. R.W. Nero, J.J. Magnuson, S.B. Brandt, T.K. Stanton, and J.M. Jech, "Finescale biological patchiness of 70kHz acoustic scattering at the edge of the Gulf Stream-Echo Front 85," *Deep-Sea Res.*, **37**, 999-1016 (1990).
  70. D.D. Sameoto, "Euphasiid distribution in acoustic scattering layers and its significance to surface swarms," *J. Plankton Res.*, **5**, 129-143 (1983).
  71. C.F. Greenlaw, and W.G. Percy, "Acoustical patchiness of mesopelagic micronekton," *J. Mar. Res.*, **43**, 163-178 (1985).
  72. P.A. Crowther, P.A., and A. Hansla, "The lifetimes, velocities, and probable origin of sonic and ultrasonic noise sources on the sea surface," in *Natural and Physical Sources of Underwater Sound* edited by B.R. Kerman (Boston: Kluwer, 1993), pp. 379-392.
  73. R.J. Kloser, "Improved precision of acoustic surveys of benthopelagic fish by means of a deep-towed transducer," *ICES J. Mar. Sci.*, **53**, 407-413 (1996).
  74. E. McCarthy, "Acoustic characterization of submerged aquatic vegetation," in *High Frequency Acoustics in Shallow Water*, edited by N.G. Pace, E. Pouliquen, O. Bergem, and A.P. Lyons (La Spezia: NATO SACLANT Undersea Research Center, 1997), pp. 363-369.
  75. H.U. Sverdrup, M.W. Johnson, and R.H. Fleming, *The Oceans: Their Physics, Chemistry, and General Biology*, (Englewood Cliffs, New Jersey: Prentice-Hall, Inc., 1942) 1087 pp.
  76. K.G. Foote, "Correcting acoustic measurements of scatterer density for extinction," *J. Acoust. Soc. Am.*, **88**, 1543-1546 (1990).
  77. T.K. Stanton, "Effects of second-order scattering on high resolution sonars," *J. Acoust. Soc. Am.*, **76**, 861-866 (1984).
  78. T.K. Stanton, P.H. Wiebe, D.Z. Chu, and L. Goodman, (1994). "Acoustic

- characterization and discrimination of marine zooplankton and turbulence," *ICES J. Mar. Sci.*, **51**, 469-479 (1994).
79. J. Dalen, and A. Lovik, "The influence of wind-induced bubbles on echo integration surveys," *J. Acoust. Soc. Am.*, **69**, 1653-1659 (1981).
  80. P.A. Crowther, H.J.S. Griffiths, and A. Hansla, "Dependence of sea surface noise in narrow beams on windspeed and vertical angle," in *Natural and Physical Sources of Underwater Sound*, edited by B.R. Kerman (Boston: Kluwer, 1993) pp. 31-44.
  81. Applied Physics Laboratory, *APL-UW High Frequency Ocean Environmental Acoustic Models Handbook*, Technical Report APL-UW TR 9407 (Seattle: University of Washington, 1994) Part III.
  82. F.R. Young, *Cavitation*. (San Francisco: McGraw-Hill, 1989).
  83. R.N. Bracewell, *The Fourier Transform and Its Applications*, 2nd edition (New York: McGraw Hill, Inc, 1986), 474 pp.
  84. J.S. Bendat, and A.G. Piersol, *Random Data: Analysis and Measurement Procedures*, 2nd edition, (New York: John Wiley & Sons, 1986) 566 pp.

TABLE I. Fish school data corresponding to Figs 6 and 7. The length, width, and height in the  $x,y,z$  dimensions are denoted  $L_{fs}, W_{fs}, H_{fs}$  respectively. The seafloor backscattering strength  $S_B$  was computed and analyzed in reference (55).

	Run 1	Run 2
maximum height above seafloor (m)	7.1	4.7
maximum along-track dimension (m)	42	32
maximum across-track dimension (m)	31	26
maximum $H_{fs}$ (m)	7	4.7
maximum $L_{fs}$ (m)	52	41
maximum $W_{fs}$ (m)	17	27
Shape Dimension ( $L_{fs}:W_{fs}:H_{fs}$ ) <sub>reduced</sub>	7.4 : 2.4 : 1	8.7 : 5.7 : 1
maximum TS (dB)	-24.3	-28.9
mean TS (dB)	-45.5	-47.3
maximum $S_V$ (dB)	-31.9	-40.1
mean $S_V$ (dB)	-56.1	-59.8
mean $S_B$ (dB) @ normal incidence	-8.0	-9.7
standard deviation of $S_B$ @ normal incidence	2.3	2.0
normal incidence $S_B$ (dB) below fish school	-8.1	-9.9

TABLE II. Data computed from the mean profiles of echo-integrated volume scattering strength in Fig 9, where  $x = -47\text{m}$  was to left of towfish's track, and  $x = +47\text{m}$  was to the right.

	RUN 1		RUN 2		RUN 3	
	$x=-47\text{m}$	$x=47\text{m}$	$x=-47\text{m}$	$x=47\text{m}$	$x=-47\text{m}$	$x=47\text{m}$
LAYER 1						
depth (m)	-	-	30	31	33	35
thickness (m)	-	-	9	11	14	18
maximum $S_V$ (dB)	-	-	-67.5	-64.1	-63.2	-64.1
depth of maximum $S_V$ (m)	-	-	29	35.5	30	30
maximum TS (dB)	-	-	-62.3	-58.5	-57.5	-58.0
depth of maximum TS (m)	-	-	29	35.5	29	30
LAYER 2						
depth (m)	40	41	47	49	58	60
thickness (m)	28	25	21	16	29	22
maximum $S_V$ (dB)	-61.5	-61.5	-64.1	-63.5	-61.5	-62.0
depth of maximum $S_V$ (m)	49	33	50.5	53	55	60
maximum TS (dB)	-62.1	-56.3	-59.5	-59.5	-57.4	-58.1
depth of maximum TS (dB)	39	33	50.5	53	50.5	60
LAYER 3						
depth (m)	70	76	70	74	-	-
thickness (m)	27	22	23	22	-	-
maximum $S_V$ (dB)	-59.5	-59.0	-64.4	-66.2	-	-
depth of maximum $S_V$ (m)	69	81	69	75	-	-
maximum TS (dB)	-56.5	-56.5	-61.5	-64.3	-	-
depth of maximum TS (m)	69	81	69	75.5	-	-

TABLE III. Average volume reverberation characteristics from Fig 12, and computed over  $N_p$  pings.  $RL_{\max}(\theta)$  is the maximum over all angles  $\theta$ , and  $RL_{\min}(\theta)$  is the minimum.

	Run 1	Run 2	Run 3
$N_p$	98	97	99
$RL_{\max}(\theta)$ (dB)	187.3	180.2	184.9
$\theta$ of $RL_{\max}(\theta)$	355°	352°	64°
$RL_{\min}(\theta)$ (dB)	174.6	166.8	169.1
$\theta$ of $RL_{\min}(\theta)$	181°	157°	130°
$RL_{\max}(\theta) - RL_{\min}(\theta)$ (dB)	12.7	13.4	15.8
$RL(0^\circ) - RL(180^\circ)$ (dB)	8.9	8.2	10.9

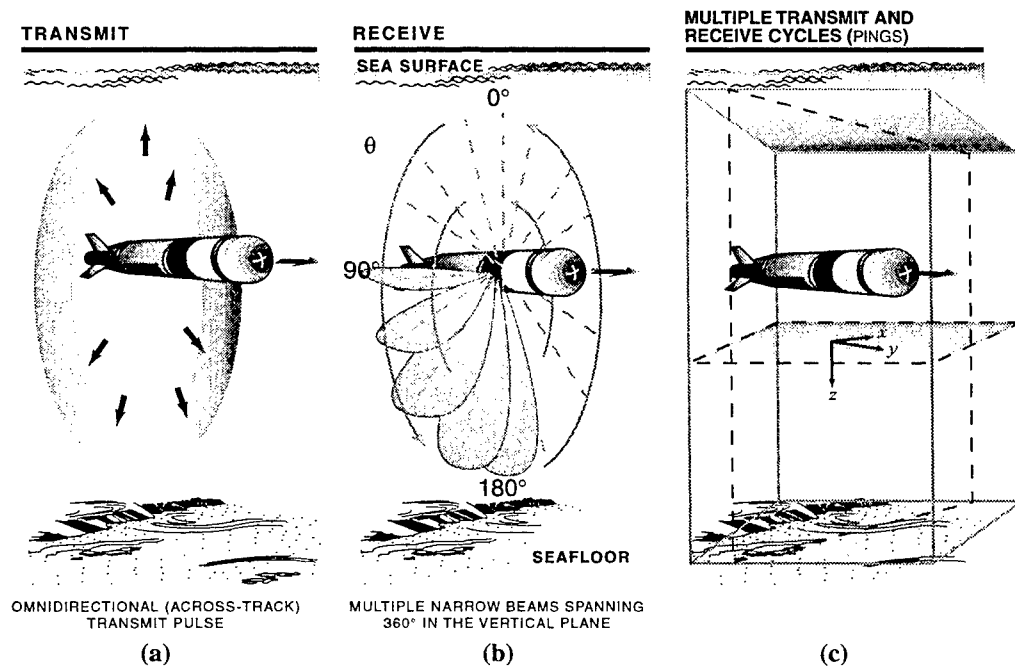


Fig. 1. The TVSS was designed for mine-hunting while deployed on an autonomous or unmanned underwater vehicle (AUV/UUV). The results in this study were obtained from data collected while the TVSS was deployed on a towed vehicle which was towed 735m astern of a towship. After transmission of a "toroidal" pulse, the sonar extracts the returned signal in directions spanning  $360^\circ$  about the TVSS's axis. This geometry is used to construct undersea imagery for multiple horizontal and vertical planes using data collected over successive transmit-receive cycles (pings). Only vertical imagery are presented in this study, where  $x$ ,  $y$ , and  $z$  correspond to across- and along-track directions relative to the towfish and depth relative to the sea surface.

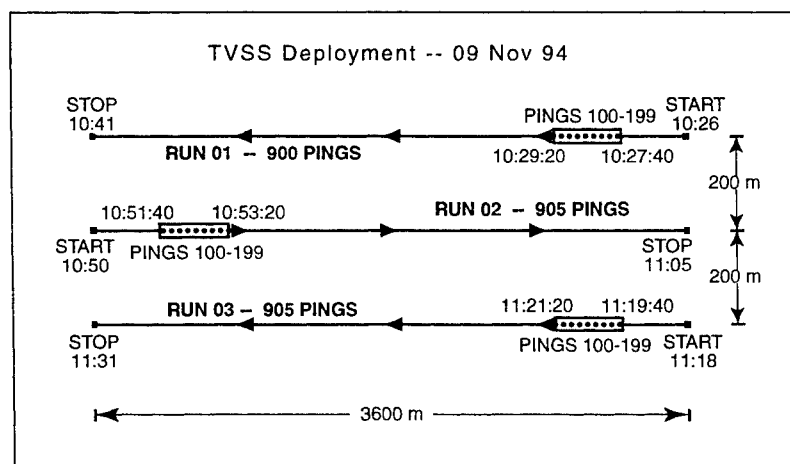


Fig. 2. TVSS track lines for runs 1-3, 9 November 1994. The data presented in this paper are processed from pings #100-199 in each of the three runs. In the figure, north is upward.



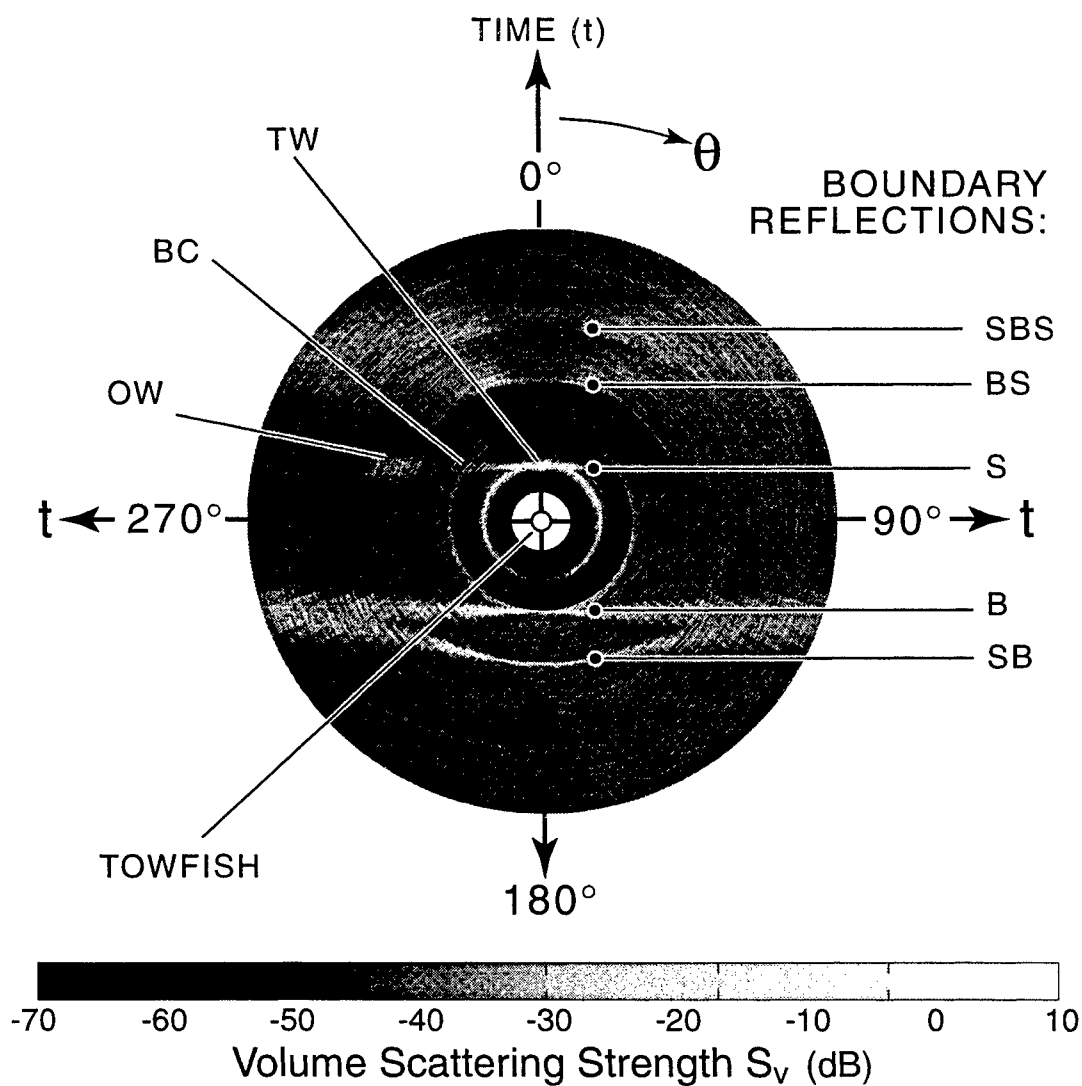


Fig. 3. One TVSS ping displayed as a vertical slice of acoustic volume scattering strength ( $S_v$ ) in polar coordinates of angle vs. two-way travel time. Labels refer to the following features: W - towship's wake; OW - towship's wake generated during previous run; BC - bubble cloud generated by a breaking bow wave from the towship; B - seafloor echo; S - sea surface echo; SB - surface-bottom (multiple) echo; BS - bottom-surface (multiple) echo; SBS - surface-bottom-surface (multiple) echo.

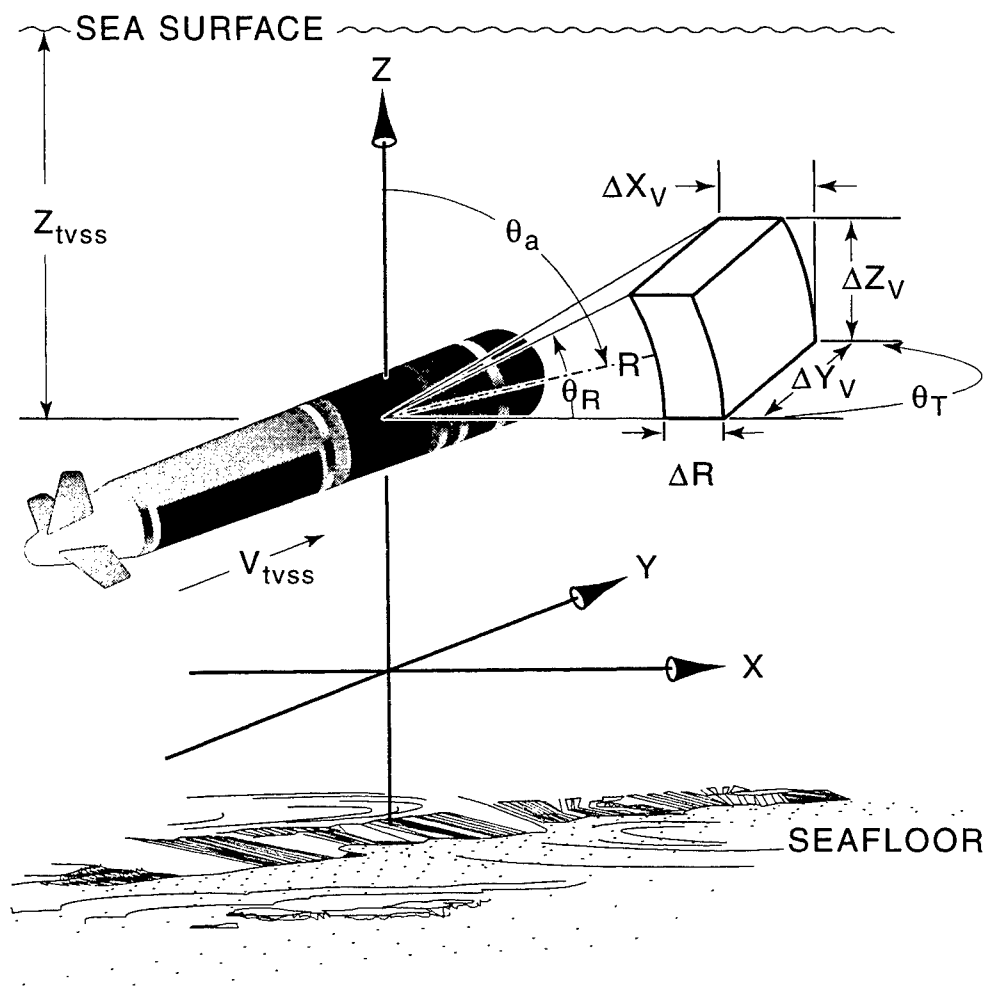


Fig. 4. The TVSS's sampling volume ( $V$ ) for a given angle of arrival ( $\theta_a$ ) is defined in terms of the transmit and receive beamwidths ( $\theta_T$ ,  $\theta_R$ ), the range ( $R$ ) from the TVSS center, and range resolution  $\Delta R$ . The spatial dimensions of  $V$  in the along-track, across-track, and vertical dimensions are  $\Delta Y_V$ ,  $\Delta X_V$ , and  $\Delta Z_V$ .

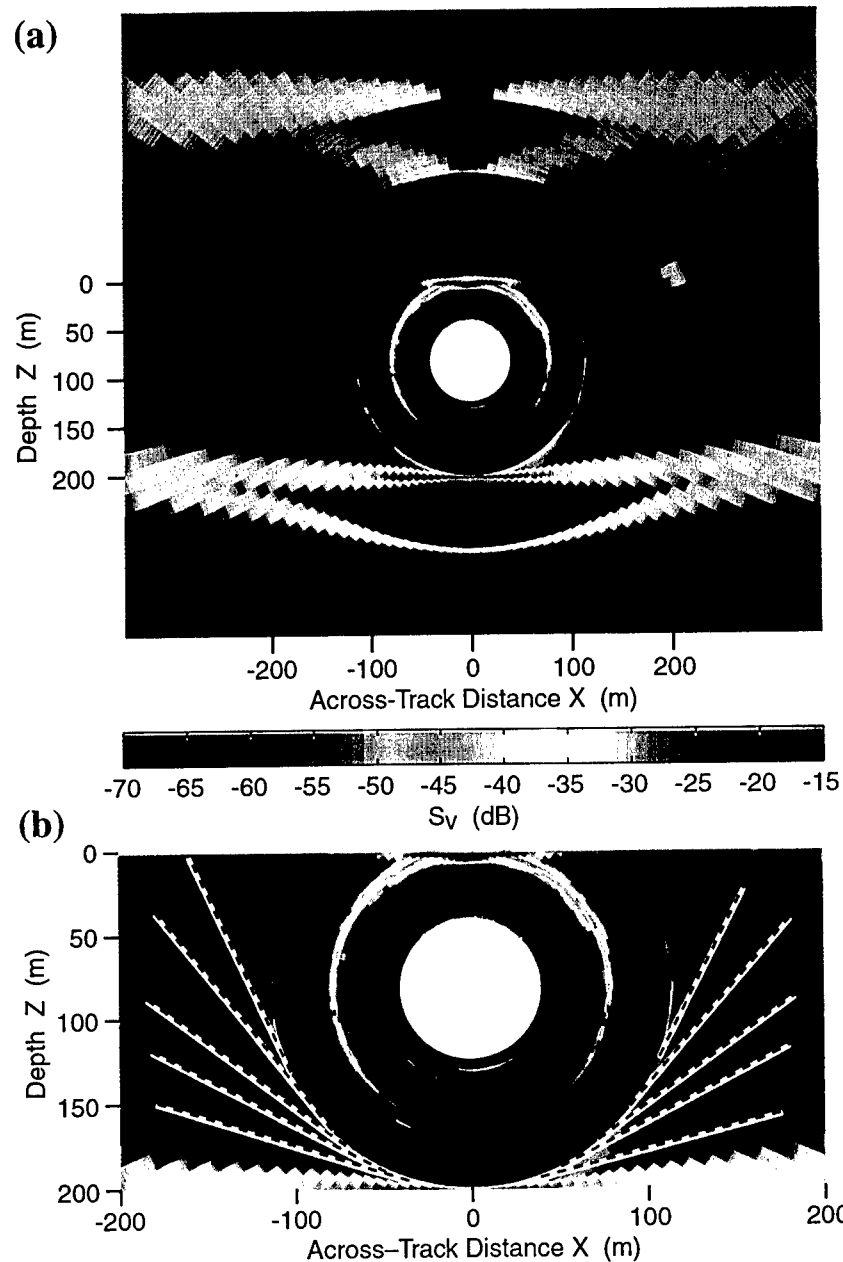


Fig. 5. (a) and (b) Average volume acoustic scattering strength of 97 pings collected during run 2. (b) Computer simulations determined the time-angle pairs (dashed lines) for which a sidelobe of a volume beam was directed towards the bottom at the time of arrival of each bottom echo.

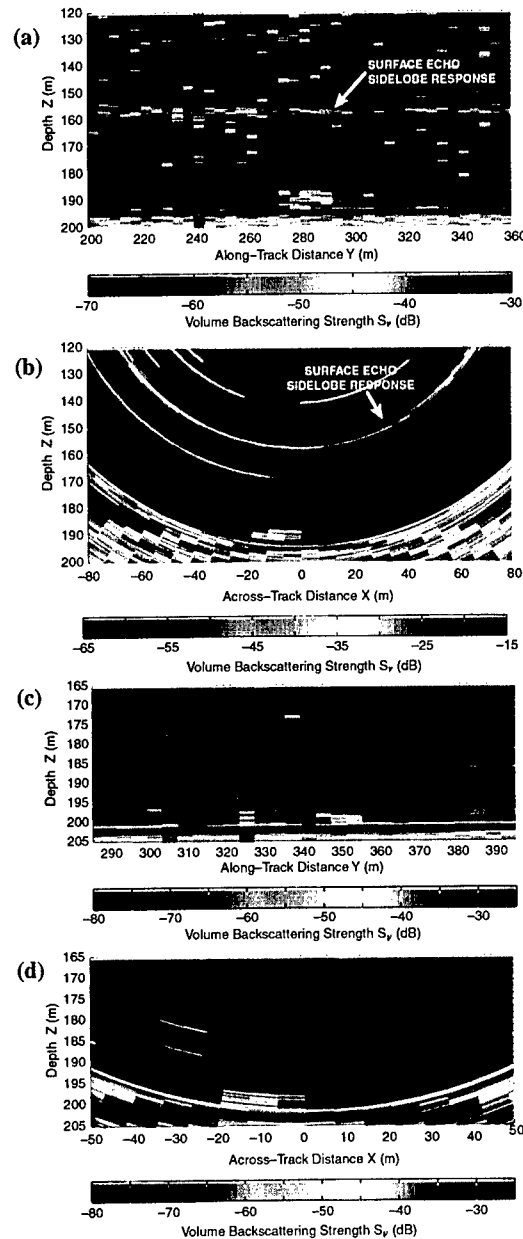


Fig. 6. Vertical volume acoustic backscattering strength ( $S_v$ ) images of two near bottom fish schools in run 1 ((a), (b)), and run 2 ((c), (d)). The seafloor is the high backscatter, horizontal feature at  $z = 193$  m ((a), (b)) and  $202$  m ((c), (d)). The horizontal feature with moderately high backscatter at  $158$  m depth in (a) is the sidelobe response of the sea surface echo, seen also in the individual (Fig. 3) and averaged (Fig. 5) ping data. The randomly distributed samples in (a) where  $S_v > -40$  dB in the water column are signals that were saturated in the TVSS data acquisition system (DAS) electronics. These appear as the thin arcs in Fig. 6b above and below the sea surface echo sidelobe return.

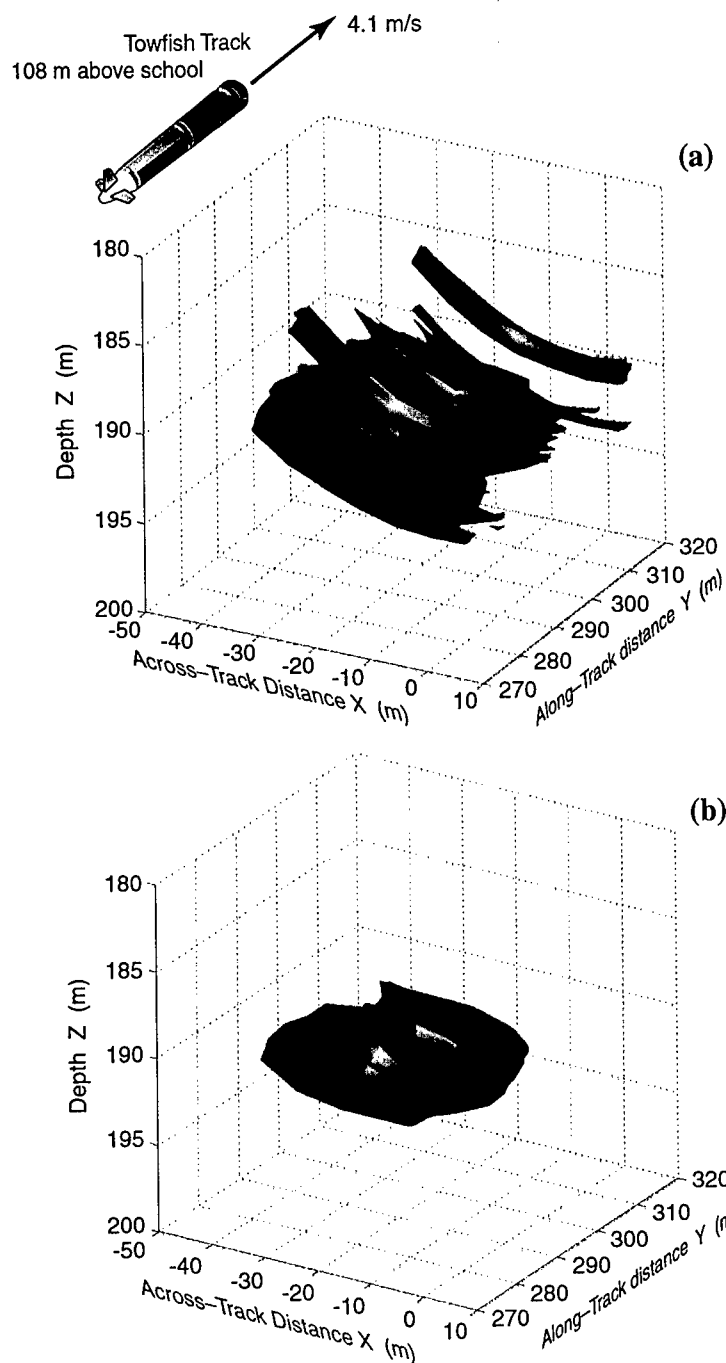


Fig. 7. (a) Three dimensional representation of the fish school detected in run 1 (Figs. 6a,b). The thin, elongated features are individual volume cells in which fish were detected, and represent the minimum volume resolution attainable with the TVSS (Fig. 4). (b) Volumetric representation of the school after filtering the samples in and around the school with a  $3 \times 3 \times 3$  moving average filter and thresholding the output 5dB above the ambient scattering strength values.

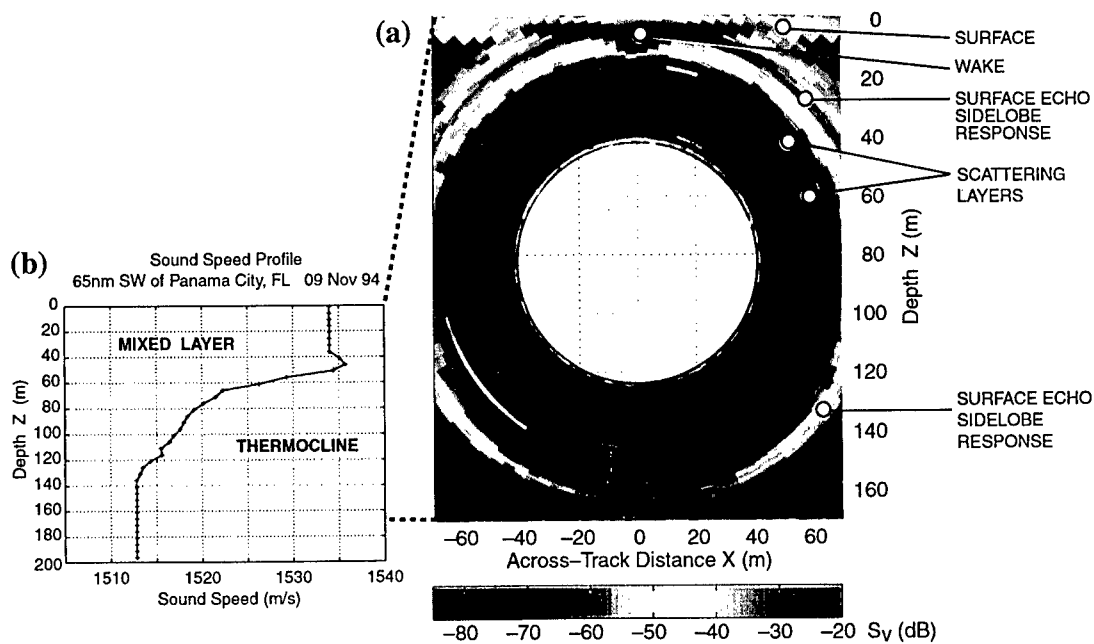


Fig. 8. (a) This 97-ping average for run 2 reveals scattering layers between 40-80m depth. These depths comprised the base of the mixed layer and upper thermocline, which was well-described by the sound speed profile obtained 100m north of the location for run 1.

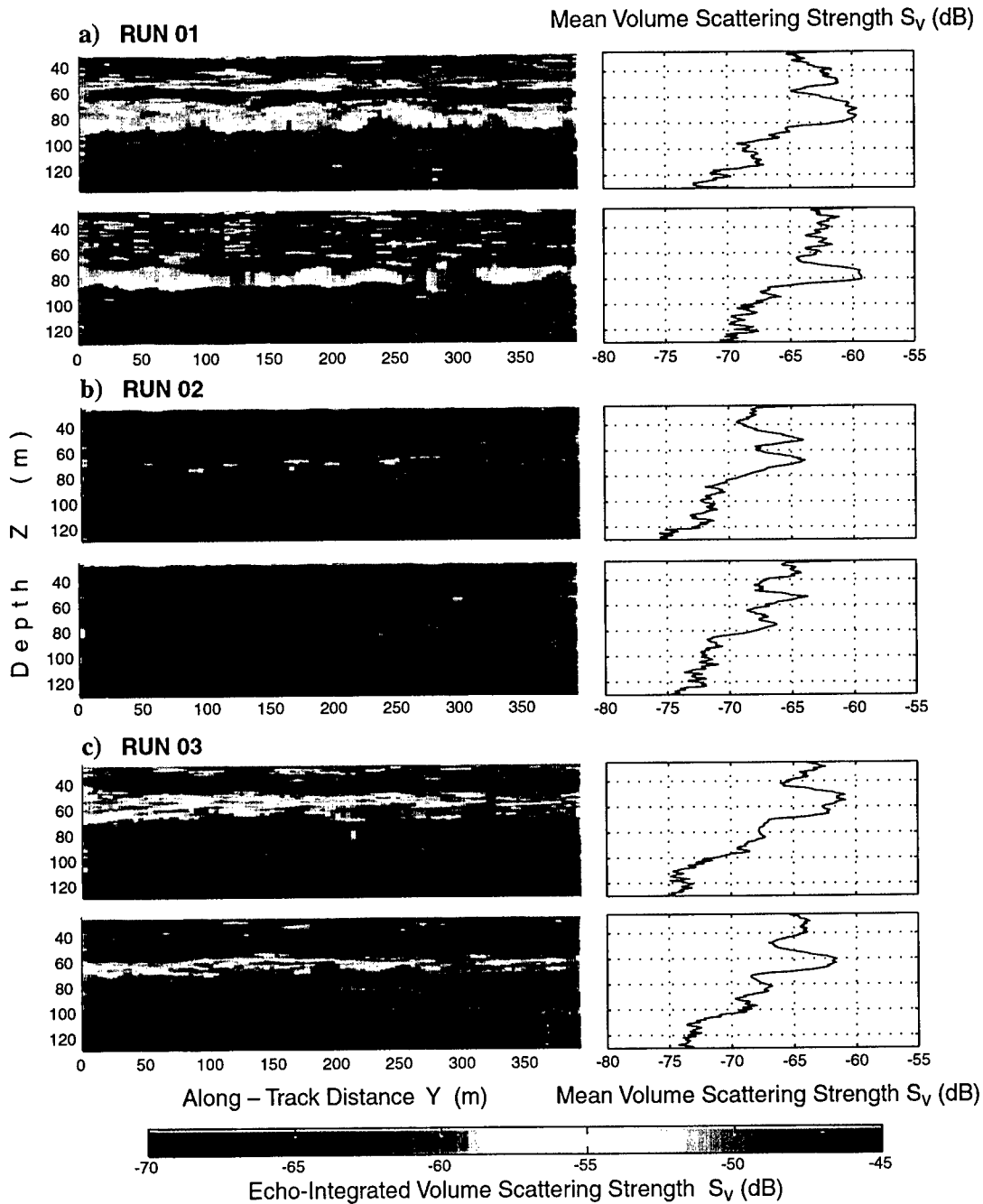


Fig. 9. (a) - (c) Along-track vertical sections of echo-integrated volume acoustic backscattering strength ( $S_V$ ) from data 47 m across-track to the left and right of the towfish (respectively top and bottom picture in each run). The corresponding mean ( $\langle S_V \rangle$ ) profiles averaged over the number of usable pings ( $N_p$ ) in each run are displayed to the right. Pings which suffered from saturation in the DAS electronics were removed from the images and not used in the averages to prevent upward biases in the  $S_V$  values.  $N_p=98, 97$ , and  $99$  for runs 1, 2, and 3, respectively.

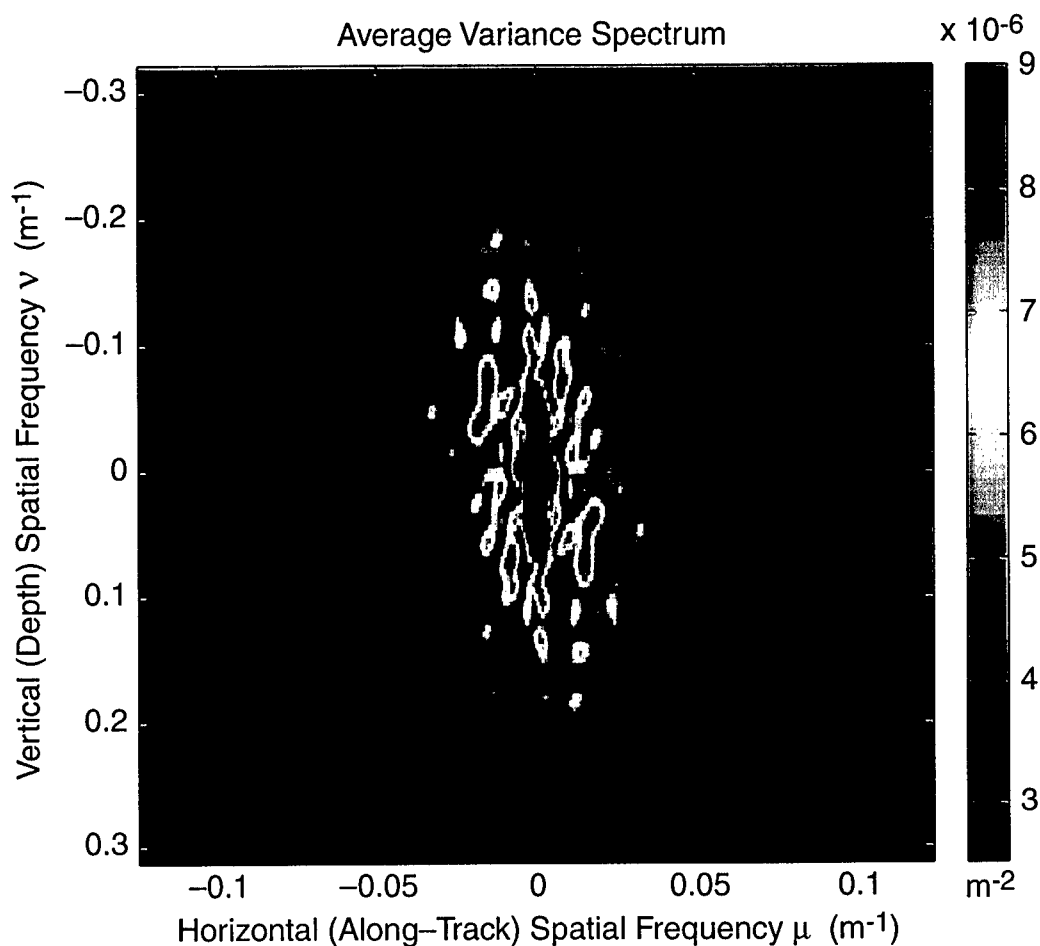


Fig. 10. The average of the six two-dimensional variance spectra of volume scattering coefficients corresponding to the images in Fig. 9a-c. The Appendix describes the calculations, which included a two-dimensional Hanning window to reduce sidelobe leakage. The maximum and minimum length scales resolved are 2.8 m and 50 m in the vertical, and 8 m and 205 m in the horizontal.



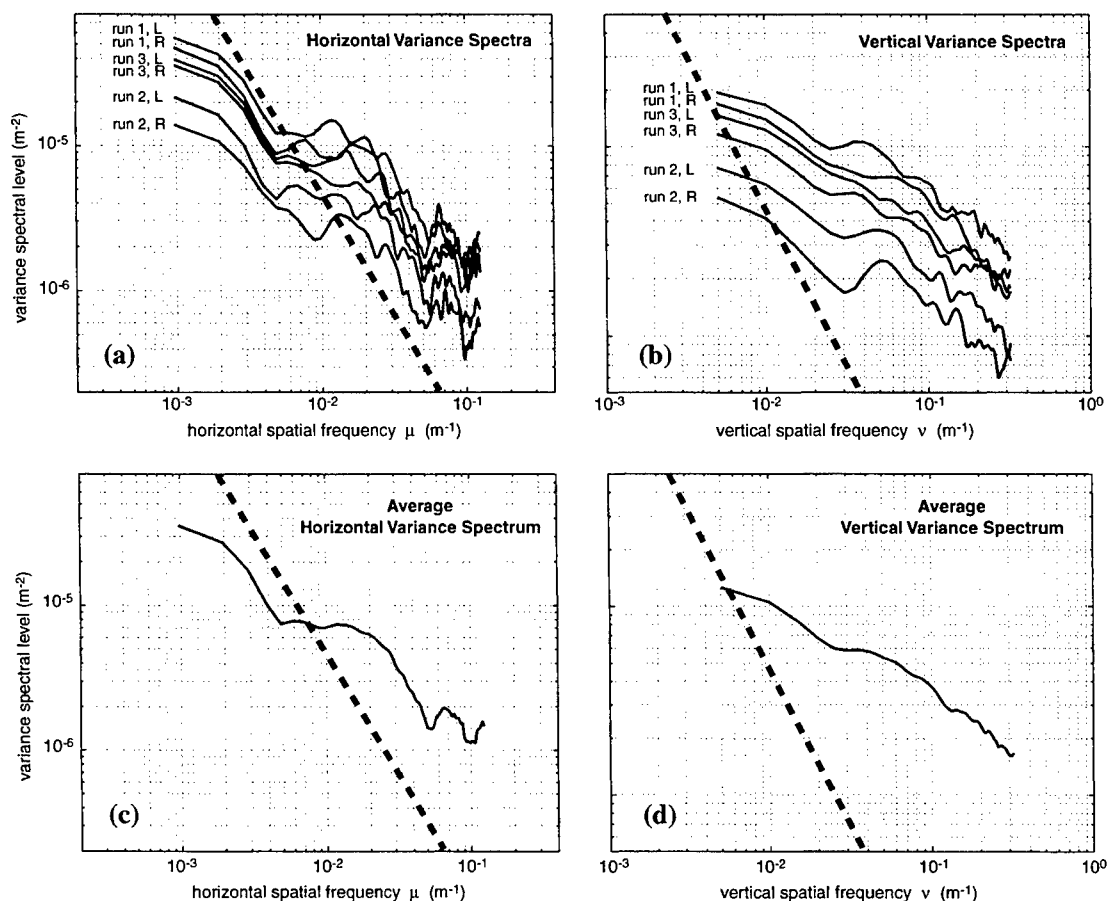


Fig. 11. Log-log plots of: (a) horizontal variance spectra averaged over all vertical spatial frequencies in the two-dimensional spectra computed from each image in Fig. 8; L and R refer to images formed 47m to the left and right side of the TVSS, respectively; (b) vertical variance spectra averaged over all horizontal spatial frequencies; (c) Average horizontal and (d) vertical variance spectrum computed from (a) and (b) respectively. The dashed line has a  $-5/3$  slope, which is the theoretical spectral slope for a process controlled by turbulent mixing (reference [33]). Details are discussed in the text.

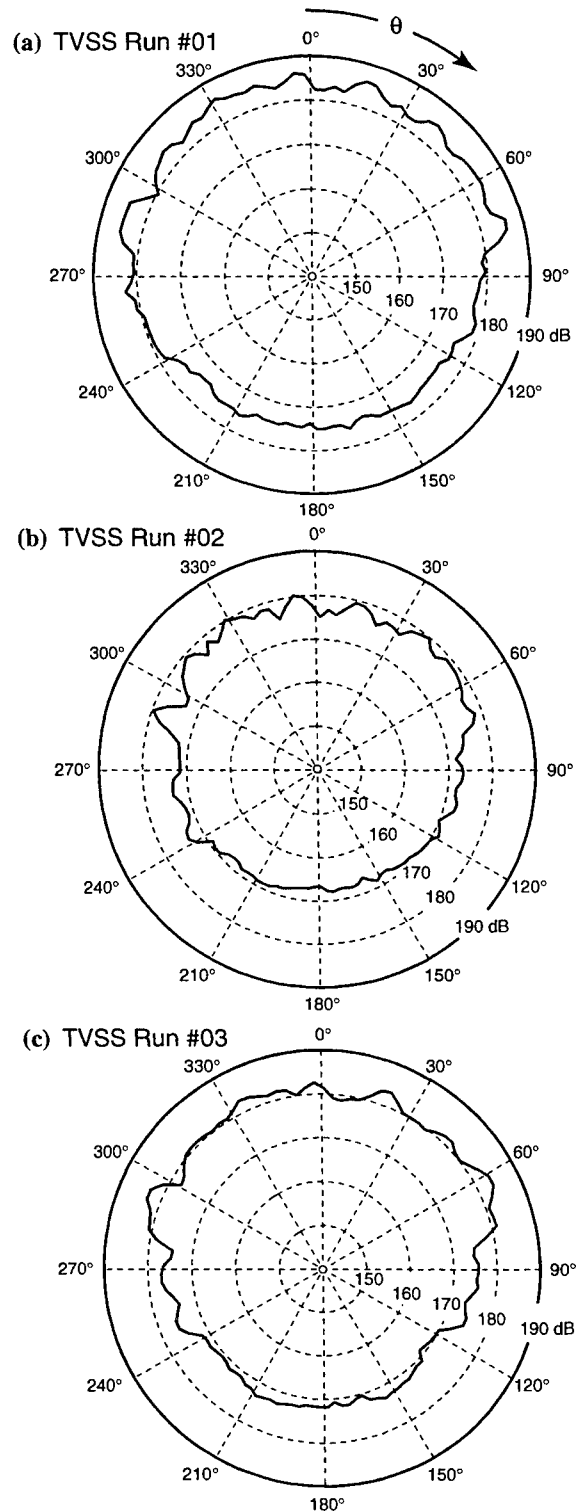


Fig. 12.  $N_p$ -ping average of volume reverberation levels ( $\overline{RL}(\theta)$ ) (dB) for runs 1-3 (a)-(c).  $\theta = 0^\circ$  and  $180^\circ$  are respectively the towfish's zenith and nadir, facing the towfish's direction of travel.

## Chapter 5

### Sea Surface and Volume Acoustic Backscattering Strength Imagery of the Microbubble Field in a Ship's Wake

#### ABSTRACT

Sea surface and near-surface volume acoustic backscattering strength imagery of a ship's wake is obtained from data collected by the Toroidal Volume Search Sonar (TVSS), a 68 kHz multibeam sonar capable of 360° imaging in a vertical plane perpendicular to its direction of travel. The backscatter data collected by the TVSS when it was towed 735m astern of a towship are processed using swath bathymetry techniques to construct sea surface relief maps, which reveal patterns produced by the towship's wake. The vertical and horizontal structures of microbubble fields associated with the towship's wake and breaking waves are represented by sea surface and near-surface volume acoustic backscattering strength images and angular dependence functions. Unlike previous acoustic studies on ship wakes, these results are obtained from data which sample the bubble field at a constant distance from the ship. The maximum acoustic volume scattering strength ( $S_V$ ) observed in the towship's wake is 17.1dB, and the average vertical attenuation through the wake is estimated to be 2.1dB/m. The data suggest that cavitation is the dominant bubble generation mechanism in the wake and that turbulent diffusion governs the spatial extent of the bubbles during the first three minutes after generation. Gas dissolution mediated by air saturation and the presence of surfactant materials in the near-surface water are hypothesized to govern the wake decay rate. Because in-situ bubble density and size distribution measurements were not collected during the experiment, an extensive reference list is cited to support the conclusions. This study demonstrates the potential for high frequency multibeam sonars in the investigation of near-surface physical processes.

#### I. INTRODUCTION

This paper presents results for an acoustic study of a ship's wake in which the data were collected by the Toroidal Volume Search Sonar (TVSS), a 68kHz cylindrical array, which was deployed on a towfish at a depth of 78m in waters 200m deep, 735m astern of a towship (Fig. 1). The deployment was conducted for engineering tests by the U.S. Navy's Coastal System Station (CSS), Panama City, Florida. The acoustic data collected by the TVSS are beamformed and processed for sea surface and volume acoustic backscattering strength imagery in horizontal and vertical planes around the towship's wake. (Fig. 2). The imagery is used to characterize the acoustic structure of microbubble clouds associated with the wake and breaking ship waves, and their influence on the angular dependence of sea surface backscattering strength. In this study, all the wake data are sampled at the same time after generation by the ship, whereas previous acoustic studies of wakes have relied on data which sampled the cross section and temporal evolution of wakes<sup>2-8</sup>. Because relatively few wake studies are found in the unclassified acoustic literature, we begin in section II with an extensive background discussion regarding ship wakes, bubbles, and sea surface acoustic backscatter. In section III, we describe the TVSS, data collection, and signal processing methods used to create sea surface relief maps and acoustic backscatter imagery in and around the towship's wake. The towship's wake is discussed in detail in section IV, and the influence of near-surface bubble clouds on sea surface backscattering strength is assessed in section V. Due to a lack of sufficient *in-situ*

data, and the relatively few acoustic studies of ship wakes in the open literature, hypotheses regarding the processes affecting the acoustic data rely on an extensive reference list. A brief summary and conclusions are given in section VI.

## II. BACKGROUND

### A. The Kelvin Wave Pattern and Turbulent Wake of a Moving Ship

The disturbance created by a moving ship on the sea surface consists of the *Kelvin wave pattern* and *turbulent wake* (Fig. 3). For a comprehensive description and literature review regarding these, the reader is referred to Reed *et al.* (1990).<sup>9</sup> The Kelvin wave pattern can be explained by a single pressure point moving at a constant velocity on the surface of the water, which sends out waves that constructively interfere. The ideal pattern consists of transverse and divergent waves confined within a wedge-shaped region behind the ship with a half angle  $\theta_K = 19^\circ 28'$ . The Kelvin wave pattern of a real ship depends upon the ship's size, speed, and hull form, and environmental conditions (Appendix A).<sup>10-16</sup> This may cause a real ship's pattern to differ slightly from the ideal pattern, and exhibit several divergent waves generated by the bow, hull, and stern (Fig. 3). Both the transverse and divergent waves are deep

$$\lambda = 2\pi v^2 / g \quad , \quad (1)$$

where  $v$  is the wave's phase velocity and  $g = 9.81\text{m/s}^2$  is the gravitational acceleration. Transverse waves are the longest waves in the Kelvin pattern, and propagate at  $v$  equal to the ship's velocity  $V_{ship}$ . Divergent waves propagate at  $v = V_{ship} \cos \theta_d$ , where  $\theta_d$  is the angle between the line perpendicular to the divergent wave's crest and the ship's course. Thus, the divergent waves are shorter than the transverse waves. Apart from the bow wave near the ship's stem, the highest amplitudes and steepest waves in the pattern are found near the cusps where the transverse and divergent wave crests meet<sup>11-13</sup>. The angle between the line tangent to the cusp crests and the ship's course is  $\theta_c = 35^\circ 16'$  (Fig. 3). The overall pattern moves with the ship and decays asymptotically as the square root of the distance aft of the ship.<sup>16</sup>

Unlike the Kelvin wave pattern, the turbulent wake has no standard terminology,<sup>9-14</sup> and definitions in the radar and acoustic literature usually differ from those used in naval architecture.<sup>15,16</sup> The turbulent wake is sometimes referred to as the white water wake,<sup>14</sup> propeller wake,<sup>16</sup> vortex wake,<sup>17</sup> and thermal wake.<sup>2</sup> We define the turbulent wake as that region behind the ship which includes surface and/or near-surface bubbles and variations in seawater particle velocities and temperature produced by the moving ship. Bubbles in the turbulent wake are produced by some combination of air entrainment in the turbulent boundary layer along the ship's hull, bow and stern wave breaking, and propeller cavitation.<sup>2</sup> The complex surface and near-surface velocity field in the turbulent wake results from the combination of: 1) forward moving flow due to viscous drag of the ship's hull<sup>14</sup>; 2) horizontal surface convergence at the wake boundaries and divergence along the centerline due to vortices shed by the ship's displacement hull and propeller(s)<sup>2,18-22</sup>, and 3) rearward moving flow from the propeller(s).<sup>5</sup> Temperature variations in the turbulent wake result from the mixing associated with the turbulent velocity variations.<sup>2</sup>

The portion of the turbulent wake produced by the propeller(s) consists of an initial region of high divergence in the near field called the initial spreading region (ISR)<sup>23</sup>. The far field portion of the turbulent wake spreads at an angle of about one degree with respect to the ship's track, and may persist over an hour.<sup>2,24</sup> The portion of the turbulent wake produced by the bow and stern waves and the turbulent boundary layer merge with the propeller wake in the ISR<sup>18</sup>. Although visible bubbles on

the surface are usually limited to the near field, thin bands of surface foam may form in the surface convergences along the wake boundaries and extend well into the far field. As with the Kelvin wave pattern, the geometry of the turbulent wake depends upon the generating ship's size, hull form, and speed, as well as the characteristics of its propeller(s) and the local environment (Appendix A). In general, the width ( $w$ ) of the turbulent wake grows rapidly to several times the ship's beam ( $B$ ) in the ISR, which may extend up to eight ship lengths ( $L$ ) aft of the ship<sup>23</sup>, and the penetration depth ( $h$ ) is typically 2-3 times the ship draft ( $D$ ).

Studies of ship wakes and wave patterns are important for applications other than naval architecture because they provide a relatively large degree of control in the measurement of naturally occurring physical processes. Ship wake studies have yielded a wealth of knowledge concerning hydrodynamics<sup>25</sup>, wave mechanics<sup>26-29</sup>, radar backscatter from the sea surface<sup>30-32</sup>, and sediment transport processes<sup>18</sup>. Furthermore, bubble distributions and their generation and dissipation mechanisms may be studied using acoustic measurements in ship wakes<sup>3,8</sup>. Such observations are important because bubbles play an important role in the gas transfer between the atmosphere and ocean<sup>33</sup>, strongly affect sound propagation in the upper ocean<sup>34</sup>, and may be used as tracers for upper-ocean dynamics<sup>35</sup>. Unfortunately, few acoustic studies of ship's wakes are available in the unclassified literature, the most extensive of which was conducted during World War II<sup>2</sup>. Subsequent wake investigations have provided useful information on the nature of acoustic scattering and propagation in near-surface bubble fields<sup>2-8</sup>, but the acoustic properties of ships wakes remain ill-understood.

## B. Sound Interaction With Near-surface Bubbles

In contrast to bubbles in a ship's wake, most of the bubbles in the ocean are formed from air entrainment in breaking waves and biologic sources<sup>36</sup>, but once formed, all oceanic bubbles are influenced by buoyancy, advection, turbulent diffusion, and gas diffusion. The buoyancy of a gas bubble affects the rate at which it will rise out of the water. The rise velocity for bubbles with radius  $a \leq 180\mu\text{m}$  in still water is given by Thorpe (1982)<sup>33</sup> as

$$v_b = (2/9) a^2 g v_k^{-1} (\sqrt{\chi^2 + 2\chi} - \chi), \quad (2)$$

where  $v_k = 1.28\text{m}^2/2$  is the kinematic viscosity of water and  $\chi = 10.82v^2g^{-1}a^{-3}$ . Thus, one can expect rise velocities of 0.4cm/s and 3cm/s for bubbles with 50 $\mu\text{m}$  and 180 $\mu\text{m}$  radii. Supporting buoyancy is the decrease in hydrostatic pressure which occurs as a bubble rises, causing its radius, hence its rise velocity, to increase. Buoyancy is counteracted by downward turbulent diffusion, which may be characterized by the vertical eddy diffusivity ( $k_v$ ). Order of magnitude estimates of  $k_v$  are useful for our study, which are given by

$$k_v \approx L_t^2/\Delta T_t \quad (3)$$

where  $L_t$  is the length scale characterizing the turbulence evolving over the time interval  $\Delta T_t$  (reference (37)). Because  $L_t$  and  $k_v$  tend to increase with wave height, bubble penetration depth and near-surface bubble layer thickness increase with sea state. Downward turbulent diffusion and horizontal advection may act together to disperse a bubble population, such as in a single breaking wave event<sup>38</sup>, or to concentrate a population of bubbles, such as in Langmuir circulation.<sup>39</sup>

Gas diffusion tends to decrease a bubble's lifetime through dissolution, which can be described by the "dirty bubble" formula for the rate of change of a gas bubble's diameter ( $d_b$ ) in seawater:<sup>40</sup>

$$\frac{d}{dt} (d_b) = -3.02 \frac{\bar{R}T_b (\Delta c) \kappa^{2/3} (v_b d_b)^{1/3}}{M_b (1.5d_b P_b - 2\tau)} , \quad (4)$$

where  $\bar{R}$  is the gas constant,  $T_b$  is the temperature of the gas,  $\Delta c$  is 100% minus the gas saturation,  $\kappa$  is the diffusion constant,  $M_b$  is the molar weight of the gas,  $P_b$  is the Laplace pressure inside the bubble, and  $\tau$  is the surface tension on the bubble. This shows that the absolute dissolution rates of air bubbles in seawater decrease as dissolved oxygen and nitrogen content increase, and no dissolution is expected for 100% saturation. The term "dirty bubble" is used because the equation assumes that the bubble surface is covered by a layer of surface active (surfactant) material which allows it to sustain a stress and behave dynamically like a rigid body<sup>33</sup>. Surfactant materials are found in all natural water bodies and are the byproducts of plant and animal life<sup>23</sup>. For practical purposes, all bubbles in seawater can be assumed to be "dirty" after a few seconds<sup>33</sup>. The presence of surfactants tends to decrease both dissolution rates and bubble rise speeds<sup>33,40,41,42</sup> and may even stabilize (i.e. stop dissolution) bubbles entirely<sup>43,44</sup>. Laboratory and model results by Johnson and Wangersky (1987)<sup>44</sup> have shown that a monolayer of particles introduces a Laplace, or surface tension pressure which opposes bubble collapse, i.e.

$$P_0 - P_b = 2\tau / r_b \quad (5)$$

where  $P_0$  is the pressure outside the bubble, and  $r_b$  is the mean radius of curvature of each interparticle gas-water interface. Dissolution occurs when the left side of (5) exceeds the right side, which may result from an increase in depth or atmospheric pressure, or when surface tension is not sufficiently high. By increasing  $2\tau/r_b$ , a surfactant coating prevents bubble dissolution. The presence of contaminants which act as surfactants inhibiting bubble dissolution, or as nuclei for bubble formation is a probable reason why observations of subsurface bubble densities in coastal waters are greater than those in the open ocean at elevated wind speed.<sup>45</sup>

The acoustic properties of bubbles are important because acoustic methods are used to measure bubble distributions<sup>46</sup> and because bubbles are a significant source of noise in most sonar applications, and particularly acoustic measurements of zooplankton, fish<sup>47</sup>, and sea surface roughness<sup>48</sup>. In these applications, the quantities most often measured are sea surface acoustic scattering strength ( $S_s$ ), volume acoustic scattering strength ( $S_v$ ), volumetric acoustic backscattering cross section per unit volume ( $M_v$ ), and target strength (TS)<sup>20</sup>. These terms are defined in Appendix B, where we also discuss the primary features of sound interaction with bubbles, which include sound speed dispersion, scattering, attenuation, and absorption. Scattering, absorption, and extinction (attenuation) are dominated by bubbles at resonance because the scattering and absorption cross sections of a bubble at resonance are  $10^3$  times its geometric cross section, and  $10^{10}$  times that of a rigid body of equal radius<sup>36</sup>. Acoustic scattering and attenuation from resonant microbubbles in the towship's wake were the most significant features in the TVSS data<sup>49</sup>. The resonant bubble radius ( $a_r$ ) can be estimated from the approximate expression<sup>49</sup>

$$a_r = \frac{3.25}{f} \sqrt{1 + 0.1z} , \quad (6)$$

where  $a_r$  and the depth  $z$  are in meters, and  $f$  is the acoustic frequency in Hz. Thus,  $a_r$  increases as frequency decreases and depth increases. For the TVSS data,  $f = 68\text{kHz}$ , so that  $a_r$  is  $48\mu\text{m}$  at the surface and  $59\mu\text{m}$  at 5m depth.

Measurements of bubble size distributions are used to learn about the physical processes affecting them. The density of bubbles in the ocean as a function of radius is related to wind speed and depth, and many authors have reported average results

expressed in terms of a power law<sup>38</sup>, i.e.  $n(a) \propto a^n$ . Instantaneous measurements exhibit a large degree of variability about the mean, and this is most likely a source of the large variability observed in sea surface backscattering strength<sup>48</sup> and near-surface sound speed measurements<sup>50</sup>.

The TVSS data are relevant to the study of naturally occurring bubbles because 48 $\mu$ m is near the center of many bubble size distributions measured under breaking waves.<sup>51,52-55</sup> For example, 48 $\mu$ m lies near the peak of the bubble distributions at 0.5m, 3.0m, and 7.1m depths measured by Vagle and Farmer (1992)<sup>51</sup> during 11 m/s winds. Su *et al.* (1988)<sup>55</sup> optically measured microbubble distributions in the NOREX 85 experiment during 12-13m/s winds and found the peak to be very close to 48 $\mu$ m, and in the laboratory measurements of bubbles under 1m high breaking waves made by Cartmill and Su (1993)<sup>54</sup>, 48 $\mu$ m occurs about mid-way between the radii corresponding to the peak and lowest values in the distribution, and the same is true for the distribution in Medwin and Brietz (1989)<sup>56</sup> for 12-15m/s winds. Despite the uncertainties of the different measurement techniques used in these studies<sup>46</sup>, it is certain that 48 $\mu$ m size microbubbles are common in the near-surface environment during breaking of surface waves of many sizes (see Farmer (1993)<sup>52</sup> for a review of these).

### C. Acoustic Backscatter From the Sea Surface

Near-surface bubbles have a profound effect on sea surface acoustic backscatter which is a limiting factor in the performance of underwater acoustic detection and communication systems, and they can be used to remotely sense the sea surface from below. Measurements of sea surface backscattering strength ( $S_s$ ) (Appendix B) are widely variable, with disparities of an order of magnitude existing between measurements obtained under similar environmental conditions<sup>48</sup>. The primary source of disparity between measurements at high frequencies (>3kHz) has been attributed to resonant scattering from subsurface microbubbles<sup>57</sup>. By comparing measurements of  $S_s$  with predictions from an appropriate scattering model, much can be learned about the near-surface bubble population.<sup>58</sup>

We use the model for  $S_s$  developed by the Applied Physics Laboratory, University of Washington (APL-UW)<sup>59</sup> because it is validated, well-documented, and incorporates the theoretical and empirical scattering characteristics of both sea surface roughness and subsurface bubbles. In this model, sea surface scattering strength is expressed as

$$S_s(\theta_g) = 10\log_{10} [\sigma_r(\theta_g) + \sigma_b(\theta_g)] , \quad (7)$$

where  $\theta_g$  is the grazing angle, and  $\sigma_r$  and  $\sigma_b$  are the dimensionless backscattering cross sections per unit solid angle per unit surface area due to sea surface roughness scattering and volumetric bubble scattering, respectively. The following is a brief description of these components; further details may be found in reference (59).

The surface roughness term  $\sigma_r$  is divided into two components:  $\sigma_f$  and  $\sigma_{sc}$ .  $\sigma_f$  is due to near-specular scattering from large-scale wave facets which occurs at steep grazing angles ( $\theta_g \geq 70^\circ$ ), and can be described by the high-frequency limit of the Kirchoff approximation. Assuming a Gaussian, isotropic distribution of surface slopes, this scattering cross section is

$$\sigma_f = ((\sec^4\theta_i)/(4\pi s^2)) \exp\left[(-\tan^2\theta_i)/s^2\right] , \quad (8)$$

where  $\theta_i = 90^\circ - \theta_g$  is the angle of incidence and  $s^2$  is the mean square surface slope which is estimated using the empirical relation in reference (59) as a function of wind speed measured at 10 meters height ( $U_{10}$ ).  $\sigma_{sc}$  is due to small-scale roughness and is described by the composite roughness theory developed by McDaniel and Gorman

(1982)<sup>57</sup> and McDaniel (1986)<sup>60</sup>. Their model is based on Bragg scattering from surface ripples satisfying the condition  $\lambda_r = \lambda_a / 2 \cos \theta_g$ , where  $\lambda_r$  is the ripple wavelength and  $\lambda_a$  is the acoustic wavelength. The ripples ride on the large-scale waves, which act to modulate the local grazing angle  $\theta_g$ , and their composite describes the surface roughness. The large-scale waves also act to shadow portions of the wave profile, but this effect is restricted to  $\theta_g < 5^\circ$  where bubble scattering dominates<sup>60</sup>. As a result, the Rayleigh-Rice formulation for the scattering cross section can be applied, giving<sup>48</sup>

$$\begin{aligned}\sigma_{sc}(\theta_g) &= G(U_{10}) \tan^4 \theta_g, \quad \theta_g \leq 85^\circ \\ \sigma_{sc}(\theta_g) &= 0, \quad \theta_g > 85^\circ,\end{aligned}\quad (9)$$

where  $G$  is an empirical function determined over the grazing angles interval  $30^\circ$ - $70^\circ$ . The total surface roughness component  $\sigma_r$  is found by interpolating between  $\sigma_f$  and  $\sigma_{sc}$  and correcting for the extinction loss through the bubble layer using an empirical relation which is a function of  $U_{10}$  and  $f_r$ .

The expression for  $\sigma_b$  is based on the formulation in Crowther (1980)<sup>61</sup> and McDaniel and Gorman (1982)<sup>57</sup> for the backscattering cross section of a horizontally homogeneous layer of near-surface bubbles, which was modified by McDaniel (1993)<sup>48</sup> to include coherent addition of two of the four paths involved (see Fig. 5 in reference (48)). The primary variable is  $\beta_l$ , defined as the depth-integrated extinction cross section per unit volume due to scattering and absorption, so that  $\sigma_b$  is given by<sup>58</sup>

$$\sigma_b = (\delta_r \sin \theta_g) / (8\pi \delta) (1 + 8\beta e^{-2\beta} - e^{-4\beta}), \quad (10)$$

where  $\delta = 2.55 \times 10^{-2} f^{1/3}$  is the total damping constant,  $\delta_r = 0.0136$  is the re-radiation damping constant at resonance, and  $\beta = \beta_l / \sin \theta_g$ . Empirical relations for  $\beta_l$  are given in reference (59) as a function of  $U_{10}$  and  $f_r$ , or one may attempt to estimate  $\beta_l$  from  $S_S$  data by inverting eqn (10) as in Dahl *et al.* (1997)<sup>58</sup>. Note that the azimuthal scattering angle is not included in eqn (10) because measurements to date have not shown the scattering cross section to depend on this angle.

At high bubble densities, eqn (10) reduces to

$$\sigma_b = (\delta_r \sin \theta_g) / (8\pi \delta) \quad (11)$$

and the backscattering cross section becomes independent of bubble density, hence wind speed, varying only with  $\theta_g$ . This condition is known as saturation and has been verified by several experiments.<sup>48</sup> The low bubble density limit when  $\beta \ll 1$  yields

$$\sigma_b = 1.5 (\delta_r \beta_l) / (\pi \delta). \quad (12)$$

Although the APL-UW model was developed for environments in which sea surface acoustic backscatter is controlled by wind generated surface roughness and subsurface bubbles, it is applicable to the TVSS data which were dominated by the presence of the towship's wake. As we show in the following, differences between model predictions and the 68kHz TVSS data may be used to evaluate the dominant acoustic features of the towship's wake and partially discriminate between the contributions of subsurface bubbles and surface roughness. Comparisons in reference (59) show that the model agrees well with data collected during winds of 3-15 m/s and for frequencies of 12-70 kHz, with an estimated uncertainty of  $\pm 5$ dB for wind speeds  $< 8$  m/s,

### III. TVSS DATA

#### A. Environmental Conditions



The acoustic data were collected by the TVSS on 9 November 1994 between 1026AM-1131AM local time in a 2 nm<sup>2</sup> area 65nm southeast of Panama City, Florida, in the northeastern Gulf of Mexico. The center of the experiment site was 29°30'N, 86°30'W, in waters 190m-202m deep. The TVSS was towed approximately 735m aft of the towship *Mr. Offshore* (Table I) at a nearly-constant depth of 78m (Fig. 1). Three runs of 100 consecutive pings of acoustic backscatter data from a 200μs CW pulse of 68 kHz transmitted at 1 Hz were obtained while the towship speed was nearly constant at 8 knots (Fig. 1). Towfish roll, pitch, yaw, heading, speed, and depth were sampled at 1 Hz (once per ping).

A single CTD cast was taken at 0658AM, which revealed the presence of an isothermal mixed layer with a temperature of 24.8°C extending to a depth of 49m, a thermocline between 49m-150m depth, and a nearly-isothermal layer above the bottom with a temperature of 15.6°C. The surface salinity was 35.1 ppt, and the surface sound speed was 1534m/s. Video and *in-situ* observations of subsurface bubble size distributions, surface wave parameters, and surface currents were not recorded during the collection of the TVSS data. The ambient surface and near-surface currents were most likely weak or absent because the towship had no bow-thruster and used very little rudder to maintain the eastward and westward tracks (Fig. 1). This is consistent with historical data for the region, which is discussed more fully in reference (47). The wind speed and sea state recorded at 0658AM onboard *Mr. Offshore* were 6 knots (3m/s) and 1.5, respectively. These conditions correspond to an ambient sea composed mostly of ripples with wavelengths on the order of 0.10m, significant wave heights of 0.25m, and rms wave heights of 0.06m according to World Meteorological Organization (WMO) codes<sup>59</sup>. We assume that small scale wave breaking occurred during the TVSS experiment because previous studies have reported a wind speed of about 2.5m/s as the lower limit for wave breaking<sup>33,58,62,63</sup> although this can vary with geography and water properties<sup>59</sup>.

## B. TVSS Data Processing

The following details regarding the TVSS help to interpret the processed data. Further information regarding the TVSS, the data, the data collection, and the signal processing is described in references (64) and (65). The TVSS includes coaxial but separate cylindrical projector and hydrophone arrays, 0.53m in diameter, deployed on a cylindrical towed vehicle (Fig. 1). The projector array has 32 elements equally-spaced 11.25° apart. Its beam pattern is meant to be omni-directional in the across-track direction and has a -3 dB beamwidth of 3.7° in the along-track direction. The hydrophone array consists of 120 elements equally-spaced every 3°. Individual element beam pattern magnitude data were provided by the manufacturer, but element pattern phase data were unavailable.

The processing scheme that we have developed for these data is designed for conformal arrays and includes: quadrature sampling, resampled amplitude shading, element-pattern compensation, and broadside beamforming on phase-compensated, overlapping subarrays with asymmetric projected element spacings<sup>65</sup>. This procedure permits split aperture processing of the beamformed output, which is used because the phase zero-crossing of the output phasor is the most accurate means to detect the arrival time of boundary reflections on the maximum response axis of the beam<sup>64</sup>.

For each ping, the acoustic signals from the 120 hydrophones are heterodyned in the data acquisition system (DAS) from 68 kHz to 6.25 kHz, low-pass filtered, and digitally recorded using 16 bit signed integer 2's complement coding at a sampling frequency of 25 kHz. The full scale of the recorded data is ±5V, so we converted the digital data to volts by

$$d_V = 10 \left[ \frac{d_I + 2^{n-1}}{2^n - 1} \right] - 5, \quad (\text{volts}) \quad (13)$$

where  $n=16$  bits,  $d_I$  is the recorded digital value, and  $d_V$  is the output voltage.

To form a beam in the direction  $\theta$  at each time sample  $t$ , the phases of the acoustic signals from 29 elements are adjusted to project the aperture on the tangent perpendicular to the direction  $\theta$ . We define  $\theta$  as the roll-corrected angle in the  $x$ - $z$  plane perpendicular to the axis of the towfish, such that the towfish's zenith is at  $\theta = 0^\circ$ , and the towfish's nadir is at  $\theta = 180^\circ$ , with  $\theta$  increasing clockwise around the towfish when facing the direction of travel (Fig. 2). The split aperture process is achieved by dividing this aperture into two overlapping 21-element subapertures whose phase centers are spaced 8 elements apart. For each time sample  $t$ , the signals from these two subapertures are phase shifted and summed separately to produce beams  $B_1(\theta, t)$  and  $B_2(\theta, t)$ , and a phasor  $P(\theta, t)$  is formed from the product

$$P(\theta, t) = B_1(\theta, t) \times B_2^*(\theta, t), \quad (14)$$

where  $*$  denotes complex conjugation. The magnitude of  $P(\theta, t)$  is the product of the magnitudes of  $B_1(\theta, t)$  and  $B_2(\theta, t)$ , hence it has units of volts<sup>2</sup>, and its phase is the phase difference between  $B_1(\theta, t)$  and  $B_2(\theta, t)$ .  $B_1(\theta, t)$ ,  $B_2(\theta, t)$ , and  $P(\theta, t)$  are all broadside with respect to the 29-element aperture. This operation is performed at every time sample  $t$  for each ping, every  $3^\circ$  for directions spanning  $360^\circ$  around the TVSS axis. The beam directions are corrected for the difference between the sound speed used in the beamforming and that of seawater at the face of the array because  $B_1(\theta, t)$  and  $B_2(\theta, t)$  are not broadside to their respective subapertures. The -3dB beamwidth of each output beam is  $4.95^\circ$  in the across-track direction.

Before an acoustic backscattering strength image is formed, raw backscatter data from (14) are converted to surface or volume acoustic scattering strength using the active sonar equation<sup>66</sup>

$$S_{S,V} = RL - SL + 2TL - 10 \log_{10}(A, V), \quad (15)$$

with  $RL = 10 \log_{10} \left( \frac{1}{2} |P(\theta, t)| \right) - RVR - FG - DI - TVG$ ,

in which  $RVR = -168$  dB *re*:  $1V_{rms}/\mu\text{Pa}$  is the average receive voltage response of each hydrophone,  $FG = 29$  dB is the preamplifier fixed gain,  $DI = 13$  dB is the array gain associated with the beamforming and split aperture processing,  $TVG$  is the system time-varying gain,  $SL$  is the calibrated transmit source level of 216.8dB *re*  $1\mu\text{Pa}$  @  $1 \text{ m}$ <sup>64</sup>,  $TL = 20 \log_{10} R + \alpha R$  is the one-way transmission loss due to spherical spreading and absorption with the logarithmic absorption coefficient  $\alpha = 0.024$  dB/m<sup>66</sup>, range  $R$  is determined from  $t$  and  $\theta$  using constant-gradient raytracing techniques<sup>66</sup>,  $A$  is the area within the receive beam<sub>3</sub> that is ensonified by the transmit pulse (for  $S_S$ ), and  $V$  is the ensonified volume in  $\text{m}^3$  (for  $S_V$ ). We divide  $P(\theta, t)$  by 2 in order to convert the units from  $V_{peak}^2$  to  $V_{rms}^2$ . Note that transmission loss through the near-surface bubble layer in the towship's wake ( $TL_b$ ) is not included in (15) because we did not have the means to measure the bubble size distribution. Therefore, our estimates of  $S_V$  represent lower bounds on the actual values, as in Trevor *et al.* (1994)<sup>3,67</sup> (e.g. reference (68); Appendix B).

Using (15), the resulting 120 phasor time-series from (14) may be displayed as a vertical slice of volume acoustic scattering strength in polar coordinates of angle vs. time (Fig. 5). In this representation, echoes from the sea surface and seafloor appear as the high backscatter, horizontal features. Scattering from resonant microbubbles in the towship's wake and from bubble clouds formed by breaking ship waves are responsible for the high backscattering strength features near the sea surface. The

structure of these features becomes more clear upon adjusting the dynamic range of the display, as discussed in sections IV and V.

### C. TVSS Acoustic Geometry

The sampling and resolution characteristics of the TVSS data are defined by the acoustic geometry (Figs. 5,6). The angular sample spacing between the maximum response axes of adjacent beams in a single ping is  $\theta_s = 3^\circ$ . The 6.25kHz quadrature sampling frequency results in a time increment within each beam of  $\tau_s = 160 \mu s$ , corresponding to a 12cm slant range sampling interval assuming a sound speed of  $c=1500m/s$ . The range resolution for each sample is

$$\Delta R = c / 2W \quad (m) \quad (16)$$

where  $W$  is the TVSS bandwidth. With the TVSS pulse length  $\tau_p = 200 \mu s$ ,  $W = 0.88/\tau_p = 4.4kHz$ , which yields a range resolution of 17cm with  $c = 1500m/s$ .

The resolution of each near-surface volume sample is determined by the volume ( $V$ ) ensonified by the TVSS transmit pulse within each receive beam (Fig. 6), which is defined by the ellipsoidal shell element formed from the intersection of the transmitted pulse within the transmitted beampattern and the receive beampattern at each sampling point

$$V = \frac{2}{3} \theta_T \sin(\theta_R / 2) [R'^3 - R^3] \quad (m^3) \quad (17)$$

where  $R$  is the range from the center of the TVSS in meters,  $R' = R + \Delta R$ , the -3dB receive beamwidth ( $\theta_R$ ) is  $4.95^\circ$ , and the -3dB transmit beamwidth ( $\theta_T$ ) is  $3.7^\circ$ . The across-track, along-track, and vertical spatial dimensions of  $V$  ( $\Delta x_V$ ,  $\Delta y_V$ ,  $\Delta z_V$ , Fig. 6) vary with range and angle of arrival ( $\theta_a$ ), which is equal to  $\theta$  in Fig. 5 for  $\theta = 0^\circ$  to  $90^\circ$ , and  $|360^\circ - \theta|$  for  $\theta = 270^\circ$  to  $360^\circ$ . At zenith ( $\theta_a = 0^\circ$ ), these dimensions can be expressed as

$$\begin{aligned} \Delta x_V &= 2R' \sin(\theta_R / 2) \\ \Delta y_V &= 2R' \sin(\theta_T / 2) \quad (m) \\ \Delta z_V &= \Delta R + R(1 - \cos(\theta_R / 2)) \end{aligned} \quad (18)$$

where the curvature of the pulse causes  $\Delta z_V$  to exceed the range resolution. In beams for which  $0^\circ < \theta_a < 90^\circ - \theta_R / 2$ , the  $x$  and  $z$  dimensions of the ensonified volume are

$$\begin{aligned} \Delta x_V &= 2R \sin(\theta_R / 2) \cos \theta_a + \Delta R \sin(\theta_a + \theta_R / 2) \\ \Delta z_V &= 2R \sin(\theta_R / 2) \sin \theta_a + \Delta R \cos(\theta_a - \theta_R / 2) \quad \text{for } 0^\circ < \theta_a < 90^\circ - \theta_R / 2. \end{aligned} \quad (19)$$

Samples in adjacent beams overlap because  $\theta_s < \theta_R / 2$ . The overlapping volume increases with range

$$V_{ol} = \frac{2}{3} \theta_T \sin((\theta_R - \theta_s) / 2) [R'^3 - R^3] \quad (m^3) \quad (\text{adjacent beams}) \quad (20)$$

The percent of overlapping volume between adjacent beams is

$$VP_{ol} = [V/V_{ol}] \times 100\% \quad (21)$$

which can be written from eqns (17) and (20) as

$$VP_{ol} = [(\sin((\theta_R - \theta_s) / 2) / \sin(\theta_R / 2))] \times 100\% \quad (\text{adjacent beams}), \quad (22)$$

yielding a range independent volume overlapping percentage of 39.4% between TVSS beams.

Over successive pings, ensonified volume cells in the same angle of arrival and range overlap as well. An approximate upper bound on this overlapping volume is

$$V_{ol} \leq \frac{2}{3} \theta_T \sin(\theta_R / 2) [ (R' - R_{ol})^3 - (R - R_{ol})^3 ] \quad , \quad (m^3) \quad (23)$$

where the range from the TVSS at which the beams first overlap is

$$R_{ol} = \Delta y_{ping} / 2 \tan(\theta_T / 2) \quad , \quad (m) \quad (24)$$

and the along-track separation between pings is defined as

$$\Delta y_{ping} = V_{ship} / prr \quad . \quad (m) \quad (25)$$

Because the average speed of the towfish was 4.1m/s, and the prr of the TVSS was 1Hz, the average  $\Delta y_{ping}$  and  $R_{ol}$  for consecutive pings were 4.1m and 62m, respectively. Eqns (23)-(25) indicate that the ping-to-ping correlation of a sample within 62m from the TVSS will be less than that for samples at greater ranges. Using eqns (20) and (23), one can then find an approximate expression for the percent overlap from eqn (21).

Sea surface relief maps and surface and volume acoustic backscattering strength images were constructed using standard swath bathymetry and sidescanning techniques described in reference (64). The data points in each are separated by an along-track sample spacing  $\delta y_S = \Delta y_{ping}$ . Assuming a flat sea surface, the across-track sample spacing in the sea surface relief maps can be expressed as:

$$\delta x_S = Z_{tvss} [ \tan(\theta_a) - \tan(\theta_a - \theta_s) ] \quad (m) \quad (\text{relief maps}) \quad , \quad (26)$$

which increases across track. In the sea surface and near-surface volume acoustic backscattering strength images, the across-track samples spacings decrease across-track, and are given by

$$\delta x_S = c \tau_s / 2 \sin(\theta_a) \quad (m) \quad (\text{images}) \quad . \quad (27)$$

This is a consequence of the sidescanning procedure, which extracts samples in each receive beam at the quadrature sampling rate  $1/\tau_s$  as the transmitted pulse travels across the beam footprint (Fig. 6).

Sample resolutions in the surface relief maps and sea surface acoustic backscattering strength images depend upon the area of the transmitted pulse that ensonifies the sea surface within each receive beam. For  $\theta_a$  near normal incidence, the area is defined approximately by an ellipse (Fig. 6):

$$A = \pi \Delta R (1 + 2Z_{tvss} / \Delta R)^{1/2} Z_{tvss} \theta_T / 2 \quad . \quad (m^2) \quad (28)$$

When the trailing edge of the pulse is touching the sea surface, its along-track, across-track, and vertical extent at nadir are given by:

$$\begin{aligned} \Delta x_S &= 2 \Delta R (1 + 2Z_{tvss} / \Delta R)^{1/2} \\ \Delta y_S &= Z_{tvss} \theta_T \quad (m) \\ \Delta z_S &= \Delta R \cos(\theta_R / 2) \quad , \end{aligned} \quad (29)$$

where  $\Delta z_S$  is less than the range resolution because of the curvature of the pulse.

Beyond a delimiting angle  $\theta_D = \cos^{-1} ( Z_{tvss} / (Z_{tvss} + \Delta R) )$ , the ensonified area is defined by an annulus sector (Fig. 6). On a flat horizontal surface, this area can be approximated by:

$$A \approx (R\Delta R\theta_T) / \sin(\theta_a) + (\Delta R^2\theta_T) / (2\sin(\theta_a)) \quad (m^2) \quad (30)$$

The across-track, along-track, and vertical extent of the pulse beyond  $\theta_D$  are:

$$\begin{aligned} \Delta x_S &= R(\theta_R/2) \cos(\theta_a) + \Delta R \sin(\theta_a + \theta_R/2) \\ \Delta y_S &= R' \theta_T \\ \Delta z_S &= R(\theta_R/2) \sin(\theta_a) \end{aligned} \quad (m) \quad (31)$$

At increasing across-track distances, the across-track width ( $\Delta x_S$ ) of the ensonified area decreases while the along-track width ( $\Delta y_S$ ) increases. The across-track increase in the vertical extent of the pulse ( $\Delta z_S$ ) implies that vertical resolution degrades across-track.

As with the ensonified volumes, ensonified areas on the sea surface overlap between consecutive pings by an amount which increases with  $R$ . An approximate expression for the percent overlap is given by:

$$AP_{ol} \approx [(R - R_{ol}) / R] \times 100\% \quad (32)$$

#### D. Sources of Error

Our calculations of the ensonified area and volume for eqn (15) assume that scattering comes from a uniformly ensonified area or volume, and that TVSS receive beampatterns are identical for each subarray of elements. Ensonification from the TVSS transmit beampattern was in fact not uniform and had maximum variations of -9dB from the calibrated source level (see Figs. in reference (64)). Ideally, we should have computed the area term with

$$A(R, \theta_a) = \frac{c}{2W\sin\theta_a} R \int_{-\theta_T/2}^{+\theta_T/2} b(\theta_a, \phi) b'(\theta_a, \phi) d\phi \quad (33a)$$

and the volume term with

$$V(R, \theta_a) = \frac{c}{2W} R^2 \int_{-\theta_T/2}^{+\theta_T/2} \int_{\theta_a - \theta_R/2}^{\theta_a + \theta_R/2} b(\theta_a, \phi) b'(\theta_a, \phi) d\theta_a d\phi \quad (33b)$$

in which,  $c$  is the speed of sound,  $\phi$  is the azimuthal angle,  $b(\theta_a, \phi)$  is the transmit beampattern, and  $b'(\theta_a, \phi)$  is the receive beampattern. We could not use these expressions because we lacked the hydrophone phase data required to correctly determine  $b'(\theta_a, \phi)$  and because they require accurate platform attitude and motion data. The roll data were undersampled at 1Hz, and the pressure derived towfish depth data were systematically biased by about 14m. We used the seafloor and sea surface backscatter data to estimate and correct for errors in depth and roll, and to compensate for variation in the transmit beampattern. These techniques are more fully described in reference (64).

Because all data were roll corrected, whereas the transmit beampattern was fixed relative to the TVSS, some of the bias in the TVSS backscattering strength data was reduced due to the TVSS roll variation along track. The maximum ping-to-ping roll difference in each run was between 0.6-1.2°, and the average was 0.1°-0.2°. Computer simulation tests which used the towfish's roll values and the calibrated transmit beam pattern yielded a maximum angular bias in  $S_V$  of about -7dB when averaged along-track. This was reduced to less than -1dB after compensating for the array patterns.

A side-effect of beamforming is illustrated in Fig. 5 where the circular features of

high acoustic backscatter tangent to the boundaries are due to the normal incidence ( $\theta = 0^\circ, 180^\circ$ ) boundary echoes that contaminate the signals received in the other beams through their sidelobes. This is partly due to our resampled amplitude shading<sup>65</sup> that was designed to produce a nearly uniform sidelobe level between -28 and -30dB in the receive beampatterns of each TVSS subarray. Lower sidelobe shading was possible, but not without an unacceptable increase in main lobe width. For the sea surface and near-surface horizontal backscattering strength imagery, our method of compensating for the array beampatterns reduced the positive bias due to the boundary echo sidelobe returns to less than 2dB. Further details regarding the boundary reverberation sidelobe response in the TVSS data are provided in reference (47).

A smaller source of error was the TVSS motion. Positional uncertainties due to roll and depth errors were reduced using the correction strategies described in reference (64) and estimated to be less than 1% of the slant range. TVSS motion also caused the effective ensonified area (A) and volume (V) terms in eqn (15) to be lower than those calculated because the expressions for A and V in eqns (17), (28), and (30) assume a monostatic case. Had we accounted for transducer motion, our values of  $S_S$  and  $S_V$  would have been no more than 1dB higher than those reported.

The TVSS data were contaminated by random hydrophone dropouts and noise spikes resulting from saturation in the receive array electronics. Pings suffering from hydrophone dropouts were easily identified as the linear features for which the  $S_S$  or  $S_V$  data were significantly different from the mean values in each image. Noise spikes were identified by inspecting orthogonal image slices for high acoustic backscatter data occurring in one to two samples over a range of beams. Saturated data typically appeared as single samples in the horizontal and vertical along-track volume images, and as arc-like features in the across-track vertical volume images. Data contaminated by the hydrophone dropouts and noise spikes were not included in the calculations of mean  $S_S$  and mean  $S_V$ .

## IV. TVSS MEASUREMENTS OF THE TOWSHIP'S WAKE

### A. Comparison With Previous Studies

Our discussion is based on extensive comparison with previous studies because we lacked the video, photographic, and *in-situ* data to correlate the TVSS acoustic data with physical processes. Two such studies are emphasized because they were conducted under environmental conditions similar to those of the TVSS experiment and with similar ships. The first is the Joint Canada-U.S. Ocean Wave Investigation Project (JOWIP)<sup>69,70</sup>, in which extensive *in-situ* and photographic observations were collected for the Kelvin wave pattern and wake of the U.S. Navy tug *USS Quapaw* (Fig. 4). We refer to the JOWIP measurements made on July 28th, 1983, during which the winds were 0.6-2.8m/s and the sea state was calm. The characteristics of the *Quapaw*, which traveled straight line tracks in Dabob Bay, Washington, were very similar to those of *Mr. Offshore* (Table I), with  $V_{ship} = 6.39\text{m/s}$ ,  $Fn = 0.26$ ,  $Fd = 0.89$ , and  $B/L = 0.19$ . (Appendix A). The second study was performed by Trevorrow *et al.* (1994)<sup>3</sup>, who recorded high frequency (28-400kHz) acoustic observations of the wake generated by the *CSS Vector* in the coastal waters of Victoria, British Columbia on 19 March 1991. The wind and sea state were calm, and the characteristics of the *Vector* very similar to those of the TVSS towship, with  $V_{ship} = 5\text{m/s}$ ,  $Fn = 0.25$ ,  $Fd = 0.77$ , and  $B/L = 0.24$ . Their estimates of  $S_V$  in the wake of the *Vector* may be compared to ours because they are not corrected for  $TL_b$  (Appendix B) (note that our  $S_V$  corresponds to  $10\log_{10}$  of the  $M_V$  in their study). We begin by discussing the surface manifestation of the towship's wake, and follow with the subsurface acoustic

structure, persistence, and decay. The angular dependence of sea surface acoustic backscattering strength is discussed next, and we finish with an assessment of the uncertainties in the TVSS data.

## B. Influence of the TVSS Towship's Wake on Sea Surface Roughness

Relief maps of the sea surface above the TVSS were generated to examine the surface roughness associated with the towship's wake (Fig. 7). The procedure for constructing sea surface relief maps was identical to that used for bathymetry in reference (64) with an additional step designed to prevent false boundary detection of the towship's wake where high acoustic backscattering resulted from a dense distribution of microbubbles. These bubbles extended 6-8m below the sea surface above the towfish and caused false sea surface boundary detections in beams within  $\pm 45^\circ$  of the towfish's zenith (Fig. 8). Therefore an estimate of the sea surface altitude relative to the TVSS was computed for each beam by fitting a horizontal plane to sea surface detections in beams outside the wake, then surface detection was performed again on samples within a range gate of  $\pm 1.5\text{m}$  of the estimated sea surface boundary in each beam. The most significant features in the relief maps for each run consist of two troughs centered at across-track distances  $x = 0\text{m}$  and  $-90\text{m}$ , and a ridge which is centered at  $x = +90\text{m}$ , all extending the entire length of each track. The troughs have average depths of  $-0.5\text{m}$  below the mean sea surface, whereas the ridge has an average elevation of  $+0.3\text{m}$  above the mean sea surface. The average across-track width of the trough at the center is  $50\text{m}$ , and the widths of the ridge and trough at  $x = \pm 90\text{m}$  are about  $20\text{m}$ . Randomly distributed depressions and elevations of  $\pm 15\text{cm}$  are apparent in each run.

Contrary to what one might expect, the trough and ridge features in the surface relief maps are not due to variations in surface roughness. Rather, they are the result of phase biases in estimates of the phase zero-crossing of the split aperture output (eqn (14)) which lead to early and late boundary detections in our relief mapping scheme. The troughs at  $x = 0\text{m}$  in each map result from the phase biases in the upward beams produced by the backscatter from bubbles within the towship's wake, whereas the troughs and ridges to the left and right of each track are caused by phase biases resulting from the sidelobe return of the first bottom echo at nadir. The geometry of this problem can be seen in the single ping volume images in Figs. 5 and 9a. The width of the wake (Table IIa, section IV(D)) is nearly identical to the widths of the centerline troughs in each sea surface relief map, whereas the intersection of the bottom echo sidelobe return (circular feature) with the sea surface corresponds directly with the across-track locations of the trough and ridge pairs to the right and left of center in each map. A trough appears to the left of track while a ridge appears to the right because the phase of  $P(\theta, t)$  switches sign near zenith.<sup>64</sup> These phase biases are analogous to those produced by sea surface interference in swath bathymetry<sup>71</sup> and are a consequence of the low signal to interference ratios for the sea surface backscatter above the wake and at the times of the first bottom echo.

Negative sound speed anomalies created by subsurface bubbles are not believed to have caused the features in Fig. 7 for two reasons. The first is that such anomalies would produce a ridge in the sea surface relief, rather than a trough, because assumed sound speeds would be higher than actual sound speeds. Negative sound speed anomalies also fail to explain the ridges and troughs to the right and left of the wake because high bubble densities at these locations were not observed consistently, only intermittently (cf. Fig. 8a). This is not to say that void fractions ( $U_b$ ) within the towship's wake were insufficient to reduce the local sound speed. Negative sound speed anomalies between  $O(1)\text{-}O(100)\text{m/s}$  are likely to have occurred, but, for example, a  $250\text{m/s}$  negative sound speed anomaly across the vertical extent of the wake

would result in a positive sea surface elevation bias of ~1m. Therefore, we conclude that their effects on the sea surface relief maps were overshadowed by interference associated with the acoustic backscatter from resonant microbubbles within the wake.

Our estimate of the sound speed anomaly in the wake is based on theoretical and experimental results near 68kHz. Using the resonant bubble approximation (RBA, Appendix B), we estimate the contributions to the void fraction from resonant bubbles ( $u_b(a_r)$ ) within the wake 735m astern of the towship to be  $O(10^{-7})$  at 6.5m depth, and  $O(10^{-3})$  at 2.5m depth, with corresponding bubble densities  $O(10^5)$ ,  $O(10^9)/m^3/\mu m$ . Although the RBA overestimates bubble density and void fraction,<sup>98</sup> it is likely that bubbles larger and smaller than 48 $\mu m$ -size resonant bubbles were present, and therefore the RBA estimates of  $u_b(a_r)$  are lower bounds for  $U_b$ . This range of void fractions encompass values that have been observed within a meter of the sea surface during 10-15m/s winds and 2-4m breaking seas,<sup>33,50-52,55,56,68</sup> or in bubble clouds transported by surf zone rip currents.<sup>35,74</sup> Evidence that such void fractions produce sound speed anomalies near 68kHz from 1-100m/s includes the results of Dahl *et al.* (1997), who estimated the negative sound speed anomaly for 70kHz sound at 4m depth during 10m/s winds to be 1m/s. In addition, Commander and Prosperetti's (1989) model<sup>99</sup> predicts a negative anomaly of ~100m/s for 68kHz sound in water with a void fraction of  $10^{-2}$ , agreeing with experimental data presented in Fox *et al.* (1955).<sup>73</sup>

There was considerable uncertainty regarding the sound speed used in this study because only one CTD cast was obtained about 100m north of the location for run 1 (Fig. 1), approximately 4.5 hours prior to the acoustic data collection. To evaluate the presence and effects of variability in the local sound speed environment, we processed seafloor bathymetry with the same methods used to process the sea surface relief maps (Fig. 7) and compared the data to known environmental information.<sup>64</sup> The bathymetry in each TVSS run revealed a fairly smooth seafloor with a gradual west-south-westward slope, which was consistent with the silt-clay bedforms previously sampled in the region and with bathymetric surveys performed by the Naval Oceanographic Office. If the sound speed profile were not representative of the local sound speed environment for each run, the sea surface relief maps and bathymetry would have "curled" upward or downward in a symmetric manner about the track's centerline. The effect of using an incorrect sound speed profile is to under- or overestimate the actual angle of arrival  $\theta_a$ , producing bathymetric errors which increase in magnitude across-track. The fact that the sea surface relief maps and bathymetry were consistent with the known environmental conditions indicates that horizontal and temporal variability in the local sound speed environment (other than that cause by near-surface bubbles) was negligible during the TVSS experiment.

Variations in sea surface roughness were ruled out as possible mechanisms for the surface relief features in Fig. 7 because they would be too small to be resolved by the TVSS. The sea surface within a ship's wake is smoother than that outside the wake because turbulence within the wake and surfactant films, which concentrate at the wake boundaries, dampen short gravity waves<sup>26</sup>. Thus, damping of the ambient sea waves would result in a maximum elevation difference across track of ~10cm, which is less than the 16.98cm vertical resolution of the TVSS at zenith and the ~50cm elevation differences associated with the centerline trough in Fig. 7. Wave heights in the towship's Kelvin wave pattern also were beyond the resolution of the TVSS. Apart from the bow wave near the towship's stem, the maximum Kelvin wave height generated by *Mr. Offshore* most likely belonged to a cusp wave (Fig. 3), which would have a wavelength  $\lambda \approx 3.5m$  using eqn (1) with  $v = V_{ship} \sin \theta_c$ . The maximum cusp wave height  $h_c$  is limited by breaking at a wave steepness  $h_c / \lambda_c = 1/9$  (reference (27)), which implies  $h_c \leq 0.39m$  in the near field of the wake. Because the heights of successive crests in the Kelvin pattern vary inversely to the square roots of their distances from the ship, the maximum Kelvin wave height was less than 1.3cm above the



TVSS. This value is realistic in view of the results of numerical models, scale models<sup>16</sup>, and full scale ship experiments.<sup>69</sup>

### C. Influence of the Towship's Wake on Sea Surface Acoustic Backscatter

Sea surface acoustic backscattering strength images were processed to characterize the surface and near-surface region in and around the towship's wake. All such images include the roll and depth corrections derived in reference (64) and were processed from the corresponding relief maps using eqn (15) for  $S_s$  and the sidescanning and transmit beampattern compensation methods discussed in reference (64). Fig. 8a is the result for run 1. The main feature in the center of the image extending the entire length of the run is the acoustic backscatter from resonant microbubbles in the towship's wake directly above the TVSS (Figs. 1,9a,b). Because the compensation method reduces the majority of the array beampattern variations and the bottom echo return in the sidelobes, surface backscatter manifestations of the trough/ridge features in the sea surface relief maps (Fig. 7) are not observed. Average surface backscattering strength values in the center of the wake (Fig. 8b) are less than those near the wake's boundaries. The large scale ( $O(10^3) \text{ m}^2$ ) high backscatter features near  $x = +100$  and  $-100\text{m}$  are hypothesized to be bubble clouds generated by breaking ship waves. The angular dependence function (Fig. 10) was computed by averaging values for the positive and negative angles of incidence.

The dominant effect of the towship's wake on sea surface acoustic backscatter is attenuation near normal angles of incidence ( $\theta_i$ ). This may be seen by comparing the plots of mean  $S_s$  in run 1 with the angular dependence results of other investigators and with predictions from the APL-UW model (Figs. 8b,10), that all show sea surface backscattering strength near 68kHz peaking at normal incidence<sup>48</sup>. A value of 28dB for the vertical two-way attenuation ( $2TL_b$ , Appendix B) through the bubble layer can be estimated by assuming that the actual value of  $S_s$  at normal incidence is accurately predicted by the APL-UW model for 68kHz (APL-UW predictions for 60kHz are shown in Fig. 10 for comparison with the 60kHz published data from other investigators). This corresponds to an average attenuation coefficient of  $\alpha_{wake} \approx -2.1 \text{ dB/m}$ , which is comparable to attenuation measurements made by other investigators in both natural environments and ship wakes. Caruthers *et al.* (1999)<sup>74</sup> found the horizontal attenuation of sound through bubbles in rip currents to peak near 70kHz at 1-4 dB/m, whereas NDRC (1947)<sup>2</sup> measurements of the vertical attenuation of 21kHz sound through the wakes 366m astern of two destroyers yielded  $3.0 \pm 0.6 \text{ dB/m}$ .

Although bubbles on and very close to the surface also may have influenced the  $S_s$  values within the towship's wake, their effects were probably masked by the vertical attenuation. Large bubbles with radii  $O(100\mu\text{m})$  were probably removed from the water within the first minute after the ship passed. This is expected in view of their rise velocities (eqn (2)) and numerous observations of the persistence of visible bubbles on the surface in a ship's wake (see photographs in references 2,10,24,26,28,30-32,69,70,75]). Using the empirical formulae of Peltzer *et al.* (1992)<sup>23</sup>, we estimate the length of the white water wake behind *Mr. Offshore* to be between 153-230m. Therefore, bubbles on the surface were not likely to have affected the mean  $S_s$  in the wake 735m astern of the ship. Smaller bubbles with radii near  $48\mu\text{m}$  probably remained between depths of a few centimeters to several meters below the surface when the TVSS imaged the sea surface behind the towship because most ship wake observations suggest that the highest bubble densities occur near the surface.<sup>2,3,18</sup> Therefore, it is likely that, within the 17cm range resolution from the surface, a population of resonant microbubbles contributed to the  $S_s$  measurements in the wake, but their contributions were not large enough to counter the effect of attenuation from bubbles in the wake several meters below the surface.

Surface roughness also is hypothesized to have made only a slight contribution to the mean  $S_s$  within the wake. Because short gravity waves are damped within ship wakes<sup>26</sup>, we would expect the mean wave slope  $s$  (eqn (8)) in *Mr. Offshore*'s wake to be less than that produced by the ambient 3m/s winds. This implies that our measurements of  $S_s$  within a few degrees of normal incidence should actually be greater than predicted by eqn (7) because of greater contributions from specular reflections. This is not apparent in our measurements (Fig. 8b,10) because of vertical attenuation through the wake. Further aspects regarding the influence of the towship's wake on the angular dependence of  $S_s$  are discussed in section V. In the following, we focus on the wake's structure and on processes that affect its variability in time.

#### D. Wake Geometry.

Orthogonal vertical (Figs. 9a,b, 12b) and horizontal (Figs. 11,12a)  $S_v$  images were used to characterize the subsurface acoustic structure of the wake. The horizontal images were constructed using techniques for sea surface and seafloor imagery with time-of-arrival values determined for predetermined depths to yield a horizontal volume slice parallel to the mean sea surface. The image of the horizontal plane 3m below the sea surface for run 1 (Fig. 11) reveals the same features as the corresponding sea surface image (Fig. 8a), including the towship's wake and clouds of resonant microbubbles (labeled A-D), which are shown also in the enlarged portions of Fig. 11. The image of the horizontal plane 3m below the sea surface for run 2 (Fig. 12a) reveals the towship's wake generated during run 2 (centered at  $x = 0$ m) as well as the wake generated during run 1 (centered at  $x = -200$ m) (cf. Fig. 1, Fig. 12c).

The main characteristics of the towship's wake are both qualitatively and quantitatively similar to the measurements made in previous studies of ship wakes generated by vessels of similar size and speed characteristics as *Mr. Offshore*, and support the general finding that wake dimensions depend upon vessel size and speed (see Appendix C for a detailed discussion). For example, the wake widths, widening rates, and width-to-beam ratios, and wake depths (Table IIa) were comparable to those for the *CSS Vector* in Trevorrow *et al.* (1994)<sup>3</sup>, as well as NDRC measurements made of the wakes of similar sized ships at similar speeds. The slight cross-wake asymmetry (Fig. 7, 8) is found to varying degrees in the majority of wake measurements<sup>6,8,17,18,21,23,69,76</sup> and probably results from a combination of wind and sea conditions and propulsion system design. The only wake characteristics that were significantly greater than measurements in previous studies were the deepening rates and depth to draft ratios ( $h/D$ ).

#### E. Processes Affecting The Acoustic Structure of the Towship's Wake

The relatively high deepening rates and  $h/D$  ratios for the towship's wake above the TVSS suggest that downward turbulent diffusion was the dominant process governing the acoustic structure of the wake within the first few minutes after generation. This was most likely due to *Mr. Offshore*'s high propeller rpm, which was over twice that of the *CSS Vector* at 10 knots.<sup>3</sup> This hypothesis is consistent with the results in Ezerskii *et al.* (1989)<sup>8</sup> and with the findings in NDRC (1946)<sup>2</sup>, which showed that  $h$  and  $h/D$  increase with vessel speed for a variety of vessel sizes. From eqn (3), order of magnitude values for the vertical turbulent eddy diffusivity ( $k_v$ ) can be estimated with  $L_t = h - D_{p2}$  (wake depth minus propeller depth) and  $\Delta T_t = 179$ s, yielding  $0.14 \leq k_v \leq 0.18 \text{ m}^2 \text{ s}^{-1}$  for the three TVSS runs. These values, which correspond to the first three minutes of the wake's lifetime, are of the order observed by Dahl and Jessup (1997)<sup>38</sup> for bubble clouds entrained in breaking waves during 7.5-9.8m/s winds.

The data for the wake over the TVSS also suggest that the effects of buoyancy and

dissolution on the 68kHz acoustic structure of the wake 3 minutes astern of the towship were relatively weak. In still water, the rise velocities of bubbles with radii near  $48\mu\text{m}$  would only be  $0.4\text{cm/s}$  (eqn (2)), and may even be as low as  $0.1\text{cm/s}$  based on the measurements made by Detsch (1991)<sup>41</sup>. Thus, bubbles in the wake would only rise  $0.2\text{--}0.7\text{m}$  in the first 3 minutes after generation. Because high acoustic backscattering strengths were observed well below the ship's draft of  $2.6\text{m}$  (Fig. 9b), turbulent diffusion appears to dominate buoyancy. Dissolution effects are more difficult to ascertain because they must be assessed over time, and the wake data above the TVSS correspond to a constant wake age of 179s. Nevertheless, the spatial extent and relatively high  $S_V$  values in the wake clearly indicate that the wake grew rapidly in the first few minutes after generation, which supports the hypothesis that the relative role of gas dissolution was minor. These hypotheses are consistent with the conclusions of Ezerskii *et al.* (1989)<sup>8</sup>, who used  $284\text{kHz}$  acoustic backscatter measurements to evaluate the processes affecting bubbles in a ship's wake, and agree with the sensitivity analysis performed by Stewart and Miner (1987)<sup>22</sup>, which showed that increasing turbulent diffusion increases the wake's size.

The bubble generation mechanisms associated with the wake also influence its acoustic structure. Propeller cavitation is probably the strongest contributor because, although the depth of maximum  $S_V$  is slightly below the ship's draft in each run (Table IIa), the attenuation ( $2\text{TL}_b$ ) estimated from the mean  $S_S$  data in Fig. 8b indicates that the maximum bubble densities were most likely near the ship's propeller axis depth of  $1.5\text{m}$ . Propeller cavitation was invoked also by Trevorrow *et al.* who cited the cavitation studies on model propellers in NDRC (1947)<sup>2</sup> to support their hypothesis. The larger propeller rates and  $h/D$  ratios for *Mr. Offshore* imply that its propellers cavitated more strongly than the *CSS Vector*'s single propeller, resulting in higher bubble densities and vertical attenuation than those associated with the *Vector*'s wake. If we account for the vertical transmission loss of  $2.1\text{dB/m}$  estimated from the  $S_S$  data, then a rough estimate for the maximum  $S_V$  for *Mr. Offshore*'s wake averaged over the 3 TVSS runs is  $-7.6\text{dB}$ , which is about  $2.0\text{dB}$  greater than their  $88\text{kHz}$  measurements at  $1\text{m}$  depth in the wake generated by the *CSS Vector* at 10 knots.

The vertical acoustic structure of the towship's wake is partially masked by not correcting for  $2\text{TL}_b$ . For example, we cannot attribute the subsurface maximum in  $M_V$  at  $3\text{m}$  depth (Fig. 9c) to an actual bubble density maximum because one may exist between the surface and that depth. Such structures are present in both ship wakes and naturally-occurring bubble distributions and deserve more attention in future acoustic ship wake studies. Hyman *et al.*'s (1995)<sup>18</sup> particle dispersion data in the wake of an aircraft carrier show that ship-generated subsurface vortices can trap particles below the surface after the passage of a ship. Terrill's (2000)<sup>17</sup> acoustic measurements in the wake of a Navy oiler reveal what are believed to be subsurface bubble density maxima trapped in ship-generated vortices. These are predicted by Stewart and Miner's (1987)<sup>22</sup> turbulent ship wake model, which couples hydrodynamic and bubble-related processes. Fig. 6 in Trevorrow *et al.* (1994)<sup>3</sup> suggests a propeller generated subsurface bubble density maximum, but mixing was believed to prevent the formation of these features in other ship's wake observations. Fig. 6 in Terrill and Melville (1997)<sup>50</sup> indicate that such subsurface bubble density maxima, as measured by sound speed anomalies, occur episodically during individual wave breaking events. Because most bubble size distribution measurements are averaged over many realizations, most of the subsurface structure and variability is undetected. Much insight into air-sea gas-flux, and heat and momentum transfer can be gained by examining individual events and their variability.<sup>38,78</sup>

The spatial structure of bubbles in the TVSS towship's wake is most likely influenced by the twin vortices that characterize most ship wakes.<sup>2,5,9,18,19</sup> Two

adjacent vortices at  $x=0\text{m}$ , rotating outward in the  $x$ - $z$  plane would explain the high backscatter center feature between  $x = \pm 25\text{m}$  and extending the entire length of the run in the horizontal  $S_V$  images (Figs. 11 and 12a) at 3m depth. This feature should be distinguished from the twin bands at  $x = \pm 35\text{m}$  in Figs. 11 and 12a, which are due to the sidelobe response to the surface echo at nadir. These images do not reveal two distinct bands near the center of the wake probably because they could not be resolved by the ensonified volumes, which had across-track dimensions  $\Delta x_V = 6.4\text{m}$  in the wake center at 3m depth. Had we adapted our processing to provide for a more narrow across-track beamwidth, twin bands of resonant microbubbles generated by propeller cavitation and trapped in ship generated vortices might be apparent, as in Fig. 13. The relatively high bubble densities at  $x=0\text{m}$  resulting from the subsurface convergence of these vortices are the most likely cause for the attenuation that produced the anomalously low sea surface backscattering strengths at and near normal incidence (Fig. 8).

Evidence for convergences produced by these vortices on the surface at the wake boundaries is also seen at  $x = -170\text{m}$  in the horizontal backscatter image of Fig. 12a, where the right boundary of the 15-18 minute old wake generated during run 1 is fairly distinct. This boundary should be diffuse if horizontal surface velocities were absent and the ambient 3m/s wind were the only factor contributing to the water particle velocities at the surface. If we assume that the vortices are shed from the towship's stern, the divergent cross-wake velocities required to move resonant microbubbles to their positions at the wake boundaries ( $x = \pm 25\text{m}$ ) would be about  $\pm 11\text{cm/s}$ . This is of the order of magnitude of cross-wake velocity estimates reported in other wake studies. Pinkel *et al.* (1994)<sup>5</sup> observed values of  $\pm 15\text{cm/s}$ , 3 minutes after passage of a single propeller tugboat at 10 knots (Fig. 13), while Meadows *et al.* (1994) reported cross wake velocities of  $\sim 20\text{cm/s}$  over 12 ship lengths astern of a surface combatant with a Froude number of 0.23.

Although the TVSS measurements of the towship's wake are generally consistent with results in the literature, slight differences may be due to a variety of factors. Wake evolution is nonlinear, so comparing data which is interpolated in time is difficult. Researchers also use different criteria to define the wake and its boundaries. For example, Milgram *et al.* (1993)<sup>76</sup> defined the wake width as the width of zones of altered surface tension, whereas Trevorrow *et al.* (1994)<sup>3</sup> defined the wake by backscatter measurements greater than 20dB over the ambient level. If we applied their definition, the older wakes in Figs. 5 and 12 would not have been detectable. For acoustic measurements, sensor resolution, sampling, and frequency also affect the measurement of geometric parameters.

## F. Persistence and Decay of the Towship's Wake.

Comparison of the wake above the TVSS (Table IIa, Figs. 8,9,11) with the older wake generated during the previous run (Table IIb, Fig. 12) suggests that turbulent diffusion, buoyancy, and gas dissolution all become important as the age of the wake increases beyond 3 minutes. Vertical and horizontal turbulent diffusion would have decreased the density of bubbles in the wake by expanding the total wake volume, thereby contributing to the decrease in maximum  $S_V$ . This effect was limited by the relatively low sea state because ship wakes tend to dissipate more quickly in higher sea states that foster greater horizontal and vertical turbulent diffusion.<sup>2</sup> Buoyancy probably accounted for a small portion of the wake decay. In still water,  $48\mu\text{m}$  bubbles would rise 1-3m in 15 minutes, but because downward turbulent diffusion is likely to have continued beyond 3 minutes, the total rise distance would have been closer to 1m. Gas diffusion causing dissolution could explain most of the wake decay. For example, eqn (4) predicts that bubbles with radii between 20-100 $\mu\text{m}$  would

dissolve in less than one and a half minutes in seawater 50% saturated with air.

Because the wake was observable beyond 20 minutes, bubble dissolution was probably mediated by the air saturation level in the near-surface waters of the TVSS experiment site. Air saturation is determined primarily by the solubilities and dissolved concentrations of nitrogen and oxygen, and most ocean waters are supersaturated with respect to oxygen<sup>48</sup>. If this were the case, we might expect no dissolution of bubbles in the wake. This is doubtful because oxygen saturation levels in the near-surface waters of the northeastern Gulf of Mexico are typically less than 100%, probably because the primary productivity maximum is typically found at the base of the euphotic zone rather than at the surface<sup>49</sup>. Volume scattering measurements and historical data<sup>47</sup> indicate that assemblages of several types of zooplankton were present throughout the mixed layer during the TVSS experiment, and their respiration probably kept the surface waters below saturation.

The strongest factor limiting bubble dissolution was most likely the presence of surfactant materials that slowed bubble dissolution in the towship's wake and could explain why the wake existed as a strong acoustic scatterer beyond 22 minutes. Similar conclusions regarding wake persistence were drawn in the wake studies of Ezerskii *et al.* (1989)<sup>8</sup> and Miner and Griffin (1986)<sup>20</sup>. Surfactants are byproducts of biological activity<sup>23</sup> and are likely to have existed in relatively high concentrations during the TVSS experiment because zooplankton were observed throughout the mixed layer in each run<sup>47</sup>. The presence of surface films in the turbulent wakes of surface ships is well-documented<sup>9,23,26,76</sup> and believed to result from scavenging of surfactants from rising bubbles within the turbulent wake. These may become concentrated at the convergences along the wake boundaries and compacted by surface currents associated with breaking ship waves<sup>9,23</sup>.

When considered with the results of other studies, the TVSS data highlight many of the complex factors affecting the acoustic structure of ship wakes. These include the generating ship's characteristics, the wake's age, the local environmental conditions, and the acoustic frequency of the sonar observing the wake. An important effect of the wake is to attenuate high frequency sound, which is clearly seen in the TVSS sea surface acoustic backscatter data. For sonars with frequencies, pulse lengths, and beamwidths close to those of the TVSS, surface roughness variations associated with the Kelvin wave pattern and turbulent wake will have little effect on the sea surface acoustic backscatter of the wake when the ship's speed is 10 knots or less and the ship's length is 50m or less. For a few minutes after generation, downward turbulent diffusion is the dominant process affecting the wake's acoustic structure, especially in the case of high propeller speeds and shallow propeller depths. After a few minutes, no single process appears to dominate, consistent with the turbulent wake model results reported by Steward and Miner (1987).<sup>22</sup> However, this depends on the acoustic frequency because measurements using higher acoustic frequencies (smaller resonant bubble sizes) are likely to be more affected by gas diffusion, whereas those at lower acoustic frequencies (larger resonant bubbles) are more likely to be affected by buoyancy.<sup>22</sup> In any case, the persistence of the wake will tend to increase as the surface water air saturation level increases, the ambient sea state and wind speed decrease, and the concentration of surfactant materials increases.

## G. Other Acoustic Scattering Sources

Boundary reverberation was the most significant source of scattering besides near-surface bubbles and surface roughness. This affected all but the single beam vertical volume images (Fig. 9b). The depth bias in the sea surface relief maps resulting from the sidelobe response to the bottom echo was not corrected so that we could illustrate this important problem, which must be considered when using multibeam

systems in shallow water studies of the sea surface and near-surface bubbles. Our transmit pattern compensation method removed the bottom echo sidelobe returns in the horizontal volume and sea surface acoustic backscatter imagery, but did not account for the elevated ambient noise resulting from bottom and surface reverberation and multipath. These are likely to have produced a slight upward bias in the  $S_V$  and  $S_S$  data.

Despite the presence of zooplankton and fish in the TVSS experimental area, their contributions to the  $S_V$  and  $S_S$  data presented here were negligible. Fish were only observed near the bottom during the TVSS experiment and are not likely to have been near the surface in view of surveys conducted by the National Marine Fisheries Service.<sup>47</sup> Zooplankton scattering layers with maximum  $S_V$  values of -59dB were observed in the upper thermocline and at the base of the mixed layer, whereas weaker layers with maximum  $S_V$  values of -65dB were observed in the upper 20m of the water column. These may have made a small contribution to the  $S_V$  measurements of the older wake (Fig. 12, Table IIb), but the sea surface backscatter and volume backscatter in the wake above the TVSS (Figs. 8,9,11) were clearly dominated by scattering from resonant microbubbles and/or surface roughness. Perhaps the strongest influence from biologics was their contribution to the ambient bubble population<sup>45,80,81</sup>, but this could not be ascertained with our limited *in-situ* data.

Scattering from turbulent microstructure is deemed insignificant as well. Turbulence scatters sound by producing gradients in the acoustic index of refraction. These gradients are controlled by turbulent fluctuations in water particle velocity, temperature, pressure, and salinity. Temperature gradients usually have the greatest effect, but the thermal gradients required to produce values of  $S_V$  near those resulting from resonant microbubbles are at least two orders of magnitude larger than those most likely to be found in the TVSS towship's wake. For example, Pelech *et al.* (1983)<sup>82</sup> observed a peak  $S_V$  of -39dB at 75 kHz for subsurface turbulent wake produced by a self propelled body traveling 0.9m/s in a stable thermocline of 1.0-1.5°C/ft. The temperature and density profiles recorded during the TVSS experiment were uniform through the entire mixed layer to a depth of 39m, and radiant heating or fluid discharge from the ship would have been the only sources of thermal microstructure. Under these conditions, thermal gradients in the towship's wake are likely to have been on the order of 0.1°C/m<sup>2</sup> (cf. reference (83)), and the acoustic scattering from turbulence would have been extremely weak. Thorpe and Brubaker (1983)<sup>84</sup> demonstrated this by measuring the backscatter of 102 kHz sound from the subsurface turbulent wake of a towed sphere; when thermal gradients were absent, backscatter from velocity fluctuations alone were rapidly decaying or unobservable.

## V. SEA SURFACE ACOUSTIC BACKSCATTER AND NEAR SURFACE BUBBLES

### A. Angular Dependence of Sea Surface Acoustic Backscattering Strength

Although the primary effect of the wake on  $S_S$  was attenuation at normal incidence, its influence was seen near the wake's boundaries as well (Figs. 8,10). For  $|\theta_i| = 10^\circ - 30^\circ$ ,  $S_S$  exceeds the APL-UW model predictions and the data collected by Urlick and Hoover (1956)<sup>85</sup> and Garrison *et al.* (1960)<sup>86</sup>. The surface and near-surface images (Figs. 8a,9,11,12a,b) show that some of this is due to backscattering from near-surface resonant microbubbles near the wake's boundaries. Outside the wake, ( $|\theta_i| > 18^\circ$ ), bubble clouds generated by breaking ship waves (e.g. Fig. 11) also contribute to these elevated  $S_S$  levels (note that the four clouds labeled in Fig. 11 were selected for analysis in the following section because they are easily

distinguishable from the  $S_S$  angular dependence, but other clouds are present closer to the wake's boundaries).  $S_S$  values between  $|\theta_i| = 10^\circ - 30^\circ$  exceed those predicted for saturation conditions (eqns (7) and (11)) probably because of surface roughness scattering in the form of  $\sigma_{sc}$  and  $\sigma_f$  (eqns (7)-(9)). Surface currents within ship wakes have been shown to increase the steepness of ambient and Kelvin waves at the wake's boundaries<sup>12</sup>, which would then increase  $\sigma_f$  in eqn (8) by increasing the surface slope term ( $s$ ). Short gravity waves may also be generated by the wake, and could contribute to the total  $S_S$  near the wake's boundary (e.g. Fig. 3 in reference (75)).

For  $|\theta_i| = 30^\circ - 60^\circ$ , the  $S_S$  curve fits generally in the middle of the published curves, and is well within the  $\pm 5$ dB uncertainty estimated for the APL-UW model prediction<sup>59</sup>. In this range of angles, scattering from resonant near-surface microbubbles accounts for much of the APL-UW model output, and has been identified as a significant component in each of the published  $S_S$  curves<sup>48</sup>. The same is true for the TVSS data. Small scale bubble clouds, which appear as the randomly distributed "speckle-like" features in Figs. 8a, 11, and 12a, are most likely generated by minor breaking events due to the ambient 3m/s winds, and appear to contribute to the mean  $S_S$  for all angles of incidence measured. The contributions from the larger scale bubble clouds generated by breaking ship waves (Fig. 11) are evident in Table III, which shows that peak  $S_S$  values are within 1dB of those predicted by eqn (11) for saturation conditions (cf. Fig. 19 in McDaniel (1993)). Such contributions from near-surface bubbles are expected in view of the TVSS beam geometry at the sea surface (Fig. 6).

Because the large scale bubble clouds are a feature unique to the far field of the ship's wake (Fig. 3), one might expect the mean  $S_S$  (Fig. 10) to be greater than the 60kHz APL-UW model predictions for  $|\theta_i| = 30^\circ - 60^\circ$ , which represent the  $S_S$  due to the ambient sea only. However, wide disparities between sea surface backscattering strength measurements made by different investigators are common.<sup>48</sup> Reasons that might explain why the TVSS-derived mean data for these angles are lower than expected include differences in acoustic frequency, near surface bubble distributions, and wind speed measurement and averaging methods. Variability in near-surface bubble populations is probably the most important. For example, the data collected by Urick and Hoover (1960), the TVSS data, and the data used for the empirical terms in the APL-UW model correspond to different open ocean environments. The data in Nutzel and Herwig (1995)<sup>62</sup> were collected 40nm from the coast, but in water depths near 30m, whereas the data reported by Garrison *et al.* were collected in Dabob Bay, Washington, which was believed to contain a larger population of ambient microbubbles than the locations where the other data were collected.<sup>48</sup> Because resonant microbubbles have been identified<sup>48</sup> as the source of anomalously high values of high frequency acoustic backscatter<sup>48</sup>, this would explain the high  $S_S$  values for  $|\theta_i| > 20^\circ$  in Garrison *et al.* Microbubble concentrations higher than those produced solely from the ambient wind and wave conditions have been associated with biological activity<sup>43,80</sup>, such as zooplankton respiration.<sup>81</sup> As in the wake, air-saturation levels and the presence of surfactant materials may also increase ambient bubble residence times.

Wind speed measurement altitude is another potential source of disparity when comparing  $S_S$  data from different studies. The standard wind speed measurement altitude above the sea surface for air-sea interaction studies is 10m. The change in wind speed with measurement height depends on the stability of the atmospheric boundary layer, which is affected mostly by the air-sea temperature difference ( $\Delta T$ ), and the largest changes occur during unstable conditions.<sup>87</sup> Knowing  $\Delta T$ , one may use the tables in Smith (1988)<sup>88</sup> to compute the equivalent 10m wind ( $U_{10}$ ) for a given measurement height, or use the formula in Large and Pond (1981)<sup>89,90</sup>. The wind speed in Nutzel and Herwig (1995)<sup>62</sup> was measured 47m from the sea surface and was not

converted to  $U_{10}$ , which partially explains why their curves differ from the others. If their wind speeds were reduced to  $U_{10}$  using the empirically-derived factor in Stolte (1994)<sup>90</sup> for their experiment, their 3m/s sea surface scattering strength data would correspond to  $U_{10} = 2.5\text{m/s}$ . For the TVSS experiment, neither the wind measurement height nor  $\Delta T$  were recorded. Garrison *et al.* (1960) measured their wind speed at a height of 3.7m and did not convert to  $U_{10}$ , whereas Urick and Hoover (1956) do not state their measurement height.

Another important factor is the acoustic data averaging period relative to the rate of change of the wind speed. When the period is too short, the measurement may emphasize small time scale gusts or quiescent periods. For wind speed to best correlate with sea surface roughness and bubble concentrations, the period should be no less than 20 minutes and no longer than 1 hour<sup>99</sup>. In the TVSS experiment, only one wind speed measurement was taken 4.5 hours prior to the acoustic data collection, which lasted over an hour (Fig. 1). The data in Garrison *et al.* (1960) were collected over a one-year period, and the data in Urick and Hoover (1956) were obtained during a one-month period. Neither Garrison *et al.* (1960) nor Urick (1956) describe whether instantaneous or average wind speeds were recorded, and how their data were combined to produce discrete wind speed intervals. It may be that data were grouped into the respective intervals by rounding, e.g. data corresponding to winds between 4.6 and 5.4 m/s were grouped into the data set for 5m/s winds. Nutzal and Herwig (1995) averaged winds over 10 minute periods, and collected their backscatter data over 20 minute periods.

## B. Bubble Clouds Generated by Breaking Ship Waves

The large scale bubble clouds (Figs. 8a and 11) which contribute to the sea surface backscattering strength curve in Fig. 10 are most likely generated by breaking ship waves. The best support for this hypothesis is the example in Fig. 13, which shows the 195kHz Doppler sonar data of Pinkel *et al.* (1995)<sup>5</sup> corresponding to the wake and Kelvin wave pattern of a single propeller tugboat traveling 10 knots in 2.5m/s winds (Fig. 13a). The vertical bands of relatively high acoustic backscatter, which occur to the left and right of the twin vortices in the wake, were due to bubbles injected by breaking divergent bow waves. This was confirmed by observers at the experiment site. As in the TVSS data, acoustic backscattering from these bubble clouds appears to be intermittent 3 minutes aft of the ship. This figure demonstrates that the divergent bow waves close to the ship's hull break most frequently (e.g. Fig. 4), but divergent bow waves in the far field and transverse waves may also break.<sup>2,16</sup> The transverse waves generated by *Mr. Offshore* were relatively high because their wavelengths from eqn (1) were about  $L/4$ , and transverse waves are reinforced by divergent bow waves when  $L$  is of order 1,2,3,4... transverse wavelengths.<sup>16</sup> Savitsky (1970)<sup>91</sup> has shown that the wave diffraction, reflection, and interference produced by the mean velocity gradients in the turbulent wake may cause wave heights outside the wake to increase by as much as 75%, while Griffin (1988)<sup>12</sup> has shown that the surface current associated with the turbulent wake of a ship can increase the wave steepness outside the wake. The ambient winds also may have enhanced breaking, especially for the steepest waves near the cusp crests.

Because bubble clouds existed 3 minutes astern of the towship, they probably were similar to the  $\gamma$  plume described in Monahan and Lu (1990)<sup>63</sup>, which is the third stage in the lifetime of a typical bubble plume generated by a breaking wave. These are the types of plumes which are found about 10 seconds after a breaking wave, with no visible signature on the surface because the largest bubbles have risen out of the water and smaller bubbles continue downward due to turbulent diffusion. The lifetimes of these clouds vary, depending upon the conditions described for the wake in



section IV, and their void fractions are of  $O(10^{-7})$ .

Volume scattering strengths for the bubble clouds in the 68kHz TVSS imagery (Table III) corresponded to the average values over the depths spanned by the ensonified volumes in each cloud, which were between 5-10m (eqn (31)). These values are comparable to those associated with the bubble cloud generated during Dahl and Jessup's (1995)<sup>38</sup> breaking *Event A* with an average 240kHz  $S_V$  of -33dB for the 0.5-1.0m depth layer (note their  $S_V$  is the decibel equivalent of volumetric back-scattering cross section per unit volume (Appendix B), so we have added  $10\log_{10}(4\pi)$  for comparison with our results). Their observations were taken during 9.8m/s winds in which the wave phase speed was estimated to be 7m/s. Bubbles produced by air entrainment after breaking experienced a downward fluid-particle entrainment velocity of 7cm/s, and the vertical extent of the associated bubble layer reached ~4m about 60s after breaking. Orbital motion from local gravity waves supported this downward turbulent diffusion, and larger bubbles at and near the surface were removed after about 30s. The lifetime of the subsurface bubble clouds was hypothesized to be of  $O(100)$  seconds based on Monahan and Lu's (1992)  $\gamma$  plume model.

Because we lacked the *in-situ* data to confirm our hypotheses, we considered and rejected two other potential explanations for the bubble clouds in the TVSS data: At first, scattering from schools of fish was ruled out because the bubble clouds appeared on both sides of the wake at nearly the same across-track distances, and a more random spatial distribution would be expected from biological scatters. Because fish were observed on the bottom during each run, but not in the mid- or upper-water column, they are unlikely to have been present near the surface. In fact, there is a widely-observed tendency for schooling fish to remain near the bottom during the day to avoid predators<sup>36</sup>, and historical data for the northeastern Gulf of Mexico support this.<sup>47</sup> Furthermore, the target strengths (TS) (Table III) of ensonified volumes within the bubble clouds are much higher than what is expected for typical fish densities near the surface.<sup>36</sup> Clouds of propeller-generated bubbles trapped in large scale vortices shed from the towship stern were ruled out as well, because the vortices observed tended to remain within the turbulent wake. The horizontal velocities required to advect the clouds from the wake's boundary to their locations across-track are excessively high. For example, Bubble cloud "A" in Fig. 11 would require a minimum horizontal velocity of 0.42m/s. This value is at least two times: the seaward velocities of bubble clouds transported in surf zone rip currents observed by Dahl (2001)<sup>35</sup>, the average particle velocities in the ship wake of Pinkel *et al.* (1995) (Fig. 13b), and the values observed by Thorpe and Hall (1983)<sup>39</sup> for bubble clouds influenced by a tidal current.

### C. Processes Affecting The Near-surface Bubble Clouds

The spatial characteristics of the bubble clouds in the surface (Fig. 8a) and volume imagery (Figs. 5,11) are influenced by the relative speed of the towship, turbulent mixing produced by breaking wind waves, and surface currents associated with the Kelvin wave pattern and wake (e.g. Fig. 13). The relative ship speed probably caused little distortion from the actual spatial characteristics because the ship's speed was an order of magnitude larger than the surface current velocities that might have been generated by the ship (e.g. Fig. 13b). Likewise, the ambient wind waves were probably too small to generate significant turbulent mixing. The strongest factor influencing the cloud shape is hypothesized to be the surface currents generated by the towship and its wake. Other factors probably included the initial injection of individual bubbles, which occurs at a velocity close to the phase speed of the breaking wave that generates them<sup>92</sup>, and the Stokes drift<sup>93</sup> associated with the Kelvin waves. A small contribution may also result from a Stokes drift associated with wake-generated short

gravity waves produced by the towship's wake. Gu and Phillips (1994)<sup>75</sup> provide an excellent photograph of these waves in the wake of the *Bay Lady*, a ship with dimensions and characteristics nearly equal to *Mr Offshore*'s ( $V_{ship} = 4\text{m/s}$ ,  $B/L = 12.19\text{m}/42.7\text{m} = 0.28$ ,  $Fn = 0.20$ ) during 3m/s winds.

A comparison with bubble cloud data reported in other studies provides clues to the relative roles of horizontal advection and turbulent mixing in affecting the spatial characteristics of the clouds. Wu (1992)<sup>94</sup> reviewed a wide range of surface whitecap data in which the characteristic length ( $L_{bc}$ ) and width ( $W_{bc}$ ), respectively measured perpendicularly and parallel to the wave crests, yield a characteristic scale  $1\text{m} \leq (s_{bc} = \sqrt{W_{bc} L_{bc}}) \leq 4\text{m}$ , and an average ratio  $W_{bc}/L_{bc} = 2.15$ . Crawford and Farmer (1987)<sup>68</sup> used a submarine mounted 119kHz upward looking sonar during 10m/s winds to observe bubble plumes at 6m depth with horizontal extents of 5-15m and width to length ratios of about 1.0 measured parallel to the wind direction. Thorpe and Hall (1983)<sup>39</sup> used a 248kHz upward-looking sidescan sonar to observe bubble clouds generated by breaking waves in 8m/s winds with widths and lengths of 3-4m and 6m respectively. For a range of wind speeds up to about 12m/s, they found the mean ratio of width to length to be about 0.7. In the presence of strong near-surface currents, however, this value decreased substantially. Windrows formed by Langmuir circulation may be an example of this as well.<sup>39</sup> Similarly, Dahl (2001)<sup>35</sup> used several 240kHz upward looking sonars to observe bubble clouds transported by rip currents in the surf zone with length scales of ~50-100m and widths of ~12m, yielding width to length ratios of ~0.12-0.24. These observations suggest that when horizontal advection is more important than downward turbulent mixing, which appears to be case for the TVSS data, bubble cloud length scales will be on the order of tens of meters, and width to length ratios will be less than one half.

## VI. SUMMARY AND CONCLUSIONS

Because there are relatively few acoustic studies of turbulent ship wakes in the open literature, our results shed more insight into their acoustic properties. The TVSS data suggest that decreasing the propeller's axis depth or increasing its rpm will increase the wake depth and the density of bubbles in the wake due to an increase in propeller cavitation. Sea surface backscattering strength imagery astern of the wake generating vessel demonstrated a 2.1 dB/m average vertical attenuation in the wake, as well as increased scattering levels due to bubble clouds generated by breaking ship waves. The acoustic data suggest that turbulent diffusion is the dominant process governing the spatial structure of the turbulent wake during the first few minutes after generation. The dominant process affecting the wake decay is hypothesized to be gas diffusion causing dissolution mediated by the air saturation and concentration of surfactant materials in the near-surface water. These observations are relevant to the study of naturally-occurring bubble distributions because the void fractions in the wake are approximately those found in the near surface bubble layer generated by breaking waves in 10-15m/s winds.

This study also demonstrates the potential for high frequency multibeam sonars in the investigation of near-surface physical processes. The horizontal and vertical coverage provided by the multibeam geometry permits a more complete characterization of the spatial structure of near-surface bubble fields than could be obtained with a single beam system. This was demonstrated also by our vertical and horizontal imagery of the towship's wake. Boundary reverberation in the sidelobes is a major limitation of a multibeam system as demonstrated by the sea surface relief maps and surface and volume acoustic backscatter imagery of the towship's wake.

Because a relatively controlled population of near-surface bubbles can be

produced by a towship with specified size and speed characteristics, future studies like this, with more extensive *in-situ* sampling, may greatly increase our understanding of both turbulent ship wakes and the processes affecting near-surface bubble distributions in the ocean.

## ACKNOWLEDGMENTS

This work was funded by the Office of Naval Research under ONR-NRL Contract No. N00014-96-1-G913. The authors would like to thank CAPT Tim Schnoor, USN (Office of Naval Research), Sam Tooma, and Maria Kalcic (Naval Research Laboratory) for their support; Candy Robertson and Lisa Tubridy (Coastal Systems Station) for information on the TVSS; and Pat Jordan (Marine Physical Lab) for administrative support. The authors would also like to thank Grant Deane (SIO) for helpful discussion about bubble scattering, Eric Terrill (SIO) for his information concerning wakes, Jerome Smith (SIO) for access to his ADCP data from reference (5), and George Marmorino (NRL) for providing references (22) and (9). Thanks are due to Jo Griffith (MPL) for help with the figures.

## APPENDIX A. FACTORS INFLUENCING THE KELVIN WAVE PATTERN AND TURBULENT WAKE OF A MOVING SHIP

### 1. Ship Characteristics

Both the Kelvin wave pattern and the turbulent wake depend upon the generating ship's characteristics.<sup>14,16</sup> Wave amplitudes in the Kelvin pattern generally increase with the ship's speed and size, but variations in hull form may result in significant deviations from the classical Kelvin pattern because the ship is an extended body and not a point pressure source.<sup>16</sup> Typical ship wave patterns are composed of divergent waves from the bow, hull, and/or stern (Figs. 3,4), and the half angle width between the wave pattern and the ship's course ( $\theta_K$ ) may be as low as 9-10° for fine, fast ships, or as high as 22°.<sup>16</sup> Fast, shallow draft vessels will have a strong divergent wave structure, while slow, deep draft vessels will have larger transverse waves.<sup>16</sup> Non-linear effects not included in the classic Kelvin wave theory are one source of these variations.<sup>9,5</sup> Short wavelength gravity waves also are generated from the ship's hull and the turbulent wake, propagating in directions nearly perpendicular to the ship's course.<sup>17,75</sup> The mean velocity gradients within the turbulent wake may cause wave diffraction, reflection, and interference which tend to decrease  $\theta_K$ , increase the angle between the cusp crests and the ship's course ( $\theta_c$ ), and increase the wave steepness at and near the cusps.<sup>12</sup>

The turbulent wake is affected by ship size, speed, and hull form, as well as propeller characteristics. The width and thickness of the turbulent wake generally increase with the vessel's size and speed, but a small vessel with a shallow propeller, more than one propeller, and/or a propeller with a high rpm can produce a turbulent wake comparable to that of a larger vessel at the same speed or a similar sized vessel at greater speed. This is because faster turning propellers will produce greater seawater particle velocities, turbulence, and bubble densities. The wake width and depth are affected by the generation of outward moving surface currents associated with the twin vortices shed by the ship's hull and reinforced by the ship's propeller(s)<sup>9,18</sup>, so a wider and deeper wake is expected when the ship's propeller(s) are turning faster. Similarly, a propeller will cavitate more strongly when it is turning faster, and therefore the bubbles in the wake will be denser. The cavitation number  $\sigma_N$ , an index used to parameterize propeller cavitation in naval architecture, is given by

$$\sigma_N = \frac{2(P_w - P_a)}{\rho n^2 d_p^2} \quad (A1)$$

where  $P_w$  is the free stream pressure,  $P_a$  is the vapor pressure of air,  $\rho$  is the density of sea water,  $n$  is the propeller rpm, and  $d_p$  is the propeller diameter.<sup>97</sup> For low thrust coefficients,

$$K_T = 2 T_p / \rho n^2 d_p^4, \quad (A2)$$

where  $T_p$  is the propeller thrust, cavitation will be greater for lower values of  $\sigma_N$ .<sup>96,15</sup> Thus, a high propeller rpm yielding a low thrust coefficient and a low cavitation number results in a high cavitation rate. A shallower propeller depth also supports a high cavitation rate because  $P_w$  decreases with decreasing depth.

## 2. Non-dimensional Parameters Used to Characterize Surface Ships

The dependencies of the Kelvin wave pattern and the turbulent wake on ship characteristics may be parameterized in several ways. One of the most common non-dimensional parameters used in naval architecture is the Froude number, defined as

$$Fn = V_{ship} / \sqrt{gL} \quad (A3)$$

where  $V_{ship}$  is the ship's speed,  $L$  is the ship's length, and  $g=9.81\text{m/s}^2$  is the gravitational acceleration. Because the hydrodynamic characteristics of vessels with similar Froude numbers are similar by a scale factor<sup>32</sup>,  $Fn$  is useful for comparing the Kelvin wave patterns and turbulent wakes of different ships. Two other non-dimensional parameters which have been related to a ship's bow wave height are the beam to length ratio  $(B/L)$ <sup>16</sup>, and the draft Froude number, which is defined as<sup>25</sup>

$$Fd = V_{ship} / \sqrt{gD}, \quad (A4)$$

where  $D$  is the vessel draft.

The parameters of the TVSS towship, *Mr. Offshore*, (Table I) provide insight into the nature of the ship's wave pattern and turbulent wake. *Mr Offshore's*  $Fn = 0.20$  is typical of ships designed for slower speeds, such as transports and tankers. Ships designed for high speed operations, such as naval destroyers, typically have values of  $Fn$  near 0.50. *Mr Offshore's*  $Fd = 0.81$  is characteristic of a medium speed, shallow draft vessel. For a typical fast, shallow draft vessel,  $Fd > 1.0$ , whereas  $Fd < 0.6$  for slow, deep draft vessels. Although bow wave height is influenced by a variety of factors, such as the shape of the bow near the waterline, ships with higher draft Froude numbers exhibit larger bow waves than similar sized ships with lower values of  $Fd$ .<sup>25</sup> Bow wave height is also proportional to  $B/L$  and  $V_{ship}^2$  for a wide variety of vessels, so the ratio is useful for comparing the bow wave heights of ships at similar speeds.<sup>16</sup> *Mr. Offshore's*  $B/L$  of 0.24 is relatively high and in the range of values for tug boats and fishing vessels, whereas  $B/L=0.10$  is typical of destroyers and cruisers.

## 3. Environmental Factors

Environmental conditions can also affect the structure and persistence of both the wake and wave pattern of a ship. In shallow water of depth  $H_w$ , if the ship's velocity  $V_{ship}$  exceeds  $\sqrt{gH_w}$ , then  $\theta_K$  will increase beyond  $19^\circ 28'$ . In most cases this corresponds to water depths on the order of several ship drafts or less. If the ambient sea is characterized by large horizontal and vertical temperature gradients, then temperature gradients across the wake boundaries may be as large as  $2^\circ\text{C}$ <sup>83</sup>, but if the upper water column consists of an isothermal mixed layer, cross-wake temperature

gradients of only 0.01° C/m or less are expected.<sup>2</sup>

## APPENDIX B. SOUND INTERACTION WITH BUBBLES

### 1. Volume Acoustic Scattering

In addition to  $S_V$  (eqn. 15), the TVSS data also were used to compute volume acoustic backscattering cross section per unit volume ( $M_V$ ), defined as the ratio of scattered power at a reference distance of 1m, to the intensity incident on a unit volume.<sup>66</sup>  $M_V$ , which has units of  $m^{-1}$ , is fairly common in the bubble backscatter literature<sup>33,34,51</sup>, and is related to  $S_V$  by

$$10 \log_{10} M_V = S_V + 10 \log_{10} 4 \pi. \quad (B1)$$

Both  $M_V$  and  $S_V$  are related to target strength (TS), which is defined as 10 times  $\log_{10}$  of the ratio of the intensity of the sound returned by a target, at a distance of 1m from its acoustic center, to the incident intensity from a distant source. TS is computed for ensonified volume cells by using the fact that  $S_V$  is the target strength of a unit volume

$$TS = S_V + 10 \log_{10} V. \quad (B2)$$

These quantities are related to bubble density in an ensonified volume by

$$S_V = 10 \log_{10} \left( \frac{1}{4\pi} \int_0^\infty \sigma_s(a) n(a) da \right), \quad (B3)$$

where  $\sigma_s(a)$  is the scattering cross section for a bubble with radius  $a$  and  $n(a)$  is the number of bubbles per unit volume with radius  $a$  (reference (68)). For an ideal bubble,  $\sigma_s(a)$  is given by

$$\sigma_s(a) = \frac{4\pi a^2}{[(f_r/f)^2 - 1]^2 + \delta^2}, \quad (B4)$$

where  $f_r$  is the resonant frequency of the bubble (eqn (6)),  $f$  is the incident acoustic frequency, and  $\delta$  is the total damping coefficient of the bubble.<sup>36</sup> For calculations of volume scattering strength from a bubble layer of thickness  $R_2 - R_1$ , the transmission loss through the layer ( $TL_b$ ) should be included. It also depends upon the bubble density according to

$$TL_b = \frac{4.34}{4\pi} \int_{R_1}^{R_2} \int_0^\infty \sigma_e(a) n(a, R) da dR, \quad (B5)$$

where  $\sigma_e(a)$  is the extinction cross section of an ideal bubble of radius  $a$ , which is given by

$$\sigma_e(a) = \sigma_s(a) + \sigma_a(a), \quad (B6)$$

where  $\sigma_a(a)$  is the bubble's absorption cross section. Measurements of  $TL_b$  and  $S_V$  are dominated by bubbles at resonance because  $\sigma_s(a)$  and  $\sigma_e(a)$  peak at  $a = a_r$  (see Fig. 4 in reference (97)).

It is apparent from (B5) that knowledge of  $n(a, R)$  is required for correcting  $S_V$  measurements for  $TL_b$  in a dense bubble layer. This may be done with *in-situ* methods<sup>46</sup> or by solving a set of Fredholm integral equations of the first kind<sup>98,51</sup> with each equation in the non-logarithmic form of (B3) representing one of a number of

different acoustic frequencies.

When multiple frequencies or *in-situ* bubble size measurements are unavailable, one may invoke the resonant bubble approximation (RBA),<sup>2,36</sup> which relies on the assumption that contributions to the total scattering and extinction from off-resonant bubbles are negligible, resulting in the following closed form expressions for  $S_V$  and  $TL_b$ .<sup>2,97</sup>

$$\begin{aligned} S_V &= \pi a_r^3 n(a_r) / (2\delta) \\ TL_b &= 8.68 a_r^3 n(a_r) / \delta_r \end{aligned} \quad (B7)$$

where  $\delta_r$  is the reradiation damping constant, and we have dropped the dependence on  $R$  for brevity.

There is considerable uncertainty in the resonant approximation because off-resonant bubble contributions are in fact significant.<sup>98</sup> If this uncertainty is unacceptable, single frequency studies such as ours and that of Trevorrow *et al.* (1994)<sup>3</sup> are forced to exclude  $TL_b$  from the calculation of  $S_V$ , making such estimates of  $S_V$  lower bounds on the actual values.

## 2. Sound Speed Dispersion Through A Bubbly Medium

The speed of sound in a bubbly medium is dispersive. Dispersion occurs because individual bubbles have a frequency response which depends upon their radii, so bubbles of different sizes will react differently to different acoustic frequencies. The complex sound speed in a mixture of bubbles with different radii is derived by Commander and Prosperetti (1989)<sup>99</sup> as:

$$c_b^{-2} = c_0^{-2} + 4\pi \int_0^\infty \frac{an(a)da}{\omega_r^2 - \omega^2 + 2i\delta\omega} \quad (B8)$$

where  $c_0$  is the bubble-free sound speed,  $c_b$  is the complex sound speed in the bubbly medium,  $\omega=2\pi f$  is the radial frequency, and  $\omega_r$  is the radial frequency at resonance. When integrated over all bubble sizes present, the real and imaginary parts of  $c_b$  describe the phase speed and attenuation of sound propagating through the medium.

For sound with a frequency much lower than the resonant frequency, dispersive effects become negligible, and sound speed depends on the void fraction ( $U_b$ , defined as the total fraction of air by volume), rather than the number and sizes of bubbles in the medium. In this case, and for  $U_b \leq 10^{-5}$ , Wood's (1955)<sup>100</sup> equation describes the sound speed which decreases as void fraction increases<sup>36</sup> (see Fig. 1 in reference (50)). The volume fraction of bubbles of radius  $a$  is typically expressed by approximating each as a sphere:<sup>72</sup>

$$u_b(a) = (4/3) \pi a^3 n(a) \quad (B9)$$

so that the total void fraction may be expressed as:<sup>72</sup>

$$U_b = (4/3) \pi \int_0^\infty a^3 n(a) da \quad (B10)$$

Data collected by Terrill and Melville (1997)<sup>50</sup> suggest that the dispersive effects of bubbles may extend to frequencies as low as 5kHz near the surface during storms. Dispersive effects are most common below 25kHz, but variations in sea surface height can produce fluctuations in the resonant frequencies of near-surface bubbles for  $f_r = 25\text{kHz}$  to  $100\text{kHz}$ .<sup>101</sup> Eqn (B8) is valid for  $U_b$  up to about 0.01. At higher void

fractions, multiple scattering effects may become significant.<sup>99,102</sup> Void fractions within a meter of the sea surface under breaking waves are typically of  $O(10^{-6})$ , but may reach up to  $O(10^{-4})$  when breaking wave heights exceed 2-3m.<sup>48,51,100,103</sup> and 0.3-0.4 in the surf zone.<sup>104</sup>

### 3. Near-surface Bubble Contributions to Sea Surface Acoustic Backscattering Strength

Contributions to the TVSS derived sea surface acoustic scattering strength ( $S_S$ ) from near-surface resonant bubbles come from the ensonified volume adjacent to and below the ensonified area (Fig. 6). Neglecting multiple scattering, absorption, and off-resonant contributions, the effective sea surface scattering strength of  $N$  bubbles may be approximated by:

$$S_{S(bubbles)} = 10\log_{10} \sigma_s(a_r) + 10\log_{10} (6N) - 10\log_{10} A \quad (B11)$$

The first term on the right side of (B11) is the target strength of one resonant bubble, which is -66dB for 68kHz. The factor 6 is included in the middle term of (B11) because such bubbles would be ensonified via four paths due to reflections from the nearby surface, two of which are reciprocal and therefore add coherently (see Fig. 2 in reference (58)). For the TVSS sea surface backscatter data at grazing angles less than  $80^\circ$ , the ensonified areas were less than or equal to  $5m^2$ , so that even a moderate number of bubbles (e.g.  $N = 10^3$ ) could produce effective sea surface scattering strengths greater than -35dB.

The APL-UW model for  $S_S$  described in the text improves upon this simplified model. Removing the dependence on  $A$  and implied scattering volume, it uses the depth integrated extinction cross section per unit volume ( $\beta_I$ ), which is related to the column scattering strength ( $S_I$ ), i.e. the depth-integrated form of  $S_V$ <sup>66</sup>

$$S_I = S_V + 10\log_{10}(l_b) \quad (B12)$$

where  $l_b$  is the thickness of the near-surface bubble layer. The empirical expressions for  $\beta_I$  as a function of wind speed ( $U_{10}$ ) and frequency may account for off-resonant scattering, whereas the expression for the backscattering cross section due to bubbles ( $\sigma_b(\theta_g)$ ) takes into account bubble-mediated attenuation along the four paths involved, as well as the coherent addition of two of them.

## APPENDIX C. GEOMETRY OF THE TVSS TOWSHIP'S WAKE

Quantitative measurements of the spatial structure of *Mr. Offshore's* wake were made with several parameters (Table II). Wake width ( $w$ ) was estimated from the near-surface horizontal  $S_V$  imagery (e.g. Figs. 11,12a) as the width of the central high acoustic backscatter feature parallel to the ship's track. We did not use the  $S_S$  image (Fig. 8a) because it was difficult to distinguish the wake boundary from the natural angular dependence function of sea surface acoustic backscatter (Fig. 10). The widths of the older wakes (Table IIb, Fig. 12) were estimated by measuring the maximum horizontal distance between samples of  $S_V$  which were more than 6dB above the ambient level. The widening rate for the wake above the TVSS in each run was computed by dividing the difference between the wake's width and the ship's beam (Table I) by the wake age ( $T$ ). The widening rates of the older wakes were computed by dividing the difference between their widths and those measured above the TVSS during the previous run by ( $T-179s$ ).

Maximum bubble depth ( $h$ ), which we use to define the wake's depth, was computed as the depth at which  $S_V$  was more than 6dB above the ambient volume

reverberation in the upward looking beams (e.g. Fig. 9b). In the older wakes,  $h$  could not be resolved because the vertical dimensions of the ensonified volumes were too large. The wake's acoustic depth ( $h_a$ ) is that defined by Trevorrow *et al.* (1994)<sup>3</sup> as the depth at which  $M_V$  drops below one tenth its peak surface value. Mean deepening rates for the wake above the TVSS were computed by dividing the difference between  $h$  and the ship's propeller depth ( $D_p$ ) by  $T$  (Table I).

The wake widths, widening rates, and width to beam ratios were nearly equal or slightly less than those reported for similar ships in previous studies. Trevorrow *et al.*'s (1994)<sup>3</sup> empirical equations for the *CSS Vector* predict  $w = 48\text{m}$  at  $T = 179\text{s}$  for  $V_{\text{ship}} = 2.5\text{m/s}$  and  $w = 54\text{m}$  for  $V_{\text{ship}} = 5\text{m/s}$ , which are 2-5m greater than the corresponding values for *Mr. Offshore* (Table IIa). The empirical equation in NDRC (1947)<sup>2</sup> derived from acoustic backscatter measurements of the wake of the *USS Jasper* ( $L = 38.7\text{m}$ ,  $B = 7.0\text{m}$ ,  $D = 3.6\text{m}$ ) predicts  $w = 55\text{m}$  for  $T = 179\text{s}$ . Milgram *et al.* (1993)<sup>76</sup> measured wake widths at the surface for several naval vessels with speeds between 6.2 and 12.9 m/s, and observed that the wake width over the ship's beam ( $w/B$ ) increased proportionally to  $(y/L)^{1/5}$ , where  $y/L$  is the number of ship lengths astern of the wake generating ship. Based on their results, with  $y/L = 735\text{m}/40.8\text{m}$  and  $B = 9.7\text{m}$ , the predicted wake width for *Mr. Offshore* would be  $\sim 48.5\text{m}$ . Wake widths and widening rates for the older towship wakes observed by the TVSS (Table IIb) are slightly less than measurements made in similar studies. NDRC (1947)<sup>2</sup> measured the wake of the research vessel *E.W. Scripps* ( $L = 31.7\text{m}$ ,  $D = 3.7\text{m}$ ,  $V_{\text{ship}} = 4.8\text{m/s}$ ,  $Fn = 0.27$ ) to be  $73\text{m}$  at  $T = 14$  minutes, which is about the width for *Mr. Offshore*'s wake at  $T = 20$  minutes (Table IIb). The widening rate for *E.W. Scripps*' wake at  $T = 30$  minutes was  $3\text{cm/s}$ , which slightly exceeded the values for the wake of *Mr. Offshore* after  $T = 15$  minutes. Trevorrow *et al.*'s (1994)<sup>3</sup> regression equation for the wake of the *CSS Vector* at  $5\text{m/s}$  predicts  $w = 85\text{m}$  at  $T = 17$  minutes, whereas Milgram *et al.*'s (1993)<sup>76</sup>  $(y/L)^{1/5}$  relationship predicts  $w = 90\text{m}$  for the same  $T$ .

As with the wake widths, the towship's wake depths ( $h$ ) above the TVSS (Table IIa) were slightly less than or equal to measurements made in similar studies, but the deepening rates and depth to draft ratios ( $h/D$ ) were significantly greater. Trevorrow *et al.*'s (1994)<sup>3</sup> empirical function for the *CSS Vector* at  $2.5\text{m/s}$  predicts  $h = 6.8\text{m}$  at  $T = 179\text{s}$ , but a deeper  $h$  than *Mr. Offshore*'s is expected because their function was fit to  $88\text{kHz}$  data, and smaller resonant bubbles tend to penetrate deeper than larger bubbles. This is illustrated by their Fig. 4, which shows that the maximum bubble depth detected by a  $120\text{kHz}$  sonar is  $2\text{m}$  greater than that detected by a co-located  $28\text{kHz}$  sonar. The deepening rates for *Mr. Offshore*'s wake were more comparable to their measurements made at  $120\text{kHz}$ , in which the *CSS Vector*'s wake deepened at  $\sim 3.1\text{cm/s}$  in the first three minutes, compared to  $2.8\text{-}3.1\text{cm/s}$  for *Mr. Offshore*. However, the wake depth/ship draft ratios ( $h/D$ ) corresponding to *Mr. Offshore*'s wake ( $2.5\text{-}2.8$ ) were greater than those for the *CSS Vector* in all cases ( $1.5\text{-}2.2$ ) despite the 2 knot speed advantage of the *CSS Vector*. The  $h/D$  ratios also exceed those measured by NDRC<sup>2</sup> for two U.S. Navy destroyers and a U.S. Coast Guard cutter with speeds between 10-13 knots, which were measured with  $21\text{kHz}$  sound to be 1.63, 1.85, and 1.52 respectively.

## REFERENCES

1. T.C. Gallaudet, and C.P. de Moustier, C.P., "Imaging the ocean boundaries and volume with the Toroidal Volume Search Sonar (TVSS)," in *Proceedings of the Fourth Annual Symposium on the Mine Problem*, March 13-16, 2000, Monterey, CA.
2. National Defense Research Committee, "Acoustic Properties of Wakes," in



- Physics of Sound in the Sea* (Los Altos: Peninsula Publishing, 1947), Part IV, pp. 441-559.
3. M. V. Trevorrow, S. Vagle, and D.M Farmer, "Acoustical measurements of microbubbles within ship wakes," *J. Acoust. Soc. Am.*, **95**, 1922-1930 (1994).
  4. H. Burch, "Development of an acoustic inversion technique for estimating near surface sound speed," PhD. Dissertation (La Jolla: University of California, San Diego, 1998), Part 2, pp. 47-100.
  5. R. Pinkel, M. Merrifield, J. Smith, and H. Ramm, "Advances in Doppler sonar technology," in *Proc. IEEE Fifth Working Conference on Current Measurement*, St Petersburg, Florida, 7-9 Feb, 1995, pp. 37-41 (1995).
  6. G.O. Marmorino, and C.L. Trump, "Preliminary side-scan ADCP measurements across a ship's wake," *J. Atmo. Ocean. Tech.*, **13**, 507-513 (1996).
  7. W.F. King III, "Sound propagation in wakes," *J. Acoust. Soc. Am.*, **54**, 736-745 (1973).
  8. A.B., Ezerskii, B.M. Sandler, and D.A. Selivanovskii. "Echo-ranging observations of gas bubbles near the sea surface." *Sov. Phys. Acoust.*, **35**, 483-485 (1989).
  9. A.M. Reed, R.F. Beck, O.M. Griffin, and R.D. Peltzer, "Hydrodynamics of remotely sensed surface ship wakes," *Soc. Nav. Arch. Mar. Eng.*, **98**, 319-363 (1990).
  10. J. Lighthill, *Waves in Fluids* (New York: Cambridge University Press, 1978), Chapter 3, pp. 204-279.
  11. F. Ursell, "On Kelvin's ship wave pattern," *J. Fluid Mech.*, **8**, 418-432 (1960).
  12. O.M. Griffin, "Ship wave modification by a surface current field," *J. Ship. Res.*, **32**, 186-193 (1988).
  13. A. Barnell, and F. Noblesse, "Far field features of the Kelvin wake," in: *Sixteenth Symposium on Naval Hydrodynamics*, (Washington, D.C.: National Academy Press, 1988) pp. 18-36.
  14. O.M. Griffin, R.D., Peltzer, A.M. Reed, and R.F. Beck, "Remote sensing of surface ship wakes," *Naval Engineers Journal*, May 1992, 245-258 (1992).
  15. E.V. Lewis, ed., *Principles of Naval Architecture, Vol. II: Resistance, Propulsion, and Vibration*, 2nd Revision (Jersey City, NJ: Society of Naval Architects and Marine Engineers, 1988), 322 pp.
  16. H.E. Saunders, H.E. (1957). *Hydrodynamics in Ship Design, Vol I & II* (New York: The Society of Naval Architects and Marine Engineers, 1957).
  17. J.D. Lyden, R.R. Hammond, D.R. Lyzenga, and R.A. Shuchman, "Synthetic aperture radar imaging of surface ship wakes," *J. Geophys. Res.*, **93**, 12293-12303 (1988).
  18. M. Hyman, J. Rohr, J. Schoonmaker, T. Ratcliffe, B. Chadwick, K. Richter, S. Jenkins, and J. Wasyl, "Mixing in the wake of an aircraft carrier," *Proc. IEEE/MTS Oceans'95*, 1730-1744 (1995).
  19. J. Smith, and R. Pinkel, R., Personal communication, 28 December 2000. In unpublished data collected with a 75kHz Doppler sonar for the wake of the USS *Navaho*, a fleet tug with twin propellers, two high backscatter bands in the wake were attributed to bubbles trapped in twin vortices shed from the ship's stern and maintained by the outward turning flow produced by the ship's propellers.
  20. E.W. Miner, and O.M. Griffin, "Near-surface bubble motions in sea water," *NRL Memorandum Report 5756*, (Washington, D.C.: Naval Research Laboratory, 1986) 31 pp.
  21. L. Meadows, G. Meadows, A. Troesch, S. Cohen, K. P.. Beier, G. Root, O. M. Griffin, and T.F. Swann, Jr., "Lagrangian velocity profiles in the wake of a high speed vessel," *Ocean Engineering.*, **21**, 221-242 (1994).
  22. M.B. Stewart, and E.W. Miner, "Bubble dynamics in a turbulent ship wake,"

- NRL Memorandum Report 6055, (Washington, D.C: Naval Research Laboratory, 1987) 44 pp.
23. R.D. Peltzer, O.M. Griffin, W.R. Barger, and J.A.C. Kaiser, "High-resolution measurement of surface-active film redistribution in ship wakes," *J. Geophys. Res.*, **97**, 5231-5252 (1992).
  24. O. Shemdin, "Synthetic aperture radar imaging of ship wakes in the Gulf of Alaska," *J. Geophys. Res.*, **95**, 16319-16338 (1990).
  25. M.A. Grosenbaugh, "Nonlinear bow flows - an experimental and theoretical investigation," in *Seventeenth Symposium on Naval Hydrodynamics* (Washington, D.C.: National Academy Press, 1989) pp. 195-213.
  26. J.H. Milgram, R.D. Peltzer, and O.M. Griffin, "Suppression of short sea waves in ship wakes: Measurements and observations," *J. Geophys. Res.*, **98**, 7103-7114 (1993).
  27. W.W. Schultz, O.M. Griffin, O.M., and S.E. Ramberg, "Steep and breaking deep water waves," in: *Sixteenth Symposium on Naval Hydrodynamics* (Washington, D.C.: National Academy Press, 1988) pp. 106-114.
  28. E.D. Brown, S.B. Buchsbaum, R.E. Hall, J.P. Penhune, K.F. Schmitt, K.M. Watson, and D.C. Wyatt, "Observations of a nonlinear solitary wave packet in the Kelvin wake of a ship," *J. Fluid Mech.*, **204**, 263-293 (1989).
  29. S.B. Buchsbaum, "Ship wakes and solitons," PhD. Dissertation (La Jolla: University of California, San Diego, 1990) 133 pp.
  30. W.H. Munk, P. Scully-Power, and F. Zachariasen, "Ships from space," *Proc. R. Soc. Lond., A* **412**, 231-254 (1987).
  31. N.R. Stapleton, "Ship wakes in radar imagery," *Int. J. Remote. Sensing*, **18**, 1381-1386 (1997).
  32. I. Hennings, R. Romeiser, W. Alpers, and A. Viola, "Radar imaging of Kelvin arms of ship wakes," *Int. J. Remote. Sensing*, **20**, 2519-2543 (1999).
  33. S. Thorpe, "On the clouds of bubbles formed by breaking waves in deep water and their role in air-sea gas transfer," *Philos. Trans. R. Soc. London, Ser. A.*, **304**, 155-210 (1982).
  34. D. Farmer, and S. Vagle, "Waveguide propagation of ambient sound in the ocean-surface layer," *J. Acoust. Soc. Am.*, **86**, 1897-1908 (1989).
  35. P.H. Dahl, "Bubble clouds and their transport within the surf zone as measured with a distributed array of upward-looking sonars," *J. Acoust. Soc. Am.*, **109**, 133-142 (2001).
  36. H. Medwin, and C.S. Clay, *Fundamentals of Acoustical Oceanography*. (San Diego: Academic Press, 1998) 712 pp.
  37. H. Tennekes, and J.L. Lumley, *A First Course in Turbulence*, (Cambridge, MASS: The MIT Press, (1972).
  38. P.H. Dahl, and A. T. Jessup, "On bubble clouds produced by breaking waves: An event analysis of ocean acoustic measurements," *J. Geophys. Res.*, **100**, 5007-5020 (1995).
  39. S.A. Thorpe, and A.J. Hall, "The characteristics of breaking waves, bubble clouds, and near-surface currents observed using side scan sonar," *Cont. Shelf Res.*, **1**, 353-384 (1983).
  40. I.A. Harris, and R.M. Detsch, "Small air bubbles in reagent grade water and seawater 2. Dissolution of 20- to 500- $\mu$ m-diameter bubbles at atmospheric pressure," *J. Geophys. Res.*, **96**, 8907-8910 (1991).
  41. R.M. Detsch, "Small air bubbles in reagent grade water and seawater 1. Rise velocities of 20- to 500- $\mu$ m-diameter bubbles," *J. Geophys. Res.*, **96**, 8901-8906 (1991).
  42. J. Wyman, Jr, P.F. Scholander, G.A. Edwards, and L. Irving, "On the stability of gas bubbles in sea water," *J. Mar. Res.*, **11**, 47-62, (1962).

43. P.J. Mulhearn, "Distribution of microbubbles in coastal waters," *J. Geophys. Res.*, **86**, 6429-6434 (1981).
44. B.D. Johnson, and P.J. Wangersky, "Microbubbles: Stabilization by monolayers of adsorbed particles," *J. Geophys. Res.*, **92**, 14641-14647 (1987).
45. S.T. McDaniel, "Acoustical estimates of subsurface bubble densities in the open ocean and coastal waters," in *Sea Surface Sound*, edited by B.R. Kerman (Boston: Kluwer, 1988) pp. 225-236.
46. S. Vagle, and D.M. Farmer, "A comparison of four methods for bubble size and void fraction measurements," *IEEE J. Oceanic Eng.*, **23**, 211-222 (1998).
47. T.C. Gallaudet, and C.P. de Moustier, "Multibeam volume acoustic backscatter imagery and reverberation measurements in the northeastern Gulf of Mexico," *J. Acoust. Soc. Am.*, submitted (2001)
48. S.T. McDaniel, "Sea surface reverberation: A review," *J. Acoust. Soc. Am.*, **94**, 1905-1922 (1993).
49. H. Medwin, "In situ acoustic measurements of microbubbles at sea," *J. Geophys. Res.*, **82**, 971-976 (1977).
50. E. J. Terrill, and W.K. Melville, "Sound-speed measurements in the surface-wave layer," *J. Acoust. Soc. Am.*, **102**, 2607-2625 (1997).
51. S. Vagle, and D.M. Farmer, "The measurement of bubble-size distributions by acoustical backscatter," *J. Atmo. Ocean. Tech.*, **9**, 630-644 (1992).
52. D.M. Farmer, "Properties of bubble distributions relevant to surface reverberation," in *Ocean Reverberation*, edited by D.D. Ellis, J.R. Preston, and H.G. Urban (Boston: Kluwer, 1993), pp. 11-24.
53. M. Y. Su, "Near-surface bubble density distribution due to wave breaking," *J. Acoust. Soc. Am.*, **91**, 2322 (1992).
54. J.W. Cartmill, and M.Y. Su, "Bubble size distribution under saltwater and freshwater breaking waves," *Dyn. Atmo. Oceans.*, **20**, 25-31 (1993).
55. M.Y. Su, S.C. Ling, and J. Cartmill, "Optical microbubble measurements in the North Sea." in *Sea Surface Sound*, edited by B.R. Kerman. (Boston: Kluwer, 1988) pp. 211-233.
56. C. Medwin, and N.D. Breitz, "Ambient and transient bubble spectral densities in quiescent seas under spilling breakers," *J. Geophys. Res.*, **94**, 12751-12759 (1989).
57. S.T. McDaniel, and A.D. Gorman, "Acoustic and radar sea surface backscatter," *J. Geophys. Res.*, **87**, 4127-4136 (1982).
58. P.H. Dahl, W.J. Plant, B. Nutz, H. Herwig, and E.A. Terray, "Simultaneous acoustic and microwave backscattering from the sea surface," *J. Acoust. Soc. Am.*, **101**, 2583-2595 (1997).
59. Applied Physics Laboratory, *APL-UW High Frequency Ocean Environmental Acoustic Models Handbook*, Technical Report APL-UW TR 9407 (Seattle: University of Washington, 1994) Part II.
60. S.T. McDaniel, "Diffractive corrections to the high-frequency Kirchhoff approximation," *J. Acoust. Soc. Am.*, **79**, 952-957 (1986).
61. P.A. Crowther, "Acoustic scattering from a near surface bubble layer," in *Cavitation and Inhomogeneities in Underwater Acoustics*, edited by W. Lauterborn (Berlin: Springer-Verlag, 1980) pp. 195-204.
62. B. Nutz, and H. Herwig, "Wind speed dependence of acoustic backscattering," *J. Geophys. Res.*, **100**, 24885-24892 (1995).
63. E.C. Monahan, and M. Lu, "Acoustically relevant bubble assemblages and their dependence on meteorological parameters," *IEEE J. Ocean. Eng.*, **15**, 340-349 (1990).
64. T.C. Gallaudet, and C.P. de Moustier, "Using environmental information to estimate and correct for errors in bathymetry and seafloor acoustic imagery,"

- IEEE J. Ocean. Eng.*, submitted (2001).
65. T.C. Gallaudet, and C.P. de Moustier, "On optimal amplitude shading for arrays of irregularly spaced or non-coplanar elements." *IEEE J. Ocean. Eng.*, **25**, 553-567 (2000).
  66. R.J. Urick, *Principles of Underwater Sound*, 3rd edition (Los Altos: Peninsula, 1983) 423 pp.
  67. D.M. Farmer, Personal communication, 27 February, 2001.  $M_V$  values reported in ss23. are lower bounds because corrections were not made for transmission loss through the bubble fields of the wake. The corrections were not made because reliable methods to estimate the bubble size distribution were not available during their experiment.
  68. G.B. Crawford, and D.M. Farmer, "On the spatial distribution of ocean bubbles," *J. Geophys. Res.*, **92**, 8231-8243 (1987).
  69. D.C. Wyatt, and R.E. Hall, "Analysis of ship-generated surface waves using a method based upon the local Fourier transform," *J. Geophys. Res.*, **93**, 14133-14164 (1988).
  70. B.A. Hughes, and T.W. Dawson, "Joint Canada-U.S. Ocean Wave Investigation Project: An overview of the Georgia Strait experiment," *J. Geophys. Res.*, **93**, 12219-12234 (1988).
  71. P.N. Denbigh, "Swath Bathymetry: Principles of operation and an analysis of errors," *IEEE J. Oceanic Eng.*, **14**, 289-298 (1989).
  72. E.T. Terrill, and W.K. Melville, "A broadband acoustic technique for measuring bubble size distributions: Laboratory and shallow water measurements." *J. Atmosph. Oceanic Tech.*, **17**, 220-221.
  73. F.E. Fox, S.R. Curley, and G.S. Larson, "Phase velocity and absorption measurements in water containing bubbles." *J. Acoust. Soc. Am.*, **27**, 534 (1955).
  74. J.W. Caruthers, J. Stanic, P.A. Elmore, and R.R. Goodman, "Acoustic attenuation in very shallow water due to the presence of bubbles in rip currents," *J. Acoust. Soc. Am.*, **106**, 617-625 (1999).
  75. D. Gu, and O.M. Phillips, "On narrow V-like ship wakes," *J. Fluid. Mech.*, **275**, 301-321 (1994).
  76. J.H. Milgram, R.A. Skop, R.D. Peltzer, and O.M. Griffin, "Modeling short sea wave energy distributions in the far wakes of ships," *J. Geophys. Res.*, **98**, 7115-7124 (1993).
  77. E. J. Terrill, Personal communication, December 2000. Unpublished data collected with a surface echo-sounder towed behind a Navy oiler ( $L \sim 100\text{m}$ ) at 15-20 knots reveal high density clouds of bubbles at depths of several meters below the surface. Video observations below the sea surface next to the hull of the Scripps *RV Roger Revelle* show intermittent bubble clouds produced by breaking bow waves entrained along the underside of the hull.
  78. P.H. Dahl, and W.J. Plant, "The variability of high-frequency acoustic backscatter from the region near the sea surface," *J. Acoust. Soc. Am.*, **101**, 2596-2602 (1997).
  79. S.Z., El-Sayed, W.M. Sackett, L.M. Jeffrey, A.D. Fredricks, R.P. Saunders, P.S. Conger, G.A. Fryxell, K.A. Steidinger, and S.A. Earle, "Chemistry, primary productivity, and benthic algae of the Gulf of Mexico," in *Serial atlas of the marine environment folio 22* (New York : American Geographical Society, 1972).
  80. H. Medwin, "Historical measurements of bubbles in coastal environments: effects of biogenic bubble on propagation at high frequency," in *High Frequency Acoustics in Shallow Water*, edited by N.G. Pace, E. Pouliquen, O. Bergem, and A.P. Lyons (La Spezia: NATO SACLANT Undersea Research Center, 1997) pp. 381-386.

81. S.C. Ling, and H.P. Pao, "Study of micro-bubbles in the North Sea." in *Sea Surface Sound*, edited by B.R. Kerman (Boston: Kluwer, 1988) pp. 197-210.
82. I. Pelech, G.G. Zipfel, and R.L. Holford, "A wake-scattering experiment in thermally stratified water," *J. Acoust. Soc. Am.*, **73**, 528-538 (1983).
83. W.D. Garrett, and P.M. Smith, "Physical and chemical factors affecting the thermal IR imagery of ship wakes," *NRL Memorandum report 5376*, (Washington, D.C.: Naval Research Laboratory, 1984) 24 pp.
84. S.A. Thorpe, and J.M. Brubaker, "Observations of sound reflection by temperature microstructure," *Limnol. Oceanogr.*, **28**, 601-613 (1983).
85. R.J. Urick, and R.M. Hoover, "Backscattering of sound from the sea surface: Its measurement, causes, and application to the prediction of reverberation levels," *J. Acoust. Soc. Am.*, **28**, 1038-1042 (1956).
86. G.R. Garrison, S.R. Murphy, and D.S. Potter, "Measurements of backscattering of underwater sound from the sea surface," *J. Acoust. Soc. Am.*, **32**, 104-111 (1960).
87. W.C. Keller, V. Wismann, and W. Alpers, "Tower-based measurements of the ocean C band radar backscattering cross section," *J. Geophys. Res.*, **94**, 924-930 (1989).
88. S.D. Smith, "Coefficients for sea surface wind stress, heat flux, and wind profiles as a function of wind speed and temperature," *J. Geophys. Res.*, **93**, 15467-15472 (1988).
89. W.G. Large, and S. Pond, "Open ocean momentum flux measurements in moderate to strong winds," *J. Phys. Ocean.*, **11**, 324-336 (1981).
90. S. Stolte, "Shallow water sonar conditions and radar backscatter," *IEEE J. Ocean. Eng.*, **19**, 30-35 (1994).
91. D.M. Savitsky, "Interaction between gravity waves and finite flow fields." in *Eighth Symposium on Naval Hydrodynamics*, (Arlington, Virginia: Office of Naval Research, 1970) pp. 389-447.
92. L. Ding, and D. Farmer, "Passive acoustical measurements of scale, probability, and intensity of wave breaking," *Proc. IEEE Oceans'93*, vol. **II**, 93-97 (1993).
93. S. Pond, and G. Pickard, *Introductory Dynamical Oceanography*, 2nd edition (New York: Pergamon Press, 1983) p. 329.
94. J. Wu, "Individual characteristics of whitecaps and volumetric description of bubbles," *IEEE J. Oceanic Eng.*, **17**, 150-158 (1992).
95. A.J. Hermans, and F.J. Brandsma, "Low Froude number expansions for the wave pattern and the wave resistance of general ship forms," in *Seventeenth Symposium on Naval Hydrodynamics*, (Washington, D.C.: National Academy Press, 1989) pp. 103-114.
96. H. Yuasa, H. Kamiirisa, and T. Nojiri, "Study on the characteristics of propeller cavitation and its noise," in *Sixteenth Symposium on Naval Hydrodynamics*, (Washington, D.C.: National Academy Press, 1988) pp. 371-385.
97. H. Medwin, "Counting bubbles acoustically: A review," *Ultrasonics*, **15**, 7-13 (1977).
98. K. Commander, and E. Moritz, "Off resonance contributions to acoustical bubble spectra," *J. Acoust. Soc. Am.*, **85**, 2665-2669 (1989).
99. K.W. Commander, and A. Prosperetti, "Linear pressure waves in bubbly liquids: Comparison between theory and experiments," *J. Acoust. Soc. Am.*, **85**, 732-746 (1989).
100. A.B. Wood, *A Textbook of Sound*, (New York: Macmillan, 1955).
101. H. Medwin, "Acoustic fluctuations due to microbubbles in the near-surface ocean," *J. Acoust. Soc. Am.*, **79**, 952-957 (1974).
102. M.V. Hall, "A comprehensive model of wind-generated bubbles in the ocean

- and predictions of the effects of sound propagation at frequencies up to 40kHz," *J. Acoust. Soc. Am.*, **86**, 1103-1117 (1989).
103. E.J. Terrill, "Acoustic Measurement of Air Entrainment by Breaking Waves," PhD. Dissertation (La Jolla: University of California, San Diego, 1998) 244 pp.
104. G.B. Deane, "Sound generation and air entrainment by breaking waves in the surf zone," *J. Acoust. Soc. Am.*, **102**, 2671-2689 (1997).

TABLE I. Characteristics of the TVSS towship, *Mr. Offshore*, an offshore supply vessel equipped with twin, fixed-pitch propellers with 4 blades each at a propeller axis depth  $D_p$ . Equations for the Froude number ( $Fn$ ) and draft Froude number ( $Fd$ ) are found in Appendix A. Appendix C describes how the quantities were estimated.

length ( $L$ )	40.8 m
beam ( $B$ )	9.7 m
draft ( $D$ )	2.6 m
$B/L$	0.24
$Fn$	0.20
$Fd$	0.81
$D_p$	1.5 m
average speed ( $V_{ship}$ )	8 kts (4.1 m/s)
propeller rpm @ 8kts	680

TABLE II. (a) Data for the towship's wake observed above the TVSS in runs 1-3. Quantities are averaged over the number ( $N_p$ ) of pings in each run that were not affected by hydrophone saturation or dropouts. (b) Data for the towship's wake generated during runs 1 and 2 and observed in runs 2 and 3. Quantities are averaged over the number ( $N_p$ ) of pings in each run that were not affected by hydrophone saturation or dropouts. The wake geometry parameters are discussed in the text and Appendix C, and equations for  $S_v$  and  $M_v$  are found in Appendix B.

(a)	Run 1	Run 2	Run 3
$N_p$	98	97	99
Age $T$ (s)	179	179	179
Width $w$ (m)	50.5	49.2	46.9
Widening Rate (m/s)	0.23	0.22	0.21
Max Bubble Depth $h$ (m)	6.5	7.2	6.6
Deepening Rate (m/s)	0.028	0.032	0.028
Acoustic Depth $h_a$ (m)	4.1	5.3	4.0
Max $S_v$ (dB)	-18.0	-19.5	-17.1
Max $M_v$ ( $m^{-1}$ )	0.14	0.13	0.19
Depth of Max $M_v$ (m)	2.7	3.3	2.6
Width/Ship's Beam $w/B$	5.2	4.8	5.1
Depth/Ship's Draft $h/D$	2.5	2.8	2.6
(b)	Run 2	Run 3	
Age in First and Last Pings $T$ (min)	15.3, 18.6	19.3, 22.6	
Width $w$ (m)	70	74	
Widening Rate (m/s)	0.02	0.02	
Max $S_v$ (dB)	-55	-58	
Decay Rate $dS_v / dt$ (dB/min)	-2.6	-2.1	
Max $M_v$ ( $m^{-1}$ )	$4 \times 10^{-5}$	$3 \times 10^{-5}$	
Width/Ship's Beam $w/B$	7.2	7.6	



TABLE III. Data for bubble clouds in Fig. 8a and labeled A-D in Fig. 11. For each bubble cloud, the maximum  $S_S$ ,  $S_V$ , and TS represent the maximum values across the range of angles spanned by the cloud after averaging along the along-track spatial extent of the cloud. The cloud length ( $L_{bc}$ ) is defined as the maximum distance of all directions across a cloud, and the cloud widths ( $W_{bc}$ ) are defined as the maximum distance perpendicular to the length.<sup>92</sup> The characteristic scale is defined as  $s_{bc} = \sqrt{W_{bc} L_{bc}}$ . Equations for  $S_S$ ,  $S_V$ , and TS are found in Appendix B.

Bubble Cloud	A	B	C	D
Max $S_S$ (dB)	-24.0	-25.2	-23.5	-23.1
Max $S_V$ @ 3m depth (dB)	-30.6	-34.8	-33.4	-35.5
Max TS @ 3m depth (dB)	-17.9	-23.8	-23.5	-21.5
$L_{bc}$ (m)	63	42	52	36
$W_{bc}$ (m)	18	14	23	12
$W_{bc}/L_{bc}$	0.29	0.33	0.43	0.33
$s_{bc}$ (m)	33.7	24.2	34.6	20.8

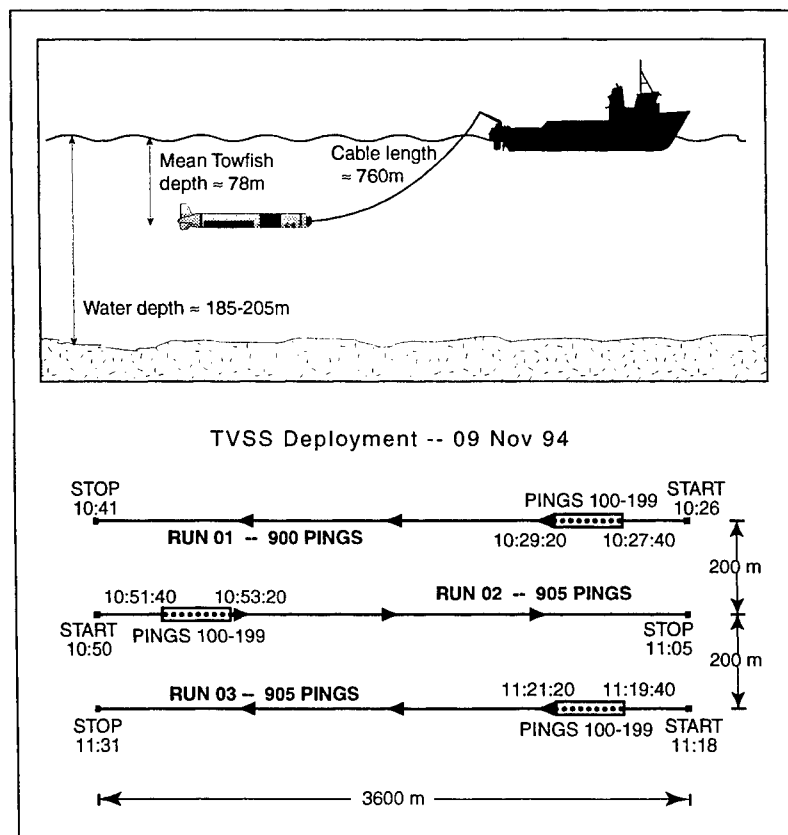


Fig. 1. (a) Depiction of TVSS data collection deployment geometry, 9 November 1994. (b) East-West track lines for runs 1-3. The data presented in this paper are processed from pings #100-199 in each of the three runs. The wind was from the southeast ( $145^\circ$ ) at 6 knots ( $3\text{m/s}$ ).

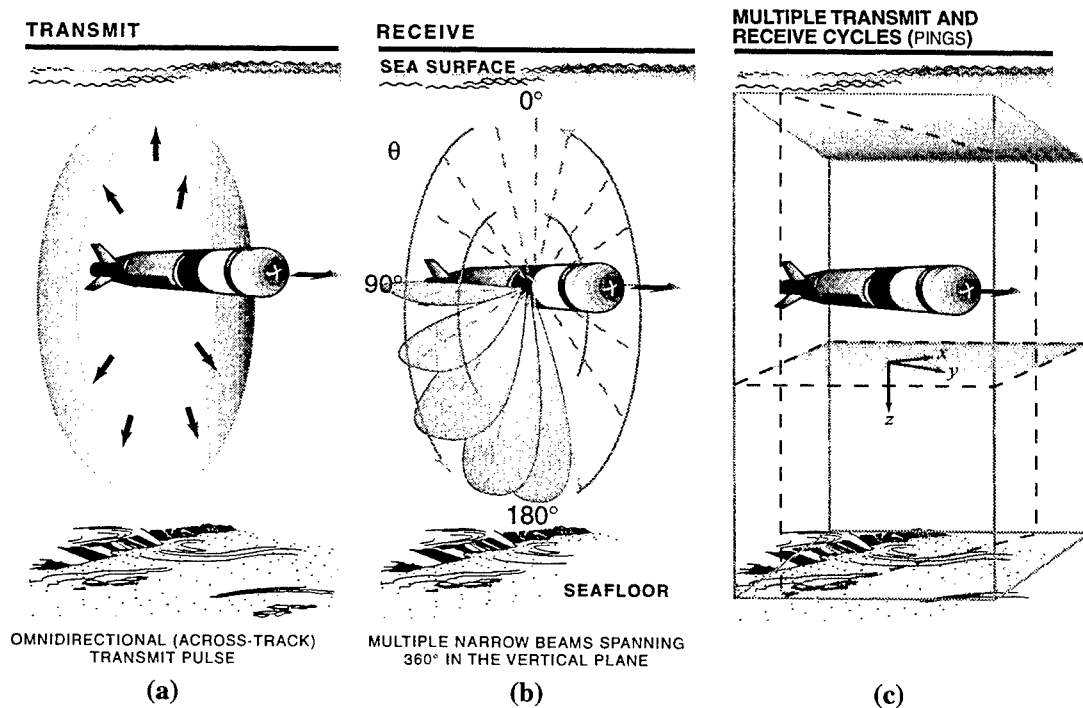


Fig. 2. The TVSS is designed for deployment aboard an AUV/UUV. After transmission of a "toroidal" pulse, the sonar records the echoes in directions spanning  $360^\circ$  about the TVSS axis. Undersea imagery is constructed for various vertical and horizontal planes using data collected over successive transmit-receive cycles.  $x$ ,  $y$ , and  $z$  correspond respectively to the across- and along-track directions relative to the towfish, and the depth relative to the sea surface.

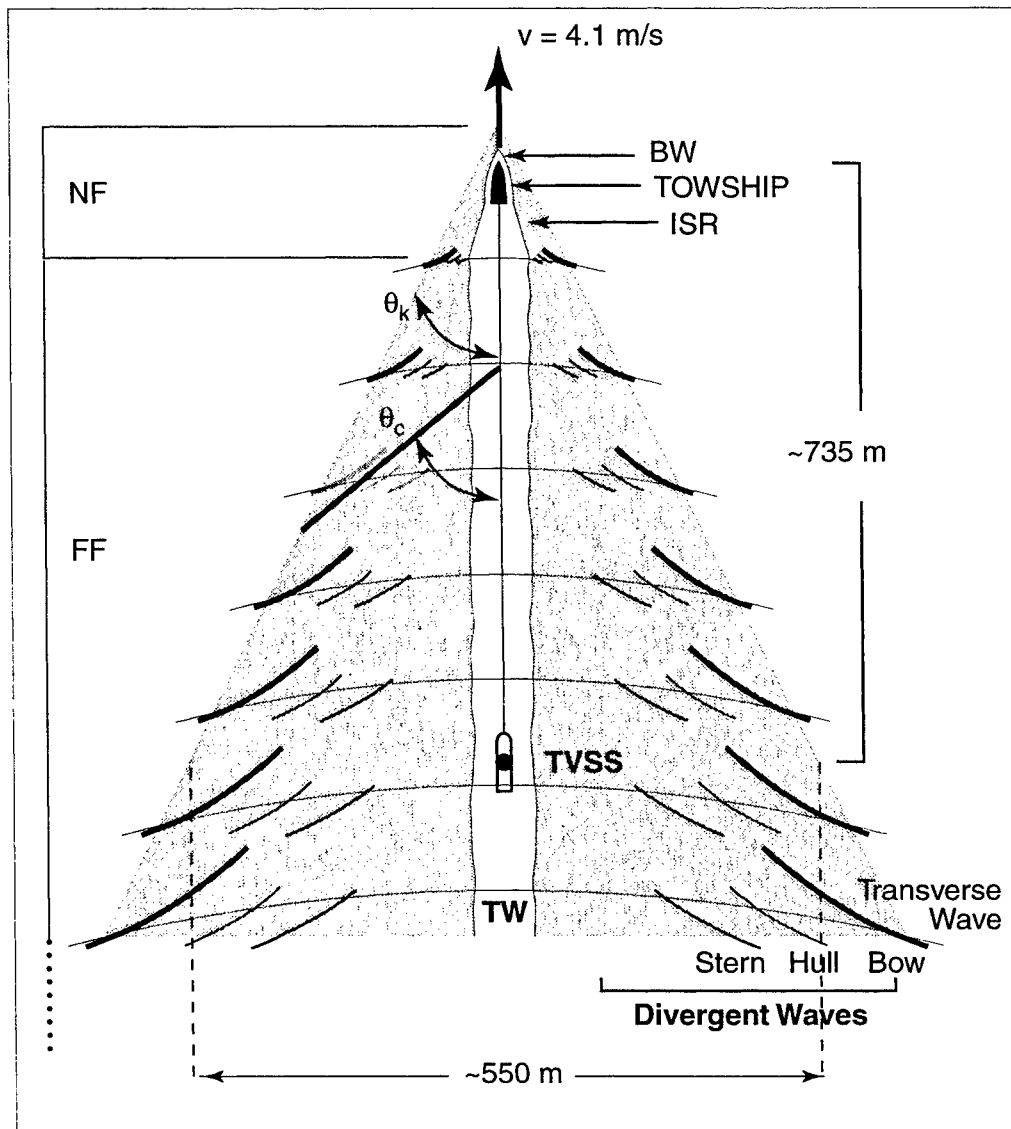


Fig. 3. Depiction of the hypothetical turbulent wake (TW) and Kelvin wave pattern for the towship in the TVSS deployment (Fig. 1). The near field (NF) includes the bow waves (BW) and the initial spreading region (ISR) and extends several ship beams ahead, to the sides, and up to a few ship lengths aft of the ship (reference [9]). The far field extends from the near field aft and outward. Variations in sea surface displacements, bubble sizes and densities, and seawater properties in the near field are much larger than those in the far field. The Kelvin wave pattern half angle  $\theta_K = 19^\circ 28'$  bounds the transverse and divergent ship waves. Cusp waves are formed from the superposition of transverse and divergent waves, and the angle between the line tangent to the outermost cusp wave crests and the ship course is  $\theta_c = 35^\circ 16'$ .



Fig. 4. Turbulent wake and Kelvin wave pattern generated by the *USS Quapaw* during the Joint Canada-U.S. Ocean Wave Investigation Project (JOWIP), from Wyatt and Hall (1988). The *Quapaw*'s speed was 8m/s and the wind speed at 10m ( $U_{10}$ ) was 1.7m/s

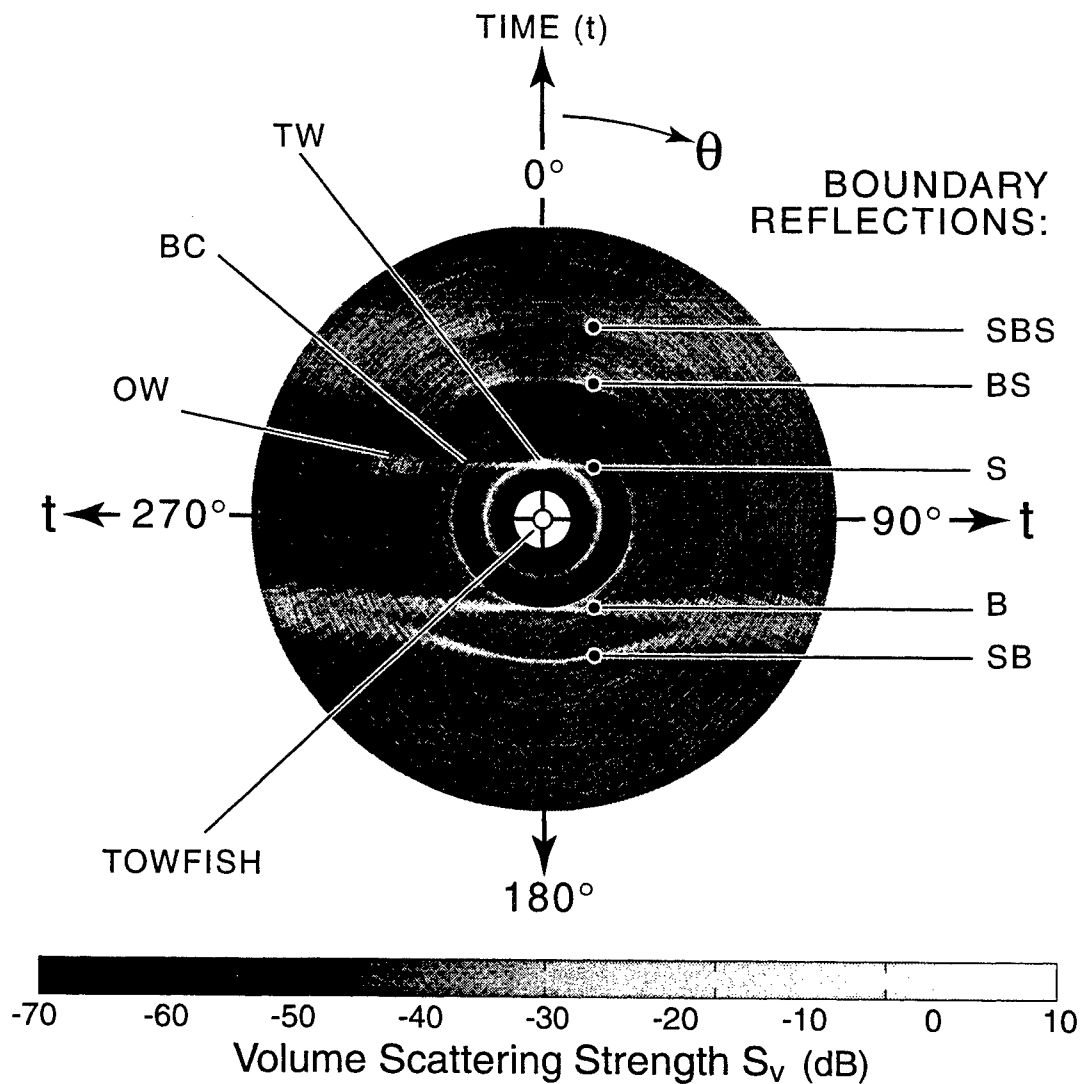


Fig. 5. One TVSS ping displayed as a vertical slice of acoustic volume scattering strength ( $S_v$ ) in polar coordinates of angle vs. two-way travel time. Labels refer to the following features: TW - towship's wake above the TVSS resulting from the deployment geometry (Fig. 1); OW - towship's wake generated during the previous run with 200m spacing between track lines for each run (Fig. 1); BC - bubble cloud generated by a breaking wave from the towship; B - seafloor echo; S - sea surface echo; SB - surface-bottom (multiple) echo; BS - bottom-surface (multiple) echo; SBS - surface-bottom-surface (multiple) echo.

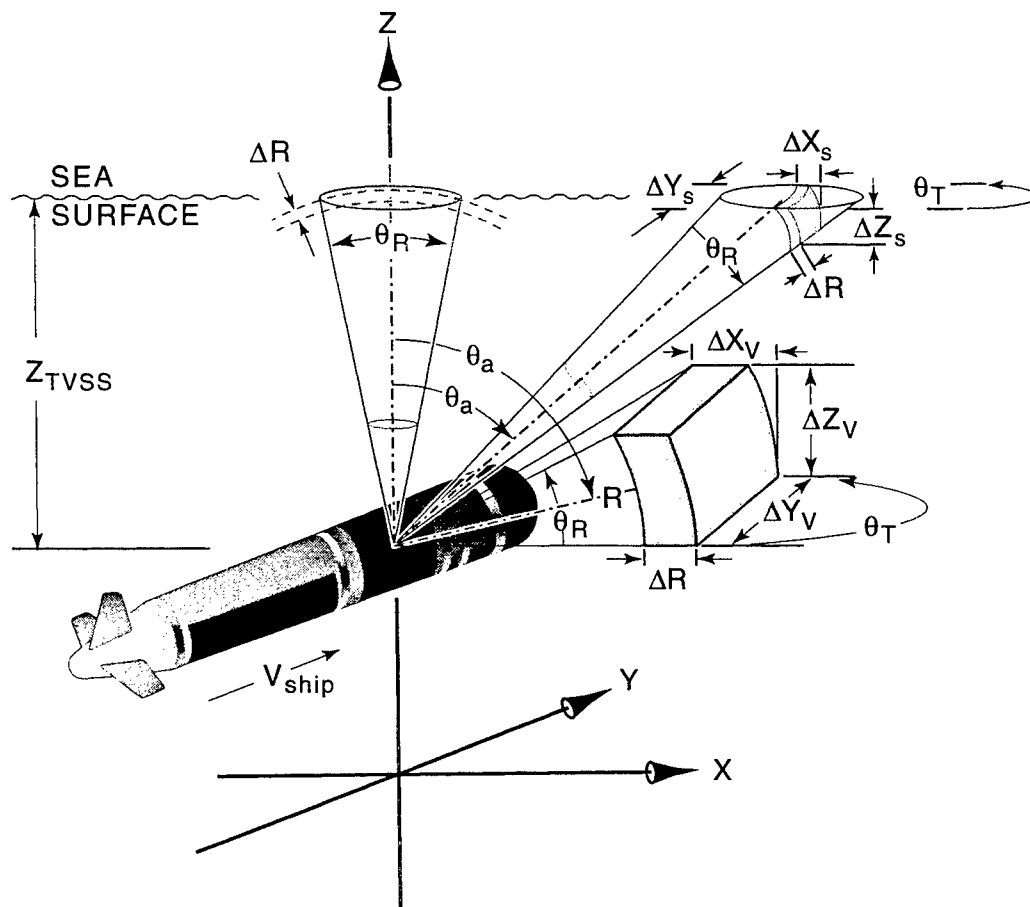


Fig. 6. The TVSS sampling volume ( $V$ ) for a given angle of arrival ( $\theta_a$ ) is defined in terms of the transmit and receive beamwidths ( $\theta_T$ ,  $\theta_R$ ), the range ( $R$ ) from the TVSS center, and range resolution  $\Delta R$ . The TVSS transmitted pulse ensonifies an area ( $A$ ) bounded by  $\theta_T$  and  $\theta_R$  yielding an ellipse at zenith and an annulus sector at angles of arrival ( $\theta_a$ ) directed away from zenith.

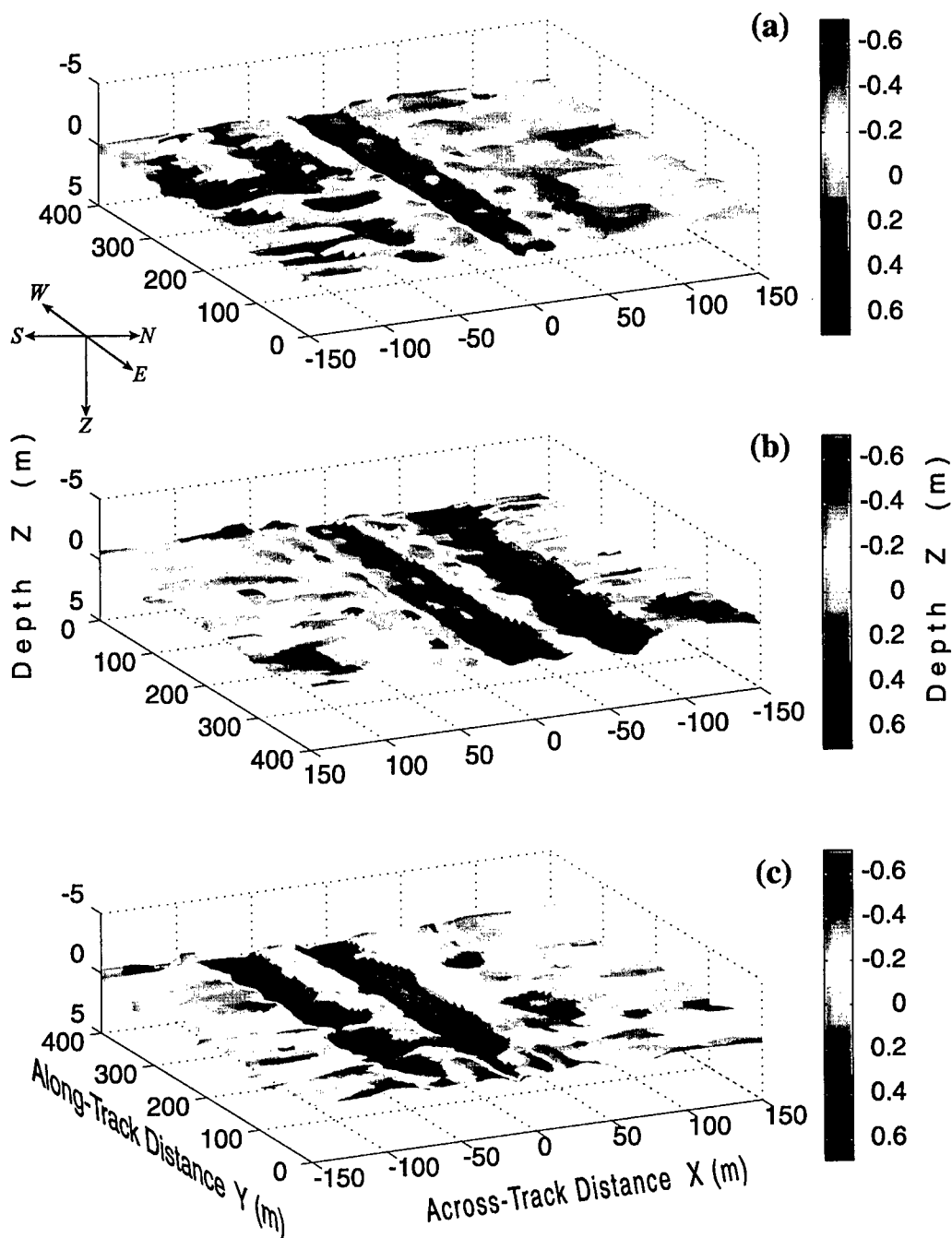


Fig. 7. Sea surface relief maps for runs 1-3 (a)-(c) are depicted with depressions in blue and elevations in red and correspond to three separate areas in the data collection region. North, South, East, and West are respectively, to the left, right, rear, and forward of each panel such that the towfish direction of travel (with increasing along-track distance  $y$ ) was from East to West in (a) and (c), and from West to East in (b).



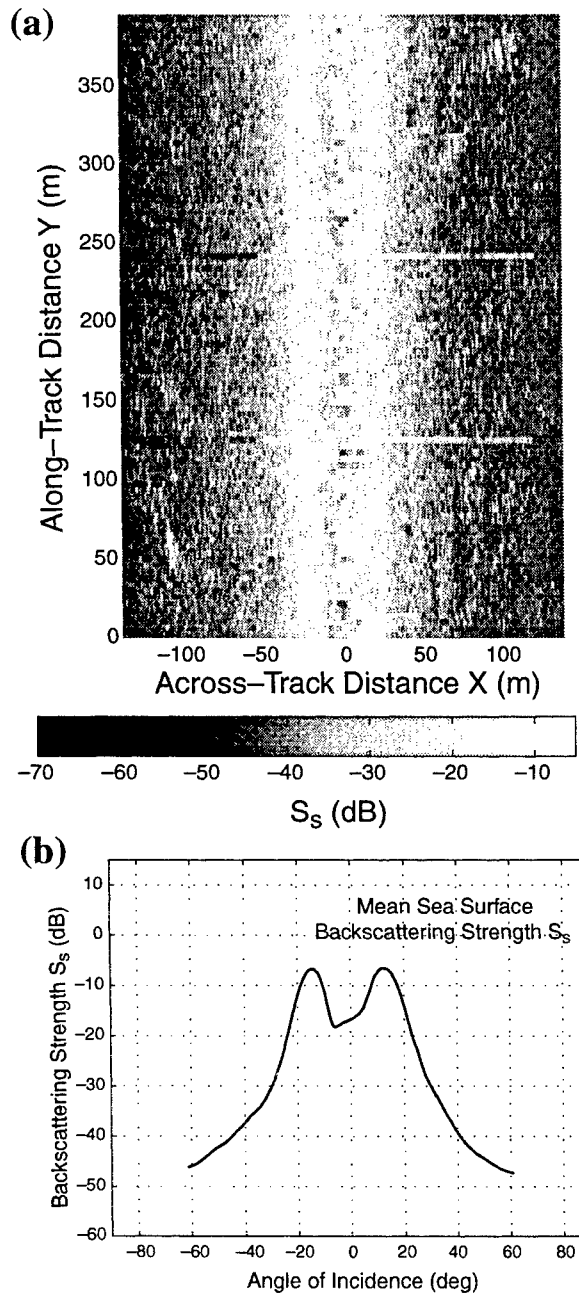


Fig. 8. (a) Sea surface acoustic backscattering strength ( $S_S$ ) image, run 1. The horizontal lines at along-track distances  $y = 130$  m and  $248$  m are pings which experienced hydrophone dropouts and were excluded from the computation of the 98-ping mean  $S_S$  vs. angle of incidence  $\theta_{inc}$  (b). The high acoustic backscattering strength feature centered at  $x = 0$  m and extending the length of the track results from microbubbles in the TVSS towship's wake.

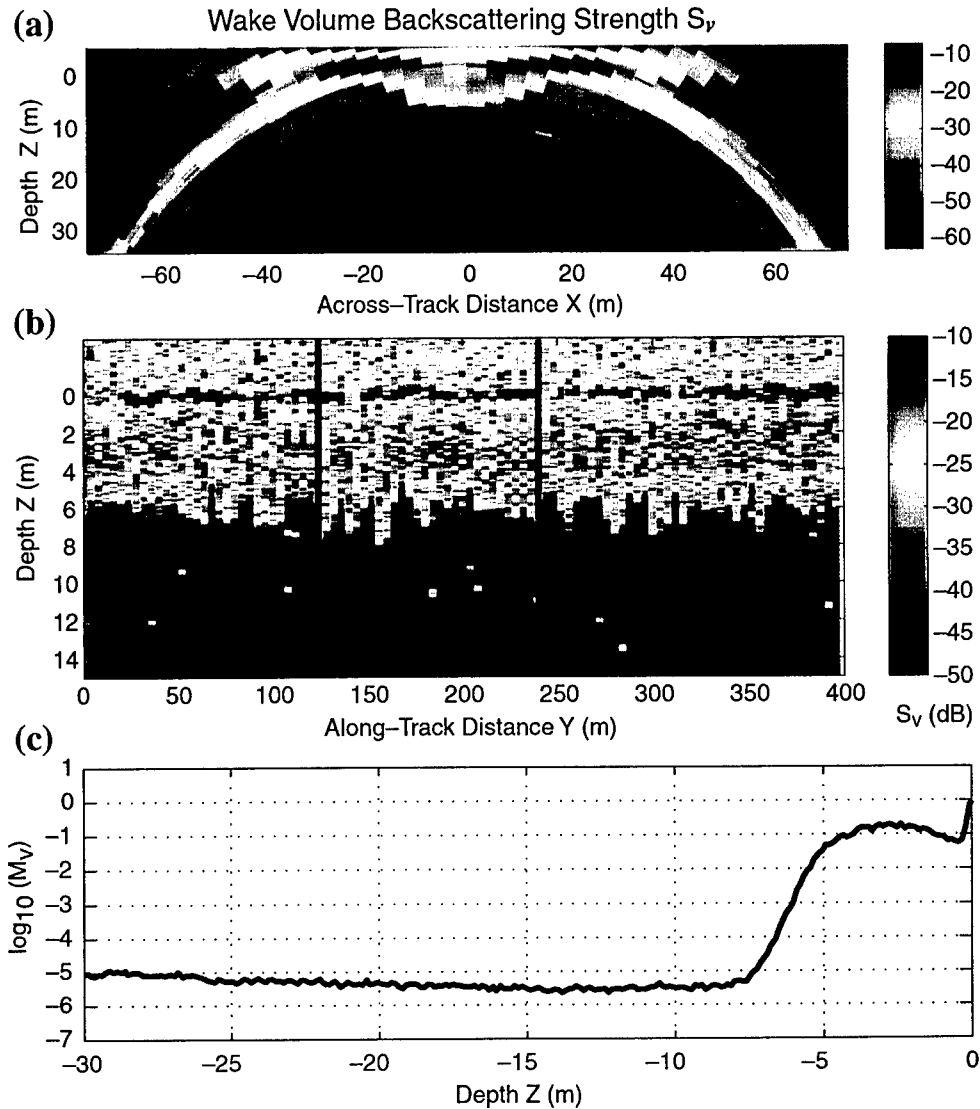


Fig. 9. (a) Vertical volume slice perpendicular to the towfish track obtained by averaging the  $S_V$  from 98 TVSS pings (e.g. Fig 5) in run 1. (b) Vertical  $S_V$  obtained by extracting the upward looking beam samples for each ping, then converting time of arrival to depth. This is identical to the processing for upward-looking echosounders. In both (a) and (b), the sea surface appears as a high backscatter, horizontal line at 0m depth, and the towship's wake is seen as the high acoustic backscatter feature extending 6-8 m below the surface. The vertical lines near  $y = 118$ m and 246m in (b) are pings which experienced saturation in the receive array electronics. (c)  $\log_{10}$  of the backscattering cross section  $M_V$  averaged over 98 pings. The two pings which experienced hydrophone saturation were excluded in the computation of the mean  $S_V$  image in (a) and the mean  $M_V$  plot in (c).

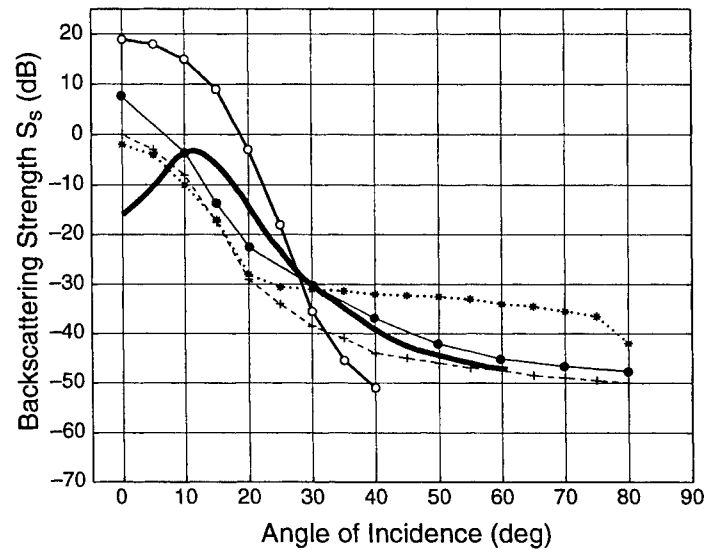


Fig. 10. Angular dependence of sea surface acoustic backscattering strength. Comparison of  $S_s$  measurements: (bold line) TVSS run 1; (+) Urlick and Hoover (1956) for 60kHz and 3m/s wind; (\*) Garrison *et al.* (1960) for 60kHz in 3 m/s wind; (o) Nutzelt and Herwig (1995) for 50kHz in 3 m/s wind; and (●) APL-UW's sea surface backscatter model for 60kHz in 3m/s wind.

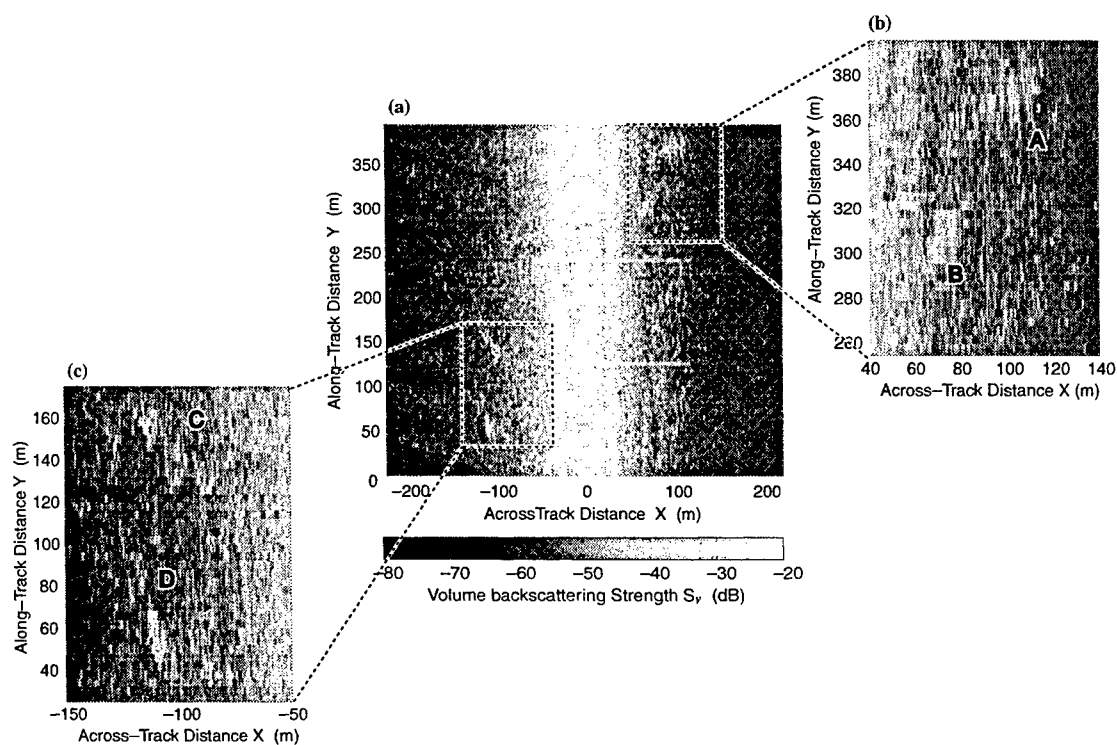


Fig. 11. (a) Horizontal volume acoustic backscattering strength ( $S_v$ ) image 3m below the sea surface for run 1. The display convention is identical to that of Fig. 8a. The horizontal lines at along-track distances  $y = 130\text{m}$  and  $248\text{m}$  are pings which experienced hydrophone dropouts. (b)-(c) Four clouds of resonant microbubbles are labeled A-D.

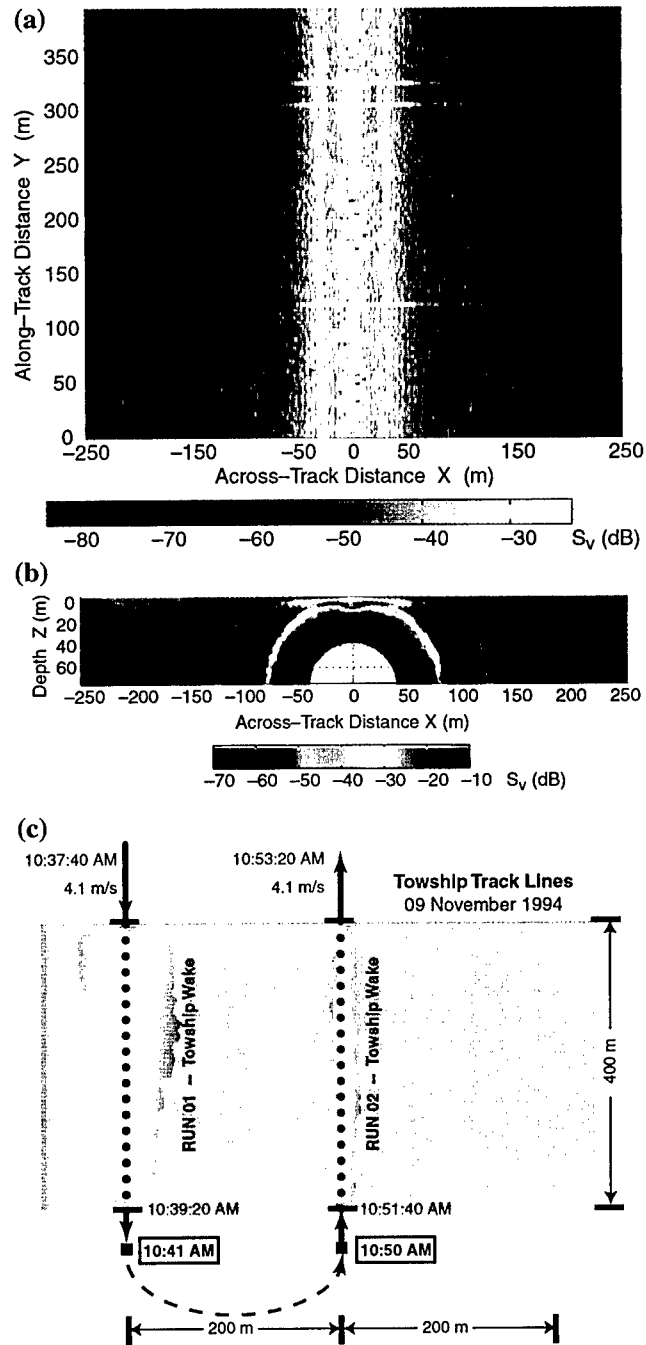


Fig. 12. (a) Horizontal ( $S_V$ ) image 3m below the sea surface for run 2. The three horizontal lines at along-track distances  $y = 120\text{m}$ ,  $298\text{m}$ , and  $320\text{m}$  are pings which experienced hydrophone dropouts. (b) Vertical  $S_V$  image averaged over the 97 pings in (a) which did not experience hydrophone dropouts. The age  $T$  of the wake from run 1 is computed by adding 3 minutes to the TVSS's track times (c) to account for the towfish's layback of 735m (Fig. 1).

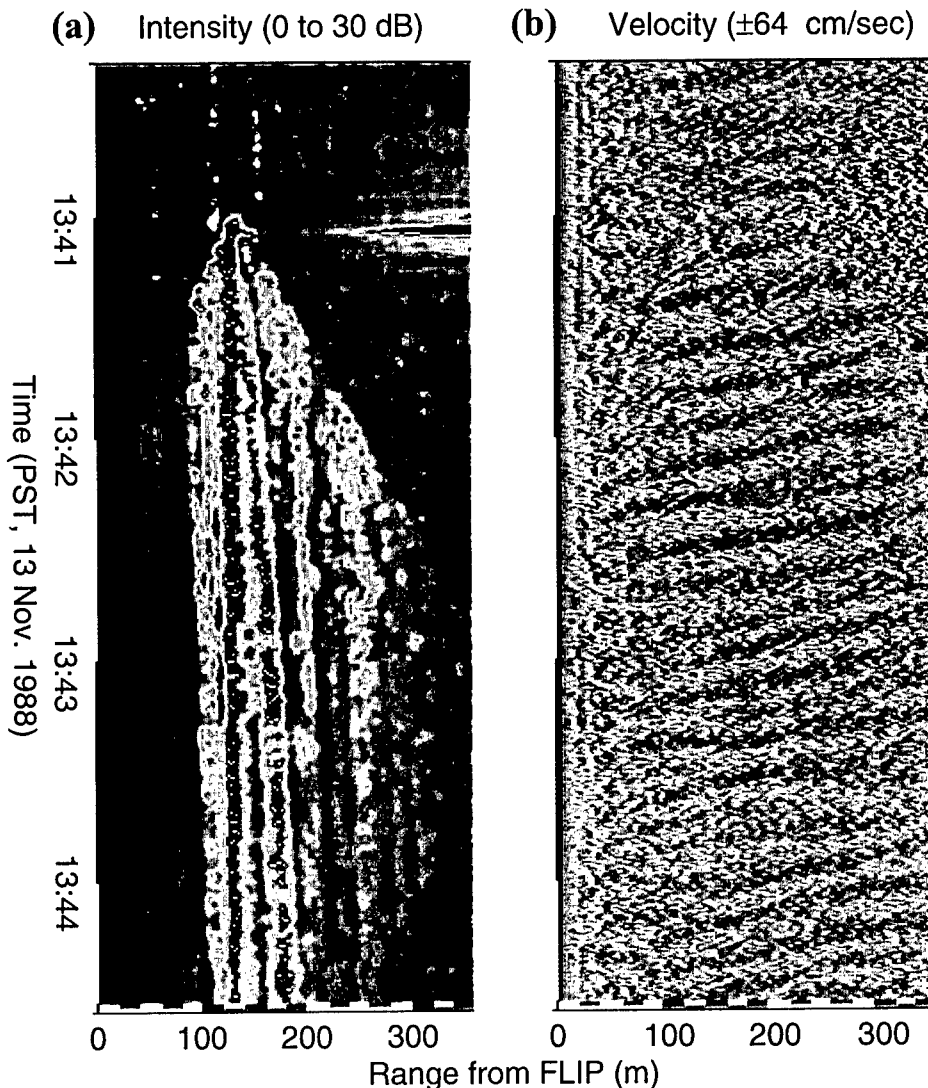


Fig. 13. Doppler sonar response to a tugboat's wake from Pinkel *et al.* (1995). The time-range images were obtained from a 195kHz surface-scan Doppler sonar mounted on the Marine Physical Laboratory's Floating Instrument Platform (FLIP). The single propeller tugboat was traveling at 10 knots in a direction normal to the sonar beam. In (a), the highest values of the acoustic backscatter intensity are displayed in black and red. A vortex pair is discernible as the red vertical bands near 140m and 190m range. Bubbles injected by breaking Kelvin waves are evident as the vertical bands to the left and right of the bands corresponding to the vortex pair. (b) Velocity component parallel to the beam with high positive values (away from FLIP) displayed in blue, and high negative values (towards FLIP) displayed in red. Both the background swell and the Kelvin wave pattern are apparent.

## Chapter 6

### High-Frequency Volume and Boundary

### Acoustic Backscatter Fluctuations in Shallow Water

#### ABSTRACT

Volume and boundary acoustic backscatter fluctuations are characterized from data collected by the Toroidal Volume Search Sonar (TVSS), a 68 kHz cylindrical array capable of 360° multibeam imaging in the vertical plane perpendicular to its direction of travel. Acoustic backscatter imagery of the seafloor, sea surface, and horizontal and vertical planes in the volume that were presented in previous studies are used to attribute non-homogeneous spatial distributions of zooplankton, fish, bubbles and bubble clouds, and multiple boundary interactions to the observed backscatter amplitude statistics. Probability distribution functions fit to the empirical distribution functions of seafloor backscatter are non-Rayleigh, and well described by Weibull, K, and Rayleigh mixture models. Sea surface and volume backscatter depart more from Rayleigh statistics, and are multi-modal in some cases with the high density portion of the distributions arising from boundary reverberation, and the tails arising from sparsely distributed scatterers such as bubbles, fish, and zooplankton. A log-normal distribution provides the best fit to the high density part of the empirical distributions for volume backscatter, and Rayleigh mixture models provide the best fits to the tails for both sea surface and volume backscatter. Fits to the volume and near-surface backscatter data were poor compared to those fit to the boundary backscatter, suggesting that these data may be better described by mixture distributions with component densities from different parametric families. Physical arguments for the observations are presented, and the consequences for target detection are discussed.

#### I. INTRODUCTION

The statistical properties of underwater acoustic backscatter and reverberation fluctuations are important for active sonar performance studies,<sup>1</sup> target detection algorithms,<sup>2</sup> and studies of the ocean boundaries and volume.<sup>3,4</sup> A useful model for understanding the statistical properties of acoustic reverberation is the point scattering model,<sup>5-10</sup> which assumes that the total backscattered signal (in-phase and quadrature components) is the sum of  $n$  replicas of the transmitted signal  $s(t)$  backscattered from a homogeneous distribution of point reflectors

$$F(t) = \sum_{i=1}^n a_i B(t_i) s(t-t_i, \xi_i) \quad (1)$$

where  $t_i$  is the time of arrival from the  $i$ -th scatterer,  $a_i$  is the stochastic amplitude which corresponds to the scatterer's acoustic cross section,  $B(t_i)$  describes the sonar's acoustic geometry and gain, and  $\xi_i$  is a set of stochastic parameters defining the characteristics of the scattered signals, which may depend upon the relative motion between the acoustic array and the scatterers, their physical properties, and their spatial distribution. In general,  $F(t)$  will fluctuate around some time-varying mean value, and it is the probability density functions (PDF's) of these fluctuations that identify the noise models against which target detection algorithms must operate.<sup>11</sup>

The model in (1) assumes that the number  $n$  is governed by a Poisson distribution,

where the scatterers producing the resulting reverberation are discrete, statistically independent in position, and homogeneously distributed within the sonar's resolution cell. If the number of scatterers in a single resolution cell is very large, and their scattering coefficient distribution ( $a_i$ ) is such that no small number of them contributes significantly to the reverberation energy, application of the central limit theorem results in a Gaussian distribution for  $F(t)$ , with a Rayleigh distributed envelope and uniformly distributed phase. In typical shallow water environments, the distributions of scatterers can rarely be assumed to be homogeneous, and different types of scatterers on different spatial scales tend to produce more extreme reverberation values, depending upon the density of scatterers relative to the sonar's resolution cell size. For envelope distributions, these appear as multiple modes and/or large tails, deviating significantly from the traditional Rayleigh PDF. PDF models which have been useful in describing non-Rayleigh reverberation include the Weibull, K, log-normal, and Rayleigh mixture distributions.<sup>12-17</sup>

Realistic reverberation models must therefore incorporate both the characteristics of the sonar's beampattern and the spatial distribution of scatterers.<sup>16,18-22</sup> Although the former is usually known through system calibration, the latter is more difficult to characterize. Acoustic and optical imaging methods have been used for this purpose, but mostly for studies of the seafloor,<sup>12,14,23</sup> although some studies of the volume and sea surface<sup>24</sup> have been performed. To the best of our knowledge, no such study has been conducted for seafloor, sea surface, and volume backscatter and reverberation simultaneously. Such a study is warranted because rarely can reverberation be considered as a single component process. For example, volume reverberation from near-surface bubbles is a major source of noise in bioacoustic applications<sup>25</sup> and strongly influences acoustic backscatter from the sea surface.<sup>4</sup>

This paper presents a statistical analysis of seafloor, sea surface, and volume acoustic backscatter data simultaneously collected by the Toroidal Volume Search Sonar (TVSS), a 68 kHz cylindrical array which was deployed on a towfish at a depth of 78m in waters 200m deep, 735m astern of a towship during engineering tests conducted by the U.S. Navy's Coastal System Station (CSS), Panama City, Florida (Fig 1). The multibeam acoustic data collected by the TVSS were processed in previous studies to construct boundary<sup>26,27</sup> and volume<sup>28</sup> acoustic backscattering strength images in horizontal and vertical planes around the towfish (Fig. 2). In this study, we examine the statistics of, and fit probability distributions to the backscatter amplitudes corresponding to these data. References to our previously published imagery provide the means for discriminating between various reverberation components and directly attributing non-homogeneous spatial distributions of scatterers, such as bubbles, zooplankton, and multiple boundary interactions to non-Rayleigh backscatter amplitude distributions.

The distribution models considered in this study are the Rayleigh, K, Weibull, log-normal, and Rayleigh-mixture distributions. We chose these because: (1) they are commonly used in underwater acoustics, (2) they have been observed in previous studies of volume and boundary backscatter and reverberation, and (3) some have been analytically related to the physical scattering mechanisms which produce them. Although a number of probability distribution models have been developed for specific boundary or volume reverberation conditions,<sup>3,4,16,19,28</sup> our objective is to determine if there is a common model flexible enough to describe both boundary and volume backscatter arising from non-homogeneous, or patchy scatterer distributions that are typical in shallow water. In this context, our work may be considered an extension of that performed by Lyons and Abraham (1999), who fit Rayleigh, K, Weibull, and Rayleigh mixture models to acoustic backscatter amplitude data from a wide variety of seafloor types, and found the 3-component Rayleigh mixture distribution to be the most robust in describing the observed data.<sup>12</sup> We add to their results by:



(1) also including the log-normal PDF in the model-data comparisons, (2) analyzing data collected on a moving platform, thereby incorporating the influence of spatial variability on the backscatter amplitude fluctuations, and (3) analyzing data from both boundaries and the volume.

We begin in section II with a description of the PDF models and parameter estimation methods used in this study. Section III describes the TVSS signal processing methods and the data preparation steps. The results are described in section IV, and the physical mechanisms influencing the results, and the implications for target detection are assessed in section V.

## II. PROBABILITY DISTRIBUTION MODELS

Each of the distribution functions discussed here may be represented as a function of one or several parameters that must be estimated from the observed amplitude data,  $A = \{A_1, A_2, \dots, A_N\}$ , which is assumed to be independent and identically distributed. For parameter estimation, we use the maximum likelihood and method of moments techniques as described in Abraham (1997).<sup>29</sup> The maximum likelihood estimate (MLE) is chosen to maximize the likelihood function given the observed data, whereas the method of moments estimate (MME) is chosen by equating the first few moments of the model and the data. Maximum likelihood estimates are both consistent and asymptotically efficient, but their primary drawback is that they are not easily expressed in simple forms, and may require the use of iterative techniques such as the expectation-maximization (EM) algorithm. Although estimates obtained using the MME method also are consistent, their primary disadvantage is their inefficiency.

The first distribution we consider is the Rayleigh distribution, which describes the reverberation amplitude when the in-phase and quadrature components are normally distributed with zero mean, and results when there are enough scatters in the sonar's resolution cell for the central limit theorem to hold.<sup>6</sup> The Rayleigh distribution has been observed for high frequency backscatter from the seafloor<sup>12</sup>, sea surface,<sup>30</sup> and volume,<sup>3,31</sup> and may be expressed as a limiting case of the Ricean distribution in which scattering is primarily incoherent.<sup>3</sup> For seafloor acoustic backscatter, Stanton (1984) has related the Rayleigh PDF to the rms roughness and correlation area of the bottom.<sup>32</sup> The Rayleigh PDF is

$$p_R(A) = \frac{2A}{\lambda_R} e^{-\frac{A^2}{\lambda_R}}, \quad (2)$$

and the corresponding cumulative distribution function (CDF), also referred to as the probability distribution function, is

$$P_R(A) = 1 - e^{-\frac{A^2}{\lambda_R}} \quad (3)$$

both for  $A \geq 0$ , where the power  $\lambda_R = E[A^2]$ , with E representing the expected value. Both the MLE and MME estimates for  $\lambda_R$  are

$$\hat{\lambda}_R = \frac{1}{N} \sum_{i=1}^N A_i^2 \quad (4)$$

The K distribution is related to the Rayleigh distribution, as it may be represented as the product of a rapidly fluctuating, Rayleigh-distributed random variable, and a slowly varying, chi-distributed variable.<sup>33-35</sup> The K distribution has been successful in describing radar sea surface clutter because it has a direct physical interpretation: the Rayleigh component, with relatively short correlation widths, results from the many

scattering contributions within the resolution cell that arise from small scale facets on the sea surface, whereas the chi-distributed component, with relatively long correlation widths, arises from the larger scale, mean sea surface tilt (e.g. swell). The K distribution also<sup>36</sup> has been successful in describing signal envelope fluctuations in wireless channels<sup>36</sup> and seafloor acoustic backscatter in sidescan sonar images.<sup>13-14</sup> The K PDF is:<sup>29</sup>

$$p_K(A) = \frac{4}{\sqrt{\alpha} \Gamma(\nu)} \left( \frac{A}{\sqrt{\alpha}} \right)^\nu K_{\nu-1} \left( \frac{2A}{\sqrt{\alpha}} \right), \quad (5)$$

and its CDF is

$$P_K(A) = 1 - \frac{1}{\Gamma(\nu) 2^{\nu-1}} \left( 2 \frac{A}{\sqrt{\alpha}} \right)^\nu K_\nu \left( \frac{2A}{\sqrt{\alpha}} \right), \quad (6)$$

for  $A \geq 0$  where  $K_{\nu-1}$  is the  $\nu-1$  order modified Bessel function and  $\Gamma()$  is the gamma function. In the limit as  $\nu \rightarrow \infty$ , the Rayleigh distribution with power  $\alpha$  is obtained from the K distribution when the scale  $1/\sqrt{\nu}$  is applied to  $A$ . Based on a tradeoff between performance and difficulty with implementation, we use the MME's instead of the MLE's for  $\nu$  and  $\alpha$ , as detailed in Abraham (1997).

The Weibull distribution also reduces to the Rayleigh distribution in certain cases, and has been successful in describing seafloor backscatter amplitude distributions.<sup>12</sup> The two-parameter Weibull PDF is:<sup>29</sup>

$$p_W(A) = \alpha \beta A^{\beta-1} e^{-\alpha A^\beta} \quad (7)$$

for  $A \geq 0$ , with its CDF given by

$$P_W(A) = 1 - e^{-\alpha A^\beta}, \quad (8)$$

where it can be seen that the Rayleigh distribution results when  $\beta = 2$  and  $\alpha = 1/\lambda_R$ . To obtain the MLE's for  $\alpha$  and  $\beta$ , we used Abraham's (1997) implementation of an iterative algorithm described in Johnson, Kotz, and Balakrishnan (1994).<sup>29,37</sup>

Whereas the K and Weibull distributions may be related to physical scattering mechanisms through their relationship with the Rayleigh distribution, the log-normal distribution has yet to reveal such an analytical connection. Nevertheless, the log-normal distribution has been observed in studies of underwater acoustic backscatter and propagation,<sup>15,38,39</sup> radar clutter from the sea surface,<sup>40</sup> and signal envelope fluctuations in wireless channels.<sup>36,41</sup> The two-parameter log-normal PDF is:<sup>42</sup>

$$p_{LN}(A) = \frac{1}{\sqrt{2\pi} \alpha A} e^{-\frac{(\ln A - \beta)^2}{2\alpha^2}} \quad (9)$$

for  $A > 0$ . It has the property that  $\ln(A)$  is normally distributed with mean  $\beta$  and variance  $\alpha^2$ . The log-normal CDF is

$$P_{LN}(A) = \Phi \left( \frac{\ln A - \beta}{\alpha} \right) \quad (10)$$

where

$$\Phi(u) = \frac{1}{\sqrt{2\pi}} \int_{-\infty}^u e^{-\frac{w^2}{2}} dw \quad (11)$$

is the CDF of a standard normal random variable  $u$ . Another property of the log-normal distribution is that if  $A$  is log-normally distributed, so is  $A^2$ ; i.e., if the echo amplitude follows eqn (9), so will the intensity.<sup>42</sup> We use the MME's for  $\alpha$  and  $\beta$

because they are more consistent than the MLE's.<sup>37</sup>

In typical shallow water environments, acoustic backscatter and reverberation result from several independent scattering mechanisms, such as bubbles, bioacoustic scatterers, and boundary roughness, and each of these may be characterized by different spatial scales. It is reasonable, then, to consider that such a scenario might be represented by a mixture of  $m$  Rayleigh random variables, each with a component probability  $\epsilon_i$  and power  $\lambda_{R,i}$ . The resulting Rayleigh mixture PDF is:<sup>29</sup>

$$p_{RM}(A) = \sum_{i=1}^m \epsilon_i \frac{2A}{\lambda_{R,i}} e^{-\frac{A^2}{\lambda_{R,i}}}, \quad (12)$$

and its CDF is

$$P_{RM}(A) = 1 - \sum_{i=1}^m \epsilon_i e^{-\frac{A^2}{\lambda_{R,i}}}, \quad (13)$$

where

$$\sum_{i=1}^m \epsilon_i = 1 \quad (14)$$

is required to ensure a valid CDF. We use the expectation maximization (EM) algorithm to obtain the MLE's for the mixture component powers  $\lambda_{R,i}$  and proportions  $\epsilon_i$ . The method requires that the number of components  $m$  be specified. Further information on the EM algorithm, as well as an excellent survey of the numerous applications of mixture distributions may be found in Titterton, Smith, and Makov (1985).<sup>43</sup>

Although the component densities in a mixture distribution need not be Rayleigh, or even members of the same parametric family, Rayleigh-mixture distributions have been successful in describing seafloor acoustic backscatter.<sup>12,17,29</sup> Because mixture distributions have yet to be evaluated for reverberation from the both boundaries and the volume, we shall test it below with data collected by the TVSS. We begin by describing the TVSS, the data, and the details of the acoustic geometry that help in understanding the results.

### III. TVSS DATA

#### A. TVSS Data Collection

The TVSS includes separate cylindrical projector and hydrophone arrays, with the same 0.53 m diameter, mounted coaxially on a cylindrical tow body. The projector array has 32 elements equally spaced 11.25° apart around the cylinder and designed to produce a "toroidal" beam pattern that is meant to be omni-directional in the plane perpendicular to the cylinder's axis (usually across-track) and 3.7° wide at -3 dB in any plane containing the cylinder's axis (usually along-track) (Fig. 2). The hydrophone array consists of 120 elements equally spaced every 3° around the cylinder. In the work presented here, beamforming of the hydrophone array yielded 120 receive beams, each 4.95° wide at -3 dB and spaced 3° apart to cover the full 360° around the array in the plane perpendicular to the array's axis.

The acoustic data were collected by the TVSS on 9 November 1994 between 1026AM-1131AM local time in a 2 nm<sup>2</sup> area 65nm southeast of Panama City, Florida, in the northeastern Gulf of Mexico. The TVSS was towed approximately 735m aft of the towship *Mr. Offshore* at a nearly-constant depth of 78m (Fig. 1). Three runs of

100 consecutive pings of acoustic backscatter data from a 200 $\mu$ s CW pulse of 68 kHz were obtained while the towship speed was nearly constant at 4.1m/s. Towfish attitude and motion data were sampled at 1Hz (once per ping) and included roll, roll rate, pitch, heading, speed, and depth. The environmental data collected during the experiment included a single CTD cast taken at 0658AM, which revealed the presence of an isothermal mixed layer with a temperature of 24.8°C extending to a depth of 49m, a thermocline between 49m-150m depth, and a nearly-isothermal layer above the bottom with a temperature of 15.6°C. The surface salinity was 35.1 ppt, and the surface sound velocity was 1534m/s. The wind speed recorded at 0658AM onboard *Mr. Offshore* was 6 knots (3m/s), and the sea state was 1.5.

## B. TVSS Data Processing

The TVSS data were processed with a scheme designed for conformal arrays and included: quadrature sampling, resampled amplitude shading, element-pattern compensation, and broadside beamforming on phase-compensated, overlapping sub arrays with asymmetric projected element spacings.<sup>44</sup> This procedure permits split aperture processing of the beamformed output, which is performed because the phase zero-crossing of the output phasor is the most accurate means to detect the arrival time of boundary reflections on the maximum response axis of the beam.<sup>26</sup>

For each ping, the acoustic signals from the 120 hydrophones are heterodyned in the data acquisition system (DAS) from 68 kHz to 6.25 kHz, low-pass filtered, digitally recorded, then converted to volts.<sup>26</sup> To form a beam in the direction  $\theta$ , at each time sample  $t$ , the quadrature sampled acoustic signals from 29 elements are adjusted to project the aperture on the tangent perpendicular to the direction  $\theta$ . We define  $\theta$  as the roll-corrected angle in the  $x$ - $z$  plane perpendicular to the axis of the towfish, such that the towfish's zenith is at  $\theta = 0^\circ$ , with  $\theta$  increasing clockwise around the towfish when facing the direction of travel (Figs. 1,2). The split aperture process is achieved by dividing this aperture into two overlapping 21-element subapertures whose phase centers are spaced 8 elements apart. For each time sample  $t$ , the signals from these two subapertures are phase shifted and summed separately to produce beams  $B_1(\theta, t)$  and  $B_2(\theta, t)$ , and a phasor  $P(\theta, t)$  is formed as:

$$P(\theta, t) = B_1(\theta, t) \times B_2^*(\theta, t) \quad , \quad (15)$$

where  $*$  denotes complex conjugation. The magnitude of  $P(\theta, t)$  is the product of the magnitudes of  $B_1(\theta, t)$  and  $B_2(\theta, t)$ , hence it has units of volts squared, and its phase is the phase difference between  $B_1(\theta, t)$  and  $B_2(\theta, t)$ .  $B_1(\theta, t)$ ,  $B_2(\theta, t)$ , and  $P(\theta, t)$  are all broadside with respect to the 29-element aperture. This operation is performed at every time sample  $t$  for each ping, every  $3^\circ$  for directions spanning  $360^\circ$  around the TVSS axis. The beam directions are corrected for the difference between the sound speed used in the beamforming and that of seawater at the face of the array because  $B_1(\theta, t)$  and  $B_2(\theta, t)$  are not broadside to their respective subapertures.

In this study, we present various results based on backscatter amplitude, backscattering strength, and backscatter intensity. Acoustic backscatter intensity, or reverberation level, is computed by correcting for the receiver gain and directivity:

$$RL = 10\log_{10}\left(\frac{1}{2}P(\theta, t)\right) - RVR - FG - DI - TVG \quad (\text{dB}), \quad (16)$$

where  $RVR = -168$  dB re:  $1 \text{ V}_{rms}/\mu\text{Pa}$  is the receive voltage response of each hydrophone,  $FG = 29$ dB is the preamplifier fixed gain,  $DI = 13$ dB is the array gain associated with the beamforming and split aperture processing, and  $TVG$  is the system time-varying gain. Acoustic backscatter amplitude is then computed as the square root of the magnitude of  $RL$  in linear units.  $RL$  is related to bottom, surface, and volume backscattering strength by:<sup>45</sup>

$$S_{B,S,V} = RL - SL + 2TL - 10 \log_{10}(A,V) , \quad (17)$$

where SL is the calibrated transmit source level of 216.8dB *re*: 1μPa @ 1m, TL = 20 log<sub>10</sub>R + α R is the one-way transmission loss due to spherical spreading and absorption with the logarithmic absorption coefficient α = 0.024 dB/m, range R is determined from *t* and θ using constant-gradient raytracing techniques,<sup>45</sup> A is the area in m<sup>2</sup> within the receive beam that is ensonified by the transmit pulse (for S<sub>S</sub> and S<sub>B</sub>), and V is the ensonified volume in m<sup>3</sup> (for S<sub>V</sub>).

### C. TVSS Acoustic Geometry

The statistical results are best interpreted with an understanding of the TVSS acoustic geometry, which may be obtained from Figs 3 and 4. Fig 3 depicts a vertical slice of volume scattering strength (S<sub>V</sub>) perpendicular to the towfish axis, formed by displaying the acoustic data in each of the 120 TVSS receive beams in a single ping around the TVSS in polar coordinates of angle vs. two-way travel time. In this representation, echoes from the sea surface and seafloor appear as the high backscatter, horizontal features. Scattering from resonant microbubbles in the towship's wake and from bubble clouds formed by breaking ship waves are responsible for the high backscattering strength features near the sea surface. The circular features result from boundary reflections received in the sidelobes of beams directed away from the boundary. The angular sample spacing in this figure, which corresponds to the spacing between maximum response axes of adjacent beams, is θ<sub>s</sub>=3°. The time sampling interval corresponds to the quadrature sampled time increment within each beam of τ<sub>s</sub> = 160 μs and results in a 12cm sampling interval assuming a sound speed in seawater c=1500m/s. The range resolution for each sample is defined in terms of the bandwidth W:

$$\Delta R = c / 2W \quad (m) \quad (18)$$

With the TVSS CW pulse length τ<sub>p</sub>=200μsec, the bandwidth W=0.88/τ<sub>p</sub> = 4.4kHz yields a range resolution of 17cm with c=1500m/s.

The volumetric resolution in each ping is determined by the spatial dimensions of the volume (V) ensonified by the TVSS transmit pulse within each receive beam (Fig. 4), which may be computed as the ellipsoidal shell formed from the intersection of the pulse, the transmit beampattern, and the receive beampattern at each sampling point:

$$V = \frac{2}{3} \theta_T \sin(\theta_R / 2) [ R'^3 - R^3 ] \quad (m^3) \quad (19)$$

where R is the range from the center of the TVSS in meters, R' = R + ΔR, the -3dB receive beamwidth (θ<sub>R</sub>) is 4.95°, and the -3dB transmit beamwidth (θ<sub>T</sub>) is 3.7°. Volume resolution is determined by the spatial dimensions of V in the across-track, along-track, and vertical dimensions (Δx<sub>V</sub>, Δy<sub>V</sub>, Δz<sub>V</sub>). These increase with range, as described by the expressions in reference (25).

Samples in adjacent beams overlap because θ<sub>s</sub> < θ<sub>R</sub> / 2. The overlapping volume increases with range:

$$V_{ol} = \frac{2}{3} \theta_T \sin((\theta_R - \theta_s) / 2) [ R'^3 - R^3 ] \quad (m^3) \quad (\text{adjacent beams}) \quad (20)$$

The percent of overlapping volume between adjacent beams is:

$$VP_{ol} = [ (\sin((\theta_R - \theta_s) / 2) / \sin(\theta_R / 2)) ] \times 100\% \quad (\text{adjacent beams}) \quad (21)$$

yielding a range independent volume overlapping percentage of 39.4% between TVSS beams.

Over successive pings, ensonified volume cells in the same angle of arrival and

range overlap beyond the range defined by:

$$R_{ol} = \Delta y_{ping} / 2 \tan(\theta_T / 2) , \quad (m) \quad (22)$$

where the along-track separation between pings is defined as:

$$\Delta y_{ping} = V_{TVSS} / prr \quad , \quad (m) \quad (23)$$

in which  $V_{TVSS}$  is the speed of the towfish, and  $pr$  is the pulse repetition rate. Because the average  $V_{TVSS}$  was 4.1m/s, and the  $pr$  of the TVSS was 1Hz, the average  $\Delta y_{ping}$  and  $R_{ol}$  for consecutive pings were 4.1m and 62m, respectively. The overlapping volume along-track increases with range, but decreases as ping separation and towfish speed increase.

On the boundaries, resolution is defined by the area (A) ensonified by the transmitted pulse within each receive beam (Fig. 4). If we define the angle of arrival ( $\theta_a$ ) as  $\theta$  in Fig. 3 for  $\theta = 0^\circ$  to  $90^\circ$ ,  $|180^\circ - \theta|$  for  $\theta = 91^\circ$  to  $270^\circ$ , and  $|\theta - 360^\circ|$  for  $271^\circ$  to  $359^\circ$ , then for  $\theta_a$  near normal incidence, the area is defined approximately by an ellipse:

$$A = \pi \Delta R (1 + 2H_{TVSS} / \Delta R)^{1/2} H_{TVSS} \theta_T / 2 \quad (\text{seafloor})$$

$$A = \pi \Delta R (1 + 2Z_{TVSS} / \Delta R)^{1/2} Z_{TVSS} \theta_T / 2 \quad (\text{seasurface}) \quad (24)$$

Beyond a delimiting angle of  $\cos^{-1}(H_{TVSS} / (H_{TVSS} + \Delta R))$  for A on the seafloor, and  $\cos^{-1}(Z_{TVSS} / (Z_{TVSS} + \Delta R))$  for A on the sea surface, the ensonified area is defined by an annulus sector (Fig. 4):

$$A = (R \Delta R \theta_T) / \sin \theta_a + (\Delta R^2 \theta_T) / (2 \sin \theta_a) \quad . \quad (m^2) \quad (25)$$

Thus, resolution increases with range because the spatial dimensions of A increase in the across-track, along-track, and vertical dimensions ( $\Delta x_{S,B}$ ,  $\Delta y_{S,B}$ , and  $\Delta z_{S,B}$ ) on the sea surface or seafloor. As in the volume, ensonified areas overlap along-track by an amount which increases with range because  $\Delta y_{ping}$  is less than the along-track extent of A ( $\Delta y_{S,B}$ ).

#### D. Data Partitioning and Description

Applying sidescan imaging techniques and eqns (15)-(17) to the TVSS data collected over multiple pings, we constructed seafloor, sea surface, and horizontal and vertical volume backscattering strength images, which are analyzed in references (25)-(26). Four of these images are shown in Fig. 5 with their along-track averages. Whereas the seafloor image appears fairly homogeneous away from the track center-line (Fig 5a), the sea surface and volume images exhibit significant spatial variability due to bubbles and bubble clouds (Fig. 5b,c) and aggregations of volume scatterers (Fig. 5d).

The acoustic backscatter amplitude data corresponding to these images were then partitioned into data sets which encompassed the analysis regions defined in Table I. The locations of the centers of these regions are indicated in Fig. 6. For 14 of the 15 analysis regions in Table I, three separate runs of 100 pings were used, and for one region (NS1), two runs of 100 pings were used. Thus, the partitioning formed a total of 44 data sets.

Ideally, we would analyze the data collected in each grazing angle/depth/across-track distance location separately. However, this would have resulted in less than 100 samples per analysis region, and the PDF models and parameter estimation methods used here perform well for much larger sample sizes.<sup>29</sup> Therefore, we grouped data into the regions defined in Table I. To ensure the data in each region did not vary significantly over the range of grazing angles within each region, they were tested for homogeneity across both grazing angles and pings, as discussed below.

The partitioned data corresponding to the seafloor analysis regions span three different grazing angle regimes: normal and near normal incidence (SF1), moderate to high grazing angles (SF2), and moderate to low grazing angles (SF3). Bathymetry constructed from the TVSS backscatter data revealed a relatively flat bottom, with a 3m/km south west slope, and an average depth of 198m. Seafloor acoustic backscattering strength imagery indicated a homogeneous spatial distribution of sediments, and the angular dependence function estimated from the acoustic backscattering strength was consistent with the silt-sand mixture of sediments previously surveyed in the region (e.g. Fig. 5a).<sup>26</sup>

The sea surface analysis regions were influenced only slightly by sea surface roughness produced by the ambient 3m/s winds. Because of the vertical extent of the transmitted acoustic pulse intersecting the sea surface (Fig. 4), the sea surface data were more strongly influenced by clouds of resonant microbubbles which were characterized by different spatial dimensions and scattering characteristics that depended upon their generating mechanisms. These included: (1) very dense bubble clouds generated primarily by propeller cavitation within the towship's wake (SS1), (2) large-scale ( $O(10^2)$  to  $O(10^3)$  m) bubble clouds generated by breaking ship waves (SS2), and (3) sparsely distributed, small scale ( $O(1)$  to  $O(10)$  m) bubble clouds generated by the ambient sea (SS3) (e.g. Fig. 5b). The SS3 region also was influenced strongly by bottom reverberation received in the sidelobes after the first bottom echo arrival. Although we did not have *in-situ* bubble size and density data, we used the resonant bubble approximation to estimate the densities of bubbles in the analysis regions from the surface and near-surface acoustic backscattering strength data in reference (27).

The near-surface volume regions were influenced by some of the same processes as those affecting the sea surface backscatter. Clouds of resonant microbubbles in the towship's wake contributed to the backscatter in both the NS1 and NS2 regions, but these clouds were more dense in NS1 than in NS2 because the wake in NS2 was about 20 minutes old, whereas the wake in NS1 was only 3 minutes old (Fig. 5c). In the same across-track location as the SS2 region, the NS3 region at 3m depth was also affected by large scale bubble clouds generated by breaking towship waves. Similarly, the NS4 region was in the same across-track location as the SS3 region, and was also influenced by bottom reverberation and smaller scale bubble clouds generated by the ambient sea. The NS5 region was influenced by both near-surface bubbles and multiple boundary reflections occurring after the first bottom-surface multiple arrival. The NS1, NS3, NS4, and NS5 regions were influenced somewhat by surface roughness, due to the vertical extent of the ensonified volume (Fig. 4).

Three of the volume regions were influenced by aggregations of zooplankton, whose density generally decreased with depth from the base of the mixed layer (VL1), through the upper (VL2) and lower thermocline (VL3) (e.g. Fig. 5d).<sup>25</sup> The VL4 region was near the bottom, and was influenced slightly by a sparse distribution of small fish, but more strongly by surface reverberation received in the sidelobes after the first surface echo arrival. As with the near-surface data, we lacked the *in-situ* data to characterize absolute densities and sizes of organisms in the volume, so we have inferred the relative densities from the corresponding volume acoustic backscattering strength data in reference (25). Although several dense fish schools were observed near the bottom, the backscatter data in these regions could not pass statistical independence tests, so they were not included in the analysis.

## E. Data Preparation

After grouping the TVSS acoustic backscatter amplitude data according to the analysis regions in Table I, the data were searched for noise spikes which sporadically

occurred during each run and resulted from saturation in the receive array electronics. Because the spatial structure of each noise spike differed significantly from those of naturally occurring scattering features, such as bubble clouds, fish schools, and surface roughness, they were easily detected. They typically had an arc-like appearance, extending 12-36cm in range, and 6-36° in angle (see Fig. 6 in reference (25)).

Because statistical analyses require independent and identically distributed data, the amplitudes were decimated by taking only those samples separated by at least a correlation width. In each analysis region, we estimated the correlation widths for each grazing angle and ping from the normalized spatial autocovariance:

$$C(\Delta r_m) = \frac{c(\Delta r_m)}{c(0)} \quad (26)$$

where the autocovariance is

$$c(\Delta r_m) = \frac{1}{M-m} \sum_{i=1}^{M-m} (A(r_i) - \mu_A)(A(r_{i+m}) - \mu_A) \quad , \quad -M < m < M \quad (27)$$

$\Delta r_m = r_i - r_m$  is the lag in meters corresponding to  $m$  samples,  $M$  is the total number of samples in the given grazing angle or ping,  $r_i$  is the vertical or horizontal location of the  $i$ -th sample, and  $\mu_A$  is the mean amplitude estimated over the  $M$  samples according to the Appendix. The correlation widths were estimated as the horizontal or vertical lags ( $\Delta r_m$ ) where  $C(\Delta r_m)$  decreased from its maximum value of 1 at  $\Delta r_m=0$  to zero; in cases where  $C(\Delta r_m)$  dropped sharply to a low value ( $< 0.1$ ), and then fell gradually to zero, we used the distance for which  $C(\Delta r_m)$  decreased to 0.1. Along-track correlation widths computed for each grazing angle in each analysis region were never greater than the average ping separation distance of 4.1m, so the data were not decimated along-track. Across-track correlation widths for data in the boundary (SF,SS) and near-surface (NS) regions were usually less than 5m, and vertical correlation widths for the volume regions (VL) were rarely greater than the vertical sampling interval. Retaining samples separated by a correlation width resulted in an average decimation factor of 3 for the boundary and near surface data, and an average decimation factor of 2 for the volume data. Estimates of  $C(\Delta r_m)$  computed from the decimated amplitude data verified that they were not correlated along-track, across-track, or in depth.

As we are interested in reverberation fluctuations, we removed nonstationarities resulting from backscatter angular dependence and irregularities in the TVSS transmit and receive beampatterns by grouping the amplitude data in each analysis region into bins 1° wide according to grazing angle and angle with respect to the TVSS, and then normalizing by the mean in the group. The normalized data were then re-grouped into each analysis region (Table I), and inspected to ensure that all beampattern artifacts were adequately removed.

To ensure that the samples in each analysis region were statistically independent and identically distributed across pings and grazing angles, we performed the one sample runs test for randomness and the Mann-Whitney  $U$  test for homogeneity twice: first, to the normalized samples in each grazing angle across pings, and next to the normalized samples in each ping across grazing angles. Most of the data in the seafloor (SF) and volume (VL) regions passed the tests at the 95% confidence level, but 20-50% of the sea surface (SS) and near-surface (NS) data failed the tests. In studies of data collected on fixed platforms, the approach is to simply remove data which do not pass the tests at the specified confidence level.<sup>11</sup> Doing so in our study was not possible because the TVSS data were collected from a moving platform. Therefore, for each analysis region, we selected only those samples within the largest contiguous regions (across pings and grazing angles) which passed both tests at the 95% confidence level. We verified that the retained samples included contributions from



the various backscattering and reverberation features in Table I by analyzing backscattering strength images formed from these data (e.g. Fig. 5).

## IV. RESULTS

### A. Backscattering Strength, Amplitude and Intensity Statistics

The data in each of the analysis regions were first characterized by averaging statistical estimates of the corresponding backscattering strength ( $S_{B,S,V}$ ), amplitude ( $A$ ), and intensity ( $A^2$ ) over the three TVSS runs (Table II). Expressions for the mean ( $\mu_A$ ), variance ( $\sigma_A^2$ ), skewness ( $\gamma_{3,A}$ ), and kurtosis ( $\gamma_{4,A}$ ) estimates are given in the Appendix. The range was computed as the difference between the maximum and minimum values. The scintillation index, which is the variance of the intensity fluctuation scaled by the square of the mean intensity, was computed as

$$\sigma_{A^2} = \frac{\langle (A^2 - \langle A^2 \rangle)^2 \rangle}{\langle A^2 \rangle^2} \quad (28)$$

where  $\langle \rangle$  denotes a mean estimate. We include this quantity because it generally indicates the extent to which the data depart from a Rayleigh distribution, as Rayleigh-distributed amplitudes result in a scintillation index of one.<sup>6,12</sup>

Compared to the scintillation indices for the surface (SS), near-surface (NS), and volume (VL) regions, those for the seafloor regions are the closest to one, suggesting that they depart the least from Rayleigh distributions. In addition, the amplitude variance, skewness, and kurtosis values are lower for the seafloor regions. Consistent with composite roughness model predictions for the silt-sand sediment type in the region, mean backscattering strengths decrease away from the nadir region (SF1) (e.g. Fig. 5a).<sup>26</sup> The region at nadir also exhibits the highest variance, skewness, and kurtosis of the three seafloor regions.

Statistics for the sea surface regions differed significantly from those for the seafloor regions. The region at zenith (SS1) had the highest mean backscattering strengths of all regions, but these were attenuated approximately 22dB below model predictions by resonant microbubbles in the towship's wake (e.g. Fig. 5b,f).<sup>27</sup> Whereas backscattering strength decreased with grazing angle, scintillation indices, and backscatter amplitude skewness and kurtosis increased with decreasing grazing angle. This trend was opposite that of the bubble densities inferred from backscattering strength imagery (Fig. 5b),<sup>27</sup> as the highest occurred near the towfish zenith (SS1), lower densities occurred in the regions influenced by large scale bubble clouds produced by breaking ship waves (SS2), and the lowest bubble densities were observed farther across track (SS3) where the near-surface bubble population consisted primarily of those generated by small scale breaking of the ambient sea waves.

Statistics for three of the near-surface regions (NS2-NS4) exhibited a grazing angle dependence similar to that of the sea surface regions (SS1-SS3), with mean backscattering strength decreasing, and skewness, kurtosis, and scintillation index increasing away from the towfish's zenith. For the NS1 and NS5 regions, backscattering strength increased with decreasing grazing angle as a result of the bottom-surface multiple echo. For the NS1 region, backscattering from microbubbles in the decaying towship's wake (Fig. 1) also increased the mean volume backscattering strength above that for the higher grazing angle region (NS4). Although the NS1 and NS5 regions were at similar across-track locations and had the largest ensonified volumes of all the analysis regions (Table I), their statistics were dramatically different. The skewness, kurtosis, and the scintillation index values for the NS5 region are among the highest values of all the analysis regions, and result from sparsely distributed bubbles

generated by small scale breaking of ambient sea waves. The corresponding values for the NS1 region are significantly lower, and are the result of scattering from the more dense distribution of bubbles in the towship's wake from the previous run.

The statistics for the volume regions were similar to those for the near-surface and sea surface regions in that they were mostly influenced by the density of scatterers. For the VL1-VL3 regions, mean backscattering strength decreased, and skewness, kurtosis, and scintillation index increased with depth, resulting from the decrease in zooplankton density with depth (e.g. Fig. 5d). Statistics for the VL4 region depart from this trend because of the influence of surface reverberation after the first surface echo.

Before fitting the various PDF models to the TVSS data, we evaluated their potential suitability for describing backscatter fluctuations by comparing plots of the skewness and kurtosis descriptors ( $\beta_1, \beta_2$ ) of the normalized backscatter amplitude data with the possible values for each PDF family (Fig. 7), where  $\beta_1 = \gamma_{3,A}^2$ , and  $\beta_2 = \gamma_{4,A} + 3$ . The Appendix describes the basis for this figure, which is taken from Abraham (1997) and Johnson, Kotz, and Balakrishnan (1994).<sup>29,46</sup> Although matching skewness and kurtosis does not imply that distributions are identical or even a good approximation to one another, estimates of  $\beta_1$  and  $\beta_2$  from real data can provide an indication of which PDF families are appropriate to consider. Except for the log-normal distribution, all PDF models appear suitable for describing the seafloor backscatter data, which is closer to being Rayleigh distributed than the amplitude data in the other regions. Skewness and kurtosis descriptors estimated from the sea surface, near-surface, and volume backscatter amplitude data are spread among all the PDF models, but only the Rayleigh mixture model is flexible enough to encompass all the measurements.

## B. Probability Distribution Functions

Rayleigh, K, Weibull, log-normal, and Rayleigh mixture distributions were fit to the empirical distribution functions corresponding to the backscatter amplitude data in each run and TVSS analysis region. Figures 8-11 show results of representative runs for the seafloor, sea surface, near-surface, and volume displayed as probabilities of false alarm ( $PFA = 1 - CDF$ ). PFA is the probability that the amplitude will be higher than or equal to a given value, and we use it to display the results because it best illustrates the non-Rayleigh nature of the data, which is mostly seen in the tails of the distributions. Although backscatter amplitude in decibels is displayed on the abscissa of each plot, the distribution fits were obtained from the data in linear units.

Two measures were used to assess the goodness of fit between the model distributions and the empirical distributions derived from the TVSS data. The first was based on the Kolmogorov-Smirnoff test statistic, defined as the maximum absolute difference between the theoretical CDF ( $P(A)$ ) and that formed from the  $N$  data samples:

$$D_{ks} = \max |P(A) - F_N(A)|, \quad -\infty < A < \infty. \quad (29)$$

When the empirical data ( $F_N(A)$ ) are drawn from a population in which the random variable  $A$  has a continuous distribution function  $P(A)$ , the limiting distribution of  $D_{ks}$  derived by Kolmogorov is:<sup>48</sup>

$$\lim_{N \rightarrow \infty} P\left(D_{ks} < \frac{h}{\sqrt{N}}\right) = Q(h) \quad (30)$$

where, for  $h > 0$ ,

$$Q(h) = \sum_{i=-\infty}^{\infty} (-1)^i e^{-2i^2 h^2} \quad (31)$$

The KS  $p$ -value is  $(1 - Q(h))$  and represents the probability from 0 to 1 of observing a more extreme value of  $D_{ks}$  under the null hypothesis that the data are distributed according to  $P(A)$ . The closer  $p$  is to one, the more likely a more extreme value of the KS test statistic  $D_{ks}$ , and hence, more likely that the observed data follow the model CDF. We use the KS test because it is nonparametric, and it allows comparison with other studies which have shown that it gives a sufficient measure of the goodness of fit between theoretical and estimated CDFs.<sup>12,29</sup>

The problem with using the KS  $p$ -value for comparing the goodness of fit for different distributions is that eqn (31) is not valid when parameters for the theoretical distribution are estimated from the empirical data,<sup>48</sup> which is the approach taken in this study. Therefore, we assessed the relative goodness of fit for the different PDF models by computing the root mean square difference between the model and the empirical distribution functions

$$D_{rms} = \left[ \frac{1}{N} \sum_{i=1}^N (P(A_i) - F_N(A_i))^2 \right]^{\frac{1}{2}} \quad (32)$$

and averaged values over the three TVSS runs for each region (Table IV). In addition, rms differences were computed and averaged only for the samples in the distributions for which the PFA was less than  $10^{-2}$  (Table V) in order to evaluate how well the model CDFs fit the TVSS data in the tails of the distributions. This "tail rms difference" was calculated because relatively high kurtosis values in the near-surface and surface data suggested that large tails would be present in the distributions of these data (Table II).

Among all analysis regions and PDF model types, the seafloor amplitude data had the lowest rms differences and best statistical fits (KS  $p$ -values). All ranges of grazing angles (SF1-SF3) were non-Rayleigh, but the moderate grazing angle region (SF2) was relatively close to Rayleigh (Fig. 8). However, K, Weibull, and Rayleigh mixture distributions provided good fits to the distributions (Tables III,IV) and the tails (Table V). The Rayleigh mixture distributions showed the best overall performance, and rms differences and KS  $p$ -values indicated that no significant advantage was gained by using more than 3-components in the Rayleigh mixture. These results are generally consistent with those in Lyons and Abraham (1997) for backscatter amplitude data from mud bottom types in the 40-60° and 60-80° grazing angle regimes. The KS  $p$ -values in Table III are slightly lower than theirs probably because of spatial variations in the bottom. Such variations were not present in their data because they were collected from fixed platforms.

Backscatter amplitude fluctuations from the sea surface (Fig. 9) were more non-Rayleigh than those from the seafloor, and depended mostly upon grazing angle and the density of bubbles relative to the vertical extents of the ensonified volumes adjacent to the sea surface (Fig. 4). For the zenith region (SS1), where very high densities of bubbles in the towship's wake attenuated the acoustic backscatter, only the Rayleigh mixture models provide statistically good fits to the observed data. Outside the wake, where bubble densities resulting from breaking waves generated by the towship were significantly lower than at zenith, KS  $p$ -values were lower and rms differences were higher, with Rayleigh mixture models again showing superior overall performance.

Backscatter amplitude distributions in the lowest grazing angle region (SS3, Fig.

9c) appeared to be multi-modal (c.f. reference (40), Fig. 4.1.4). Analysis of Fig. 6 and the sea surface backscattering strength imagery corresponding to these data (e.g. Fig. 5b) indicates that the centers of the distributions for the SS3 regions were dominated by bottom reverberation, and the tails were dominated by randomly distributed bubbles within a meter of the sea surface. In terms of rms differences and KS  $p$ -values, the log-normal model provided the best overall fits to the data in the SS3 regions (Tables III, IV). This appears to result from the fact that the KS  $p$ -value and rms difference emphasize samples near the center of the distribution. As indicated by Fig. 9c and the rms differences for PFA values less than  $10^{-2}$  (Table V), the Rayleigh mixture models provided the best fits to the tails in the SS3 regions.

Similar to the SS3 region, most of the near-surface data were best described by the log-normal model (Table III), but the Rayleigh mixture models provided the best fits to the tails (Fig. 10; Table V). Results for the NS1 and NS3 regions were split, with the Rayleigh mixture and log-normal models both providing the best fits for different data runs (Table III). Overall, the model-data fits were statistically poor, and characterized by the highest rms differences and lowest KS  $p$ -values of all the analysis regions (Tables III, IV). Sidelobe returns from the bottom-surface multiple occur in the NS1 and NS5 regions, and sidelobe returns from the bottom echo are evident in the NS4 region. The outer edges of the NS1 region are influenced by sidelobe returns from the first surface echo at the towfish's zenith, and the NS3 region is influenced by sidelobe returns from the first surface echo. The best fits for the log-normal distribution were in the regions where the boundary reverberation was the strongest (i.e. NS2, after the first surface echo; and NS4, after the first bottom echo).

Analysis of backscattering strength imagery indicated that the dominant mechanisms contributing to the tails of the near-surface distributions were scattering from resonant microbubbles and bubble clouds, with bubble density controlling the tail shape. When the bubbles were sparsely distributed, such as those generated by the breaking ambient sea waves, the tail was well-separated from the distribution center, resulting in what appeared to be a multi-modal distribution (NS4, Fig. 10d; NS5, Fig. 10c). When the bubbles were more densely packed, such as in the towship's wake (NS1,2) and in the region affected by large scale bubble clouds generated by ship-waves (NS3), the distributions appeared unimodal, with the largest tails occurring in the regions with the highest bubble densities (NS2, Fig. 10b). As with the sea surface results, little or no improvement in fitting the tails of the distributions occurred when we increased the number of components in the Rayleigh mixture above 3, and 2 components were sufficient in most cases.

Results for the volume backscatter amplitude data (Fig. 11) were generally similar to those for the near-surface data: they were best fit by the log-normal model over the entire distribution and the Rayleigh mixture distributions in the tails. In addition, the fits were not statistically good, with relatively low KS  $p$ -values and high rms differences (Table III-V). The best fits to the log-normal model were obtained when boundary reverberation was present, i.e. in data for the VL4 region (Fig. 11d) that contained sidelobe returns after the first surface echo (Fig. 5). When boundary reverberation was not present, the shapes and tails of the distributions were affected by the density of the scatterers (zooplankton). For the highest scatterer densities (VL1, Fig. 11a), the distributions appeared to be unimodal with lower tails. As the density of scatterers decreased, the distributions became multi-modal, with heavier tails (VL2, Fig. 11b; VL3, Fig. 11c). These observations are somewhat consistent with those for the surface and near-surface regions, in that a sparse, non-homogeneous spatial distribution of scatterers (bubbles) resulted in distributions with more complex (multi-modal) shapes (c.f. SS3, Fig 9c; NS4; Fig. 10d).

## V. DISCUSSION

### A. Nonstationarity of Shallow Water Reverberation Fluctuations

The empirical distribution functions were formed from contiguous subsets of the data collected in each analysis region because none of the regions could be considered stationary across all pings and grazing angles. The primary factors contributing to the observed nonstationarities were the towfish's motion through the generally non-homogeneous spatial distribution of scatterers in each region, and boundary reverberation received in the sidelobes. This is evident in Table VI, which lists the samples sizes and percent of data in each analysis region that were validated across pings and grazing angles as stationary and homogeneous. The lowest percentages occur in regions where multiple reverberation components with widely-varying characteristics are present. For example, the NS1 region had the smallest percentage of contiguous samples satisfying stationarity and was influenced by microbubbles within the decaying ship's wake, bubbles associated with breaking waves in the ambient sea, and multiple boundary reflections received in the sidelobes. Similarly, the NS3 region also had a small percentage of contiguous samples satisfying stationarity, and it was influenced by large and small scale bubble clouds, sea surface backscatter, and sea surface reverberation in the sidelobes. On the other hand, the VL1 region had the largest percentage of contiguous samples satisfying stationarity, and it was influenced almost entirely by scattering from zooplankton.

Although the TVSS data set is unique in that it contains a wide variety of backscatter and reverberation processes received in narrow beams simultaneously, it is consistent with other scattering studies which have observed that shallow water acoustic reverberation fluctuations received by moving and fixed platforms is often nonstationary.<sup>15,22</sup> Consequently, our results regarding probability distribution functions pertain to locally stationary reverberation fluctuations embedded in larger scale, nonstationary processes.

### B. Suitability of Rayleigh Mixture Distributions

The Rayleigh mixture distributions provided the best fits to the observed data in most of the boundary regions (SF1-3, SS1-2), and some of the near-surface regions (NS1,3). Thus, the Rayleigh mixture model adequately handles patchy, non-homogeneously (non-Poisson) distributed scatterers. For example, the seafloor in the area of the TVSS experiment has a bimodal sediment composition of sand and silt,<sup>26</sup> making the mixture of two Rayleigh random variables a logical model for the observed backscatter amplitude distributions. Three, five, and seven component Rayleigh mixtures sometimes provided better fits probably because bottom roughness and the spatial variability of the bottom across each run introduced additional components.

For the sea surface and near-surface backscatter data in the SS1, SS2, and NS3 regions, bubble clouds with varying spatial scales are the most likely sources for the different components of the Rayleigh mixture distributions that were fit to the observed data. Previous analyses<sup>27</sup> indicate that the bubble densities in the towship's wake (SS1) and in the bubble clouds generated by breaking ship waves (SS2, NS3) were relatively high, suggesting that the empirical distribution of backscatter in these regions could be modeled by a mixture of Rayleigh variables, each accounting for the different scales of the bubble clouds and scattering from the sea surface. This is supported by backscattering strength images constructed from the data in these regions (e.g. Fig. 5b) which revealed a patchy distribution of bubble clouds with varying length scales along- and across-track.<sup>27</sup>

Although the Rayleigh mixture models did not fit the observed near-surface and

volume backscatter data well, they were effective in fitting the distribution tails for every type of analysis region (Table V). This is most noticeable for the regions in which bubbles contributed to the tails of the distributions (e.g. SS3, Fig. 9d; NS2, Fig 10b; NS4), indicating that scattering from bubbles and bubble clouds could be described as a mixture of Rayleigh distributed random variables. These figures also suggest that acoustic backscatter and reverberation from these regions is probably best described by a mixture of both Rayleigh and non-Rayleigh random variables, and that the Rayleigh mixture model is flexible enough to describe that portion of the empirical distribution resulting from a mixture of Rayleigh random variables, even if the entire distribution does not fit such a model.

The flexibility of the Rayleigh mixture model comes from its unification of a number of physically based models. On one end, a Rayleigh mixture distribution dominated by a single component can approximate a single Rayleigh distribution, a Weibull distribution with  $\beta = 2$ , and a K distribution in the limit as  $\nu \rightarrow \infty$  when the scale  $1/\sqrt{\nu}$  is applied to the data.<sup>29</sup> A Rayleigh mixture distribution can also approximate the K distribution by quantizing the Rayleigh speckle and chi-distributed components, and equating the later with the mixture proportions.<sup>12</sup> This explains why the Rayleigh mixture model fits the data well when the Weibull or K distributions do (e.g. SF2, Tables III, IV). In addition, Lyons and Abraham (1999) have related the Rayleigh mixture model to other models based on physical processes, such as Crowther's (1980) and McDaniel's (1990) for seafloor backscatter.<sup>16,19</sup>

### C. Scattering Processes Approximated by Log-normal Distributions

The log-normal distribution provided the best fits to most of the near-surface and volume backscatter data, but the fits were only good in the centers of the distributions where boundary reverberation in the sidelobes (NS1,2,4,5; VL4) or scattering from patchy aggregations of zooplankton (VL1,2,3) dominated the acoustic backscatter. Here, we offer several explanations for these results in terms of approximately log-normal distributions. Approximate results are sufficient because the model-data fits were never statistically good (KS  $p$ -value  $> 0.9$ ), so it cannot be claimed that the data actually fit a log-normal distribution. Rather, the log-normal model was only the best in describing the distribution centers.

First, we consider the near-surface and volume data in which boundary reverberation in the sidelobes dominated the distribution centers (NS1,2,4,5,VL4). Because the amplitude data are validated as stationary, independent, and identically-distributed across-grazing angles and pings, we can use the model in (1) to express the corresponding in-phase and quadrature components as:<sup>6</sup>

$$V_{I,Q}(r) = \frac{1}{g(r)} \sum_{i=1}^n a_i B(r_i) s(r-r_i, \xi_i) \quad (33)$$

where the generalized variable  $r$  is used in place of  $t$  to represent the ranges of grazing angle, depth, along-track, or across-track distance in Table I, and  $g(r)$  is the transient function whose reciprocal transforms the nonstationary reverberation sum in eqn (1) to the stationary form  $V(r)$ . For the TVSS data,  $g(r)$  represents the normalization procedure. Eqn (33) can be rewritten as

$$V_{I,Q}(r) = \sum_{i=1}^n v_i(r) \quad , \quad (34)$$

where  $v_i(r)$  is the reverberation component in the sum of (33) stationarized by  $g(r)$ . If we assume that each  $v_i(r)$  can be expressed in terms of a random proportion of the preceding term  $v_{i-1}(r)$ , then

$$v_i(r) = v_{i-1}(r) + \zeta_i v_{i-1}(r) \quad (35)$$

where the random set  $\{\zeta_i\}$  is mutually independent and independent of the set  $\{v_i(r)\}$ . This assumption is reasonable if the scattered amplitudes  $a_i$  and stochastic parameters  $\xi_i$  are random, as assumed in (1) and (33). Rearranging (35), we have

$$\frac{v_i(r) - v_{i-1}(r)}{v_{i-1}(r)} = \zeta_i, \quad (36)$$

so that

$$\sum_{i=1}^n \frac{v_i(r) - v_{i-1}(r)}{v_{i-1}(r)} = \sum_{i=1}^n \zeta_i. \quad (37)$$

Now, supposing the difference between successive reverberation components  $v_i(r)$  is small,

$$\sum_{i=1}^n \frac{v_i(r) - v_{i-1}(r)}{v_{i-1}(r)} \approx \int_{v_1(r)}^{v_n(r)} \frac{dv}{v} = \ln(v_n(r)) - \ln(v_1(r)), \quad (38)$$

which, from (37), becomes

$$\ln(v_n(r)) = \ln(v_1(r)) + \zeta_2 + \dots + \zeta_n. \quad (39)$$

For large  $n$ , the central limit theorem implies that  $\ln(v_n(r))$  is normally distributed, so  $v_n(r)$  is log-normally distributed by the properties of the log-normal distribution discussed in section II. If the minimum number for which (39) converges to log-normal is much less than the total number of scatterers ( $n$ ), then  $V_{I,Q}(r)$  in eqn (33) will be approximately log-normal because the sum of log-normal variables is approximately log-normal.<sup>41</sup> By the same virtue, the TVSS amplitude data that are related to the in-phase and quadrature components by

$$A(r) = \sqrt{V_I^2(r) + V_Q^2(r)} \quad (40)$$

are approximately log-normal because a log-normal variable raised to a power is also log-normally distributed.<sup>42</sup>

A question which arises from this development is: if eqn (39) converges to a normal distribution, why not eqn (33)? The central limit theorem may be invoked for eqn (33) when  $n$  is large, but the value of  $n$  for which eqn (33) converges to normal will be smaller if the variables  $v_i(r)$  are from the same underlying distributions. This can be expected when the total scattered signal arises from numerous scatterers of the same type. The value of  $n$  for which the eqn (33) converges to normal will be larger when each  $v_i(r)$  arises from a different underlying distribution, especially those which are highly skewed or have large tails.<sup>47,49</sup> This is likely to occur for volume backscatter dominated by boundary sidelobe returns because each sidelobe is directed towards a different grazing angle with respect to the boundary (see reference (44) for the receive beampatterns of the TVSS). The total reverberation will be the sum of the components arriving in each sidelobe, where each component follows a different parent distribution. Thus, a log-normal distribution may approximate the observed data better than a normal distribution when the underlying distributions for the proportions  $\zeta_i$  are less skewed, with lighter tails, than those for  $v_i(r)$ .

The reasons why the log-normal model best fit the volume backscatter data in and above the thermocline (VL1,2,3) are probably related to the fact that several biological and physical factors affecting the distribution of zooplankton are log-normally distributed. In observations made by Dugan *et al.* (1992), the distribution of horizontal temperature fluctuations in the seasonal thermocline followed a log-normal distribution on scales from 10cm to 1km,<sup>50</sup> whereas Campell's (1995) analysis showed that a

variety of factors related to phytoplankton, such as chlorophyll concentration and cell size, are log-normally distributed.<sup>51</sup> The spatial distribution of zooplankton in the northeastern Gulf of Mexico can be related to both of these. Zooplankton have been shown to be concentrated near the mixed layer depth, which is influenced by both weather and mixing processes, and also near the depth of the primary productivity maximum, which is related to phytoplankton, hence chlorophyll, distribution.<sup>25</sup> Because these factors influence the number  $n$  of scatterers in (33), they directly influence the empirical distributions of the backscatter amplitude fluctuations.

It is interesting to note that the log-normal distribution has been used to describe a wide variety of physical phenomena which may be indirectly related to volume acoustic backscatter fluctuations. In theoretical biology, for example, species abundance has been successfully described by the log-normal model, and organism growth was the first application that used the development in eqns (34)-(39), which is known as the law of proportional effect.<sup>52</sup> The TVSS reverberation fluctuations are directly influenced by the size and species abundance distribution of sound scattering zooplankton through their backscattering cross sections, which are represented by the  $a_i$  terms in (33). Although backscattering strength imagery indicated that the spatial distribution of zooplankton was non-homogeneous,<sup>25</sup> we lacked the *in-situ* data to determine if the biological sound scatterers did in fact exhibit a log-normal size or species abundance distribution. We do not claim that a log-normal distribution of scatterer sizes and/or densities will result in log-normally distributed reverberation statistics. However, such observations are not likely to be purely coincidental, and deserve further investigation, in view of other studies in which high frequency volume acoustic backscatter from biological sound scatterers was approximately log-normal.<sup>31,39,53</sup>

A final explanation for approximately log-normal acoustic backscatter and reverberation distributions is that a log-normal distribution can be expressed as mixture of several physically relevant distributions. Although we do not think this is the reason for our observations, this might explain others (e.g. references (38),(15)). For example, Titterton *et. al* (1985) shows an example in which two Gaussian distributions are used to approximate a two-parameter log-normal distribution.<sup>43</sup> Thus, two Ricean distributed scattering processes, each dominated by a coherent scattering component, might yield a distribution which is approximately log-normal. Similarly, the log-normal distribution may be closely approximated by the gamma distribution,<sup>54</sup> which has been directly related to a variety of scattering processes by Middleton (1999).<sup>55</sup> This is appropriate for shallow water reverberation, which typically includes multiple components from the boundaries and volume. These considerations are consistent with our previous conclusions that mixture distributions with component densities from different parametric families may better describe fluctuations of acoustic backscatter and reverberation in shallow water.

#### **D. Implications for Target Detection**

This study has several implications for undersea target detection. The non-Rayleigh nature of envelope fluctuations that arise from non-homogeneous spatial distributions of scatterers is seen in large tails and/or multimodality in the distributions. For a pre-determined probability of false alarm (PFA), this implies that threshold detectors which assume Rayleigh-distributed envelope fluctuations will experience significantly higher false alarm rates. However, even with the appropriate PDF model for envelope fluctuations due to the environment, target detection is difficult for data within the tails of the distributions. For these data, combining statistical techniques with analyses of multibeam imagery, as we have done here, may be a more effective method for discriminating between noise and features of interest.



## VI. SUMMARY AND CONCLUSIONS

In this study, we have analyzed the fluctuations of seafloor, sea surface, and volume acoustic backscatter data simultaneously collected by the Toroidal Volume Search Sonar (TVSS) while it was towed in a shallow water region in the northeastern Gulf of Mexico. The 68 kHz acoustic backscatter data were grouped according to 15 analysis regions in which scattering contributions from the volume and/or boundaries were present. After normalizing for backscatter variations due to grazing angle dependence and nonuniformity in the TVSS's beampatterns, the data were validated as independent and identically distributed. Various moments and statistics were estimated for the data in each region, and Rayleigh, K, Weibull, log-normal, and Rayleigh mixture probability distributions were fit to the empirical distribution functions in each region. We used previously published volume and boundary acoustic backscattering strength images constructed from the multibeam data collected by the TVSS to interpret the observed backscatter and reverberation statistics in terms of the spatial distribution of scatterers.

Backscatter amplitude fluctuations from both boundaries and the volume were non-Rayleigh. Rayleigh mixture models provided the best fits to the backscatter data collected from both boundaries, and in most cases, 3-components adequately described the observed data. For the near-surface and volume regions, none of the models that were considered yielded statistically good fits. The Rayleigh mixture distributions provided the best fits to the heavy tails in the data for these regions, which were mostly due to sparse distributions of bubbles near the surface or zooplankton in the mixed layer and thermocline. The log-normal distribution best fit the centers of the distributions for the near-surface and volume regions, particularly when single and multiple boundary interactions were received in the sidelobes. Together, these observations suggest that mixture distributions with component densities from different parametric families might better describe the multiple-component reverberation that is typical of most shallow water environments.

A problem one may encounter with mixture distributions concerns identifiability, because one may not know the number of components required to represent the data, or the appropriate PDF families that should be used. The problem is made more difficult by the fact that several different mixtures can be used to approximate the same distribution. This problem can be remedied by adopting an approach similar to the one in this study, where coincident backscattering strength imagery are used to identify candidate mixture components based on the observed spatial distribution of scattering features,

The results were displayed as probability of false alarms (PFA's) in order to emphasize the heavier tails of the non-Rayleigh backscatter statistics. The tails corresponding to data in the near-surface, sea-surface, and volume were much heavier than those for the seafloor. Heavy tails resulted mostly from non-homogeneous spatial distributions of bubbles near the sea surface and zooplankton at the base of the mixed layer and in the thermocline. Multi-modal distributions with extended tails were observed when the data were influenced by both discrete scatterers and multiple boundary interactions received in the sidelobes. The results demonstrate that resonant scattering from microbubbles make target detection near the surface more difficult than on the boundaries or in the middle of the water column, and that aggregations of zooplankton will cause target detection to be more difficult in the mixed layer and upper thermocline than below the thermocline in shallow water environments.

## ACKNOWLEDGMENTS

This work was funded by the Office of Naval Research under ONR-NRL Contract No. N00014-96-1-G913. The authors would like to thank CAPT Tim Schnoor, USN (ret) (ONR), Sam Tooma, and Maria Kalcic (NRL) for their support; Candy Robertson and Lisa Tubridy (CSS) for information on the TVSS; and Pat Jordan (MPL) for administrative support. Special thanks are due to Doug Abraham for providing reference (29), which was essential in completing this work. Thanks are due to Jo Griffith (MPL) for helping with the figures.

## APPENDIX. SKEWNESS AND KURTOSIS DESCRIPTORS

Expressions for the skewness and kurtosis descriptors in Fig. 7 are given by

$$\begin{aligned}\beta_1 &= \gamma_{3,A}^2, \text{ and} \\ \beta_2 &= \gamma_{4,A} + 3,\end{aligned}\tag{A1}$$

which are obtained from the moments

$$\begin{aligned}\mu_A &= E[A] \quad (\text{mean}) \\ \sigma_A^2 &= E[(A - \mu_A)^2] \quad (\text{variance}) \\ \gamma_{3,A} &= \frac{E[(A - \mu_A)^3]}{\sigma_A^3} \quad (\text{skewness}) \\ \gamma_{4,A} &= \frac{E[(A - \mu_A)^4]}{\sigma_A^4} \quad (\text{kurtosis}).\end{aligned}\tag{A2}$$

Skewness and kurtosis are measures of departure from normality. Skewness represents asymmetry in the PDF, and high kurtosis indicates a relatively large number of values near the mean of the distribution, and far from it (i.e. in the tails).

For the TVSS data, the sample moments were calculated using (A2) with

$$E[u] = \frac{1}{N} \sum_{i=1}^N u_i,\tag{A3}$$

for the expected value.

For the PDF models, expressions for  $\beta_1$  and  $\beta_2$  in terms of the non-central moments

$$\alpha_i = E[A^i] = \int_{-\infty}^{\infty} A^i p(A) dA,\tag{A4}$$

where  $p(A)$  is the probability density function of  $A$ , can be obtained by using the  $k$  central moments

$$E[(A - \mu_A)^k] = \int_{-\infty}^{\infty} (A - \mu_A)^k p(A) dA,\tag{A5}$$

yielding:<sup>55</sup>

$$\beta_1 = \frac{(\alpha_3 - 3\alpha_1\alpha_2 + 2\alpha_1^3)^2}{(\alpha_2 - \alpha_1^2)^3},\tag{A6}$$

and

$$\beta_2 = \frac{\alpha_4 - 4\alpha_1\alpha_3 + 6\alpha_1^2\alpha_2 - 3\alpha_1^4}{(\alpha_2 - \alpha_1^2)^2} \quad (A7)$$

From these expressions and knowledge of the non-central moments of the various PDF models, one can obtain the skewness and kurtosis descriptors plotted in Fig. 7. The  $k$ -th non-central moment of the Rayleigh distribution (eqn (2)) is:<sup>37</sup>

$$E[A^k] = \lambda_R^2 \Gamma\left(1 + \frac{k}{2}\right) \quad (A8)$$

which can be used with (A6) and (A7) to show that it is represented by a single point in the  $(\beta_1, \beta_2)$  plane:

$$\beta_1 = \frac{4\pi(\pi - 3)^2}{(4 - \pi)^3} \quad (A9)$$

and

$$\beta_2 = \frac{32 - 3\pi^2}{(4 - \pi)^2} \quad (A10)$$

This is a consequence of the fact that the Rayleigh distribution is fully represented by a single scale parameter ( $\lambda_R$ ), and skewness and kurtosis are scale invariant descriptors.

One can use the  $k$ -th non-central moments of the two-parameter K, Weibull, and log-normal distributions to show that each of these is represented by a line in the  $(\beta_1, \beta_2)$  plane (Fig. 7). The non-central moments of the K distribution (eqn (5)) are:<sup>29</sup>

$$E[A^k] = \alpha^2 \Gamma\left(1 + \frac{k}{2}\right) \frac{\Gamma\left(v + \frac{k}{2}\right)}{\Gamma(v)} \quad (A11)$$

those for the Weibull distribution (eqn (7)) are:<sup>37</sup>

$$E[A^k] = \alpha^\beta \Gamma\left(1 + \frac{k}{\beta}\right) \quad (A12)$$

and the moments of the log-normal distribution (eqn (9)) are:<sup>42</sup>

$$E[A^k] = e^{(k\beta + \frac{1}{2}k^2\alpha^2)} \quad (A13)$$

where  $\alpha$ ,  $\beta$ , and  $v$  are the parameters of the various distributions as defined in the text.

The  $m$ -component Rayleigh mixture distribution (eqn (12)) is represented by a region in the  $(\beta_1, \beta_2)$  plane, which can be seen by using the equation for the  $k$ -th non-central moment:<sup>29</sup>

$$E[A^k] = \sum_{i=1}^m \epsilon_i \lambda_{R,i}^2 \Gamma\left(1 + \frac{k}{2}\right) \quad (A14)$$

in (A6) and (A7) and by varying the proportions ( $\epsilon_i$ ) over the interval  $[0,1]$  and the powers  $\lambda_{R,i}$  over  $[0,\infty]$ . Fig. 7 shows the example of a two component Rayleigh mixture distributions taken from Abraham (1997).<sup>29</sup>

## REFERENCES

1. Y. Sudo, "A fast simulation method for underwater reverberation," in: *Proc. 3rd Int. Conf. Theoretical and Computational Acoustics (ICTCA)*, July 14-18, 1997, Newark, NJ, pp. 381-392 (1997).
2. D. Middleton, "Channel modeling and threshold signal processing in underwater acoustics: an analytical overview," *IEEE J. Oceanic Eng.*, **OE-12**, 4-28 (1987).
3. T.K. Stanton, and C.S. Clay, "Sonar echo statistics as a remote sensing tool: volume and seafloor," *IEEE J. Ocean. Eng.*, **OE-11**, 79-96 (1986).
4. S.T. McDaniel, "Sea surface reverberation fluctuations," *J. Acoust. Soc. Am.*, **94**, 1551-1559 (1993).
5. P. Faure, "Theoretical model of reverberation noise," *J. Acoust. Soc. Am.*, **36**(2), 259-266 (1964).
6. V.V. Ol'shevskii, *Characteristics of sea reverberation.*, (Consultants Bureau, New York, 1967).
7. D. Middleton, "A statistical theory of reverberation and similar first-order scattered fields: Part I: Waveforms and the general process," *IEEE Trans. Info. Theory*, **IT-13**, 372-392 (1967).
8. D. Middleton, "A statistical theory of reverberation and similar first-order scattered fields: Part II: Moments, spectra, and special distributions," *IEEE Trans. Info. Theory*, **IT-13**, 393-414 (1967).
9. D. Middleton, "A statistical theory of reverberation and similar first-order scattered fields: Part III: Waveforms and fields," *IEEE Trans. Info. Theory*, **IT-18**, 35-67 (1967).
10. D. Middleton, "A statistical theory of reverberation and similar first-order scattered fields: Part IV: Statistical models," *IEEE Trans. Info. Theory*, **IT-18**, 68-90 (1967).
11. S. Stanic, and E. G. Kennedy, "Reverberation fluctuations from a smooth seafloor," *IEEE J. Oceanic Eng.*, **OE-18**, 95-99 (1993).
12. A.P. Lyons, and D. A. Abraham, "Statistical characterization of high-frequency shallow-water seafloor backscatter," *J. Acoust. Soc. Am.*, **106**, 1307-1315 (1999).
13. H. Griffiths, J. Dunlop, and R. Voles, (1997). "Textural analysis of sidescan sonar imagery using statistical scattering models," in: *High Frequency Acoustics in Shallow Water*, edited by N.G. Pace, E. Pouliquen, O. Bergem, and A.P. Lyons (NATO SACLANT Undersea Research Center, La Spezia, 1997) pp. 187-194.
14. J. Dunlop, "Statistical modeling of sidescan sonar images," in: *Proc. MTS/IEEE Oceans '97*, **vol. 1**, 33-38 (1997).
15. M. Gensane, "A statistical study of acoustic signals backscattered from the sea bottom," *IEEE J. Ocean. Eng.*, **14**, 84-93 (1989).
16. P.A. Crowther, "Fluctuation statistics of sea-bed acoustic backscatter," in: *Bottom-Interacting Ocean Acoustics*, edited by W.A. Kuperman and F.B. Jensen (Plenum Press, New York, 1980), pp. 609-622.
17. W.K. Stewart, D. Chu, S. Malik, S. Lerner, and H. Singh, "Quantitative seafloor characterization using bathymetric sidescan sonar," *IEEE J. Oceanic Eng.*, **19**, 599-610 (1994).
18. S. Stanic, and E. Kennedy, "Fluctuations of high-frequency shallow-water seafloor reverberation," *J. Acoust. Soc. Am.*, **91**, 1967-1973 (1992).
19. S.T. McDaniel, "Seafloor reverberation fluctuations," *J. Acoust. Soc. Am.*, **88**, 1530-1535 (1990).
20. T.D. Plemons, J. A. Shooter, and D. Middleton, "Underwater acoustic scattering from lake surfaces. I. theory, experiment, and validation of the data," *J. Acoust. Soc. Am.*, **52**, 1487-1502 (1972).

21. T.D. Plemons, J. A. Shooter, and D. Middleton, "Underwater acoustic scattering from lake surfaces. II. covariance functions and related statistics," *J. Acoust. Soc. Am.*, **52**, 1503-1515 (1972).
22. N.P. Chotiros, H. Boehme, T.G. Goldsberry, S.P. Pitt, R.A. Lamb, A.L. Garcia, and A. Altenburg, "Acoustic backscattering at low grazing angles from the ocean bottom: Part II. Statistical characteristics of bottom backscatter at a shallow water site," *J. Acoust. Soc. Am.*, **77**, 975-982 (1985).
23. C. de Moustier, "Beyond bathymetry: mapping acoustic backscattering from the deep seafloor with Sea Beam," *J. Acoust. Soc. Am.*, **79**, 316-331 (1986).
24. T.K. Stanton, "Sea surface scattering: Echo peak PDF," *J. Acoust. Soc. Am.*, **77**, 1367-1369 (1985).
25. T.C. Gallaudet, and C.P. de Moustier, "Multibeam volume acoustic backscatter imagery and reverberation measurements in the Northeastern Gulf of Mexico," *J. Acoust. Soc. Am.*, (submitted, 2001).
26. T.C. Gallaudet, and C.P. de Moustier, "Using environmental information to estimate and correct for errors in bathymetry and seafloor acoustic imagery," *IEEE J. Ocean. Eng.*, (submitted, 2001).
27. T.C. Gallaudet, and C.P. de Moustier, "Sea surface and volume acoustic backscatter imagery of the microbubble field of a ship's wake," *J. Acoust. Soc. Am.*, (submitted, 2001).
28. P.H. Dahl, and W.J. Plant, "The variability of high-frequency acoustic backscatter from the region near the sea surface," *J. Acoust. Soc. Am.*, **101**, pp. 2596-2602 (1997).
29. D. A. Abraham, *Modeling non-Rayleigh reverberation*, SACLANT Undersea Research Center Report SR-266, (SACLANT Undersea Research Center, La Spezia, June 1997).
30. M.E. Frazer, "Some statistical properties of lake surface reverberation," *J. Acoust. Soc. Am.*, **64**, 858-868 (1978).
31. V.C. Anderson, "Frequency dependence of reverberation in the ocean," *J. Acoust. Soc. Am.*, **41**, 1467-1474 (1967).
32. T. K. Stanton, "Sonar estimates of seafloor microroughness," *J. Acoust. Soc. Am.*, **75**, 809-817 (1984).
33. K.D. Ward, "Compound representation of high resolution sea clutter," *Electronics Letters*, **17**, 561-563 (1981).
34. S. Watts, "Radar detection prediction in sea clutter using the compound K distribution model," *IEE Proc. Radar Sig. Proc.*, **7**, 613-620 (1985).
35. E. Jakeman, and P.N. Pusey, "A model for non-Rayleigh sea echo," *IEEE Trans. Antennas Propag.*, **24**, 806-814 (1976).
36. A. Abdi and M. Kaveh, "K distribution: an approximate substitute for Rayleigh-lognormal distribution in fading shadowing wireless channels," *Electronics Letters*, **34**, 851-852 (1998).
37. N. L. Johnson, S. Kotz, and N. Balakrishnan, *Continuous Univariate Distributions*, vol. 1, 2nd edition (John Wiley & Sons, New York, 1994).
38. G.V. Frisk, "Intensity statistics for long-range acoustic propagation in the ocean," *J. Acoust. Soc. Am.*, **N64**, 257-259 (1978).
39. B. Castile, "Characterization of Acoustic Reverberation in the Ocean for High Frequency, High Resolution, Sonar Systems," Ph.D. Thesis (University of California, San Diego, 1978).
40. Trunk, G.V., and George, S.F. (1970). "Detection of targets in non-Gaussian clutter." *IEEE Trans. Aerosp. Electron. Syst.*, **AES-6**(5), pp. 620-628.
41. N.C. Beaulieu, A.A. Abu-Dayya, and P.J. McLane, "Estimating the distribution of a sum of independent lognormal random variables," *IEEE Trans. Comm.*, **43**, 2869-2873 (1995).

42. K. Shimizu and E.L. Crow, "History, genesis, and properties," in: *The Lognormal Distribution: Theory and Applications*, edited by E.L. Crow and K. Shimizu (Marcel Dekker, New York, 1988), Chap. 1, pp. 1-26.
43. D.M. Titterton, A.F.M. Smith, and U.E. Makov, *Statistical Analysis of Finite Mixture Distributions*, (John Wiley & Sons, New York, 1985).
44. T.C. Gallaudet, and de C. P. Moustier, "On optimal amplitude shading for arrays of irregularly spaced or non-coplanar elements," *IEEE J. Ocean. Eng.*, **25**, 553-567 (2000).
45. R. J. Urick, *Principles of Underwater Sound*, 3rd edition, (Peninsula Publishing, Los Altos, 1983).
46. J.S. Bendat, and A.G. Piersol, *Random Data: Analysis and Measurement Procedures*, 2nd edition, (John Wiley & Sons, New York, 1986).
47. J.A. Rice, *Mathematical Statistics and Data Analysis*, (Duxbury Press, Belmont, California, 1995), Chap. 5. pp. 163-176.
48. M. Fisz, *Probability Theory and Mathematical Statistics*, 3rd edition (John Wiley & Sons, New York, 1963).
49. I.T. Joliffe, "Sample sizes and the central limit theorem: The Poisson distribution as an illustration," *The American Statistician*, **49**, 269 (1995).
50. J.P. Dugan, B.W. Stalcup, and R.L. DiMarco, "Small scale activity in the upper ocean," *J. Geophys. Res.*, **97**, 5665-5675 (1992).
51. J. Campbell, "The lognormal distribution as a model for bioptical variability in the sea," *J. Geophys. Res.*, **100**, 13237-13254 (1995).
52. Aitchison, and J.A.C. Brown, *The Lognormal Distribution*, (Cambridge University Press, London, 1969).
53. P. Greenblatt, "Distributions of volume scattering observed with an 87.5kHz sonar," *J. Acoust. Soc. Am.*, **71**, 879-885 (1982).
54. J.R. Clark, and S. Karp, "Approximations for lognormally fading optical signals," *Proc. IEEE*, **58**, 1964-1965 (1970).
55. D. Middleton, "New physical-statistical methods and models for clutter and reverberation: The KA-distribution and related probability structures," *IEEE J. Ocean. Eng.*, **24**, 261-284 (1999).

TABLE I. Analysis regions for the TVSS data set. Negative across-track distances are left of the towfish's track. Grazing angles for the regions VL1 & VL2 are defined with respect to the vertical plane 47m to the left of the towfish's track. Grazing angles for the regions NS1 - NS5 are defined with respect to the horizontal plane at 3m depth. Ensonified areas are listed in the last column for the boundary regions (SF,SS), and ensonified volumes are listed for the volume regions (NS,VL).

Analysis Region	Primary Acoustic Scattering & Reverberation Features	Across-Track Distance(s)	Depth(s)	Grazing Angles	Areas or Volumes
SF1	seafloor backscatter	-35 to +35	192 - 202	72° - 90°	4.5 - 73
SF2	seafloor backscatter + surface reverberation after 1st surface echo	-50 to -100	192 - 202	48° - 66°	2.6 - 4.0
SF3	seafloor backscatter + surface & bottom reverberation after surface-bottom multiple	-150 to -200	192 - 202	29° - 37°	2.6 - 3.1
SS1	sea surface backscatter + attenuation from bubbles in towship's wake	-30 to +30	0	68° - 90°	2 - 40
SS2	sea surface backscatter + backscatter from bubble clouds generated by ship & ambient waves	40 to 80	0	44° - 66°	2
SS3	sea surface acoustic backscatter + backscatter from bubble clouds generated by ship & ambient waves + bottom reverberation from 1st bottom echo	100 to 150	0	27° - 38°	2

TABLE I. (Continued).

Analysis Region	Primary Acoustic Scattering & Reverberation Features	Across-Track Distance(s)	Depth(s)	Grazing Angles	Areas or Volumes
NS1	near-surface volume & sea surface backscatter + backscatter from bubbles in towship's wake generated during previous runs + surface & bottom reverberation after bottom-surface multiple	180 to 220 & -180 to -220	3	18° - 23°	37 - 52
NS2	near-surface volume backscatter from + bubbles within the towship's wake + surface reverberation after 1st surface echo	-30 to +30	3	68° - 90°	5 - 6
NS3	near-surface volume & surface backscatter from bubble clouds generated by ship waves + surface reverberation after 1st surface echo	40 to 80	3	42° - 62°	6 - 12
NS4	near-surface volume backscatter from bubble clouds generated by ship & ambient waves + surface & bottom reverberation after 1st surface & bottom echoes	100 to 150	3	26° - 37°	15 - 27
NS5	surface & bottom reverberation after bottom-surface multiple	200 to 250 & -200 to -250	3	16° - 20°	44 - 66
VL1	volume backscatter from densely distributed zooplankton in mixed layer & upper thermocline	-47	40 to 70	50° - 81°	2 - 4
VL2	volume backscatter from sparsely distributed zooplankton in middle & lower thermocline	-47	90 to 120	47° - 76°	2 - 4
VL3	volume backscatter from sparsely distributed zooplankton in lower thermocline	0	125 to 140	89-90°	2 - 4
VL4	volume backscatter below thermocline from sparsely distributed fish + surface reverberation after 1st surface echo	0	165-180	89-90°	7 - 10



TABLE II. Average TVSS backscatter amplitude statistics. The backscattering strengths were computed using eqn (17) in the text, and the scintillation index is computed from eqn (28) in the text. The Range is the maximum minus the minimum amplitude, and all other terms are computed from expressions in the Appendix. Because they were computed from the normalized amplitudes, all quantities except the backscattering strength are dimensionless. The statistics have been averaged over runs 1-3, except those for the NS1 region, which were averaged over runs 2-3.

Analysis Region	Mean Number of Samples	Mean Backscattering Strength	Mean Normalized Amplitude	Range	Variance	Skewness	Kurtosis	Scintillation Index
	N	$S_{B,S,V}$ (dB)	$\mu_A$		$\sigma_A^2$	$\gamma_{3,A}$	$\gamma_{4,A}$	$\sigma_A^2$
SF1	1505	-19.4	1.0292	3.2242	0.3115	0.9022	1.4171	1.2262
SF2	3840	-22.6	1.0037	3.1795	0.2794	0.6447	0.1927	1.0156
SF3	4406	-28.7	0.9962	3.4766	0.2793	0.7185	0.4448	1.0646
SS1	1330	-12.9	1.0108	4.4545	0.4469	1.1528	1.6478	1.8328
SS2	2725	-41.5	0.9943	7.6032	0.4834	2.0793	10.329	3.6730
SS3	3951	-51.3	0.9981	13.3277	0.3479	6.2665	119.56	14.358
NS1	2500	-51.7	1.0604	3.5567	0.2902	0.9185	0.9124	1.0575
NS2	1823	-28.4	1.0139	5.1983	0.3963	1.6726	4.7479	2.2058
NS3	2350	-50.7	1.0159	8.0735	0.5233	2.4721	14.042	4.6218
NS4	4985	-60.7	0.9977	9.0243	0.2773	3.6466	38.646	4.8148
NS5	7296	-59.4	1.0010	9.2410	0.1785	4.2419	61.760	3.1274
VL1	2835	-65.5	1.0001	3.8499	0.2687	1.0841	1.4969	1.0282
VL2	2522	-73.4	1.0094	5.1744	0.5285	1.6516	3.0865	2.5656
VL3	2732	-76.3	1.0015	5.3451	0.4954	2.3111	6.9617	3.2434
VL4	2591	-72.2	1.0167	3.6934	0.2919	1.3342	2.3139	1.3993

TABLE III. KS statistic  $p$ -values computed from the model-data PDF fits to the TVSS acoustic backscatter amplitude data in each of the analysis regions. The highest value for each run is in bold and corresponds to the best fit.

Region Run/	Rayleigh	K	Weibull	Log-normal	Rayleigh 2-Mixture	Rayleigh 3-Mixture	Rayleigh 5-Mixture	Rayleigh 7-Mixture
SF1/01	0.466	0.886	0.708	$3.01 \times 10^{-4}$	0.936	0.932	0.936	<b>0.940</b>
/02	0.015	0.765	0.263	$2.09 \times 10^{-4}$	0.890	0.890	0.982	<b>0.984</b>
/03	0.689	---	<b>0.928</b>	$9.25 \times 10^{-4}$	0.689	0.518	0.503	0.500
SF2/01	0.442	0.878	0.907	$1.94 \times 10^{-21}$	0.443	0.901	<b>0.939</b>	<b>0.939</b>
/02	0.867	0.989	<b>0.993</b>	$8.18 \times 10^{-17}$	0.869	0.907	0.890	0.878
/03	0.868	---	<b>0.913</b>	$6.02 \times 10^{-17}$	0.861	0.859	0.855	0.854
SF3/01	0.055	0.329	0.241	$1.16 \times 10^{-13}$	<b>0.568</b>	0.520	0.489	0.541
/02	0.298	0.973	0.969	$3.26 \times 10^{-15}$	<b>0.987</b>	0.978	0.967	0.960
/03	0.419	0.724	0.587	$3.65 \times 10^{-25}$	0.432	0.769	0.424	<b>0.788</b>
SS1/01	$2.19 \times 10^{-9}$	0.739	0.392	0.002	0.819	0.942	<b>0.973</b>	0.969
/02	$1.05 \times 10^{-25}$	0.358	0.322	$3.54 \times 10^{-5}$	0.267	<b>0.999</b>	<b>0.999</b>	<b>0.999</b>
/03	$6.67 \times 10^{-13}$	0.666	0.764	0.013	0.901	<b>0.998</b>	<b>0.998</b>	<b>0.998</b>
SS2/01	$2.18 \times 10^{-67}$	$2.48 \times 10^{-4}$	$7.41 \times 10^{-9}$	$5.17 \times 10^{-4}$	0.131	0.840	0.975	<b>0.983</b>
/02	$3.12 \times 10^{-16}$	0.395	0.011	$2.69 \times 10^{-4}$	<b>0.997</b>	<b>0.997</b>	0.996	0.992
/03	$5.81 \times 10^{-63}$	$1.97 \times 10^{-7}$	$7.27 \times 10^{-14}$	<b>0.370</b>	0.034	0.311	0.234	0.235
SS3/01	$4.53 \times 10^{-23}$	$3.14 \times 10^{-23}$	$3.64 \times 10^{-29}$	<b>0.342</b>	$7.53 \times 10^{-11}$	$7.52 \times 10^{-11}$	$7.44 \times 10^{-11}$	$1.56 \times 10^{-12}$
/02	$7.96 \times 10^{-60}$	$2.36 \times 10^{-53}$	$4.45 \times 10^{-70}$	<b>0.260</b>	$7.28 \times 10^{-19}$	$7.16 \times 10^{-19}$	$1.33 \times 10^{-22}$	$1.39 \times 10^{-22}$
/03	$3.10 \times 10^{-64}$	---	$3.58 \times 10^{-14}$	<b>0.045</b>	$5.21 \times 10^{-73}$	$5.21 \times 10^{-73}$	$5.21 \times 10^{-73}$	$5.20 \times 10^{-73}$

TABLE III. (Continued).

Region Run/	Rayleigh	K	Weibull	Log-normal	Rayleigh 2-Mixture	Rayleigh 3-Mixture	Rayleigh 5-Mixture	Rayleigh 7-Mixture
NS1/02	0.031	0.043	0.038	$1.13 \times 10^{-4}$	0.063	<b>0.069</b>	0.057	0.063
/03	$3.03 \times 10^{-9}$	---	$2.58 \times 10^{-4}$	<b>0.009</b>	$2.93 \times 10^{-9}$	$6.57 \times 10^{-10}$	$3.69 \times 10^{-10}$	$3.13 \times 10^{-10}$
NS2/01	$5.25 \times 10^{-10}$	$1.40 \times 10^{-4}$	$1.29 \times 10^{-5}$	<b>0.113</b>	$1.43 \times 10^{-4}$	$1.44 \times 10^{-4}$	$1.44 \times 10^{-4}$	$1.73 \times 10^{-4}$
/02	$3.15 \times 10^{-32}$	$2.21 \times 10^{-6}$	$3.02 \times 10^{-11}$	<b>0.649</b>	0.016	$6.12 \times 10^{-4}$	$6.26 \times 10^{-4}$	$6.26 \times 10^{-4}$
/03	$7.97 \times 10^{-11}$	0.022	$8.22 \times 10^{-4}$	<b>0.433</b>	0.083	0.081	0.082	0.079
NS3/01	$5.65 \times 10^{-29}$	0.033	$2.55 \times 10^{-5}$	$1.95 \times 10^{-4}$	0.266	0.943	0.924	<b>0.958</b>
/02	$5.29 \times 10^{-25}$	0.029	$1.11 \times 10^{-5}$	0.004	0.485	<b>0.632</b>	0.627	0.631
/03	$3.13 \times 10^{-53}$	$2.37 \times 10^{-14}$	$6.76 \times 10^{-21}$	<b>0.277</b>	0.031	0.100	0.093	0.088
NS4/01	$2.63 \times 10^{-35}$	---	$5.64 \times 10^{-28}$	<b>0.122</b>	$1.44 \times 10^{-49}$	$1.43 \times 10^{-49}$	$1.44 \times 10^{-49}$	$1.43 \times 10^{-49}$
/02	$1.01 \times 10^{-41}$	$1.53 \times 10^{-44}$	$1.07 \times 10^{-54}$	<b>0.167</b>	$3.04 \times 10^{-25}$	$3.03 \times 10^{-25}$	$3.02 \times 10^{-25}$	$2.92 \times 10^{-25}$
/03	$1.22 \times 10^{-59}$	---	$5.57 \times 10^{-13}$	<b>0.003</b>	$1.29 \times 10^{-70}$	$1.29 \times 10^{-70}$	$1.29 \times 10^{-70}$	$1.29 \times 10^{-70}$
NS5/01	$1.87 \times 10^{-91}$	---	$4.23 \times 10^{-30}$	<b>1.03</b> $\times 10^{-4}$	$1.25 \times 10^{-108}$	$1.24 \times 10^{-108}$	$1.25 \times 10^{-108}$	$1.25 \times 10^{-108}$
/02	$3.29 \times 10^{-77}$	---	$2.17 \times 10^{-19}$	<b>1.94</b> $\times 10^{-4}$	$1.86 \times 10^{-84}$	$1.86 \times 10^{-84}$	$1.86 \times 10^{-84}$	$1.86 \times 10^{-84}$
/03	$3.26 \times 10^{-145}$	---	$5.02 \times 10^{-13}$	<b>7.58</b> $\times 10^{-6}$	$3.26 \times 10^{-145}$	$3.26 \times 10^{-145}$	$3.26 \times 10^{-145}$	$3.26 \times 10^{-145}$
VL1/01	$9.75 \times 10^{-8}$	---	$7.59 \times 10^{-6}$	<b>0.023</b>	$3.59 \times 10^{-9}$	$9.74 \times 10^{-8}$	$4.21 \times 10^{-8}$	$5.08 \times 10^{-9}$
/02	$1.56 \times 10^{-10}$	$6.55 \times 10^{-6}$	$1.15 \times 10^{-7}$	<b>0.303</b>	$1.21 \times 10^{-7}$	$1.48 \times 10^{-7}$	$1.79 \times 10^{-7}$	$1.61 \times 10^{-9}$
/03	$1.11 \times 10^{-7}$	---	$9.67 \times 10^{-4}$	<b>5.88</b> $\times 10^{-4}$	$1.11 \times 10^{-7}$	$1.61 \times 10^{-8}$	$1.07 \times 10^{-8}$	$9.76 \times 10^{-9}$
VL2/01	$5.22 \times 10^{-68}$	$3.44 \times 10^{-7}$	$8.16 \times 10^{-14}$	<b>0.029</b>	$7.16 \times 10^{-5}$	$7.82 \times 10^{-5}$	$6.76 \times 10^{-5}$	$6.62 \times 10^{-5}$
/02	$7.32 \times 10^{-89}$	$6.25 \times 10^{-12}$	$2.91 \times 10^{-19}$	<b>2.20</b> $\times 10^{-4}$	$1.84 \times 10^{-5}$	$1.88 \times 10^{-5}$	$1.07 \times 10^{-5}$	$9.06 \times 10^{-6}$
/03	$2.20 \times 10^{-70}$	$1.58 \times 10^{-14}$	$1.05 \times 10^{-22}$	<b>2.29</b> $\times 10^{-4}$	$1.28 \times 10^{-7}$	$1.28 \times 10^{-7}$	$1.37 \times 10^{-7}$	$1.36 \times 10^{-7}$
VL3/01	$1.41 \times 10^{-104}$	$3.09 \times 10^{-28}$	$2.98 \times 10^{-39}$	<b>4.96</b> $\times 10^{-11}$	$1.36 \times 10^{-18}$	$1.39 \times 10^{-18}$	$1.52 \times 10^{-18}$	$1.44 \times 10^{-18}$
/02	$3.21 \times 10^{-26}$	$1.14 \times 10^{-26}$	$3.36 \times 10^{-35}$	<b>2.04</b> $\times 10^{-6}$	$2.68 \times 10^{-25}$	$2.68 \times 10^{-25}$	$2.69 \times 10^{-25}$	$2.71 \times 10^{-25}$
/03	$4.20 \times 10^{-121}$	$1.70 \times 10^{-38}$	$2.65 \times 10^{-48}$	<b>2.04</b> $\times 10^{-11}$	$3.87 \times 10^{-19}$	$3.89 \times 10^{-19}$	$4.32 \times 10^{-19}$	$2.46 \times 10^{-19}$
VL4/01	$8.27 \times 10^{-10}$	---	$2.66 \times 10^{-8}$	<b>0.323</b>	$2.38 \times 10^{-13}$	$2.40 \times 10^{-13}$	$2.44 \times 10^{-13}$	$2.86 \times 10^{-13}$
/02	$4.30 \times 10^{-9}$	---	$3.01 \times 10^{-8}$	<b>0.848</b>	$1.78 \times 10^{-14}$	$1.78 \times 10^{-14}$	$1.80 \times 10^{-14}$	$1.86 \times 10^{-14}$
/03	$1.13 \times 10^{-15}$	$1.39 \times 10^{-7}$	$9.09 \times 10^{-11}$	<b>0.092</b>	$2.92 \times 10^{-8}$	$2.98 \times 10^{-8}$	$3.62 \times 10^{-8}$	$3.00 \times 10^{-8}$

TABLE IV. RMS differences ( $D_{rms}$ ) between model and TVSS-derived empirical CDF's averaged over runs 1-3. The lowest value for each region is displayed in bold and corresponds to the model with the best overall fit to the empirical distribution function.

Analysis Region	Rayleigh	K	Weibull	Log-normal	Rayleigh 2-Mixture	Rayleigh 3-Mixture	Rayleigh 5-Mixture	Rayleigh 7-Mixture
SF1	0.0132	0.0070	0.0072	0.0359	<b>0.0060</b>	0.0063	0.0062	0.0063
SF2	0.0045	<b>0.0029</b>	0.0032	0.0425	0.0045	0.0036	0.0034	0.0034
SF3	0.0067	0.0041	0.0047	0.0395	0.0041	<b>0.0039</b>	<b>0.0039</b>	<b>0.0039</b>
SS1	0.0694	0.0091	0.0102	0.0287	0.0074	0.0040	<b>0.0039</b>	0.0040
SS2	0.0836	0.0191	0.0300	0.0180	0.0086	0.0045	<b>0.0041</b>	<b>0.0041</b>
SS3	0.0685	0.0649	0.0611	<b>0.0096</b>	0.0490	0.0490	0.0490	0.0490
NS1	0.0195	0.0155	0.0200	<b>0.0192</b>	0.0213	0.0219	0.0219	0.0219
NS2	0.0586	0.0246	0.0341	<b>0.0091</b>	0.0154	0.0153	0.0153	0.0153
NS3	0.0863	0.0282	0.0387	0.0164	0.0105	<b>0.0061</b>	<b>0.0061</b>	<b>0.0061</b>
NS4	0.0592	0.0601	0.0503	<b>0.0099</b>	0.0542	0.0542	0.0542	0.0542
NS5	0.0713	---	0.0348	<b>0.0125</b>	0.0744	0.0744	0.0744	0.0744
VL1	0.0291	0.0265	0.0258	<b>0.0130</b>	0.0237	0.0243	0.0240	0.0240
VL2	0.1142	0.0376	0.0476	<b>0.0179</b>	0.0203	0.0203	0.0203	0.0203
VL3	0.1164	0.0670	0.0766	<b>0.0317</b>	0.0459	0.0459	0.0459	0.0459
VL4	0.0411	0.0258	0.0369	<b>0.0082</b>	0.0322	0.0322	0.0322	0.0322

TABLE V. RMS differences ( $d_{rms}$ ) between model and TVSS-derived empirical CDF's for PFA values below  $10^{-2}$ , averaged over runs 1-3. The lowest value for each region is displayed in bold and corresponds to the model with the best overall fit to the empirical distribution function.

Analysis Region	Rayleigh	K	Weibull	Log-normal	Rayleigh 2-Mixture	Rayleigh 3-Mixture	Rayleigh 5-Mixture	Rayleigh 7-Mixture
SF1	0.0020	0.0012	0.0015	0.0220	0.0011	0.0010	<b>0.0009</b>	<b>0.0009</b>
SF2	0.0007	0.0006	<b>0.0005</b>	0.0320	0.0007	0.0006	0.0006	0.0006
SF3	0.0011	<b>0.0004</b>	0.0007	0.0272	<b>0.0004</b>	0.0006	0.0005	0.0005
SS1	0.0050	0.0018	0.0014	0.0200	0.0020	0.0014	<b>0.0013</b>	<b>0.0013</b>
SS2	0.0054	0.0009	0.0024	0.0087	0.0007	0.0007	<b>0.0005</b>	<b>0.0005</b>
SS3	0.0077	0.0043	0.0034	0.0015	0.0017	0.0017	0.0011	<b>0.0008</b>
NS1	<b>0.0005</b>	<b>0.0005</b>	0.0007	0.0100	0.0009	0.0008	0.0007	0.0008
NS2	0.0011	0.0006	0.0007	0.0031	<b>0.0006</b>	0.0007	<b>0.0006</b>	0.0007
NS3	0.0010	0.0007	0.0009	0.0026	0.0006	<b>0.0002</b>	<b>0.0002</b>	<b>0.0002</b>
NS4	0.0011	0.0012	0.0011	0.0010	<b>0.0002</b>	<b>0.0002</b>	<b>0.0002</b>	<b>0.0002</b>
NS5	0.0017	---	0.0011	<b>0.0007</b>	0.0009	0.0009	0.0009	0.0009
VL1	0.0027	0.0015	0.0030	0.0091	0.0013	0.0016	0.0011	<b>0.0010</b>
VL2	0.0055	<b>0.0010</b>	0.0020	0.0048	0.0014	0.0013	0.0012	0.0013
VL3	0.0057	0.0030	0.0041	0.0028	0.0020	0.0020	0.0020	<b>0.0019</b>
VL4	0.0046	0.0019	0.0041	0.00382	<b>0.0007</b>	0.0008	0.0008	0.0008

TABLE VI. Sample sizes for the TVSS analysis regions. The total number of samples (column 2) corresponds to each region defined in Table I (column 1), averaged across the 3 runs. The validated samples (column 3) correspond to the data used to form the empirical distribution functions displayed in Figs 7-10, and are the largest contiguous subsets of the regions validated as stationary and homogeneous across-pings and grazing angles.

Analysis Region	Total Number of Samples	Number of Validated Samples	Percent of Validated Samples
SF1	2185	1505	69
SF2	5529	3840	69
SF3	9296	4406	47
SS1	2616	1330	51
SS2	6537	2725	42
SS3	8374	3951	47
NS1	10036	2500	25
NS2	2829	1823	64
NS3	6672	2350	35
NS4	11383	4985	44
NS5	12510	7296	58
VL1	3412	2835	83
VL2	3914	2522	64
VL3	3974	2732	69
VL4	4020	2591	64

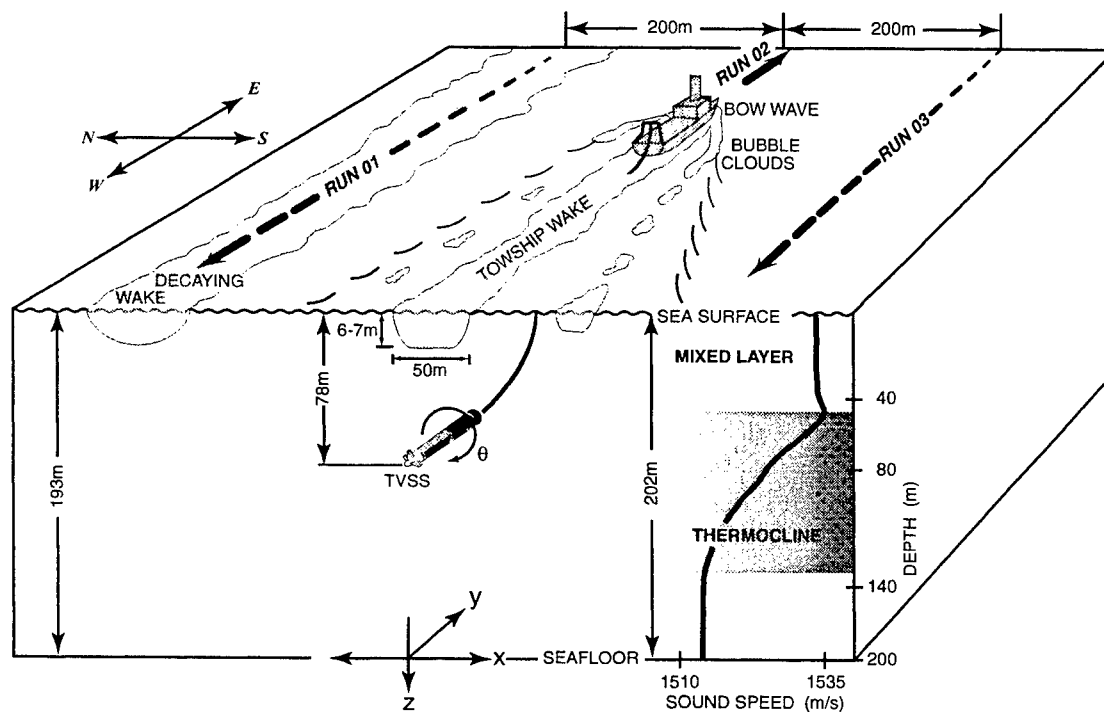


Fig. 1. Depiction of the TVSS deployment of 9 November 1994. Although each of the three parallel runs consisted of over 800 pings, the data presented in this paper are processed from only 100 pings in each of the three runs. The environmental conditions are summarized in the text, and more complete descriptions and analyses are presented in references [26]-[28].

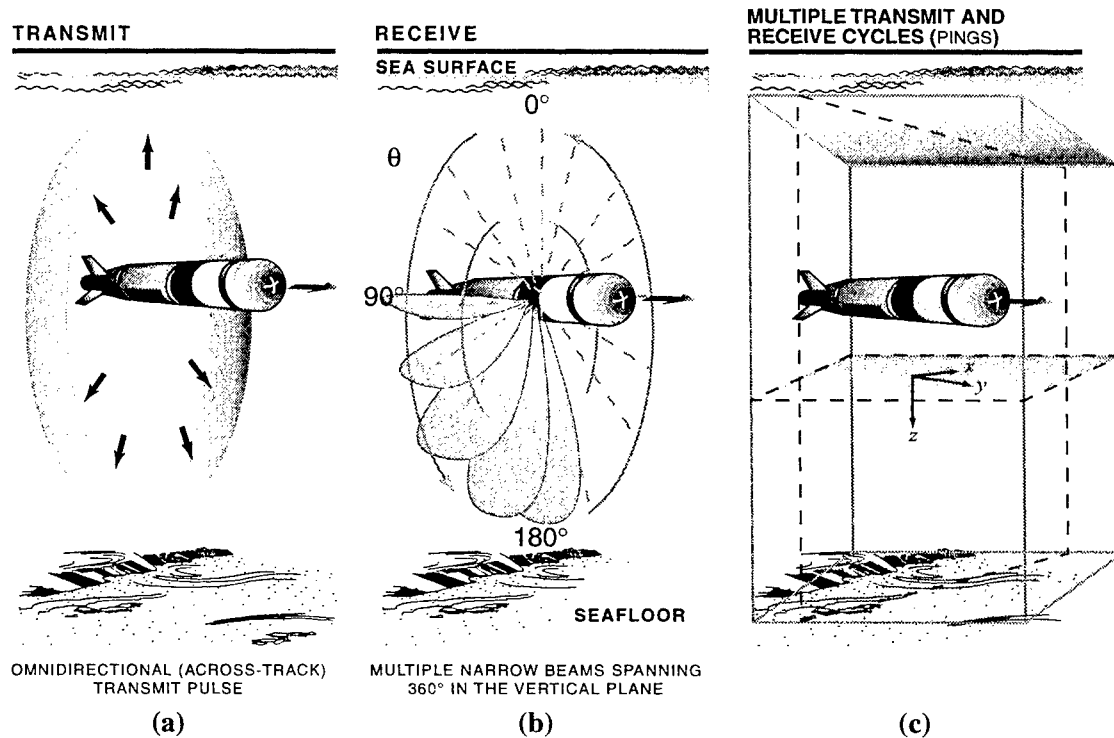


Fig. 2. The TVSS was designed for mine-hunting while deployed on an autonomous or unmanned underwater vehicle (AUV/UUV). The results in this study were obtained from data collected while the TVSS was deployed on a towed vehicle 735m astern of a towship. After transmission of a "toroidal" pulse, the sonar extracts the returned signal in directions spanning  $360^\circ$  about the TVSS axis. In previous studies (references [26]-[28]), this geometry was used to construct undersea imagery for multiple horizontal and vertical planes in the volume and on the boundaries using data collected over successive transmit-receive cycles (pings). In this study, probability distribution functions are fit to backscatter amplitude data corresponding to these volume and boundary images.



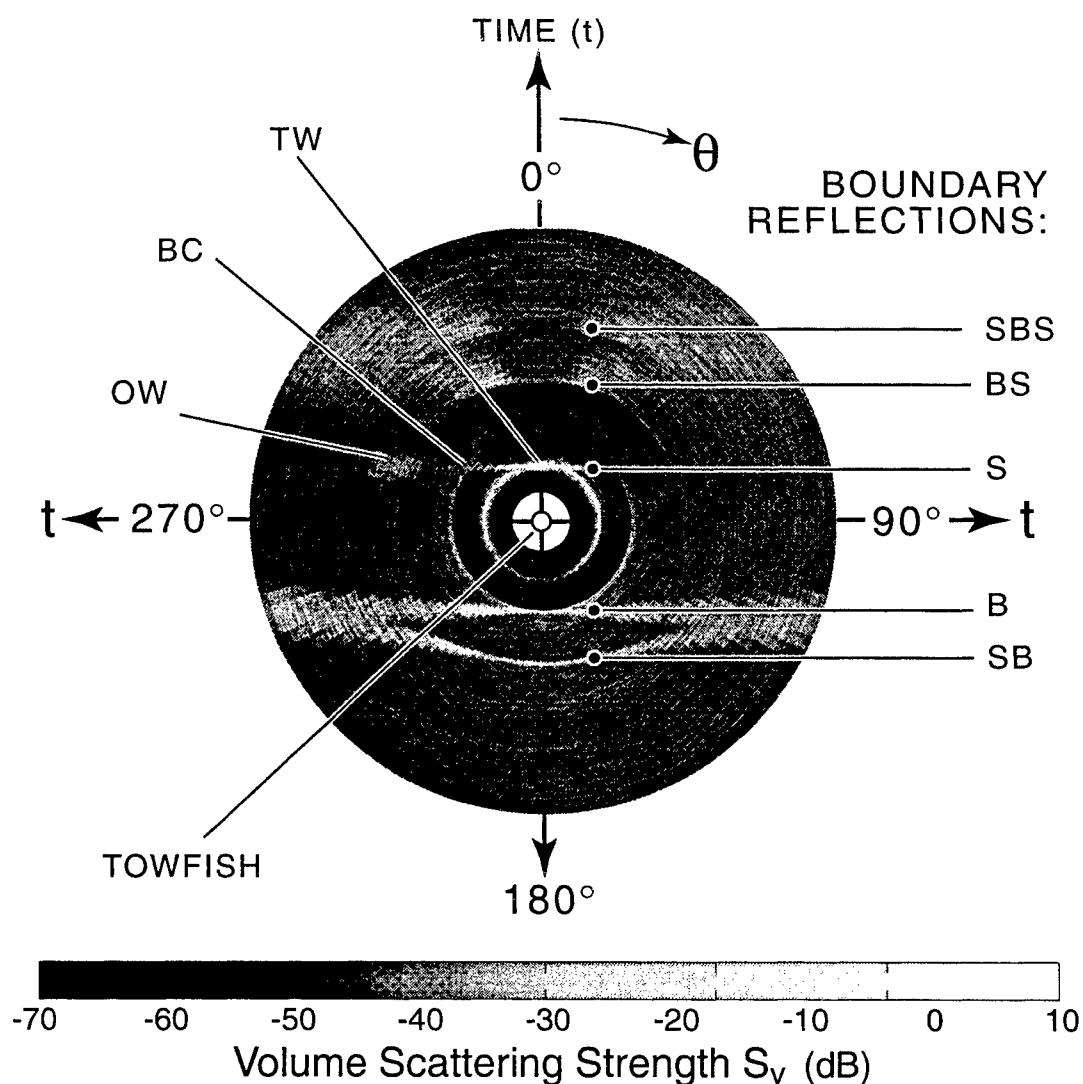


Fig 3. One TVSS ping displayed as a vertical slice of acoustic volume scattering strength ( $S_v$ ) in polar coordinates of angle vs. two-way travel time. Labels refer to the following features: W - towship's wake; OW - towship's wake generated during previous run; BC - bubble cloud generated by a breaking bow wave from the towship; B - seafloor echo; S - sea surface echo; SB - surface-bottom (multiple) echo; BS - bottom-surface (multiple) echo; SBS - surface-bottom-surface (multiple) echo.

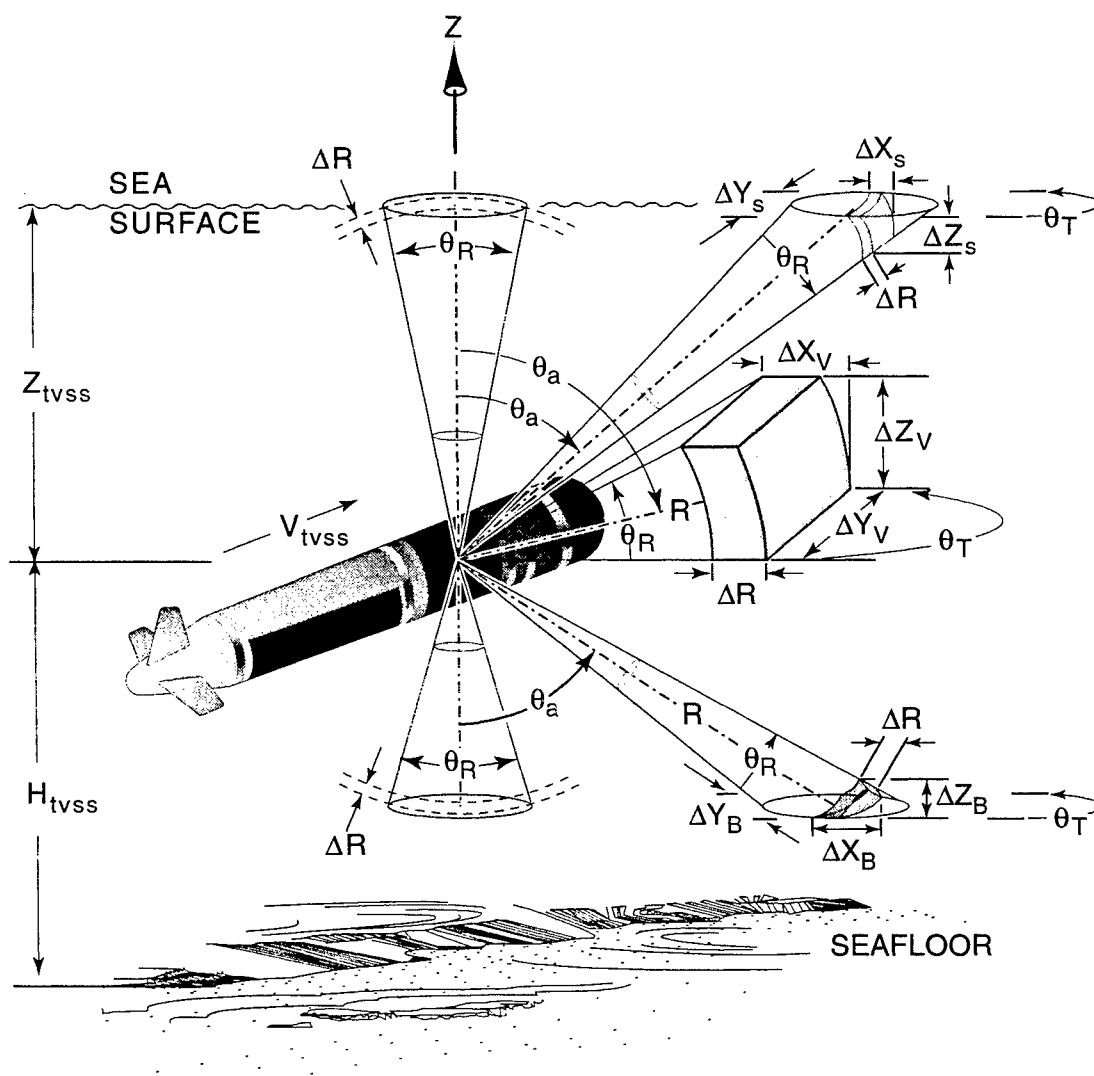


Fig. 4. TVSS acoustic geometry. The TVSS sampling volume ( $V$ ) increases with range ( $R$ ), and is defined for any angle of arrive ( $\theta_a$ ) as the ellipsoidal shell formed by the intersection of the transmitted pulse and receive beam. The transmit and receive beamwidths are  $\theta_T$  and  $\theta_R$  respectively, and the range resolution is  $\Delta R = c/2W$ , where  $W$  is the bandwidth.  $Z_{tvss}$  is the towfish's depth, and  $H_{tvss}$  is the towfish's altitude above the seafloor.  $\Delta X_V$ ,  $\Delta Y_V$ , and  $\Delta Z_V$  are the horizontal and vertical dimensions of  $V$ . On the boundaries, the area ( $A$ ) ensonified by the transmitted pulse within the receive beam is approximately an ellipse at nadir and zenith, and an annulus sector as  $\theta_a$  increases.  $\Delta X_{B,S}$ ,  $\Delta Y_{B,S}$  and  $\Delta Z_{B,S}$  are the horizontal and vertical dimensions of  $A$  on the boundaries, with subscripts ( $B$ ) and ( $S$ ) referring to the bottom and sea surface, respectively.

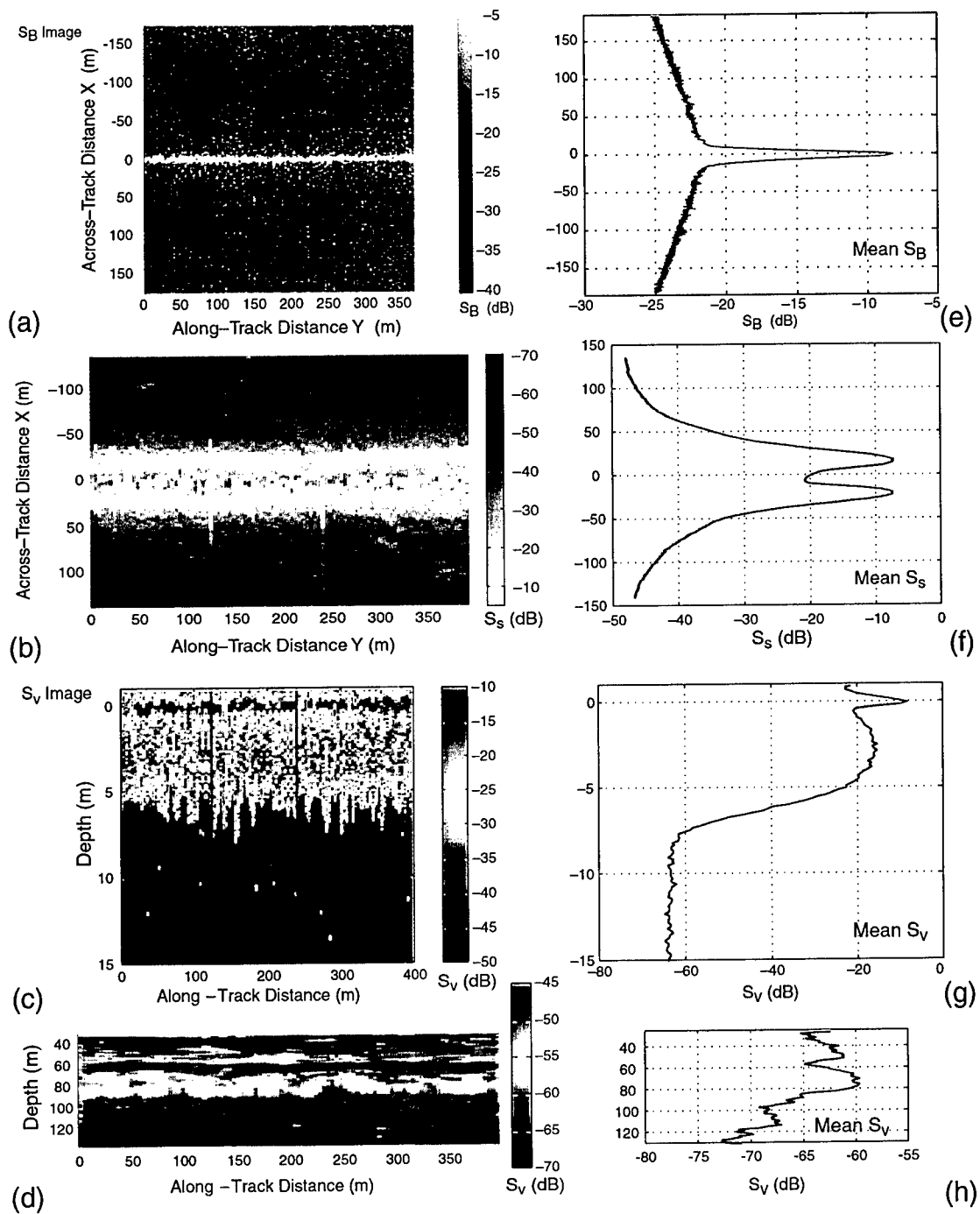


Fig. 5. TVSS-derived acoustic backscattering strength images displayed in coordinates relative to the towfish (a)-(d) and their corresponding along-track averages (e)-(h).

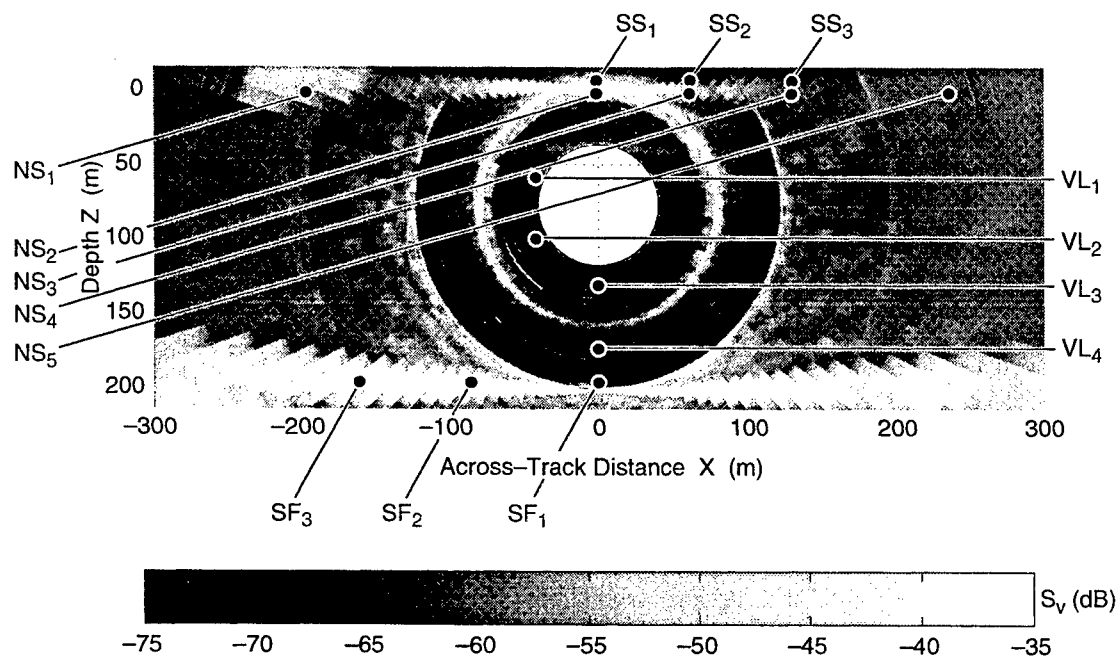


Fig. 6. Center locations of the analysis regions used in this study for a single TVSS ping. The data sets for each region consisted of 100 pings of data and spanned the horizontal and vertical dimensions listed in Table I.

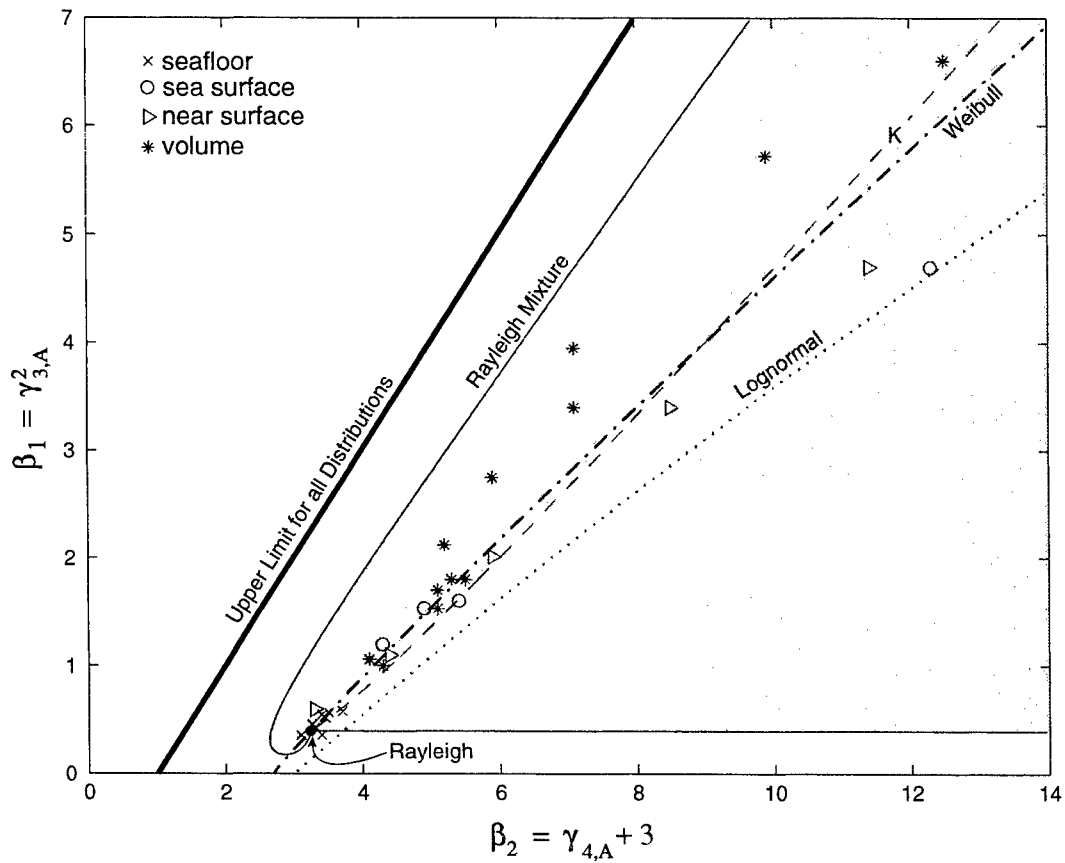


Fig. 7. Plot of  $\beta_2$  vs.  $\beta_1$  values computed from the backscattered amplitude data collected in each run and analysis region in Table I. The Rayleigh distribution is represented by a point, whereas the K, Weibull, and log-normal distributions are represented by lines. The 2-component Rayleigh mixture model is represented by a region. The basis for this figure is presented in the Appendix.

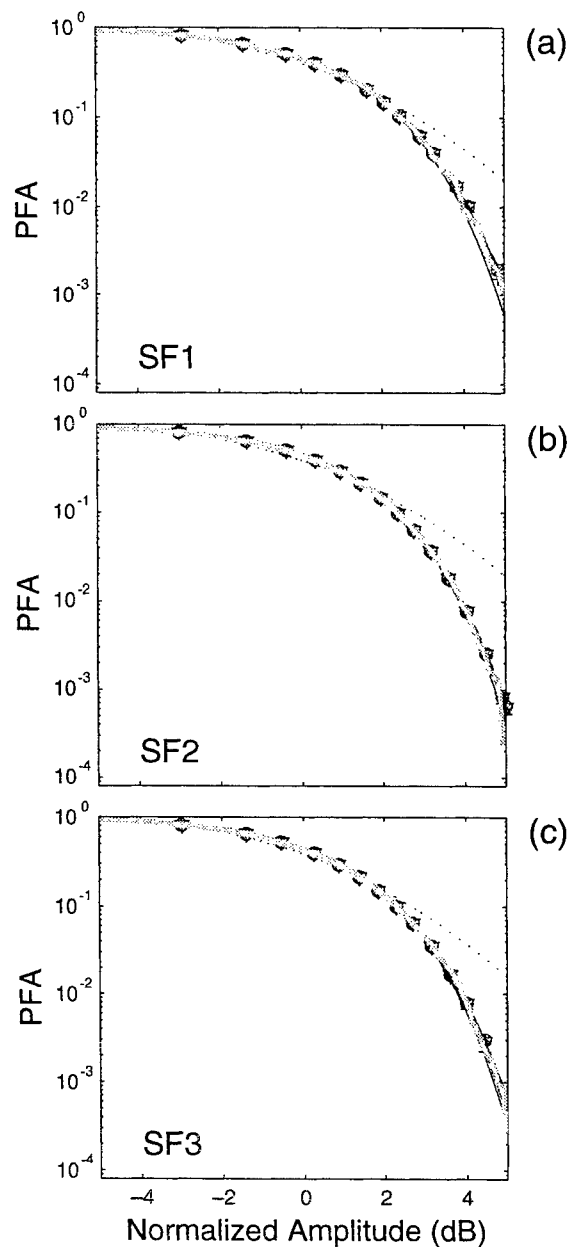


Fig. 8. Acoustic backscattered amplitude distributions displayed as probability of false alarm (PFA) for the three different seafloor regions in run 1. In this and each of the following figures like it, the gray line corresponds to the empirical distribution of the data, the dotted line is the log-normal distribution fit to the TVSS data, and the solid line is the Rayleigh fit. The K distribution fit is plotted as a dashed line, the Weibull fit with the (+) symbol, the 2-component Rayleigh Mixture with a dash-dot line, the 3-component Rayleigh mixture with the (o) symbol, the 5-component Rayleigh mixture with the (\*) symbol, and the 7-component Rayleigh mixture with the (∇) symbol.

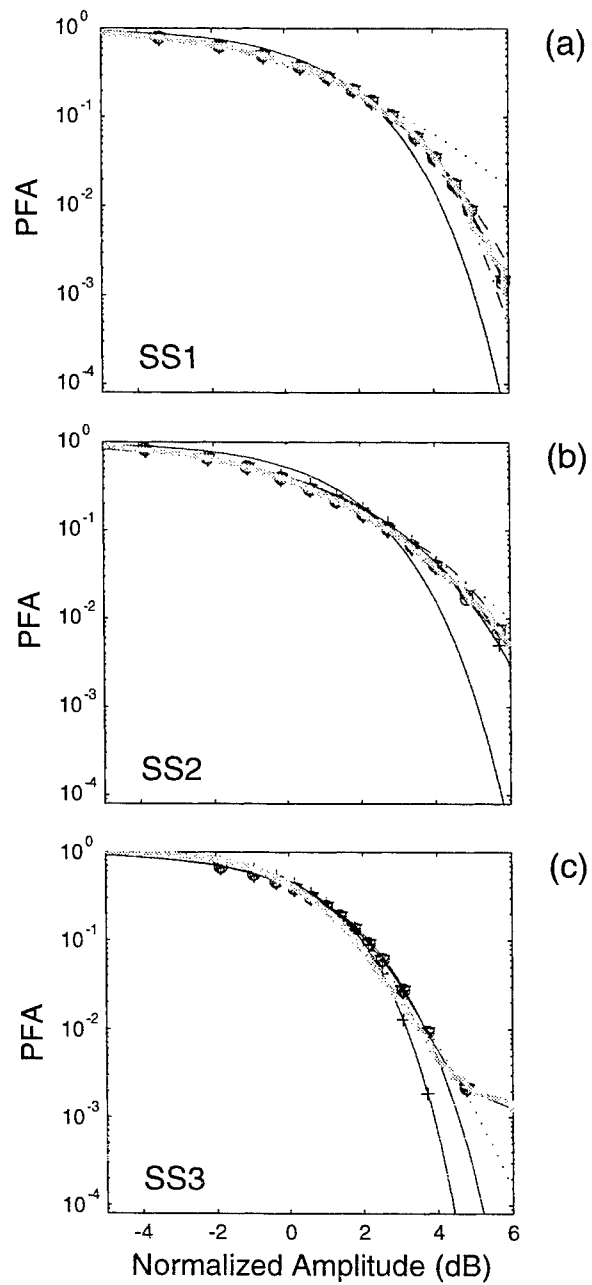


Fig. 9. PFA plots corresponding to the backscattered amplitude data from the sea surface regions in run 3. Line types for the distributions are as in Fig 8.

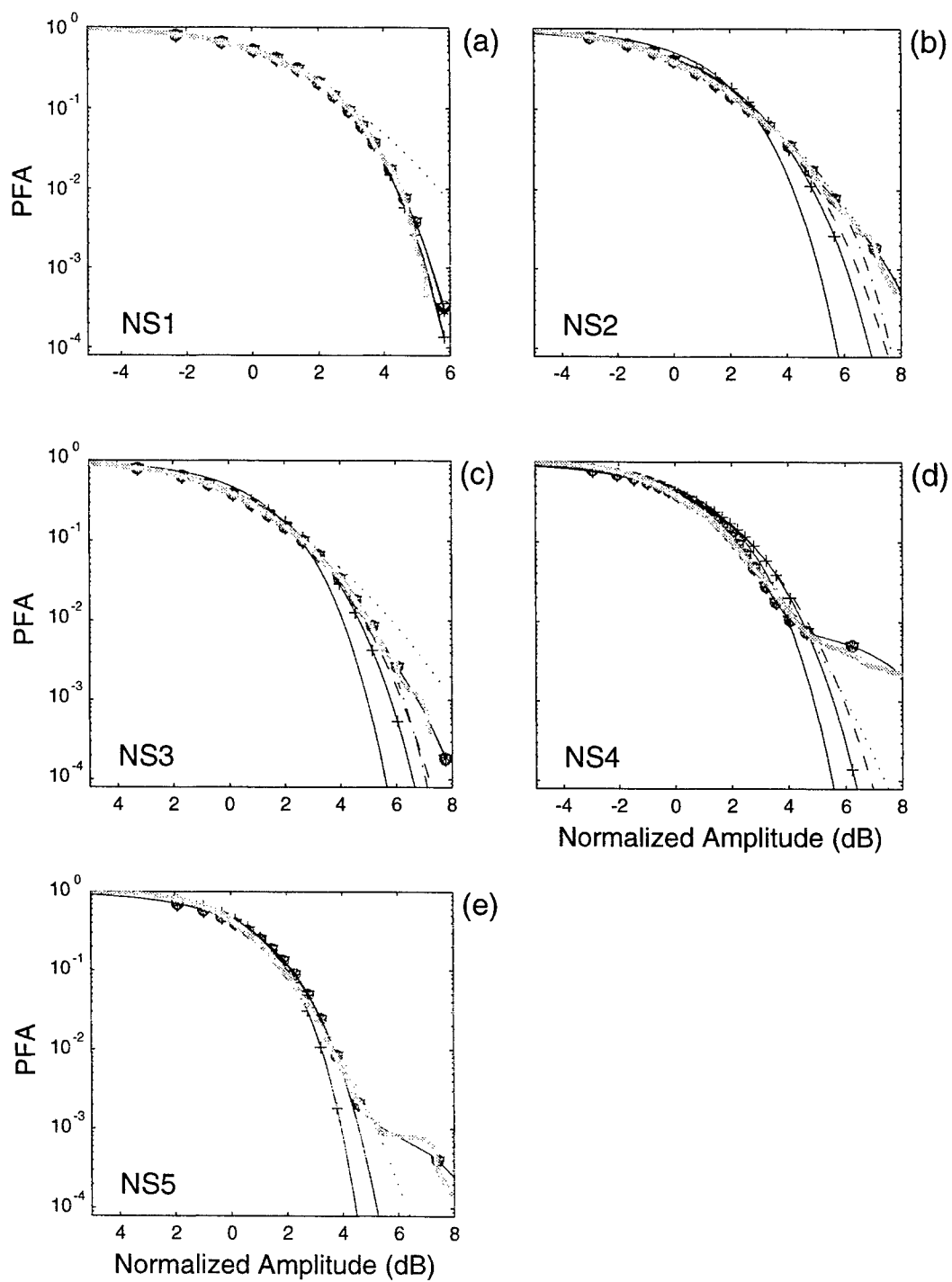


Fig. 10. PFA plots corresponding to the backscattered amplitude data from the near-surface regions in run 2. Line types for the distributions are as in Fig 8.



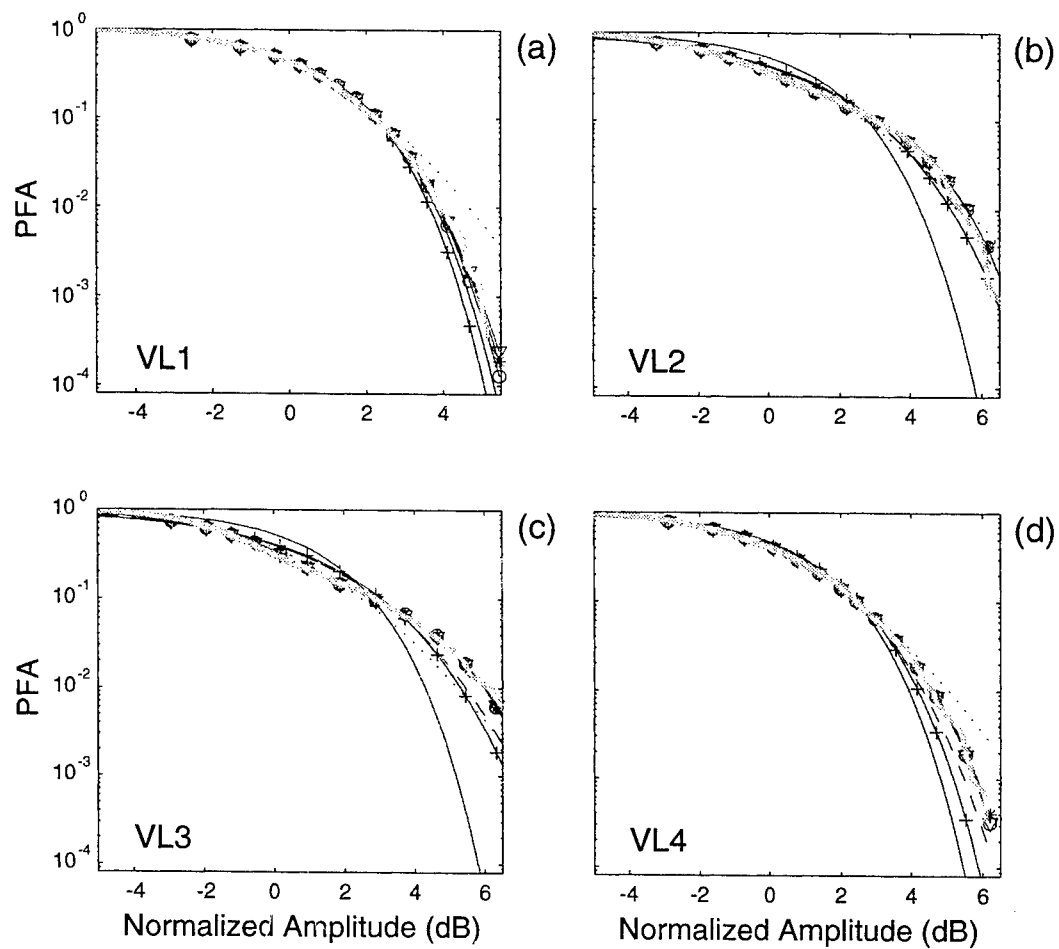


Fig. 11. PFA plots corresponding to the backscattered amplitude data from the volume regions in run 3. Line types for the distributions are as in Fig 8.

## Chapter 7

### Summary and Conclusions

In this dissertation, 68 kHz acoustic data collected by the Toroidal Volume Search Sonar (TVSS) were used to characterize volume and boundary backscatter and reverberation in a shallow water environment in the Northeastern Gulf of Mexico. The approach has been to construct acoustic backscatter imagery of the ocean boundaries, and of horizontal and vertical planes in the ocean volume. The processed imagery was used to characterize and discriminate between scattering features such as boundary roughness, multiple boundary echoes, fish, zooplankton, and near-surface bubble clouds, and provided the means for relating different spatial distributions of scatterers to various probability distribution models.

Diffraction, irregular element patterns, and high sidelobe levels were shown to be the most serious problems affecting cylindrical arrays such as the TVSS, and simulation results showed that the amplitude shading method presented in Chapter 2 reduced the peak sidelobe levels of irregular-line and non-coplanar arrays.

Errors in the towfish's attitude and motion sensor, and irregularities in the TVSS's transmitted beampattern produced artifacts in the TVSS-derived bathymetry and seafloor acoustic backscatter imagery. In Chapter 3, specific correction strategies were developed using environmental information extracted from both ocean boundaries. These are potentially useful in future AUV/UUV studies.

In Chapter 4, volume acoustic backscatter imagery was used to examine the three-dimensional structure of near-bottom pelagic fish schools and the patchiness of zooplankton in the mixed layer and upper thermocline. The results were consistent with previous studies of zooplankton and schooling fish in the Northeastern Gulf of Mexico, showing that zooplankton distributions were directly linked with mixed layer depth. The TVSS data processed in multiple narrow beams were also used to characterize the angular dependence of volume reverberation due to bioacoustic scattering layers. Although boundary reverberation in the sidelobes of TVSS receive beams directed towards the volume limited the usable range of the TVSS for bioacoustic applications, the simultaneous horizontal and vertical coverage of the TVSS were shown to warrant further use of multibeam or toroidal sonars in bioacoustic applications.

Sea surface and near-surface volume acoustic backscattering strength imagery was used in Chapter 5 to characterize the horizontal and vertical distribution of bubbles in the towship's wake and bubbles entrained in breaking waves generated by the towship and waves in the ambient sea. The acoustic data suggested that turbulent diffusion was the dominant process governing the spatial structure of the turbulent wake during the first three minutes after generation. The dominant processes affecting the wake decay were hypothesized to be gas diffusion causing dissolution, mediated by air saturation and the concentration of surfactant materials in the near-surface water. These observations are relevant to the study of naturally-occurring bubble distributions because the void fractions in the wake were approximately those found in the top 1m of the near-surface bubble layer generated by breaking waves in 10-15m/s winds. This chapter demonstrates the advantages and limitations of using multibeam sonars in studies of near-surface processes, which have been studied mostly with single beam systems.

The statistical analyses in Chapter 6 showed that the TVSS-derived seafloor and sea surface backscatter envelope (amplitude) fluctuations were well described by Weibull, K and Rayleigh mixture probability distributions, but volume backscatter envelope fluctuations were better described by the log-normal distribution. The log-normal distribution provided the best fits to volume data that were strongly influenced by boundary reverberation received in the sidelobes, or by patchy aggregations of zooplankton, but the fits to these data were not statistically good. Because these approximately log-normal distributions arose from different scattering processes, and because the tails of most of the distributions were best fit by Rayleigh mixture models, it is concluded that mixture models whose component densities are from different parametric families may be more suitable for modeling volume and near-surface backscatter and reverberation fluctuations in shallow water.

This study has several implications for undersea target detection. The non-Rayleigh nature of envelope fluctuations that arise from non-homogeneous spatial distributions of scatterers is seen in large tails and/or multimodality in the distributions. For a pre-determined probability of false alarm (PFA), this implies that threshold detectors which assume Rayleigh-distributed envelope fluctuations will experience significantly higher false alarm rates. However, even with the appropriate PDF model for envelope fluctuations due to the environment, target detection is difficult for data within the tails of the distributions. For these data, combining statistical techniques with analyses of multibeam imagery is effective in discriminating between noise and features of interest.

Possible extensions of this research exist in a number of diverse fields. The results from Chapter 2 can be applied to future conformal array design and processing applications, which are likely to increase by the nature of their economy and suitability for deployment onboard AUVs, UUVs, and ROVs. The roll error correction schemes presented in Chapter 3 are directly applicable in AUV/UUV navigation algorithms that incorporate environmental information, which, until, now have relied only on seafloor data. The results of Chapter 4 suggest an increased role for multibeam sonars in zooplankton and fisheries acoustics, especially in view of their capability for habitat characterization through seafloor imaging and bottom mapping. Similarly, Chapter 5 suggests an increased role for multibeam sonars in the study of both ship wakes and near-surface physical processes. Finally, the statistical results in Chapter 6 indicate that realistic backscatter and reverberation amplitude distributions deviate significantly from the Rayleigh model which is often assumed. Future statistical studies of backscatter and reverberation in shallow water should strive to identify the appropriate distributions that may be formed as mixtures of physically relevant PDFs from different parametric families.